Characterizing eukaryotic evolutionary environments across the Mesoproterozoic-Neoproterozoic boundary

Timothy M. Gibson

Department of Earth and Planetary Sciences

McGill University

Montréal, Quebec

May 2018

A thesis submitted to McGill University in partial fulfillment of the requirements of the degree of Doctor of Philosophy

Table of Contents

List of Figures

Chapter 1.
Introduction

Chapter 2.
Depositional history and tectonostratigraphic evolution of the Bylot Supergroup in the Borden Basin, Baffin and Bylot islands, Nunavut

Chapter 3
Precise age of *Bangiomorpha pubescens* dates the origin of oxygenic photosynthesis

Chapter 4.
Radiogenic isotope (Sr, Os, Nd) evidence for episodic hydrologic restriction in the latest Mesoproterozoic Borden Basin, Arctic Canada

Chapter 5.
Redox boundary fluctuations kick-started vigorous benthic particulate shuttling in the 811 Ma upper Fifteenmile Group, Yukon

List of Tables

Chapter 3.
Precise age of *Bangiomorpha pubescens* dates the origin of oxygenic photosynthesis

Chapter 4.
Radiogenic isotope (Sr, Os, Nd) evidence for episodic hydrologic restriction in the latest Mesoproterozoic Borden Basin, Arctic Canada

Chapter 5.
Redox boundary fluctuations kick-started vigorous benthic particulate shuttling in the 811 Ma upper Fifteenmile Group, Yukon

Acknowledgements

To my partner, Claire, for your support in all aspects of my life. You are truly my rock and I cannot thank you enough. I must also thank my parents, Mary and Mark, for introducing me to all the things that are now my passions and for encouraging me to pursue them.

This thesis would never have been possible without the perpetual generosity, positivity, and intellectual support of my supervisor, Galen Pippa Halverson. Your willingness to sign off on all my various endeavors provided me with an unusually diverse set of experiences both in the lab and in the field.

I would also like to acknowledge the many co-authors who contributed to each chapter of this work. Your contributions cannot be overstated, and many of you opened my eyes to new fields. Specifically, all of my colleagues and friends who participated in the field work that went into thesis, thanks for the tremendous support during some arduous, but mostly incredible times.

Past and present members of the PROPS Group at McGill University, as well as Paul Myrow, Justin Strauss, Alan Rooney, Mark Schmitz, Christie Rowe, and Bos Wing—thank you for your advice and encouragement throughout this endeavor. Additionally, I would like to thank my friends for their distractions and attempts to bring levity to my various predicaments. And thanks to the rest of my family for generally being great.

This thesis was funded in large part by the generous support of the Eric Mountjoy Legacy Fund, as well as from the Agouron Institute, the Geo-mapping for Energy and Minerals Program, the Polar Continental Shelf Program, the Natural Sciences and Engineering Research Council of Canada, the Yukon Geological Survey, the Yukon Foundation, the Geological Association of Canada, the Geological Association of America, and McGill University.

Finally, I would like to extend special thanks to Anita Mountjoy, my dear friend and hero, for making me feel at home in a foreign city.

Abstract

This thesis implements a combination of sedimentology, stratigraphy, geochemistry, and geochronology to characterize 1200 and 800 Ma eukaryotic evolutionary environments and elucidate the complex interplay between the Proterozoic biosphere, atmosphere, hydrosphere, and lithosphere.

The late Mesoproterozoic Bylot Supergroup in the Borden Basin provides a rare window into late Mesoproterozoic biology and geochemistry but lacked reliable depositional ages beyond broad maximum and minimum constraints (1270–720 Ma). New Re-Os radiometric dates from the middle Bylot Supergroup constrain the first known appearance of *Bangiomorpha pubescens*, the earliest crown group and photosynthetic eukaryote to ca. 1045 Ma. We calibrated molecular clock analyses with this new fossil age in order to estimate the origin of the chloroplast via primary endosymbiosis at ca. 1250 Ma. This date provides a chronological framework for understanding the role of eukaryotic oxygenic photosynthesis in global biogeochemical cycles. Results from this study also indicate that deposition of the Bylot Supergroup coincided with peak collision of the Grenville orogeny and the amalgamation of Rodinia ca. 1090–1020 Ma. Furthermore, comparing the sedimentary records between various depocentres in the Borden Basin highlights asynchronous deposition across the basin and raises the possibility that the upper Bylot Supergroup is younger than previously considered.

Radiogenic isotope (Sr, Os, and Nd) chemostratigraphic data from throughout the Bylot Supergroup elucidate complex, multi-phase tectonically-driven paleo-environmental changes in the epicratonic Borden Basin. These results demonstrate that tectonic events throughout the Uluksan Group's depositional history altered the configuration of the basin and drove episodic restriction and marine incursion. Variable marine and freshwater or brackish environments in epeiric seaways, like the Borden Basin, which were relatively widespread in the late Mesoproterozoic Era, may have exerted unique selective pressure on eukaryotic evolution. Marine limestone samples from the Bylot Supergroup provide a new age-calibrated record of the terminal Mesoproterozoic Sr isotopic composition of seawater. These data display a secular trend to more evolved compositions that likely reflects increased chemical weathering of active orogens during the amalgamation of Rodinia.

Whereas some geochemical studies suggest atmospheric oxygen increased earlier, most metal proxies indicate late Proterozoic oxygenation commenced ca. 800 Ma along with eukaryotic diversification. A multi-proxy (iron isotopes, iron speciation, and redox-sensitive elements) investigation of transgressive shale intervals from the ca. 811 Ma upper Fifteenmile Group in Yukon reveals the redox structure and highlights the processes that governed the distribution of redox-sensitive metals within the basin. Relative sea-level change in a weakly restricted basin with a redox-stratified water column kick-started vigorous dissimilatory iron reduction and benthic particulate shuttling, which produced large variations in sedimentary redox proxies that do not directly reflect changes in the redox state of the global ocean at this time.

Résumé

Cette thèse est la mise en œuvre de plusieurs approches sédimentologique, stratigraphique, géochimique et géochronologique combinées afin de caractériser l'évolution des environnements dans lesquels les eucaryotes ont évolué de 1200 à 800 Ma, et ainsi élucider l'interaction complexe existant entre la biosphère, l'atmosphère, l'hydrosphère et la lithosphère au Protérozoïque.

Le Supergroupe de Bylot au Mésoprotérozoïque supérieur, dans le bassin de Borden, offre une rare opportunité d'étudier la biologie et la géochimie à cette période, mais manque de données géochronologiques fiables,au-delà des contraintes d'âges maximum et minimum (1270–720 Ma). Nouveaux âges par datation radiométrique Re-Os du milieu du Supergroupe de Bylot restreindre la première apparition de *Bangiomorpha pubescens*, le premier eucaryote appartenant à un groupe-couronne et photosynthétique à environ 1045 Ma. Nous avons calibré des analyses d'horloge moléculaire avec ce nouvel âge fossile afin d'estimer l'origine des chloroplastes via l'endosymbiose primaire à environ 1250 Ma. Cet âge fournit un cadre chronologique permettant de mieux comprendre le rôle de la photosynthèse oxygénée chez les eucaryotes dans les cycles biogéochimiques globaux. Les résultats de cette étude indiquent également que la déposition du Supergroupe de Bylot coïncident avec la collision maximale au cours de l'orogénèse de Grenville et de l'assemblage de Rodinia à environ 1090–1020 Ma. De plus, la comparaison des données sédimentaires entre les divers dépocentres dans le bassin de Borden met en évidence une déposition asynchrone des sédiments et soulève la possibilité que la partie supérieure du Supergroupe de Bylot soit plus jeune que ce qui avait été précédemment envisagé.

Un ensemble de données chimiostratigraphiques basé sur les isotopes radiogéniques (Sr, Os et Nd) provenant de l'ensemble du Supergroupe de Bylot permettent d'élucider les changements paléo-environnementaux complexes se produisant en plusieurs étapes et contrôlés par la tectonique dans le bassin épicratonique de Borden. Ces résultats démontrent que les évènements tectoniques tout au long de l'histoire sédimentaire du Groupe Uluksan ont altéré la configuration du bassin et entraîné une restriction épisodique ainsi qu'une incursion marine. Une variation entre environnements marins et ceux d'eaux douces ou saumâtres dans un contexte de mer épicontinentales relativement répandues à la fin du Mésoprotérozoïque, tel que le bassin de Borden, peut avoir exercé une unique pression sélective sur l'évolution des eucaryotes. Les échantillons de calcaire marin provenant du Supergroupe de Bylot apportent un enregistrement,

calibré avec de nouveaux âges, de la composition isotopique en Sr de l'océan à la fin du Mésoprotérozoïque. Ces données montrent une tendance séculaire à des compositions plus évoluées reflétant vraisemblablement une altération chimique accrue lors des orogénèses au cours de l'assemblage de Rodinia.

Alors que certaines études géochimiques suggèrent que l'oxygène atmosphérique a augmenté plus tôt, la plupart des proxies métalliques indiquent que l'oxygénation de la fin du Protérozoïque a commencé à environ 800 Ma simultanément avec la diversification des eucaryotes. Une approche multi-proxies (isotopes du Fer, spéciation du Fer et les éléments sensibles aux conditions redox) sur des argiles marquant une transgression, de la partie supérieure du Groupe de Fifteenmile au Yukon à environ 811 Ma, révèlent un bassin structuré par les conditions redox et met en évidence les mécanismes régissant la distribution des métaux sensibles à l'oxydoréduction. Le changement relatif du niveau marin dans un bassin faiblement restreint avec une colonne d'eau stratifiée selon les conditions redox a déclenché une forte réduction dissimilatoire du Fe et le transport de particule benthique, ce qui a produit de grandes variations des proxies redox ne reflétant pas directement les changements d'état d'oxydorédcution de l'océan global à cette époque.

Traduit par Sarah Wörndle

Preface and Co-Author Contributions

This thesis comprises an introduction, four main chapters based on manuscripts that are either published or will be submitted for publication, and a conclusion. The four principal chapters each contain a preface that links them with the previous section in a logical and cohesive manner. The contributions of co-authors to each of these chapters are outlined below.

Chapter 2: This chapter is expanded from the manuscript entitled "Composite stratigraphic section of exceptionally exposed middle Bylot Supergroup carbonate rocks along Tremblay Sound, northwestern Baffin Island, Nunavut", which was published in the *Canada-Nunavut Geoscience Office Summary of Activities 2017* with Sarah Wörndle, Galen Halverson, Heda Agić, Kelsey Lamothe, Rob Rainbird, and Tom Skulski as co-authors. Galen Halverson and I originally conceived this project. Sarah Wörndle, Galen Halverson, Peter Crockford, Kelsey Lamothe, Heda Agić, Rob Rainbird, and Tom Skulski measured stratigraphic sections and contributed to fieldwork for this project.

Chapter 3: This chapter was published in *Geology* in 2017. Patrick Shih, Viv Cumming, Woody Fischer, Peter Crockford, Malcolm Hodgskiss, Sarah Wörndle, Rob Creaser, Rob Rainbird, Thomas Skulski, and Galen Halverson are co-authors. Galen Halverson, Patrick Shih, Woody Fischer, Rob Rainbird, Tom Skulsky, and I conceived this project, and Patrick Shih, Woody Fischer, Galen Halverson and I wrote the manuscript with input from other coauthors. Viv Cumming and I carried out Re-Os measurements and data analysis with input from Rob Creaser. Patrick Shih and Woody Fischer executed molecular clock analyses. Viv Cumming, Peter Crockford, Sarah Wörndle, Malcolm Hodgskiss, Galen Halverson, and I conducted fieldwork and sample collection.

Chapter 4: This chapter has been submitted for publication to *Geological Association of America Bulletin* with co-authors Sarah Wörndle, Peter Crockford, Hao Bui, Rob Creaser, and Galen Halverson. Galen Halverson and I conceived this project. Sarah Wörndle, Hao Bui, and I conducted carbonate sample preparation and ICP-OES analyses, and Hao Bui and I conducted TIMS analyses for Sr isotope data. Galen Halverson oversaw all carbonate chemistry and analyses.

Peter Crockford and Hao Bui prepared mudstone samples and acquired TIMS and MC-ICP-MS Nd isotope data. I prepared shale samples and analyzed their Os isotopes via TIMS under the supervision of Rob Creaser. Sarah Wörndle, Galen Halverson, Peter Crockford, and I conducted fieldwork, and I wrote the manuscript with input from co-authors.

Chapter 5: This chapter will be submitted for publication to *Geochimica et Cosmochimica Acta* with Marcus Kunzmann, André Poirier, Dirk Schumann, Nick Tosca, and Galen Halverson as co-authors. Marcus Kunzmann, Galen Halverson and I conceived the project. Marcus Kunzmann and Galen Halverson collected samples in the field. I conducted all iron isotope sample preparation and acquired MC-ICP-MS iron isotope data with significant analytical assistance from André Poirier. I prepared and analyzed samples for iron speciation (ICP-OES) and major and minor elemental composition (ICP-MS and ICP-OES) with help from Marcus Kunzmann. Dirk Schumann acquired image mosaics and conducted SEM-EDS analyses. Nick Tosca did XRD analyses and data reduction. I wrote the manuscript with input from all co-authors, most notably Marcus Kunzmann.

Chapter 1

Introduction

The late Proterozoic Eon was perhaps the most dynamic interval in all of Earth's history. Various crown group eukaryotic clades originated between 850 and 700 million years ago (Ma; Cohen and Macdonald, 2015), spanning the demise of the supercontinent Rodinia. These perturbations disrupted one billion years of apparent carbon cycle stability (Buick et al., 1995; Halverson et al., 2005) and subsequently led to oxygenation of the atmosphere and oceans (Lyons et al., 2014) and Cryogenian (720 to 635 Ma) Snowball Earth glaciations (Hoffman et al., 2017). The two Cryogenian Snowball glacial epochs in turn may have triggered the rise of algae to ecological dominance (Brocks et al., 2017; Hoshino et al., 2017) and the appearance of the first animals (Love et al., 2009). Ultimately, this chapter of our planet's history ushered in the complex life and hospitable environment fundamental to our existence on Earth today.

Considerable research is directed toward examining the complex interplay between various Earth systems in driving these globally transformative events. Many studies evoke perturbations to the global silicate weathering regime and resulting atmospheric CO_2 sequestration to explain large carbon isotope excursions directly preceding Cryogenian glaciations. Potential triggers for Snowball glaciation must meet the following criteria: (1) they are consistent with the geological record, and (2) they are capable of overriding the temperature-dependent silicate weathering feedback in climate models constructed using reasonable boundary conditions. Schrag et al. (2002) originally implicated the distribution of continental landmasses at low latitudes with modulating organic carbon burial. In this case, methane hydrate accumulation and its eventual oxidation in the atmosphere reduced the global greenhouse gas effect. Horton (2015) and Cox et al. (2016) argued that continental flood basalt emplacement and tropical weathering played a prominent role in CO_2 drawdown between ca. 850 and 720 Ma. Goddéris et al. (2003) and Donnadieu et al. (2004) proposed elevated continental weathering from changes in run-off during the fragmentation of Rodinia in low latitudes ca. 800 Ma. Gernon et al. (2016) elicit increased chemical weathering along submarine spreading ridges that accompanied the rifting of Rodinia. Alternately, various biological mechanisms, such as the radiation and diversification of algae (Feulner et al., 2015) and

other eukaryotic organisms (Tziperman et al., 2011), are also suggested triggers for Cryogenian cooling through enhancing organic carbon export and remineralization in the deep ocean.

Other work focuses on secular variation in the sources or greenhouse gasses, rather than their sinks. McKenzie et al. (2014) and McKenzie et al. (2016) interpret a nadir in global detrital zircon age spectra just before Cryogenian glaciations to reflect a reduction in continental arc magmatism—and by extension reduced volcanic degassing. Alternately, Macdonald and Wordsworth (2017) demonstrate that the ca. 720 Ma Franklin Large Igneous Province erupted through overlying sulfate evaporite deposits in the Amundsen Basin. They infer that abundant sulfur was injected into the stratosphere and converted to sulfate aerosols to increase planetary albedo. While there is no clear consensus on the specific triggers for late Proterozoic upheaval, perhaps the most likely scenario involves a series of proposed mechanisms acting in concert to produce the climatic and environmental anomalies of the Neoproterozoic Era. In order to understand how and when global biogeochemical cycles were thrown out of steady state, we must shift our attention back in time to the transition from environmental stability in the Mesoproterozoic Era (1600–1000 Ma).

Although the Mesoproterozoic climate is thought to have been particularly stagnant, the biological realm experienced tremendous innovations through this interval. Whereas the origin of the Eukarya remains unresolved, various ornamented acritarchs with likely eukaryotic affinity emerged by the beginning of the Mesoproterozoic Era (ca. 1600 Ma; Knoll and Nowak, 2017). Perhaps the most influential biological revolution since cyanobacteria evolved oxygenic photosynthesis (prior ca. 2400 Ma; Buick, 2008; Shih et al., 2016), is the transfer of this metabolic pathway to the Eukarya. All but one member of modern Archaeplastida (i.e., plants and algae) share a common organelle used for photosynthesis—the chloroplast (Keeling, 2010). Photosynthetic eukaryotes acquired the chloroplast by engulfing an ancient photosynthetic cyanobacterium in an event termed ‘primary plastid endosymbiosis’ (McFadden, 2014). Considering plants and algae are responsible for the lion’s share of modern primary productivity, identifying when this event occurred is integral to understanding the biogeochemical evolution of our planet. Many molecular clock studies have proposed age estimates for this fundamental evolutionary event and they all hinge upon the most ancient, taxonomically resolved photosynthesis eukaryote—the red algal fossil *Bangiomorpha pubescens* (Fig. 1) from the late Mesoproterozoic Bylot basins in arctic Canada (Fig. 2).

This thesis implements sedimentology and stratigraphy, geochemistry, geochronology, and molecular biology to interrogate late Mesoproterozoic to early Neoproterozoic environments in which key eukaryotes, such as *Bangiomorpha pubescens*, evolved. The goal of this work is to elucidate the relative influences of and interactions between geochemical, biological, and tectonic processes in driving environmental change across the Mesoproterozoic-Neoproterozoic boundary. The following research questions are addressed to accomplish this aim:

1. How did the tectonic history of the Borden Basin influence sedimentation patterns and facies distributions? (Chapter 2)
2. What is the age of the Bylot Supergroup? When was the chloroplast transferred to eukaryotes via primary plastid endosymbiosis? (Chapter 3)
3. What was the global chemical weathering regime during the amalgamation of Rodinia? How did the tectonic evolution of the Borden Basin influence its environment and ecology? (Chapter 4)
4. What were the effects of relative sea level change on iron biogeochemical cycles under a redox stratified water column directly preceding Neoproterozoic carbon isotope anomalies? (Chapter 5)

Chapter 2 addresses the sedimentation history of the late Mesoproterozoic Bylot Supergroup in the Borden Basin, Nunavut and makes inferences about its tectonostratigraphic history. Chapter 3 provides depositional ages for the Bylot Supergroup that constrain the first appearance of *Bangiomorpha pubescens*. This fossil age is then used to calibrate the acquisition of photosynthesis within the Eukarya. Chapter 4 investigates tectonically driven changes to the ecosystems in the Borden Basin and also tracks global changes in chemical weathering during continental collision that resulted in Rodinia. Finally, Chapter 5 reveals how iron and other redox-sensitive elements were mobilized and distributed during sea level fluctuations under a redox-stratified water column within the early Neoproterozoic Fifteenmile Group rift basin, Yukon.

This project is multidisciplinary by nature and relies on collaborative relationships between geologists and biologists from diverse fields. Results from this work elucidate the complex interplay between the Proterozoic biosphere, atmosphere, hydrosphere, and lithosphere. By characterizing eukaryotic evolutionary environments spanning the Mesoproterozoic-

Neoproterozoic boundary, this thesis will help shape our understanding of the timing and mechanisms driving global transformation.

Figures

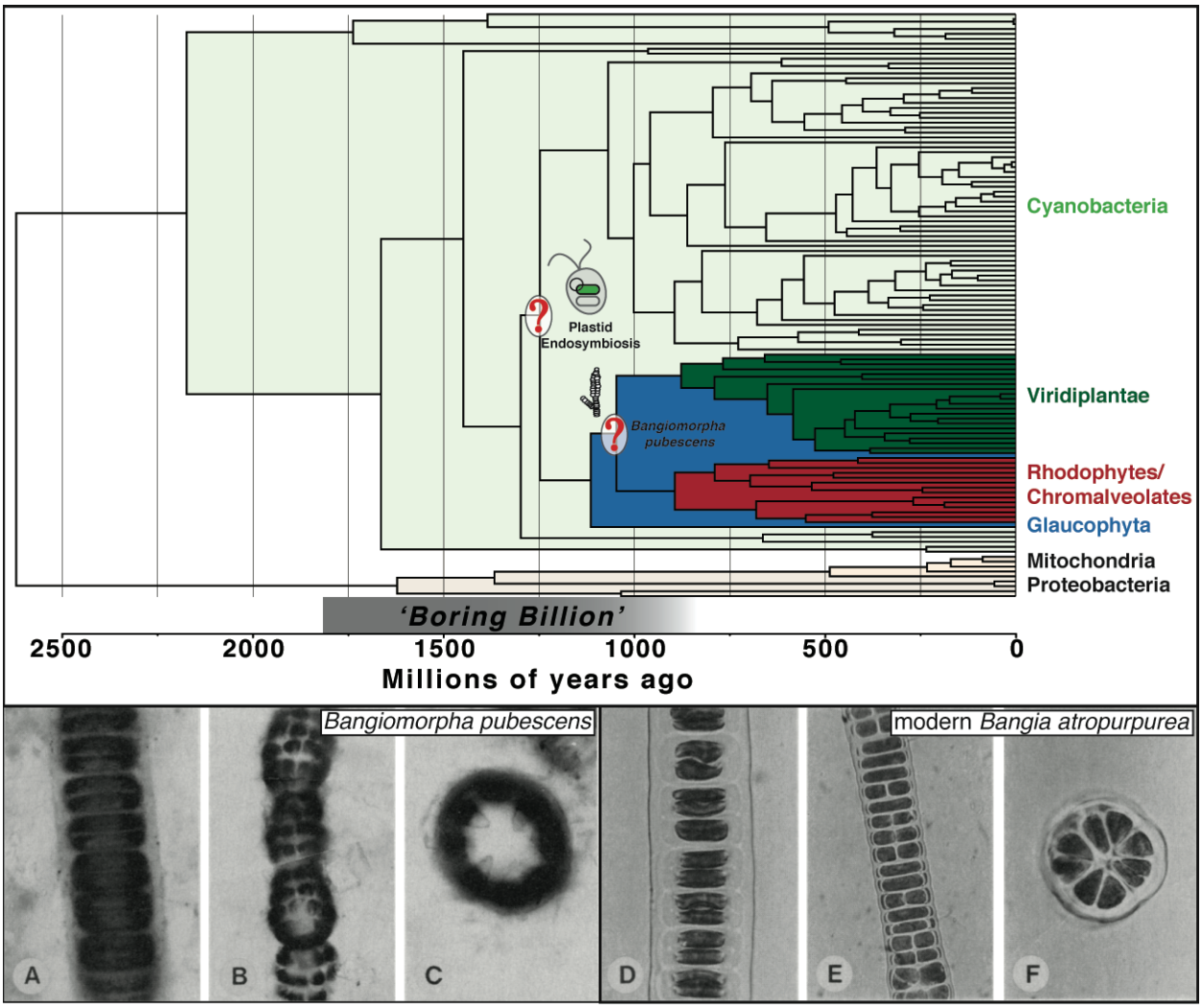

Figure 1: Schematic timeline showing primary plastid endosymbiosis calibrated by *Bangiomorpha pubescens* sometime during the 'boring billion'. Longitudinal and transverse cross-sections highlighting morphological similarities between *Bangiomorpha pubescens* fossil and modern bangiophyceaen algal filaments from Butterfield et al. (1990).

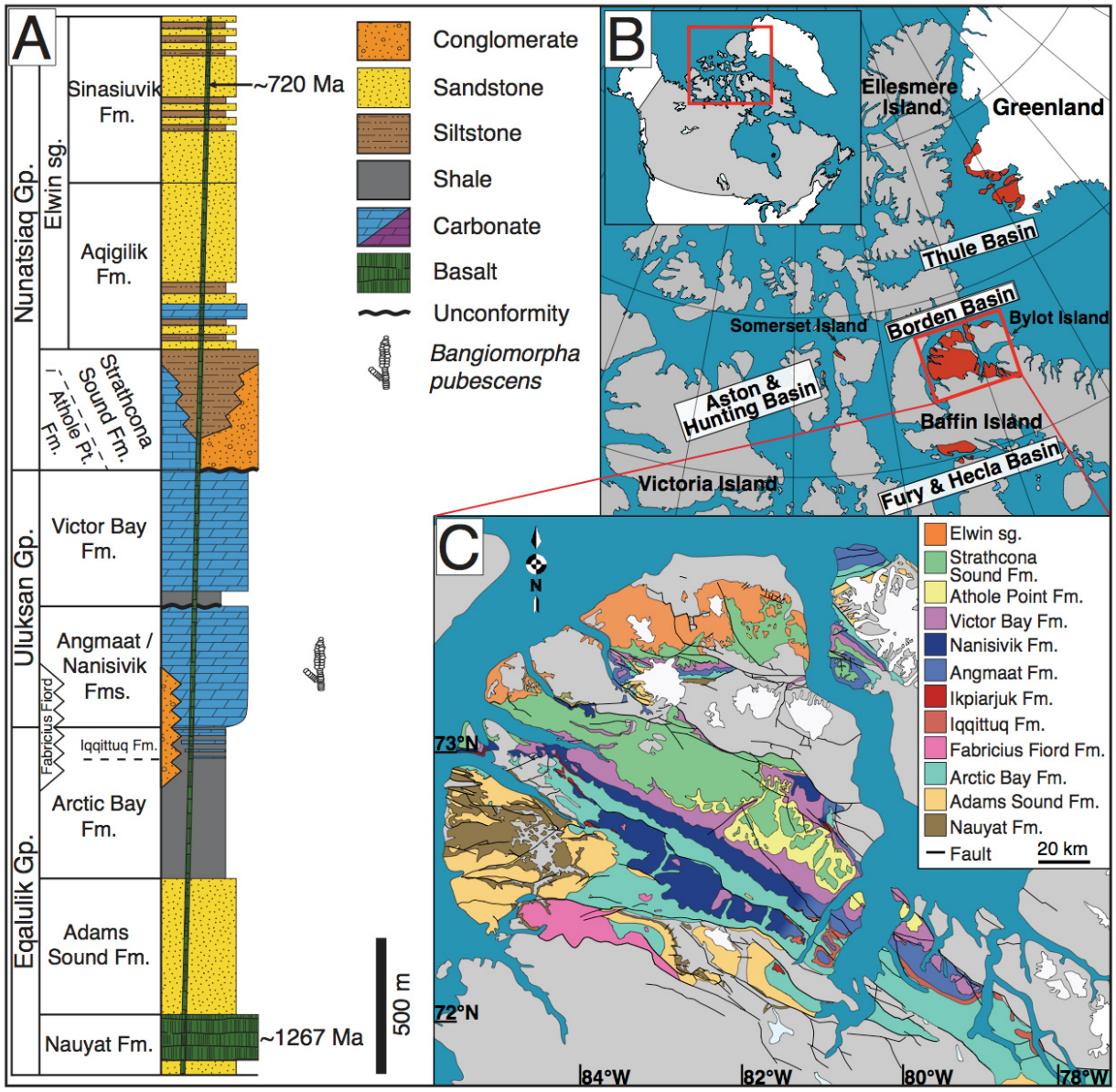

Figure 2: Location and geological context of the Bylot Supergroup in the Borden Basin. (A) Schematic lithostratigraphy of the Bylot Supergroup in the Borden Basin and stratigraphic position of *Bangiomorpha pubescens* fossils (Knoll et al., 2013). Age constraints are from LeCheminant and Heaman, (1989), Heaman et al., (1992), and Pehrsson and Buchan (1999). Gp.—Group; sg.—subgroup; Fm.—Formation; Pt.—Point. (B) Locations of the Bylot basins in northwest Canada and west Greenland (in red). (C) Map of the Borden Basin adapted from Scott and de Kemp (1998) and Turner (2009).

References

Brocks, J. J., Jarrett, A. J. M., Sirantoine, E., Hallmann, C., Hoshino, Y., and Liyanage, T., 2017, The rise of algae in Cryogenian oceans and the emergence of animals: Nature, v. 506, p. 307-318.

Buick, R., 2008, When did oxygenic photosynthesis evolve?: Philosophical Transactions of the Royal Society B: Biological Sciences, v. 363, p. 2731-2743.

Buick, R., Des Marais, D. J., and Knoll, A. H., 1995, Stable isotopic compositions of carbonates from the Mesoproterozoic Bangemall Group, northwestern Australia: Chemical Geology, v. 123, p. 1-19.

Cohen, P. A., and Macdonald, F. A., 2015, The Proterozoic Record of Eukaryotes: Paleobiology, v. 41, p. 610-632.

Cox, G. M., Halverson, G. P., Stevenson, R. K., Vokaty, M., Poirier, A., Kunzmann, M., Li, Z.-X., Denyszyn, S. W., Strauss, J. V., and Macdonald, F. A., 2016, Continental flood basalt weathering as a trigger for Neoproterozoic Snowball Earth: Earth and Planetary Science Letters, v. 446, p. 89-99.

Donnadieu, Y., Goddéris, Y., Ramstein, G., Nedelec, A., and Meert, J. G., 2004, A 'snowball Earth' climate triggered by continental break-up through changes in runoff: Nature, v. 428, p. 303-306.

Feulner, G., Hallmann, C., and Kienert, H., 2015, Snowball cooling after algal rise: Nature Geoscience, v. 8, p. 659-662.

Gernon, T., Hincks, T., Tyrrell, T., Rohling, E., and Palmer, M., 2016, Snowball Earth ocean chemistry driven by extensive ridge volcanism during Rodinia breakup: Nature Geoscience, v. 9, p. 242.

Goddéris, Y., Donnadieu, Y., Nedelec, A., Dupré, B., Dessert, C., Grard, A., Ramstein, G., and Francois, L. M., 2003, The Sturtian 'snowball' glaciation: fire and ice: Earth and Planetary Science Letters, v. 211, p. 1-12.

Halverson, G. P., Hoffman, P. F., Schrag, D. P., Maloof, A. C., and Rice, A. H. N., 2005, Toward a Neoproterozoic composite carbon-isotope record: Geological Society of America Bulletin, v. 117, p. 1181-1207.

Heaman, L. M., LeCheminant, A. N., and Rainbird, R. H., 1992, Nature and timing of Franklin igneous events, Canada: Implications for a Late Proterozoic mantle plume and the break-up of Laurentia: Earth and Planetary Science Letters, v. 109, p. 117-131.

Hoffman, P. F., Lamothe, K. G., LoBianco, S. J. C., Hodgskiss, M. S. W., Bellefroid, E. J., Johnson, B. G., Hodgin, E. B., and Halverson, G. P., 2017, Sedimentary depocenters on Snowball Earth: Case studies from the Sturtian Chuos Formation in northern Namibia: Geosphere, v. 13, p. 811-837.

Horton, F., 2015, Did phosphorus derived from the weathering of large igneous provinces fertilize the Neoproterozoic ocean?: Geochemistry, Geophysics, Geosystems, v. 16, p. 1723-1738.

Hoshino, Y., Poshibaeva, A., Meredith, W., Snape, C., Poshibaev, V., Versteegh, G. J. M., Kuznetsov, N., Leider, A., van Maldegem, L., Neumann, M., Naeher, S., Moczydlowska, M., Brocks, J. J., Jarrett, A. J. M., Tang, Q., Xiao, S., McKirdy, D., Das, S. K., Alvaro, J. J., Sansjofre, P., and Hallmann, C., 2017, Cryogenian evolution of stigmasteroid biosynthesis: Science Advances, v. 3, p. e1700887.

Keeling, P. J., 2010, The endosymbiotic origin, diversification and fate of plastids: Philosophical Transactions of the Royal Society B: Biological Sciences, v. 365, p. 729-748.

Knoll, A. H., and Nowak, M. A., 2017, The timetable of evolution: Science advances, v. 3, p. e1603076.

Knoll, A. H., Worndle, S., and Kah, L. C., 2013, Covariance of microfossil assemblages and microbialite textures across an upper Mesoproterozoic carbonate platform, v. 28 , p. 453-470.

LeCheminant, A. N., and Heaman, L. M., 1989, Mackenzie igneous events, Canada: Middle Proterozoic hotspot magmatism associated with ocean opening: Earth and Planetary Science Letters, v. 96, p. 38-48.

Love, G. D., Grosjean, E., Stalvies, C., Fike, D. A., Grotzinger, J. P., Bradley, A. S., Kelly, A. E., Bhatia, M., Meredith, W., and Snape, C. E., 2009, Fossil steroids record the appearance of Demospongiae during the Cryogenian period: Nature, v. 457 , p. 718.

Lyons, T. W., Reinhard, C. T., and Planavsky, N. J., 2014, The rise of oxygen in Earth's early ocean and atmosphere: Nature, v. 506, p. 307-315.

Macdonald, F. A., and Wordsworth, R., 2017, Initiation of Snowball Earth with volcanic sulfur aerosol emissions: Geophysical Research Letters, v. 44, p. 1938-1946.

McFadden, G. I., 2014, Origin and Evolution of Plastids and Photosynthesis in Eukaryotes: Cold Spring Harbor Perspectives in Biology, v. 6, p. a016105-a016105.

McKenzie, N. R., Horton, B. K., Loomis, S. E., Stockli, D. F., Planavsky, N. J., and Lee, C.-T. A., 2016, Continental arc volcanism as the principaldriver of icehouse-greenhouse variability: Science, v. 352, p. 444-447.

McKenzie, N. R., Hughes, N. C., Gill, B. C., and Myrow, P. M., 2014, Plate tectonic influences on Neoproterozoic-early Paleozoic climate and animal evolution: Geology, v. 42, p. 127-130.

Pehrsson, S. J., and Buchan, K. L., 1999, Borden dykes of Baffin Island, Northwest Territories: a Franklin U-Pb baddeleyite age and paleomagnetic reinterpretation: Canadian Journal of Earth Sciences, v. 36, p. 65-73.

Schrag, D. P., Berner, R. A., Hoffman, P. F., and Halverson, G. P., 2002, On the initiation of a snowball Earth: Geochemistry, Geophysics, Geosystems, v. 3, p. 1-21.

Scott, D., and De Kemp, E., 1998, Bedrock Geology Compilation Northern Baffin Island and Northern Melville Peninsula, Northwest Territories, Geological Survey of Canada, Natural Resources Canada.

Shih, P. M., Hemp, J., Ward, L. M., Matzke, N. J., and Fischer, W. W., 2016, Crown group Oxyphotobacteria postdate the rise of oxygen: Geobiology, v. 15, p. 19-29.

Turner, E. C., 2009, Mesoproterozoic carbonate systems in the Borden Basin, Nunavut: Canadian Journal of Earth Sciences, v. 46, p. 915-938.

Tziperman, E., Halevy, I., Johnston, D. T., Knoll, A. H., and Schrag, D. P., 2011, Biologically induced initiation of Neoproterozoic snowball-Earth events, v. 108, p. 15091-15096.

Preface to Chapter 2:

The ca. 1270–800 Ma Bylot Supergroup in northwestern Baffin and Bylot islands, Nunavut records evolutionary milestones, fundamental transitions in global geochemical cycles, and the tectonic development of northern Canada throughout the assembly of Rodinia. In particular, the Angmaat Formation (former Society Cliffs Formation; Turner, 2009) hosts the first occurrence of the phylogenetically important fossil, *Bangiomorpha pubescens* (Butterfield et al., 1990; Butterfield, 2000; Knoll et al., 2013), and also provides estimates for late Mesoproterozoic atmospheric CO_2 and O_2 levels (Kah and Riding, 2007; Cole et al., 2016; Gilleaudeau et al., 2016) and marine sulfate concentrations (Kah et al., 2004; Johnston et al., 2005). Fluctuations in the Bylot Supergroup $\delta^{13}C$ carbonate record from –2 to 4‰ document a first order transition in global steady-state carbon cycling (Kah et al., 1999; Kah et al., 2001) following the long-lived stasis that persisted since the late Paleoproterozoic Era (ca. 1800 Ma; Buick et al., 1995) and presaging the more dramatic oscillations characteristic of the Neoproterozoic Era (Halverson et al., 2005). Yet, despite key insights into late Mesoproterozoic Earth history provided by the Bylot Supergroup, the age and tectonic context of this remarkably well-preserved sedimentary record are poorly constrained.

The following chapter assimilates new and existing facets of the sedimentology and stratigraphic architecture of the Bylot Supergroup in the Milne Inlet Graben and Eclipse Trough. Differences in the sedimentary records between these distinct depocentres highlight the asynchronous tectonic evolution of the Borden Basin. These interpretations inform the basin-wide sequence stratigraphic correlations necessary to decipher autogenic versus allogenic controls on facies distributions in the Bylot Supergroup. Improvements in the sequence stratigraphy of the Bylot Supergroup and a new model for the tectonic evolution of the Borden Basin will eventually provide the basis for stratigraphic correlation to other basins of similar age in northern Laurentia and worldwide. Correlating the tectonostratigraphic histories of late Proterozoic intracratonic basins of northern Canada is key to unravelling the geodynamic evolution of Laurentia as part of Rodinia. Finally, results from this work will enable diverse paleontological, geochemical, and tectonostratigraphic datasets to be integrated into a coherent stratigraphic and paleoenvironmental framework.

References

Buick, R., 2008, When did oxygenic photosynthesis evolve?: Philosophical Transactions of the Royal Society B: Biological Sciences, v. 363, p. 2731-2743.

Butterfield, N.J., 2000, *Bangiomorpha pubescens* n. Gen., n. sp.: Implications for the evolution of sex, multicellularity, and the Mesoproterozoic/Neoproterozoic radiation of eukaryotes: Paleobiology, v. 26, p. 386–404.

Butterfield, N.J., Knoll, A.H., and Swett, K., 1990, A bangiophyte red alga from the Proterozoic of arctic Canada: Science, v. 250, p. 104–107.

Cole, D. B., Reinhard, C. T., Wang, X. L., Gueguen, B., Halverson, G. P., Gibson, T., Hodgskiss, M. S. W., McKenzie, N. R., Lyons, T. W., and Planavsky, N. J., 2016, A shale-hosted Cr isotope record of low atmospheric oxygen during the Proterozoic: Geology, v. 44, p. 555-558.

Gilleaudeau, G. J., Frei, R., Kaufman, A. J., Kah, L. C., Azmy, K., Bartley, J. K., Chernyavskiy, P., and Knoll, A. H., 2016, Oxygenation of the mid-Proterozoic atmosphere: clues from chromium isotopes in carbonates: Geochemical Perspectives Letters, v. 2, p. 178-186.

Halverson, G. P., Hoffman, P. F., Schrag, D. P., Maloof, A. C., and Rice, A. H. N., 2005, Toward a Neoproterozoic composite carbon-isotope record: Geological Society of America Bulletin, v. 117, p. 1181-1207.

Johnston, D. T., Wing, B. A., Farquhar, J., Kaufman, A. J., Strauss, H., Lyons, T. W., Kah, L. C., and Canfield, D. E., 2005, Active Microbial Sulfur Disproportionation in the Mesoproterozoic: Science, v. 310, p. 1477-1479.

Kah, L. C., and Riding, R., 2007, Mesoproterozoic carbon dioxide levels inferred from calcified cyanobacteria: Geology, v. 35, p. 799.

Kah, L. C., Lyons, T. W., and Frank, T. D., 2004, Low marine sulphate and protracted oxygenation of the Proterozoic biosphere: Nature, v. 431, p. 834-838.

Kah, L.C., Sherman, A.G., Narbonne, G.M., Knoll, A.H. and Kaufman, A.J. 1999, d13C stratigraphy of the Proterozoic Bylot Supergroup, Baffin Island, Canada: implications for regional lithostratigraphic correlations: Canadian Journal of Earth Sciences, v. 36, p. 313–332.

Kah, L. C., Bartley, J. K., and Teal, D. A., 2012, Chemostratigraphy of the Late Mesoproterozoic Atar Group, Taoudeni Basin, Mauritania: Muted isotopic variability, facies correlation, and global isotopic trends: Precambrian Research, v. 200-203, p. 82-103.

Knoll, A.H., Wörndle, S. and Kah, L.C. 2013: Covariance of microfossil assemblages and microbialite textures across an upper Mesoproterozoic carbonate platform: Palaios, v. 28, p. 453–470.

Turner, E.C. 2009: Mesoproterozoic carbonate systems in the Borden Basin, Nunavut: Canadian Journal of Earth Sciences, v. 46, p. 915–938.

Chapter 2

Depositional history and tectonostratigraphic evolution of the Bylot Supergroup in the Borden Basin, Baffin and Bylot islands, Nunavut[1]

[1] This chapter is expanded from the published article: "Gibson, T.M., Wörndle, S., Halverson, G.P., Agić, H., Lamothe, K.G., Rainbird, R.H., and Skulski, T., 2017, Composite stratigraphic section of exceptionally exposed middle Bylot Supergroup carbonate rocks along Tremblay Sound, northwestern Baffin Island, Nunavut. In: *Summary of Activities 2017*, Canada-Nunavut Geoscience Office, p.81–92."

Abstract

Over the course of four field seasons between 2014 and 2017, colleagues and I measured, logged and sampled 32 stratigraphic sections of the latest Mesoproterozoic Bylot Supergroup from 17 camp locations in the Borden Basin, northwestern Baffin and Bylot islands, Nunavut. These stratigraphic sections offer new insights into the depositional history of the Bylot Supergroup and elucidate distinct aspects of its architecture within the Milne Inlet Graben and Eclipse Trough. Whereas the Milne Inlet Graben has been the focus of most studies of the Bylot Supergroup, here, we provide insight into the nature and timing of sedimentation in Eclipse Trough in order to reconcile disparities in the sedimentary records across the basin. First, we highlight a previously understated tectonic event that resulted in the sub-Victor Bay Formation unconformity. We also demonstrate that uplift of the Navy Board High and half graben rotation in the Milne Inlet Graben produced asynchronous deposition of the lower Nunatsiaq Group across the basin. The complex, multiphase subsidence history in the Borden Basin makes correlations between strata in the lower Nunatsiaq Group tenuous and raises the possibility that the upper Bylot Supergroup is younger than previously considered. Results from this study provide key new insights into the geodynamic evolution of intracratonic basins in northern Laurentia as part of Rodinia.

1. Introduction

The Bylot Supergroup in northern Baffin and Bylot islands, Nunavut (Figs. 1 and 2) has been the focus of numerous studies interrogating late Mesoproterozoic biology, marine geochemistry, sedimentology, and the geodynamics of Laurentia. Nevertheless, crucial aspects of this sedimentary record remain unresolved. Perhaps the greatest uncertainty lies in the tectonic context in which the Borden Basin developed, in large part due to poor radiometric control on the timing of basin modifying events. Originally, the Bylot Supergroup was interpreted to reflect the opening of an ocean basin and subsequent transition to passive margin sedimentation (Jackson et al., 1981). Subsequently, Sherman et al., (2002) interpreted changes in the tectonic stress regime affecting the basin in the middle Bylot Supergroup in terms of continental collision along Laurentia's northern margin. More recently, Turner et al. (2016) challenged both of these models by evoking far-field trans-continental stress from Grevillian collision ~1000 km away to explain the diverse, polyphase deformation history of the Borden Basin.

Complex stratal geometry and laterally facies discontinuity indicate that syn-depositional faulting along graben-bounding faults controlled sedimentation patterns in the upper Uluksan and lower Nunatsiaq groups; however, interpretations for the tectonostratigraphic evolution of the Borden Basin have been largely based on the depositional history in the Milne Inlet Graben (Fig. 2). The primary aim of this study is to compare the sequence stratigraphic architecture of the middle to upper Bylot Supergroup in Milne Inlet Graben, which has been the primary focus of investigations here, to that of Eclipse Trough. Results from this study will help characterize the timing and nature of tectonic events that affected various depocentres in the Borden Basin. Characterizing these aspects of the tectonostratigraphic evolution of the Bylot Supergroup throughout the Borden Basin is a crucial step toward illuminating the regional tectonic context of late Mesoproterozoic intracratonic basin formation.

2. Geological Background

2.1. The Bylot Supergroup in the Borden Basin

The Borden Basin, along with the Fury and Hecla, Aston and Hunting, and Thule basins in the eastern Canadian Arctic Archipelago and west Greenland, represent broadly contemporaneous, late Mesoproterozoic intracratonic sedimentary basins collectively known as the Bylot basins (Fig. 3; Fahrig et al., 1981). These basins were originally considered to be a series of aulacogens that formed in response to the emplacement of the Mackenzie large igneous province (LIP) during the opening of the Poseidon Ocean (Jackson and Iannelli, 1981; Dostal et al., 1989). An alternate model links early extension and subsequent tectonostratigraphic evolution to far-field deformation from the ca. 1100 million year-old (Ma) Grenville orogeny during the formation of the supercontinent Rodinia (Turner et al., 2016).

The ~6 km-thick Bylot Supergroup in the Borden Basin is the best studied stratigraphic sequence of any Bylot basin (Figs. 1 and 2). Nauyat Formation basalt at the base of the succession nonconformably overlie Archean (ca. 3000–2700 Ma) orthogneiss and granite (Jackson and Berman, 2000), and are considered a distal expression of the ca. 1270 Ma LIP (LeCheminant and Heaman, 1989) due to the similarity of their paleomagnetic poles (Fahrig et al., 1981) and geochemistry (Dostal et al., 1989). Franklin dykes that crosscut the entire Bylot Supergroup constrain it to older than ca. 720 Ma (Heaman et al., 1992; Pehrsson and Buchan, 1999). Within this 1270–720 Ma interval, only a few depositional ages have been determined. Turner and Kamber (2012) estimated a depositional age for the Arctic Bay Formation of 1092 ±59 Ma using whole-rock black shale U-Th-Pb geochronology. Whole-rock black shale Re-Os geochronology yielded isochron ages of 1048 ±12 Ma for the middle Arctic Bay Formation and 1046 ±16 Ma for the lower Victor Bay Formation (Gibson et al., 2018). Together, these dates provide the only in situ depositional age control for any of the Bylot basins and suggest that the middle and upper Bylot Supergroup is younger than 1050 Ma.

The lower Eqalulik, middle Uluksan, and upper Nunatsiaq groups of the Bylot Supergroup occupy a series of northwest-trending troughs. The Milne Inlet graben on the Borden Peninsula is the largest of these and functioned as the main depocentre of the Bylot Supergroup (Fig. 2; Jackson and Iannelli, 1981). The Eclipse and North Bylot troughs occur to the northeast of the Milne Inlet

graben and contain similar Eqalulik and Uluksan group successions (Kah et al., 2001), though their tectonostratigraphic evolutionary histories during deposition of the Nunatsiaq Group may be distinct.

2.2. Tectonic Evolution of the Borden Basin

The Borden Basin encompasses three northwest trending and plunging grabens separated by basement horsts. The North Bylot, Eclipse, and Milne Inlet "troughs" or grabens are delineated by graben-bounding and intra-graben fault systems (Jackson et al., 1980; Jackson and Cumming, 1981; Jackson and Iannelli, 1981). The Bylot Supergroup primarily occurs in the Milne Inlet Graben (formerly the Milne Inlet Trough), which has an abrupt boundary on its northeastern margin formed by the White Bay Fault Zone and a more gradual boundary on its southwestern margin formed by the Central Borden Fault Zone. These structures and those that bound the Eclipse (Hartz Mountain and Aktineq fault zones) and North Bylot (Cape Hay Fault Zone) troughs were thought to accommodate early extension and govern the distribution of the basal Nauyat and Adams Sound formations in the basin (Jackson et al., 1980; Jackson and Cumming, 1981; Jackson and Iannelli, 1981). However, Long and Turner (2012) contend that early sedimentation was only minimally controlled by these graben-defining faults, and that east-directed paleocurrent data from basal strata in the Borden and Fury and Hecla basins resulted from plume-related domal uplift beneath Victoria Island. The Borden Basin would then be a distal expression of sagging that produced that Amundsen Basin (Rainbird et al., 1996; Thomson et al., 2015) rather than a series of structurally related grabens.

Graben-bounding faults were episodically active throughout the history of the Borden Basin (Jackson et al., 1980; Jackson and Iannelli, 1981; Sherman et al., 2002; Turner, 2009). Normal faulting and marine transgression resulted in the deposition of Arctic Bay Formation black shale and siltstone on a northwest-deepening terrigenous ramp within a restricted or lacustrine basin (Jackson and Iannelli, 1981; Turner and Kamber, 2012; Hahn et al., 2015). Shallow subtidal to supratidal Angmaat Formation carbonate, chert and evaporite facies in the southeast (Kah and Knoll, 1996; Kah et al., 2001) are time-correlative with rhythmically laminated, thinly bedded, carbonate-slope facies of the Nanisivik Formation in the northwest (Turner, 2009). Alluvial fans of the Fabricius Fiord Formation were deposited contemporaneously with deposition of the middle

Arctic Bay Formation through the early Angmaat and Nanisivik formations in response to rejuvenation of graben-bounding faults in the southern portion of the basin. At the same time, deep-water carbonate mounds of the Ikpiarjuk Formation precipitated from fault-controlled fluid vents in deeper portions of the basin (Turner, 2009; Hahn and Turner, 2013, 2017; Hahn et al., 2015).

Uplift and subaerial exposure of the carbonate rocks of the Angmaat, Nanisivik and Ikpiarjuk formations was succeeded by foundering of the basin and deposition of lowermost Victor Bay Formation black shale atop an erosional unconformity in the Milne Inlet Graben (Sherman et al., 2001; Turner, 2009, 2011). The basal Victor Bay shale member is absent in the Eclipse Trough (Sherman et al., 2000). Continued subsidence promoted the westward progradation of cyclically packaged carbonate-ramp facies of the upper Victor Bay Formation, along with pulses of stromatolite-reef growth (Narbonne and James, 1996). Sherman et al. (2002) interpreted the transition in facies distribution after the deposition of the Victor Bay Formation as recording differential uplift resulting from a change in basin polarity, whereby subsidence and drowning in the east accommodated deep-water Athole Point Formation calciturbidites. Simultaneously, uplift in the west eroded underlying strata and newly formed basement highs to generate the siliciclastic influx of the Strathcona Sound Formation. This bathymetric reversal is interpreted to represent the onset of contractional tectonics in the Borden Basin as a result of far-field lithospheric deformation, either due to displacement along the present northern margin of Laurentia (Sherman et al., 2002) or to Grenvillian orogenesis (Turner et al., 2016). Crucially, interpretations for an overhaul to the Borden Basin's stress regime at this time rely on tenuous correlations between diverse and laterally discontinuous siliciclastic facies of the poorly studied Strathcona Sound Formation, and interpolation about regional uplift from a single locale (Strathcona River; Fig. 2).

3. Stratigraphy

The Bylot Supergroup in the Borden Basin is cut by steeply dipping (normal) faults and Franklin diabase dykes but is otherwise minimally deformed. Thirty-two stratigraphic sections were measured, logged and sampled from 17 camp locations in the Borden Basin between 2014 and 2017 and are described below. Figure 4 contains the key to symbols used in all stratigraphic columns.

3.1. Nauyat and Adams Sound Formations

The Nauyat Formation unconformably overlies Archean to Paleoproterozoic basement of the Rae Province and occurs exclusively in the western portion of the Borden Basin and primarily in the Milne Inlet Graben between Adams Sound and Fabricius Fiord; however, there are exposures near Elwin Inlet, at the intersection between the Milne Inlet Graben and Eclipse Trough and in the North Bylot Trough (Jackson et al., 1980). Its thickness varies from ~150 to ~450 m. In some locations the Nauyat Formation contains a basal cross-bedded sandstone and conglomerate member that was initially interpreted as fluvial by Jackson et al. (1981) but reinterpreted by Turner and Kamber (2012) as shallow marine. The remaining Nauyat Formation consists of between one and five tholeiitic basalt flows. Nauyat volcanics were initially interpreted as having been extruded along graben-bounding faults (Jackson et al. 1980), but Long and Turner (2012) argue that these faults developed later in the basin's history and had little or nothing to do with early sedimentation.

The Adams Sound Formation primarily outcrops in the west and south of the Milne Inlet Graben, and like the Nauyat Formation, it also occurs near the intersection between the Milne Inlet Graben and Eclipse Trough and in the North Bylot Trough. The Adams Sound and Nauyat formations contact appears to be conformable throughout the basin, and the thickness of the Adams Sound Formation thickens from ~50 m in the eastern Milne Inlet Graben to up to ~600 m in the western Milne Inlet Graben. In the Eclipse Trough, the formation is between 300 and 400 m-thick and at least ~150 m-thick in the North Bylot Trough (Jackson et al., 1980; Jackson et al., 1981; Jackson et al., 1985). During Adams Sound Formation deposition, the Borden Basin deepened to the northwest at a very low gradient. Sandstone and conglomerate in the lower ~30 m of the Adams Sound Formation in the southeastern-most Borden Basin (near Paquet Bay) record braided fluvial deposition. These facies transition both to the northwest and up-section into shallow marine (above storm wave bae) sandstone and siltstone with minor gravel lag and dune-scale cross-stratification (Long and Turner, 2012).

Composite stratigraphic section R1607-R1608 (Fig. 5) above Adams Sound includes a near complete exposure of the Nauyat and Adams Sound formations. The basal Nauyat Formation here contains ~50 m thin- to thick-bedded, coarse to very coarse, pebbly sub-arkose sandstone with unidirectional northwest-dipping dune-scale cross-bedding (paleocurrent direction ranges 295°–355°; average = 325°; n=12). The volcanic member of the Nauyat Formation contains three distinct

basalt flows. The first flow is ~65 m-thick of massive, fine to medium grained clinopyroxene-phyric basalts with extensive chlorite and hematite alteration. The top of the first flow is highly vesicular with pillow structures, chlorite rimmed vesicles, and pipe vesicles. The second flow is ~30 m-thick and similar to the first with vesicles and pillow structures near its top. Long and Turner (2012) observed stromatolitic carbonate at the top of this flow near section R1607-R1608. The third flow comprises ~40 m-thick of massive, fine grained basalt. The uppermost ~10 m of the Nauyat Formation contains a fine grained, dark tuffaceous basalt in contact with Adams Sound Formation sandstone.

The Adams Sound Formation from section R1607-R1608 comprises predominantly well-sorted, medium to coarse grained quartz arenite (Fig. 5). Most sandstone is silica-cemented, but recessive, carbonate-cemented interbeds produce a flaggy, "sugary" weathering. Dune-scale trough (Fig. 6) and tabular cross-stratification are abundant throughout the section and up to two m-thick soft sediment slump structures become more common up-section. Low angle cross-stratification, preserved wave ripples on bedding planes, and quartz pebble lag also occur.

3.2. Arctic Bay and Ikpiarjuk Formations

The Arctic Bay Formation marks abrupt foundering of the Borden Basin. The formation thickens from ~800 m near Alpha River in the southeast to ~350 m at Shale Valley to the northwest and comprises fine-grained, often organic-rich siliciclastic and minor carbonate sediment deposited on a tectonically active, northwest-deepening terrigenous ramp. Intra-formational truncation surfaces and rotation as well as lateral thickness and facies variation suggest extensive syn-depositional seismicity along intra-graben faults (Turner, 2009; Turner and Kamber, 2012). In all locations, meter-scale shallowing-upward cycles are preserved through the lower part of the formation before grading upward into predominantly shale as a result of continued subsidence of the basin. In the deeper, northwestern portion of the Milne Inlet Graben, up to 300-m thick, deep-water carbonate mounds of the late Arctic Bay time-equivalent Ikpiarjuk Formation occur in the vicinity of major faults (Turner, 2009). Ikpiarjuk Formation mounds contain massive and clotted dolostone with isopachous dolomite cement and intraclast rudstone and can be up to hundreds of meters thick and kilometers in diameter. They are thought to have precipitated from the water

column due to interaction with fluids venting from faults and were perhaps mediated by chemotrophic microbes (Hahn and Turner, 2015; Hahn et al., 2017).

Three stratigraphic sections of the Arctic Bay Formation in the northwest Milne Inlet Graben (T1601, T1603, and T1413; Fig. 7) comprise very organic-rich, laminated shale to siltstone facies with occasional grainstone and dolomitic shale intervals (Fig. 6). Stratigraphic section T1604 of the Ikpiarjuk Formation (Fig. 7) represents the 250 m-thick "Uluksan" mound, which forms the St. Georges Society Cliffs just outside of the Hamlet Arctic Bay (Fig. 6), after which the former Society Cliffs Formation was named. This Society Cliffs Formation has since been subdivided and revised to the Ikpiarjuk, Iqqittuq, Nanisivik, and Angmaat formations in light of revised sequence-stratigraphic interpretations (Turner, 2009). Uluksan mound at section T1604 is ~260 m-thick and dominated by massive, red dolostone with abundant calcite- and dolomite-filled vugs. Microbial textures occur primarily in the lower half of the section and intraclast rudstone beds become more common toward the top.

3.3. Iqqittuq Formation

The Iqqittuq Formation thins across the study area from ~350 m in the southeast to ~150 m near Tremblay Sound and is completely absent in the northwestern-most portion of the Milne Inlet graben. It has a gradational basal contact with the underlying Arctic Bay Formation defined as the lowermost dolostone bed. This transition records initial northwest progradation toward the northwest of a distally steepened, mixed siliciclastic-carbonate ramp over the shale-dominated basin represented by the Arctic Bay Formation (Turner, 2009), perhaps coinciding with marine incursion into the basin (Kah et al., 2001). The result is interfingering of fine-grained siliciclastic facies indistinguishable from the underlying Arctic Bay Formation but with diverse carbonate facies that become more abundant up-section.

Five stratigraphic sections of the Iqqittuq Formation in the Milne Inlet Graben (stratigraphic sections T1412, SW1605, SW1604, T1410, T1411, and T1409; Fig. 8) exhibit fining and thinning trends to the northwest – sand and silt facies dominate near the type section at Angmaat Mountain (T1409) and shale and carbonate facies dominate near Alpha River, north of Tremblay Sound (T1412; Fig. 9). All sections from the Milne Inlet Graben contain interbedded orange-weathering nodular, microbial to stromatolitic, and intraclast dolomite, and rhythmically

laminated and parted lime mudstone with molar tooth structures and occasional slump folds. West-dipping dune-scale sand waves occur in the southwest. One stratigraphic section of the Iqqittuq Formation in Eclipse Trough (SW1701; Fig. 10) contains monotonous silty shale with sandstone, siltstone, and dolo-grainstone interbeds. The contact with the overlying Angmaat Formation throughout the basin is gradational and is marked by the top of the uppermost terrigenous bed (though sabkha facies in the lower Angmaat Formation contain minor siltstone horizons in the shallowest portions of the basin).

3.4. Fabricius Fiord Formation

The Fabricius Fiord Formation represents a submarine fan delta complex that developed along the Central Borden Fault Zone, which bounds the Milne Inlet Graben to the southwest, and similar facies occur in limited extent along the White Bay Fault Zone, which bounds the graben to the northwest (Jackson et al., 1980; Jackson and Iannelli, 1981). This formation conformably overlies the Adams Sound Formation and occupies the same stratigraphic position as the Arctic Bay Formation (Jackson et al., 1980). Fabricius Fiord conglomerate facies also interfinger with lower Angmaat Formation carbonates in the Central Borden Fault Zone in the southwestern Milne Inlet Graben (Fig. 2; Jackson and Iannelli, 1981). Ranging from 400 to over 2000 m-thick, Fabricius Fiord quartzarenite and subarkose sandstone, conglomerate and minor shale extend up to ~10 km from graben-bounding faults and record northward progradation of marine fan delta complexes in response to active faulting Jackson and Iannelli, 1981). No sections of the Fabricius Fiord Formation were measured for this study.

3.5. Angmaat and Nanisivik Formations

Originally, the Uluksan Group was divided into the lower Society Cliffs and upper Victor Bay formations, but its stratigraphy was subsequently revised in light of detailed sedimentological and sequence-stratigraphic data (Turner, 2003, 2004, 2009). The Society Cliffs Formation previously included all of the resistant and generally well-exposed dolostone between the black shale units of the Arctic Bay and lower Victor Bay formations. It was formally sub-divided by Turner (2009) into the Ikpiarjuk, Iqqittuq, Angmaat and Nanisivik formations. Following

development of the Iqqittuq Formation mixed carbonate-siliciclastic ramp, a peritidal carbonate environment was established in the shallowest, southeastern Milne Inlet Graben and Eclipse Trough. Subsequent northwest progradation of carbonate facies led to the stabilization of a restricted carbonate platform bound by an ooid grainstone barrier (Turner, 2009). Highly silicified peritidal and grainstone facies in the southeast (Kah and Knoll, 1996; Knoll et al., 2013; Manning-Berg and Kah, 2016) grade laterally to the northwest to thin, rhythmically bedded limestone of the Nanisivik Formation. The Nanisivik Formation both overlies the Arctic Bay Formation and onlaps relict topography created by the Ikpiarjuk Formation (Turner, 2009).

Stratigraphic sections of the Angmaat Formation (K1702, SW1605, SW1604, SW1703, T1410-G1432, and M1406 in the southeastern Milne Inlet Graben; Fig. 8; and T1701-SW1701 and G1612 in the Eclipse Trough; Fig. 10) clearly display subtidal, lagoonal, and sabkha facies near present day Tay Sound in the Milne Inlet Graben and Tay Bay in Eclipse Trough separated from the basinal, thinly bedded limestone slope facies in the northwest by a ooid grainstone barrier between White Bay and Tremblay Sound in the Milne Inlet Graben. Restricted facies are strongly silicified in the vicinity of the stratotype section at Angmaat Mountain and near White Bay (Fig. 11). These facies include rhythmically packaged alternations of mudstone–grainstone laminae and microbialite that contain abundant black and white chert nodules and beds, seafloor cement fans, and symmetric ripples. Minor green and red silt beds with desiccation cracks and laterally continuous gypsum beds occur in the lower third of the formation. Widespread dolomite-replaced, laterally extensive calcium sulfate evaporite deposits occur up to ~350 m from stratigraphic section T1701-SW1701, above which point facies preservation dramatically improves and rhythmically laminated dololutite with symmetric ripples and abundant fenestrae and primary gypsum are evident (Fig. 11). The Angmaat Formation between White Bay and Tremblay Sound in the Milne Inlet Graben and near Elwin Inlet in Eclipse Trough are dominated by grainstone facies deformed by teepee-water escape structures, though microbial lamination and stromatolites are also abundant. Seafloor-cement and interbedded black and white chert beds and nodules are also common. In the northwestern Milne Inlet Graben, near Arctic Bay, the Nanisivik Formation (stratigraphic sections T1602 and T1603; Fig. 7) contains thinly bedded limestone and dolostone with flat-pebble intraclast conglomerate and some massive dolostone facies reminiscent of the Ikpiarjuk Formation. The Nanisivik Formation is not observed in the Eclipse or North Bylot troughs.

3.6. Victor Bay Formation

The Victor Bay Formation unconformably overlies the Angmaat and Nanisivik formations, and locally, the Ikpiarjuk Formation. In the southeastern Milne Inlet Graben, up to tens of meters of karst breccia occur at this contact and the upper Angmaat Formation exhibits hundreds of meters of paleo-relief (Turner, 2011). In the northwestern Milne Inlet Graben, the Nanisivik Formation was tilted to the northeast (present coordinates), resulting in an angular and erosional contact locally. In other places this contact is manifested by an abrupt facies transition from carbonate facies to shale and mudstone of the overlying Victor Bay Formation (Turner, 2009, Turner, 2011). The informal lower member of the Victor Bay Formation in the Milne Inlet Graben comprises organic-rich mudstone interbedded with rhythmically laminated dolomitic mudstone and intraclast floatstone deposited during a marine transgression that was likely a result of local tectonic subsidence (Jackson and Iannelli, 1981). In the Eclipse Trough, the Angmaat-Victor Bay contact is less distinct and is expressed as a transition to from supratidal carbonate and evaporite facies to limestone rhythmites with minor interbedded shale. Subsequent southwestern progradation of a distally steepened carbonate ramp resulted in multiple shallowing-upward cycles of the informal upper Victor Bay member (Sherman et al., 2000; Sherman et al., 2001).

Large stromatolite reef complexes in the upper Victor Bay Formation occupy a narrow, (1–2 km wide) reef tract perpendicular to the inferred ramp paleo-strike (WNW-ESE). The reef tract separates shallower water dololutite and minor sabkha facies to the northeast from deeper water facies in the southwest. Deep water carbonate facies include thin rhythmically laminated carbonaceous limestone, nodular (ribbon) limestone and dolostone and various rudstone and floatstone limestone facies that are often packaged in 20–50 m thick shallowing upward cycles (Sherman et al., 2000; 2001). Tempestites, wave ripples, hummocky cross-stratification, and scoured surfaces in the upper Victor Bay Formation suggest deposition on a storm-dominated carbonate ramp. Molar tooth structures are common in limestone rhythmite facies, and widespread soft sediment slumps are interpreted to reflect deposition on steep slopes. The Victor Bay Formation ranges in thickness from ~150 m in the west to ~750 m in the east, though this thickness variation is in part due to erosion beneath the sub-Strathcona Sound unconformity (Jackson and Iannelli, 1981).

Ten stratigraphic sections of the Victor Bay Formation (T1707, SW1603, SW1601, SW1509, SW1703, G1431, G1432, MB1501, PWC1503, and T1508) were measured, logged and sampled from the Milne Inlet Graben (Fig. 12) and one (T1701) from the Eclipse Trough (Fig. 10). All sections in the Milne Inlet Graben have a basal organic-rich unit draping the Victor Bay-Angmaat unconformity, which is interpreted to record a rapid, tectonically induced marine transgression (Jackson and Iannelli, 1981; Sherman et al., 2000). In the Tremblay Sound area, the Victor Bay Formation (section T1707) sits atop an erosional unconformity identified by karst breccia up to tens of meters thick in the uppermost Angmaat Formation (section K1702). This erosional surface displays significant paleo-topography, but because it forms a dip slope its full thickness is difficult to measure.

The entire Victor Bay Formation comprises two broad transgression-regression (T-R) sequences. The basal Victor Bay organic-rich unit is between 10 and 40 m-thick and consists of black to gray shale except near Angmaat Mountain where it is black, organic-rich limestone and calcareous shale. Throughout the Milne Inlet Graben, the lowermost organic-rich unit grades up to progressively more carbonate-rich calcareous shale and thin bedded organic-rich rhythmite, ribbonite, and nodular limestone (Fig. 13). Together these basal units are between 80 and 120 meters thick and represent transgressive systems tract (TST) deposition within the Milne Inlet Graben (Sherman et al., 2000, 2001, 2002). The remainder of the first sequence comprises 1 to 10 m-thick shallowing upward cycles of peritidal, shallow-subtidal and deep-subtidal facies due to southwest carbonate ramp progradation of a during high stand systems tract (HST; Sherman et al., 2000; 2001). Two pulses of oblate stromatolite reef growth at this time also produced a well-developed linear northwest-southeast trending reef tract from Strathcona River in the northwest to White Bay in the southeast, trending parallel to the paleo-shoreline and White Bay Fault Zone (Narbonne and James, 1996; Sherman et al., 2002). Stratigraphic section SW1509 follows the distal margin of a ~300 m stromatolite reef in Pingo Valley (Sherman et al., 2000; 2001). Rounded to tabular intraclast rudstone and floatstone are common adjacent to reefs throughout the middle to upper Victor Bay Formation and resulted from mass wasting along the steep topography of reef buildups (Fig. 13). Many sections also exhibit evidence for mass wasting and slumping, indicative of steep antecedent topography and/or active faulting (Sherman et al., 2001). This sequence culminates with exposure of the inner ramp and development of a falling stage-lowstand wedge at the mid-ramp, outboard of the reef tract during the LST.

Through the second T-R sequence, rapid flooding during the TST and transition to HST led to aggradation and back-stepping of morphologically diverse reefs in the reef tract and laterally equivalent ramp facies that occupy the remainder of the upper Victor Bay Formation (Sherman et al., 2001; 2002). On Tremblay Peninsula (section T1707) stromatolite reefs up to 10 m wide and 6 m tall are exhumed near the contact with the overlying Athole Point Formation and grade laterally into debrite deposits, interpreted as material shed along the steep flanks of reef buildups. Abrupt relative sea level fall again exposed the reefs and significant karsting affected reef tops in the northwestern Milne Inlet Graben, especially at Strathcona River (Narbonne and James, 1996) concomitant to the creation of accommodation space and deepening in the southeast from Mala River to White Bay.

In Eclipse Trough, the Victor Bay conformably overlies Angmaat Formation stromatolitic to microbial dolostone with abundant black chert, fenestrae, and bedded gypsum (section T1701; Fig. 13). The lowermost Victor Bay Formation contains thin bedded red limestone with halite casts and numerous laterally extensive, fibrous/selenite gypsum beds and minor silty shale interbeds. Shallow water carbonate deposition appears to have continued uninterrupted across the Angmaat-Victor Bay formations contact in Eclipse and North Bylot Troughs" (Sherman et al., 2002). The basal organic-rich unit is absent in Eclipse Trough, confirming previous observations and interpretations that the early Victor Bay transgressive event resulted from faulting and subsidence restricted to the Milne Inlet Graben.

3.7. Athole Point and Strathcona Sound Formations

Uplift in the northwestern Milne Inlet Graben near Strathcona River and subsidence in the southeast resulted in deposition of distinct sedimentary successions across the basin above the Victor Bay Formation. Fine grained siliciclastic facies and minor reef-derived conglomerate delivered to the western Borden Basin represent coalescing alluvial fan-delta deposits of the Strathcona Sound Formation, which overlies the Victor Bay Formation atop an erosional unconformity (Jackson and Iannelli, 1981). In the eastern Borden Basin, the Athole Point Formation conformably overlies the Victor Bay Formation and comprises lower polymictic debrites and rapidly accreted *Conophyton* stromatolite reefs overlain by deep water carbonaceous limestone, calcareous shale, and calcisiltite facies (Sherman et al. 2001; 2002). Siliciclastic

sediment was derived from erosion of the uplifted region near Strathcona River and transported along an east-facing storm-dominated carbonate ramp by submarine density flows (i.e. turbidity currents) to the newly deepened central-eastern portion of the basin. The discordance in relative sea level change after Victor Bay Formation time is interpreted to reflect synchronous, differential uplift along the central axis of the basin in the west and subsidence in the east due to initiation of a compressional tectonic regime in the Borden Basin (Sherman et al., 2002).

The Athole Point Formation (stratigraphic sections T1509, SW1601, SW1602-R1609 in the Milne Inlet Graben; Fig. 14) is ~450 m thick and conformably overlies the Victor Bay Formation in the Tremblay Sound area but does not occur in Eclipse or North Bylot troughs. Facies are dominated by hummocky cross-stratified, fine-grained grainstone and rhythmically laminated, muddy limestone facies, which are interbedded with sandstone beds at the base. Many beds are deformed by soft-sediment slump and load structures. The siliciclastic contribution to the Athole Point Formation becomes more abundant up-section, where carbonate grainstone, rhythmites and microbialite facies alternate with channelized conglomerate and sandstone beds. However, sand and conglomerate beds are prevalent throughout stratigraphic section T1509 at Mala River, which is directly adjacent the White Bay Fault Zone, suggesting contemporaneous uplift of the Navy Board High. In section SW1602, a 5.5 cm-thick, green, aphanitic, clayey to silicified volcanic tuff bed at a stratigraphic height of 122 m (latitude 72°29"55.3’ N, longitude 80°36"16.6’ W) was identified and sampled. This tuff marks the first evidence for post-Nauyat Formation volcanism in the Bylot Supergroup.

Stratigraphic sections of the Strathcona Sound Formation from this study include T1602 and T1509 in the Milne Inlet Graben (Figs. 7 and 14) and T1605, T1606, T1511, T1704-SW1702, HA1704, and K1701 in the Eclipse Trough (Fig. 15). At Mala River, stratigraphic section T1509 is ca. 550 m-thick and comprises fining-upward sand-silt cycles and polymict cobble to boulder conglomerate with a high proportion of alkali feldspar granite clasts. Channels and soft-sediment slump folds are common. The only other stratigraphic section in this study from the Milne Inlet Graben is near Arctic Bay (T1602) and is dramatically different in character: ~90 m of primarily thinly bedded limestone and minor sand and silt facies (Fig. 16).

Facies and thicknesses (~250 m) are more consistent in Eclipse Trough. The lower portions of most sections contain thick (5–20 m) packages of monotonously laminated red and green siltstone to very fine sandstone with minor rounded dolostone-clast pebble to cobble conglomerate.

Facies coarsen to the west from predominantly siltstone at Elwin Inlet (T1605 and T1606) to interbedded sandstone and siltstone at Charles Yorke River (T1511) and Nunatsiaq Point (T1704-SW1702, HA1704, and K1701; Fig. 15). All sections of the Strathcona Sound Formation broadly coarsen and become less mature up-section. Muddy to sandy limestone and dolostone facies with cm-scale pisoids occur in the lower half of sections at Charles Yorke River and Nunatsiaq Point along with rare microbialite. The upper contact with the Aqigilik Formation is gradational, although the sub-Paleozoic unconformity truncates the Strathcona Sound Formation at Nunatsiaq Point.

3.8. Elwin "Subgroup": Aqigilik and Sinasiuvik Formations

The former Elwin Formation was divided into a lower and upper member by Jackson and Iannelli (1981) and later subdivided into the lower Aqigilik and upper Sinasiuvik formations, which together are make up the Elwin "subgroup" (this nomenclature is retained for this study; Knight and Jackson, 1994). The Elwin subgroup is up to ~1000 m thick and occurs only in Eclipse Trough and the northwestern-most Milne Inlet Graben, between Strathcona Sound and Elwin Inlet. Both the Aqigilik and Sinasiuvik formations are made up almost entirely of siliciclastic facies deposited in shallow marine to alluvial braidplain environments after the Borden Basin transitioned from active faulting (during Strathcona Sound Formation deposition) to thermal subsidence (Jackson and Iannelli, 1981; Jackson et al., 1985; Knight and Jackson, 1994).

The base of the Aqigilik Formation is conformable and gradational with the underlying Strathcona Sound Formation everywhere and is marked by a transition from interbedded green siltstone and thin sandstone beds to massive and dune-scale cross-bedded sub-arkose and quartz arenite. In western Eclipse Trough (stratigraphic sections T1606-T1607, T1511, and T1512; Fig. 17) where the Aqigilik Formation is up to ~500 m-thick, facies grade upwards to interbedded quartz arenite or sub-lithic-arenite and siltstone with abundant thick-bedded, medium to coarse, poorly carbonate- or glauconite-cemented quartz arenite (Fig. 18). Distinct ~5–20 m thick parallel laminated red and green siltstone beds in the middle of the Aqigilik Formation are laterally traceable in eastern Eclipse Trough, and minor wavy bedded calcilutite facies also occur. The Aqigilik Formation in western Eclipse Trough (stratigraphic sections T1704-SW1702 and K1701) is significantly thinner (~200 m) because the sub-Cambro-Ordovician (Admiralty Group; Trettin,

1969) erosional unconformity cuts down into it. Sedimentary features common in the Aqigilik Formation across the basin include symmetric and asymmetric ripples, dune-scale tabular cross-beds, mud rip-up clasts, carbonate flat pebble conglomerate, red beds, soft sediment slump folds, halite casts, and gutter casts. Knight and Jackson (1994) interpreted the Aqigilik Formation to represent a stable, shallow-marine shelf. The lower Aqigilik Formation contains shallow marine deposits overlain by northeast prograding sheet-flood-dominated alluvial braidplain and laterally equivalent intertidal deposits, which are then succeeded by lower shoreface to lagoonal deposits.

The contact between the Aqigilik and Sinasiuvik formations is defined as a transition back to shallow marine deposits as a result of marine transgression (Knight and Jackson, 1994). Three transgressive-regressive cycles define the Sinasiuvik Formation, which is only preserved in the eastern Eclipse Trough near Elwin Inlet, presumably because the sub-Cambro-Ordovician erosional unconformity cuts it out elsewhere. Stratigraphic sections T1607 and T1510 (Fig. 19) represent a composite of the Sinasiuvik Formation stratotype section above Elwin Inlet (Knight and Jackson, 1994) which is ~430 m thick. Much of the Sinasiuvik Formation comprises symmetric thinning-fining and thickening-coarsening cycles of parallel laminated to tabular cross-bedded quartzarenite sandstone interbedded with and gray to black or maroon siltstone and silty shale (Fig. 18). Consistent shallow marine deposition between storm and fair-weather wave base with new evidence for syn-depositional tectonism indicate that Eclipse Trough experienced gradual subsidence throughout deposition of the Sinasiuvik Formation.

4. Discussion

The Borden Basin consistently deepened from the east-south east to the west-northwest throughout deposition of the Arctic Bay through Angmaat formations. Uplift in the northwestern Borden Basin then tilted the Nanisivik-Angmaat formations carbonate system down the northeast, resulting in an angular unconformity beneath the Victor Bay Formation. This angular contact is most pronounced in the vicinity of the hamlet of Arctic Bay (Fig. 2). Sherman et al. (2002) interpreted changes in the polarity of the Borden Basin during late Victor Bay Formation time as resulting from a novel tectonic regime; however, uplift in the northwestern Milne Inlet Graben and transformation to a southwest-deepening profile in the lower Victor Bay Formation represents an earlier tectonic event that could have resulted from similar kinematics as late Victor Bay uplift in

the Strathcona River region. This event that produced uplift and widespread erosion of the Angmaat and Nanisivik Formations beneath the sub-Victor Bay unconformity, was limited to the Milne Inlet Graben and did not affect Eclipse Trough. Further stratigraphic analysis, regional mapping, or additional data sets are required to characterize the stress regime affecting the basin at this time.

Although the Victor Bay Formation unconformably overlies the Angmaat Formation everywhere in the Milne Inlet Graben, this contact is marked by a conformable flooding surface in Eclipse Trough (Fig. 10). This relationship suggests that the unconformity in the Milne Inlet Graben represents a relatively short amount of time, which is consistent with the ~2 Myr difference in Re-Os depositional ages for the Arctic Bay (ca. 1048 Ma) and basal Victor Bay (ca. 1046 Ma) formations (Gibson et al., 2018). Deposition of the Athole Point and Strathcona Sound formations has been interpreted as broadly coeval and their differences a result of simultaneous subsidence in the eastern Borden Basin and uplift in the west (Sherman et al. 2002). Therefore, since the Athole Point Formation conformably overlies the Victor Bay Formation and the Elwin subgroup is conformable with the Strathcona Sound Formation, the Nunatsiaq Group as a whole should not be significantly younger than the Uluksan Group.

A critical aspect of this interpretation is the observation that Athole Point Formation calci-turbidites transition gradationally into the overlying immature siliciclastic facies of the Strathcona Sound Formation and therefore sedimentation was uninterrupted in some portions of the basin. However, the Athole Point Formation only occurs in the Milne Inlet Graben and the Elwin subgroup only occurs in Eclipse Trough. Furthermore, facies of the Strathcona Sound Formation that interfinger with and overlie the Athole Point Formation represent localized fan deltas shedding off basement highs and so correlation across the various depocentres of the basin is complicated by dramatic lateral facies variation. Therefore, these relationships rely on tenuous correlation between sedimentologically distinct siliciclastic units in the Milne Inlet Graben and Eclipse Trough that is based largely on their stratigraphic positions and not on observable contacts or geometries (Fig. 15). This raises the possibility that stratigraphic relationships in the lower Nunatsiaq Group (i.e., the Victor Bay and Strathcona Sound formations are broadly coeval) have been previously misinterpreted and that the sub-Strathcona Sound Formation unconformity represents a basin-wide depositional hiatus. In this case, what was previously interpreted as a gradational transition from the Athole Point to Strathcona Sound Formation in the Milne Inlet

Graben simply reflects localized sediment shedding off the Navy Board High during activation of the White Bay Fault Zone, contemporaneous with Athole Point carbonate deposition (Fig. 2). Therefore, the Strathcona Sound Formation and Elwin subgroup could in fact be much younger than the rest of the Bylot Supergroup.

The Strathcona Sound Formation in the Milne Inlet Graben at Mala River contains abundant pebble to boulder K-keldspar granitoid clasts and is approximately twice as thick as compared to anywhere in Eclipse Trough (Figs. 2 and 15). These aspects of stratigraphic section T1509, which is directly adjacent the White Bay Fault Zone, are indicative of syn-depositional normal faulting and uplift of the modern Navy Board High. In Eclipse Trough, a black shale transgressive interval at the base of the Strathcona Sound Formation at Elwin Inlet South (T1605; Fig. 15) fills in a large paleo-valley along the sub-Strathcona Sound Formation unconformity, where the Victory Bay Formation and much of the Angmaat Formation were eroded (Fig. 16A). The Strathcona Sound Formation in Eclipse Trough generally fines and deepens to the south and west toward the Hartz Mountain Fault Zone, which forms the opposite margin of the Navy Board High but exhibits no sedimentary evidence for contemporaneous faulting.

The inconsistent depositional histories of the Strathcona Sound Formation in each location require that subsidence occurred asynchronously between these depocentres. First, northeast-side down half graben rotation promoted submarine fan-delta growth along the White Bay Fault Zone in the eastern Milne Inlet Graben and concomitant uplift in the western Borden Basin that resulted in erosion of underlying strata. These tectonic adjustments were likely instrumental in the transformation of the Borden Basin's geometry during early Nunatsiaq Group time. Gentle subsidence in the Eclipse Trough commenced later and generated a marine transgression once the topography of the uplifted Navy Board High had largely eroded. These observations and interpretations are counter to those of Jackson et al. (1980) and Jackson and Iannelli (1981), who interpreted early Strathcona Sound sedimentation to record coalescing alluvial fan complexes on either side of Navy Board High; however, the presence of polymict conglomeratic alluvial fan facies along the Hartz Mountain Fault Zone in Eclipse Trough were never observed, only inferred (see Figs. 46.3 and 46.4 form Jackson et al., 1980 and Fig. 16.22 from Jackson and Iannelli, 1981). Rather, Eclipse Trough deepened gently to the west and south at this time, toward the intersection with the Milne Inlet Graben at Strathcona Sound (Fig. 2). These distinct tectonostratigraphic records highlight problems associated with correlations between the Strathcona Sound Formation

between these two depocentres. Additional work is required to confirm the difference in timing between deposition of the lower Nunatsiaq Group in the Milne Inlet Graben versus the Strathcona Sound Formation. If deposition was wholly asynchronous, as proposed herein, the current subdivision of the upper Uluksan and lower Nunatsiaq groups must be reconsidered.

The Elwin Formation was subdivided into the lower Aqigilik and upper Sinasiuvik formations by Knight and Jackson (1994), who also changed its status to "subgroup". Similar to the Strathcona Sound Formation, the Elwin subgroup is only preserved in Eclipse Trough and in the far northwestern Milne Inlet Graben, near where the two intersect. Both the Aqigilik and Sinasiuvik formations are dominantly sandstone and neither contain significant shale or conglomerate facies. No conclusive evidence for fluvial deposition was observed in the Elwin subgroup over the course of this study, and sedimentary features proposed by Knight and Jackson (1994) to reflect fluvial (i.e., sheet-flood or braidplain) deposition, also form in shallow water environments. Therefore, deposition of nearly the entire ~1000 m-thick Elwin subgroup may have occurred exclusively in environments between subtidal and storm wave-base. Facies trends suggest the basin deepened gently to the west at this time and that there was no intrabasinal faulting, so accommodation space was likely created by broad subsidence, similar to the Strathcona Sound Formation in Eclipse Trough. Finally, we propose changing the nomenclature of these units to follow the North American Stratigraphic Code (2005). The "Elwin subgroup" should be discarded, and the Aqigilik and Sinasiuvik formations should stand on their own as part of the Nunatsiaq Group, keeping their original stratotype sections from Knight and Jackson (1994).

5. Conclusions

They Bylot Supergroup in the Borden Basin is the most thoroughly studied stratigraphic succession of any Bylot basin, yet there remain many outstanding questions regarding its tectonostratigraphic evolution and timing of depositional events. Previous work focused on tectonically driven changes in basin geometry during late Uluksan to early Nunatsiaq group time. Stratigraphic analysis reveals that uplift of the Navy Board High and half graben rotation was responsible for these changes. We also highlight that Borden Basin underwent an earlier tectonic reconfiguration of the between deposition of the Nanisvik/Angmaat and Victor Bay formations, and that half graben rotation that was confined to the Milne Inlet Graben is kinematically consistent

with both events. Finally, complex facies relationships in the lower Nunatsiaq Group have obscured correlation between the Milne Inlet Graben an Eclipse Trough, but sedimentological data herein demonstrates that deposition of the Strathcona Sound Formation occurred asynchronously between these two depocentres. Although more data is required to conclusively link these new insights into the tectonic history of the Borden Basin to continental-scale tectonic events, results from this study represent an integral step toward understanding the geodynamics associated with anomalous intracratonic basin formation in northern Laurentia as part of Rodinia.

Acknowledgements

A thoughtful review of a previous version of this chapter was provided by L. Kah. This project is supported by the Geo-mapping for Energy and Minerals (GEM) and GEM-2 programs of Natural Resources Canada, the Natural Sciences and Engineering Research Council, the Polar Continental Shelf Program, the Northern Science Training Program, the Agouron Institute and McGill University. The authors thank the Qikiqtani Inuit Association, Nunavut Planning Commission, Nunavut Research Institute and both the Sirmilik National Park of Canada office and Nunavut Field Unit of Parks Canada. Malcolm Hodgskiss, Peter Crockford, Vivien Cumming, Devon Cole and Noah Planavsky assisted with fieldwork.

Figures

Figure 1: The Bylot basins in northeast Arctic Canada and west Greenland.

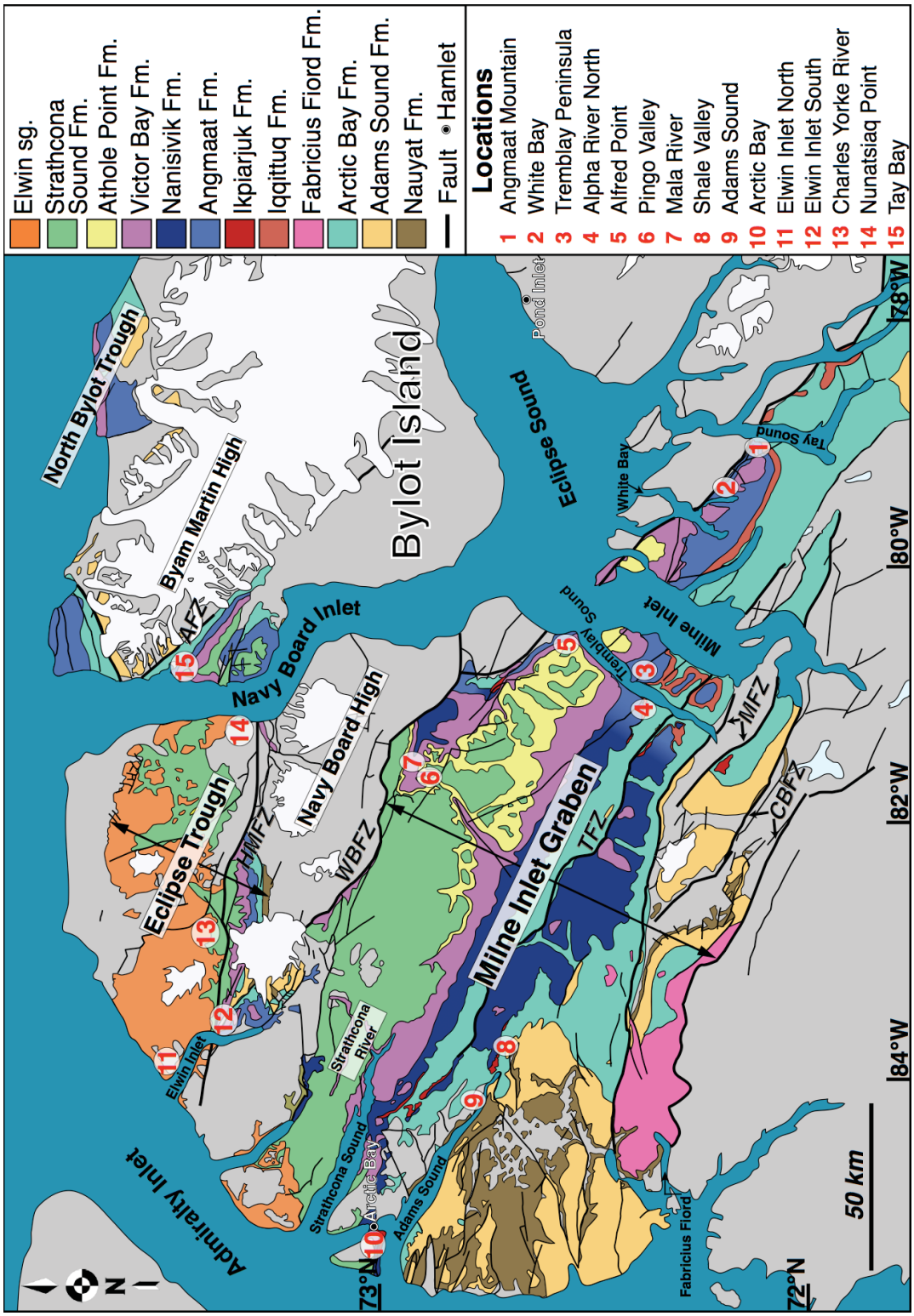

Figure 2: Geological map of the Borden Basin on northern Baffin and Bylot islands (After Scott and de Kemp, 1998 and Turner, 2009). Abbreviations for structural features: CBFZ—Central Borden Fault Zone; MFZ—Magda Fault Zone; TFZ—Tikirarjuaq Fault Zone; WBFZ—White Bay Fault Zone; HMFZ—Hartz Mountain Fault Zone; AFZ—Actineq Fault Zone. Red numbers correspond to camp locations visited as part of this thesis.

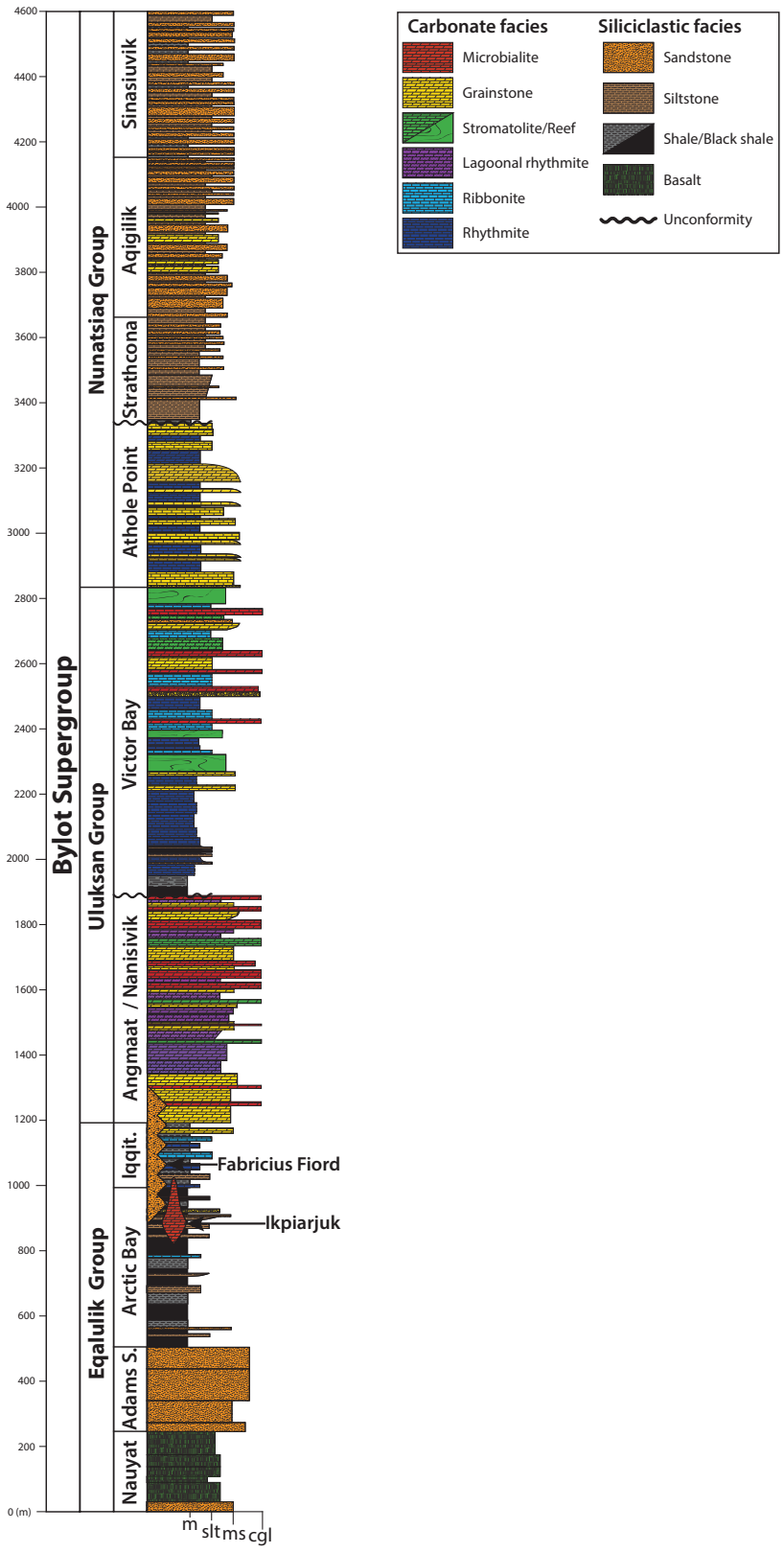

Figure 3: Schematic stratigraphic column of the Bylot Supergroup.

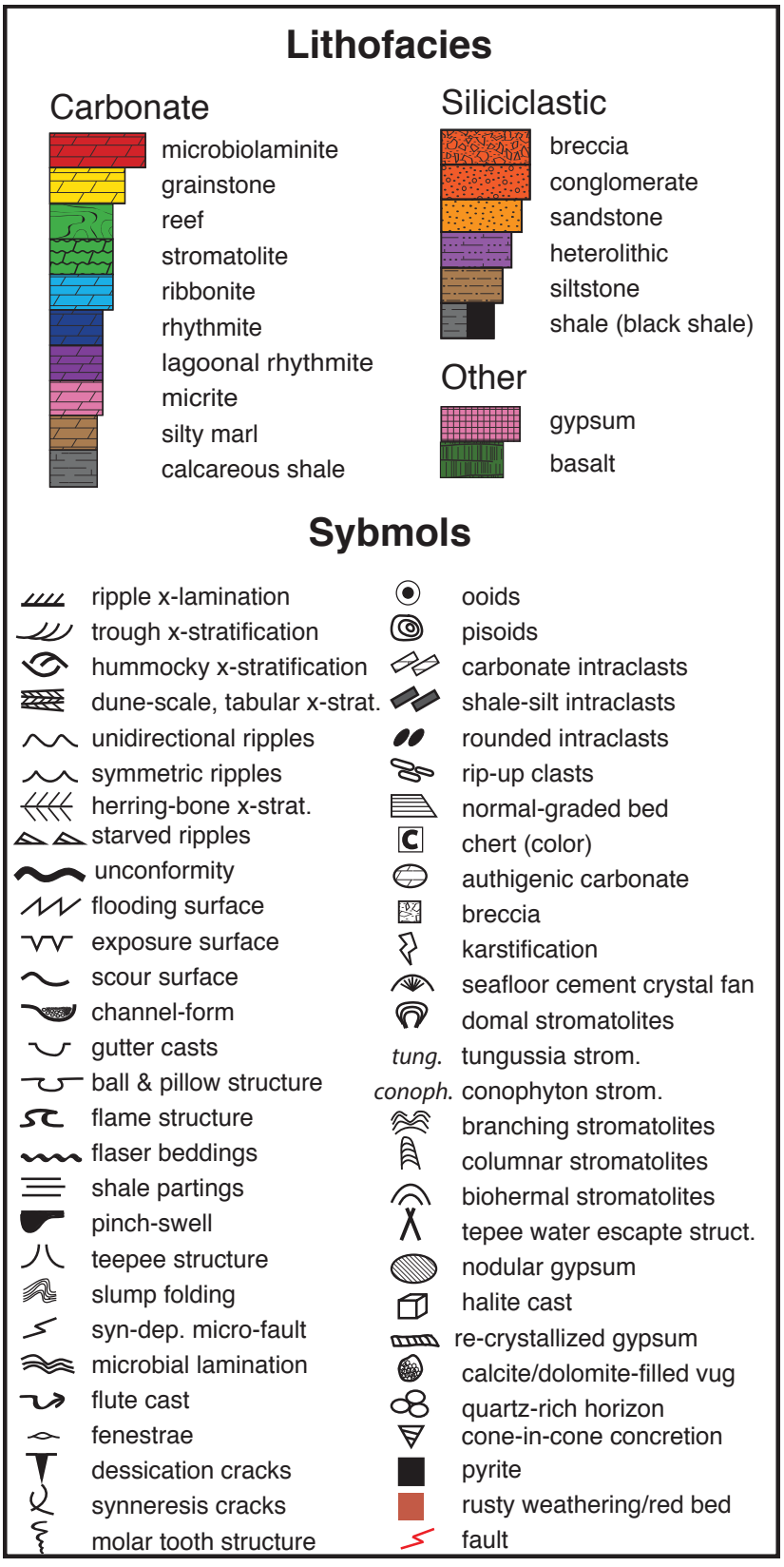

Figure 4: Key to symbols and lithologies used in all stratigraphic columns.

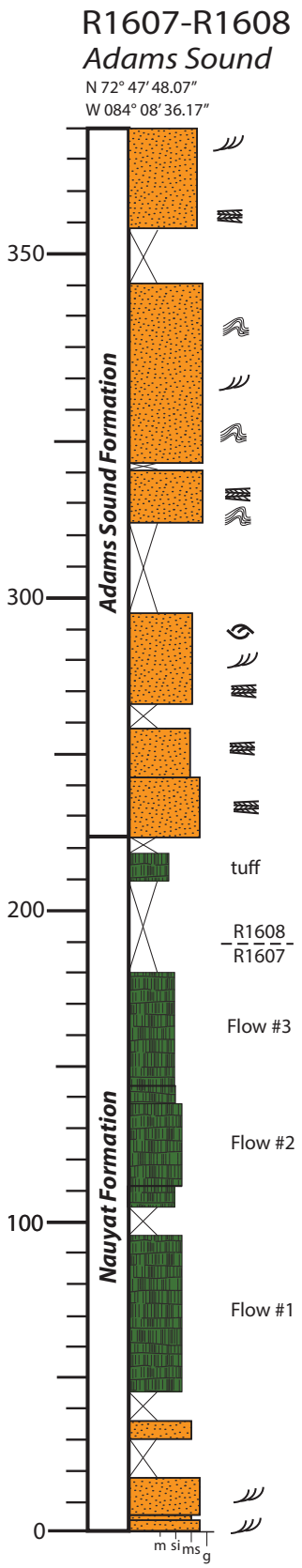

Figure 5: Stratigraphic column of the Nauyat and Adams Sound formations from above Adams Sound.

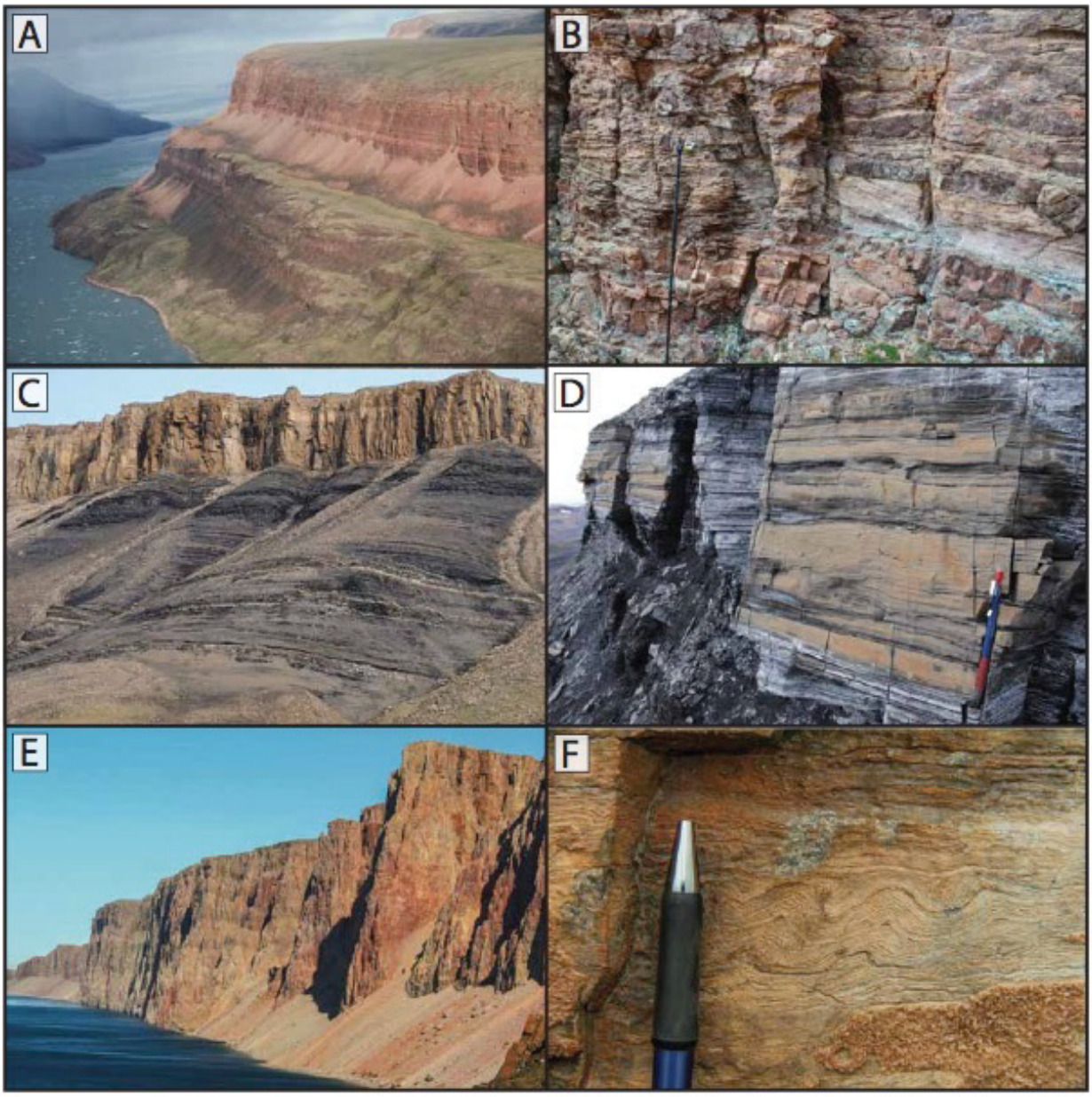

Figure 6: Photo plate of the Nauyat, Adams Sound, Arctic Bay, Iqqittuq, and Ikpiarjuk formations. (A) The Nauyat and Adams Sound formations above Adams Sound. Composite stratigraphic section R1607-R1608 is just out of view to the right of the photo. (B) Trough cross-bedded sub-arkose sandstone of the Adams Sound Formation from ~320 m stratigraphic height from section R1607-R1608. (C) Arctic Bay and Ikpiarjuk formations at Shale Valley. Stratigraphic section T1413 follows the rounded ridge on the right. (D) Upper Arctic Bay Formation thinly laminated dolomitic shale from 263 m stratigraphic height from section T1413. (E) Uluksan mound of the Ikpiarjuk Formation, also known as St. Georges Society Cliffs near Arctic Bay. Stratigraphic section T1604 follows talus-filled gully on the right. (F) Microbialite of the Ikpiarjuk Formation from section T1604.

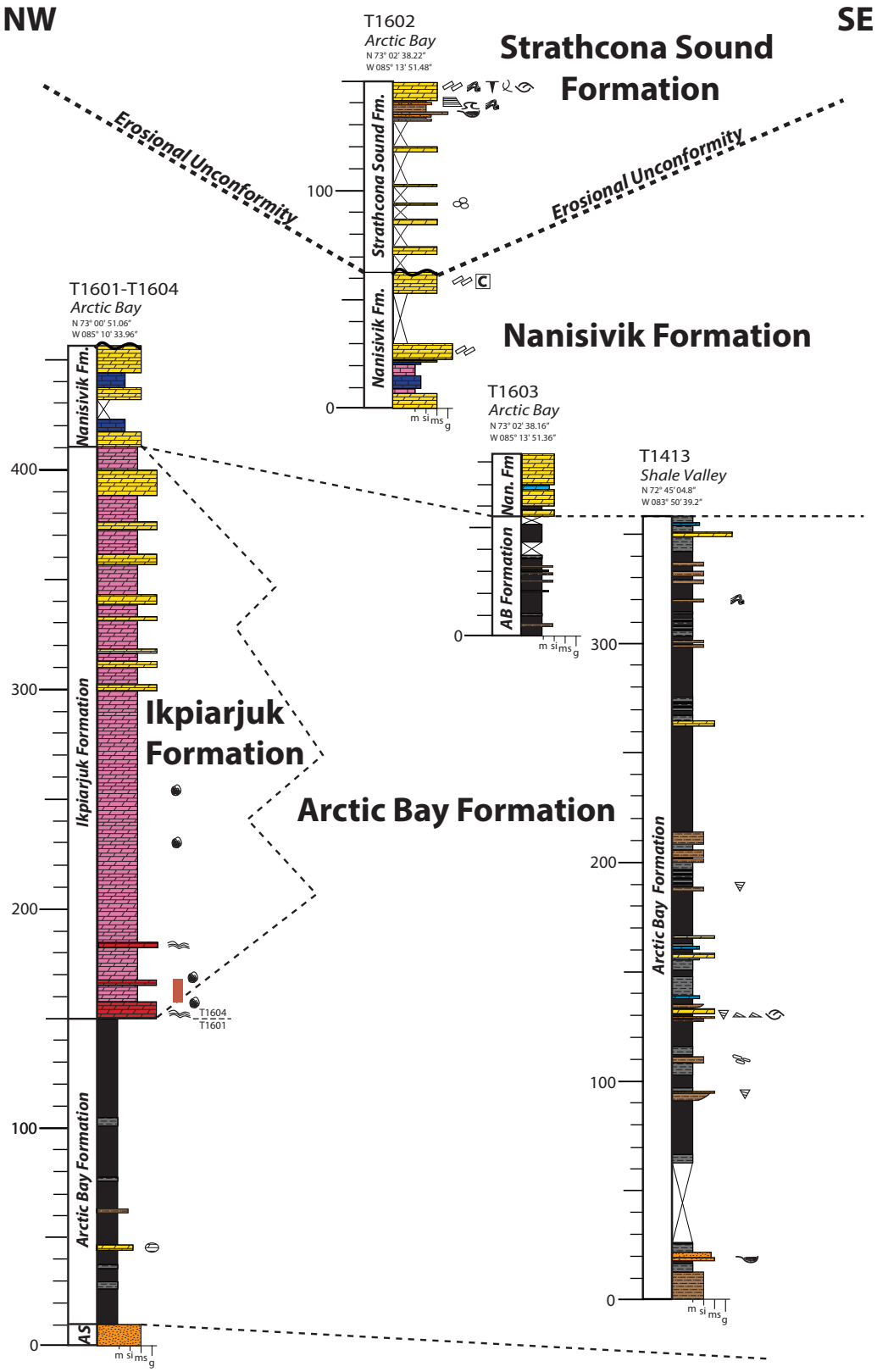

Figure 7: Stratigraphic columns of the Arctic Bay, Nanisivik, and Ikpiarjuk formations in the northwestern Milne Inlet Graben.

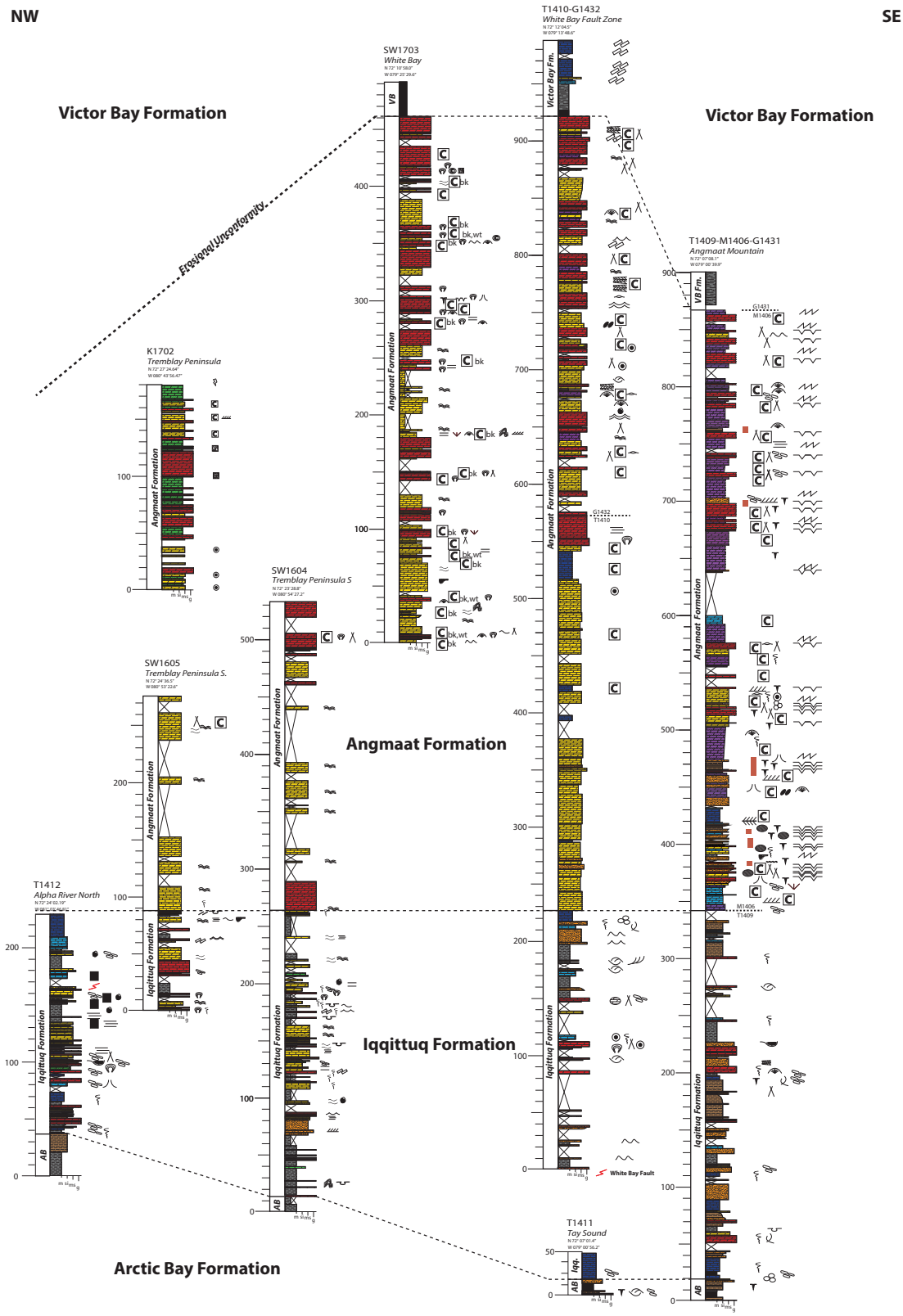

Figure 8: Stratigraphic columns of the uppermost Arctic Bay, Iqqittuq, Angmaat, and lowermost Victor Bay formations in the southeastern Milne Inlet Graben.

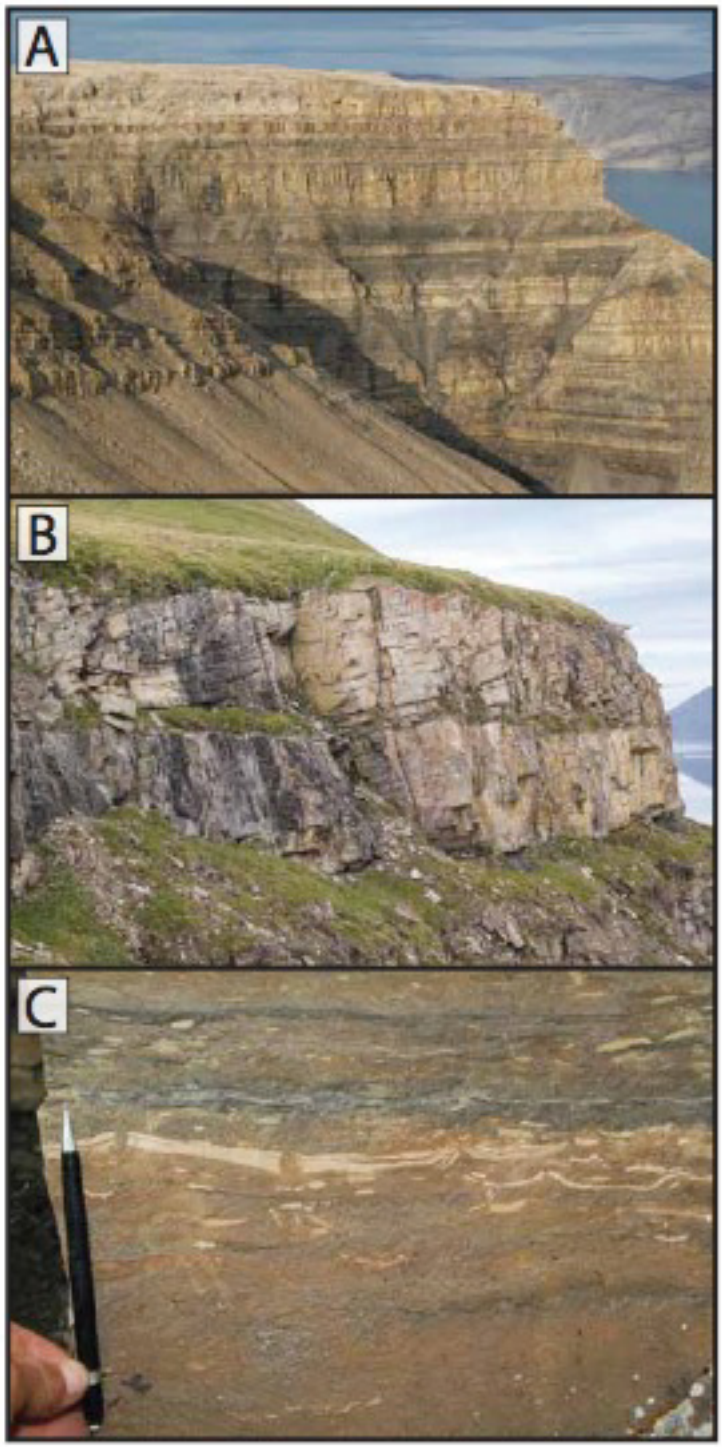

Figure 9: Photo plate of the Iqqittuq Formation in the southeastern Milne Inlet Graben. (A) Iqqittuq Formation at Alpha River North above Tremblay Sound. Stratigraphic section T1412 follows the face and ridge on the right. (B) West-dipping clinoforms at 205.3 m stratigraphic height at section T1409 near Angmaat Mountain. (C) Water-escape structures in dololutite from 180.2 m stratigraphic height from section T1409.

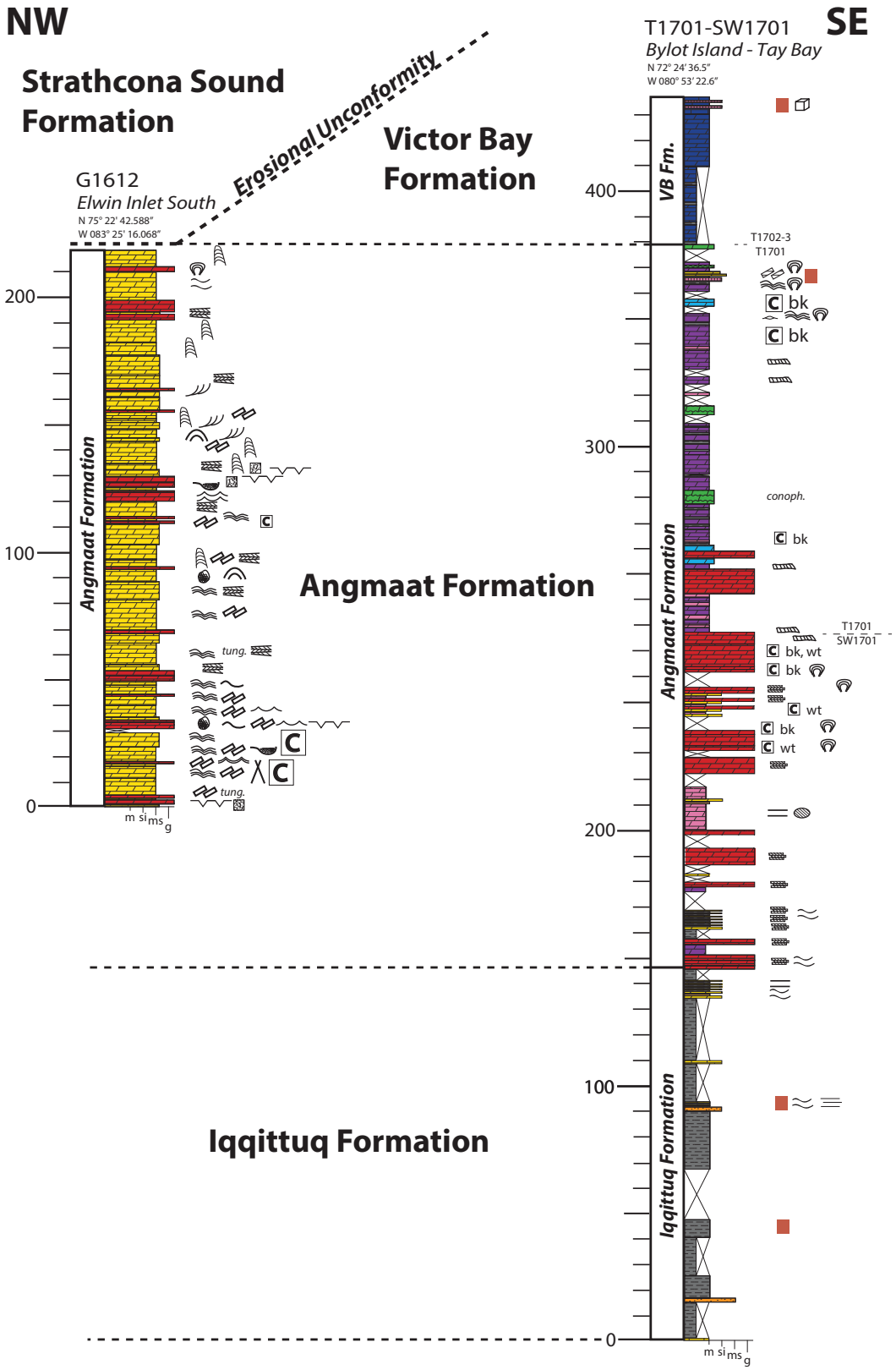

Figure 10: Stratigraphic columns of the Iqqittuq, Angmaat, and lowermost Victory Bay formations in the Eclipse Trough.

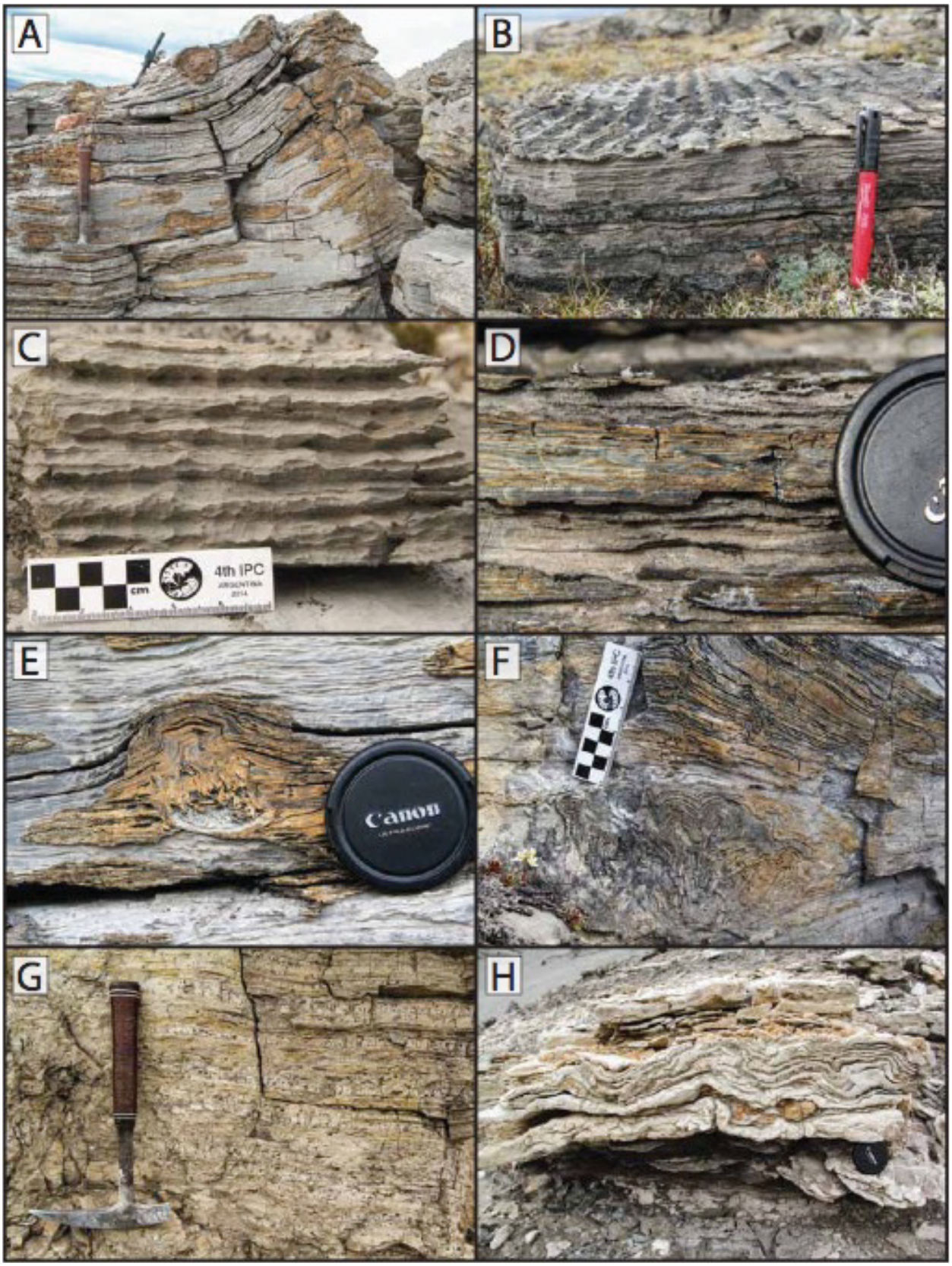
A
B
C
4th IPC
D
E
Canon
F
G
H

Figure 11: Photo plate of various facies of the Angmaat Formation. (A) Silicified water-escape structure cross-cutting stromatolitic dolostone and chert nodule from stratigraphic section SW1703. (B) Silicified syneresis-cracked symmetric ripples in dolograinstone with chert nodules from section SW1703. (C) Thin, rhythmically bedded normally graded dolograinstone from section SW1703. (D) Silicified symmetric ripple-scale cross-laminae from section SW1703. (E) Silicified acicular seafloor cement crystal fan, section SW1703 (?). (F) Silicified acicular seafloor cement crystal fan, section SW1703. (G) Thin, rhythmic dololutite beds with symmetric ripples and abundant fenestrae from section T1701. (H) Dolomite-replaced, laterally continuous, folded calcium-sulfate evaporite beds from section T1701.

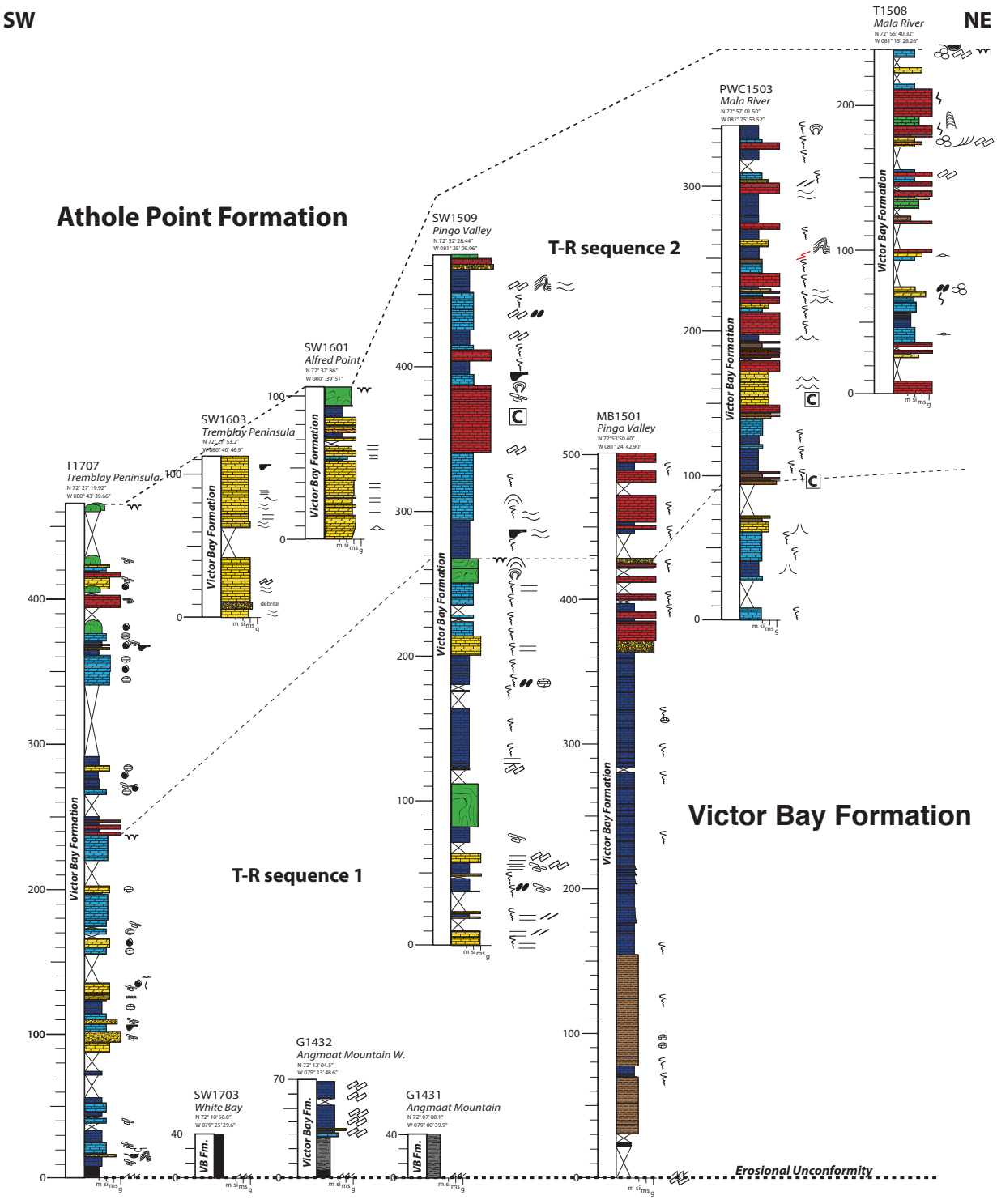

Figure 12: Stratigraphic columns of the Victory Bay Formation in the Milne Inlet Graben showing the two transgressive-regressive sequences.

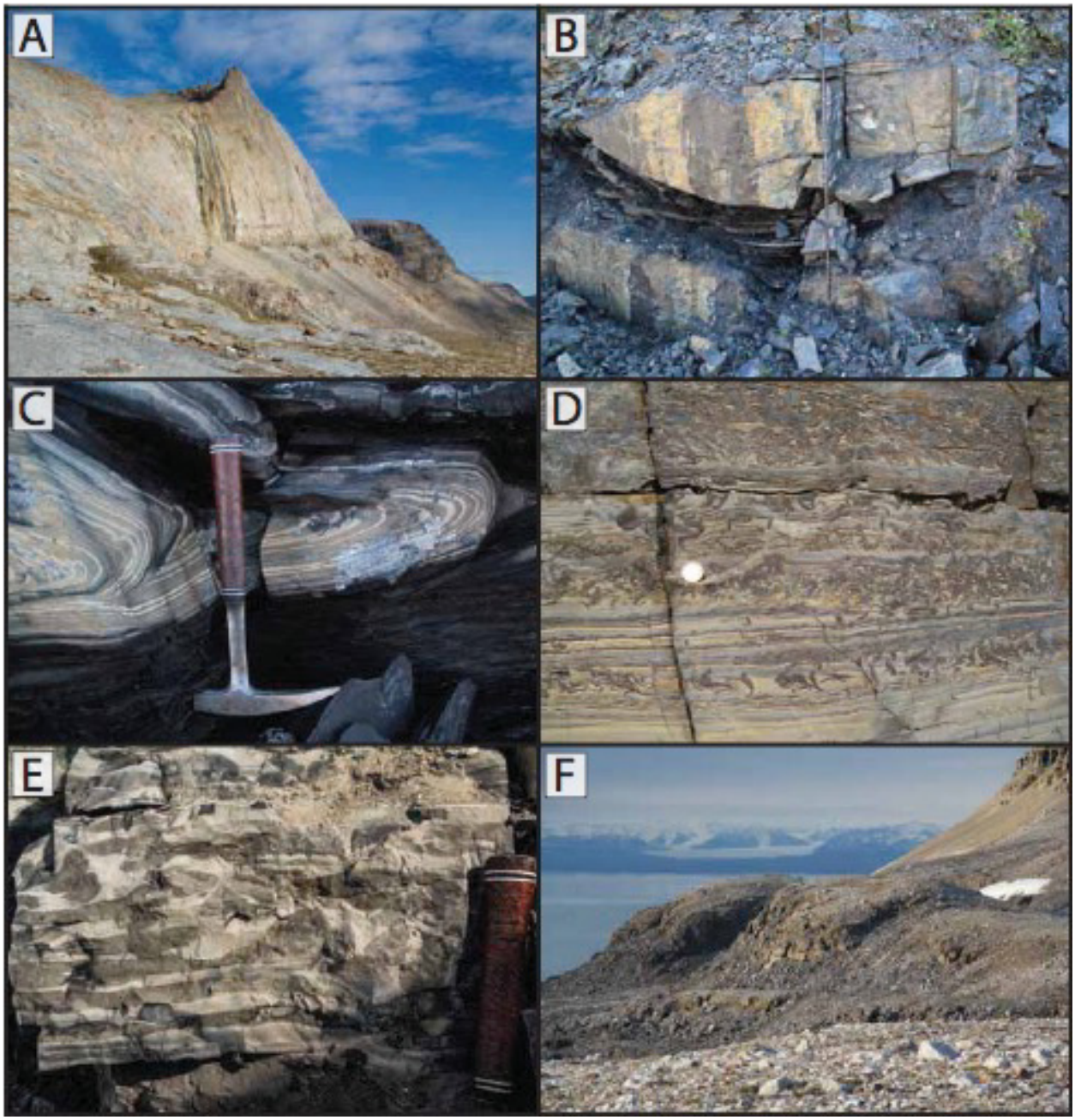

Figure 13: Photo plate of the Victor Bay Formation. (A) Large (~150 m tall) stromatolite reef between stratigraphic sections SW1509 and MB1501 in the middle Victor Bay Formation. (B) Lime rudstone channel within basal Victor Bay formation calcareous black shale from section T1707. (C) Soft-sediment slump of the lower Victor Bay Formation limestone rhythmite from section T1707. (D) Molar tooth structures in thin, rhythmically bedded dolostone from section SW1509. (E) Nodular limestone facies from section T1707. (F) Two exhumed ~3 m-tall by ~10 m-diameter stromatolite bioherms at the contact between the Victor Bay and Athole Point formations from the top of section T1707.

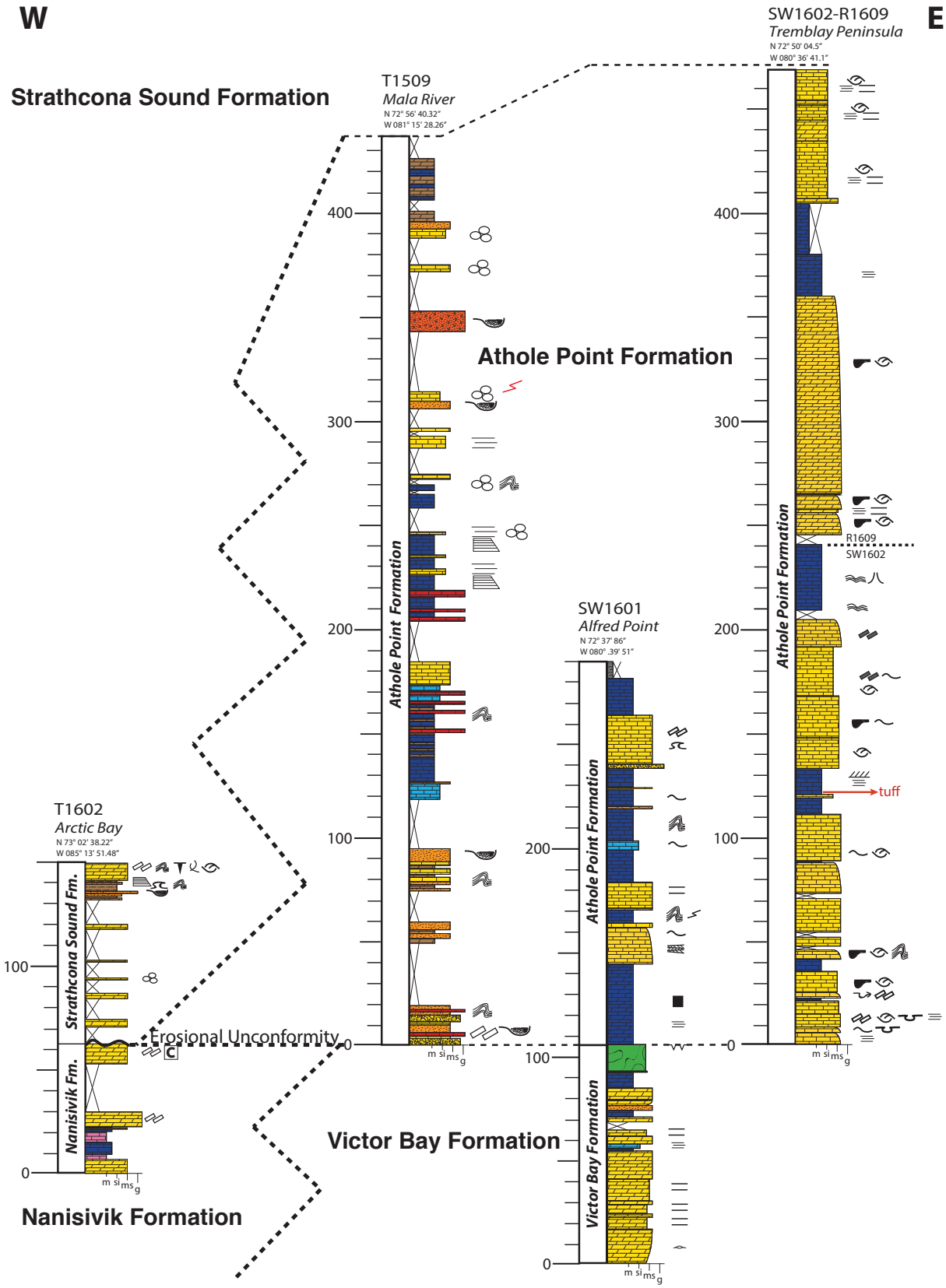

Figure 14: Stratigraphic columns of the Athole Point Formation in the Milne Inlet Graben.

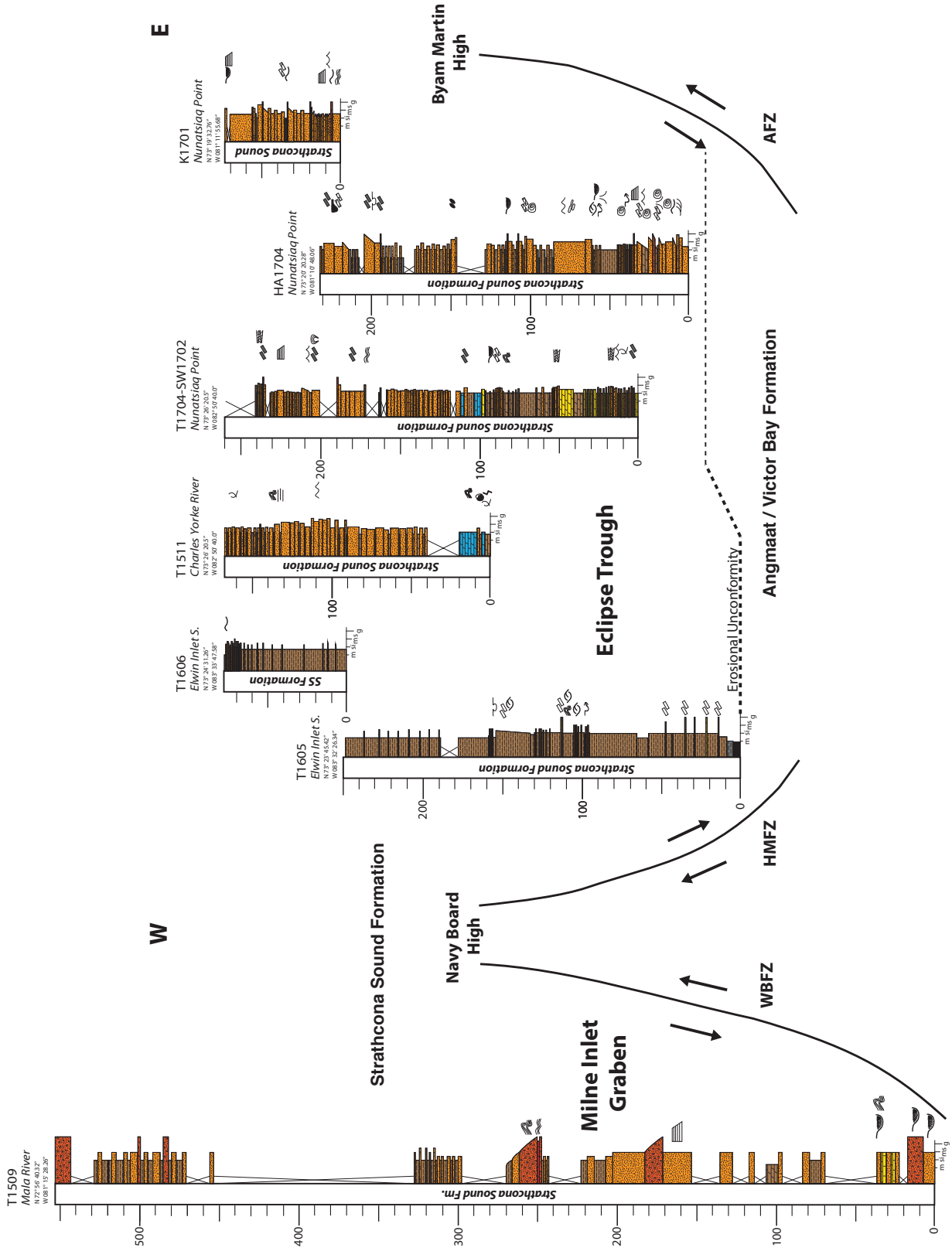

Figure 15: Stratigraphic columns of the Strathcona Sound Formation. WBFZ—White Bay Fault Zone; HMFZ—Hartz Mountain Fault Zone; AFZ—Actineq Fault Zone.

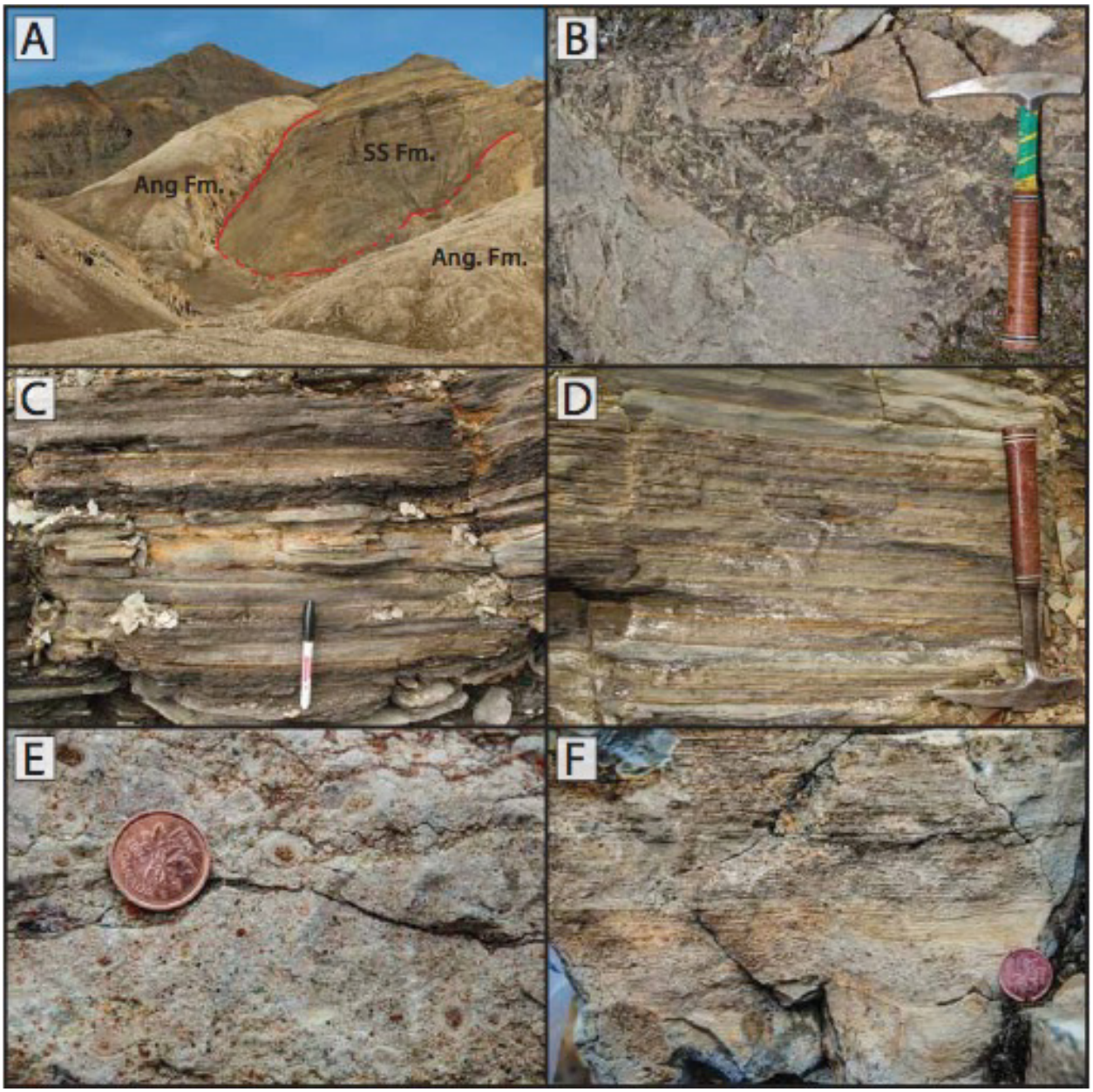

Figure 16: Photo plate of the Strathcona Sound and Athole Point formations. (A) Thin-bedded Strathcona Sound Formation siltstone and sandstone filling in decimeter paleo-relief within Angmaat Formation dolostone at Elwin Inlet. The Victor Bay Formation was removed beneath the erosional unconformity at this location. (B) Karst-breccia at the Strathcona Sound-Athole Point formations unconformity at Mala River (stratigraphic section T1509). (C-D) Parallel laminated siltstone from stratigraphic section T1605. (E) Dolograinstone with pisolites nucleated around red siltstone from stratigraphic section HA1704. (F) Microbialaminated dolostone from stratigraphic section HA1704.

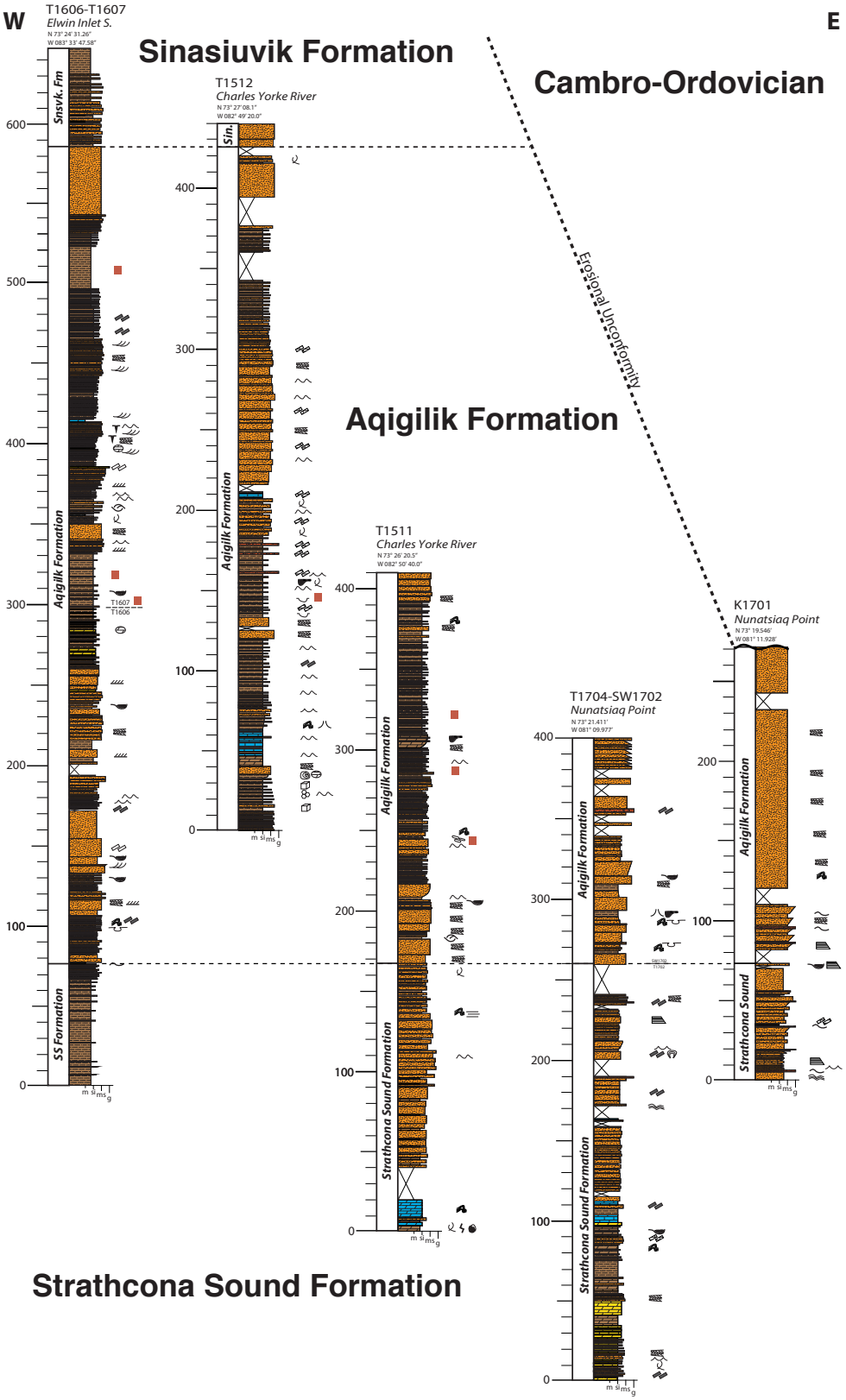

Figure 17: Stratigraphic columns of the Aqigilik Formation in Eclipse Trough along with underlying upper Strathcona Sound and overlying lower Sinasiuvik formations.

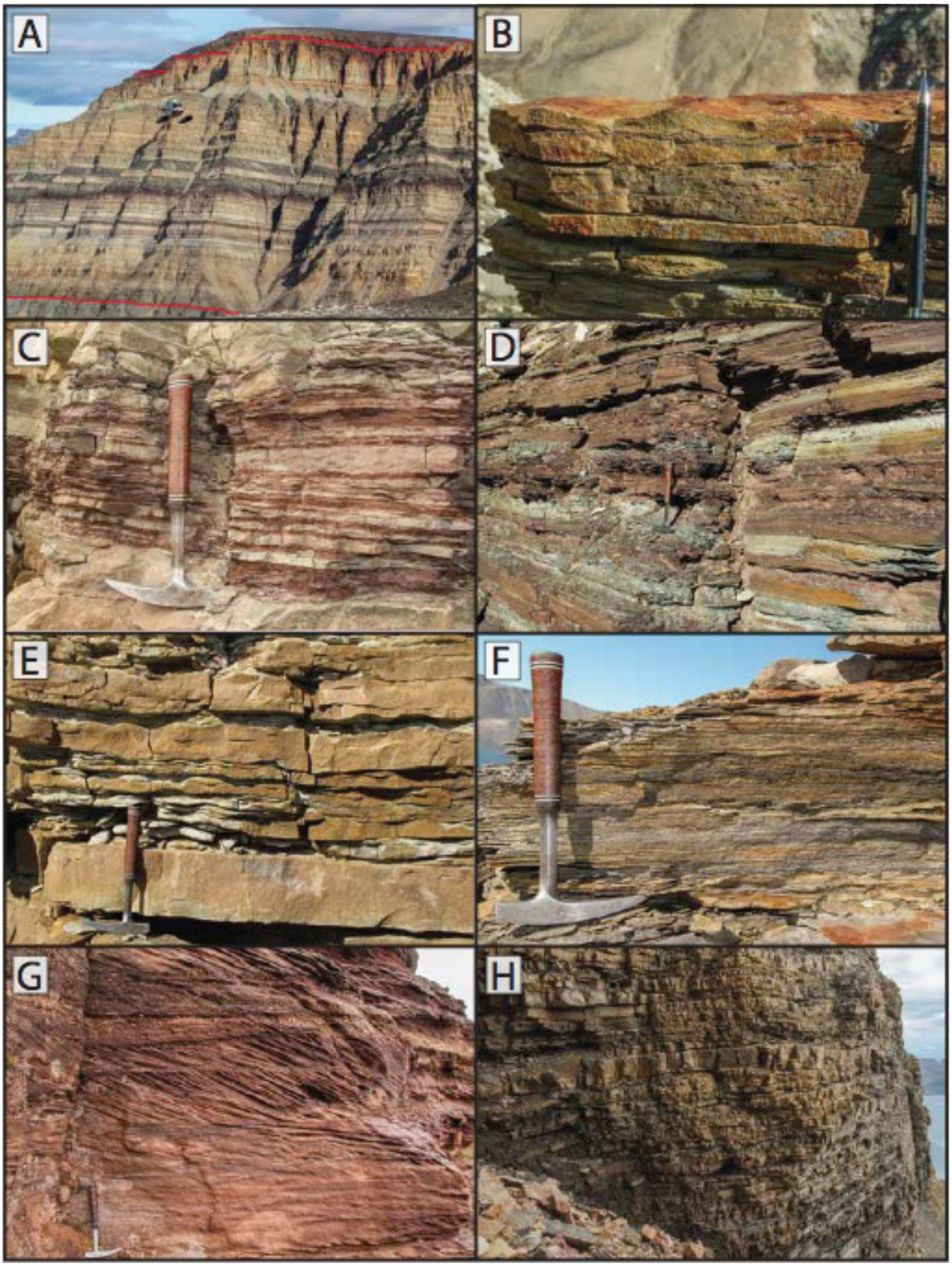
A
B
C
D
E
F
G
H

Figure 18: Photo plate of the Aqigilik and Sinasiuvik formations. (A) Complete exposure of the Aqigilik Formation at Elwin Inlet south with lower contact with the Strathcona Sound Formation and upper contact with the Sinasiuvik Formation traced in red. (B) Preserved symmetric ripples at 335 m from stratigraphic section T1606-T1607 of the Aqigilik Formation at Elwin Inlet south. (C) Immature sandstone and red siltstone flaser beds at 250 m from stratigraphic section T1606-T1607 of the Aqigilik Formation at Elwin Inlet south. (D) Variegated siltstone and shale and fine sandstone interbeds at 306 m from stratigraphic section T1606-T1607 of the Aqigilik Formation at Elwin Inlet south. (E) Pinch and swell structures at 398 m from stratigraphic section T1606-T1607 of the Aqigilik Formation at Elwin Inlet south. (F) Thin, wavy bedded calcisiltite at 331 m from stratigraphic section T1606-T1607 of the Aqigilik Formation at Elwin Inlet south (G) Tabular dune-scale cross-bedding at 251 m from stratigraphic section K1701 of the Aqigilik Formation at Nunatsiaq Point. (H) Tabular sandstone-siltstone interbeds at 43 m of stratigraphic section T1510 of the Sinasiuvik Formation at Elwin Inlet north.

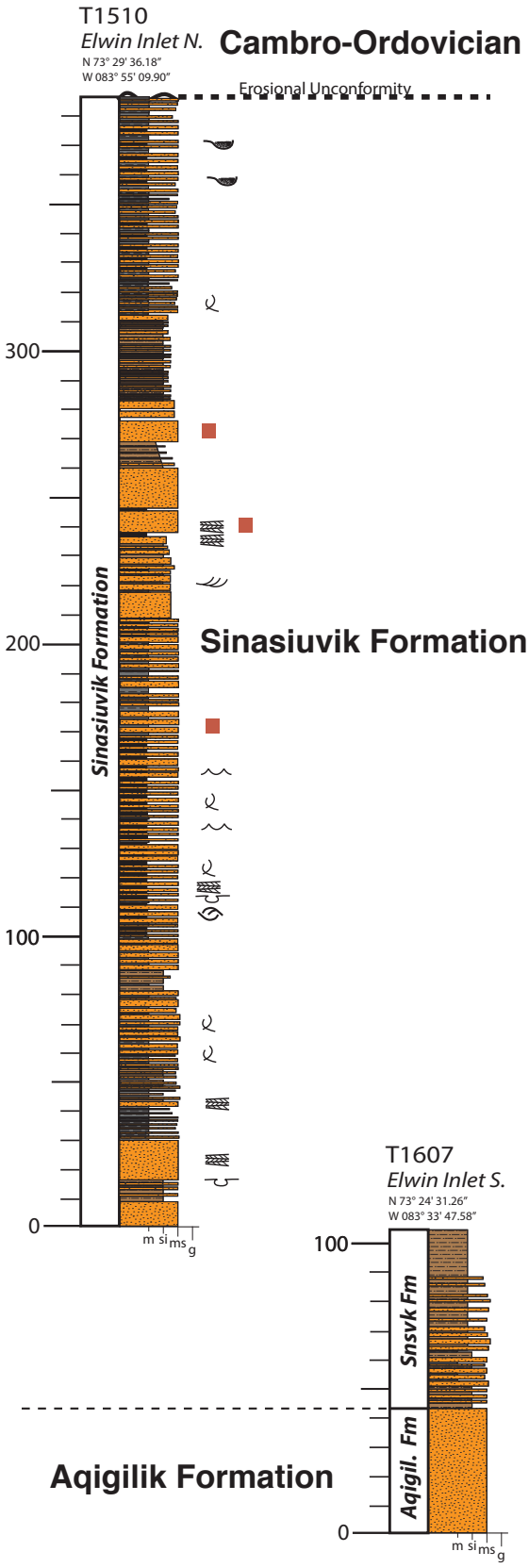

Figure 19: Stratigraphic columns of the Sinasiuvik Formation in Eclipse Trough.

References

Blackadar, R. G., 1970, Precambrian geology northwestern Baffin Island, District of Franklin: Geological Survey of Canada, Department of Energy, Mines and Resources.

Dostal, J., Jackson, G.D. and Galley, A., 1989, Geochemistry of Neohelikian Nauyat plateau basalts, Borden rift basin, northwestern Baffin Island, Canada: Canadian Journal of Earth Sciences, v. 26, p. 2214–2223.

Fahrig, W.F., Christie, K.W. and Jones, D.L. , 1981, Paleomagnetism of the Bylot basins: evidence for Mackenzie continental tensional tectonics: in Proterozoic Basins of Canada, F.H.A. Campbell (ed.) Geological Survey of Canada, Paper 80-10, p. 303–312.

Geldsetzer, H., 1973, The tectono-sedimentary development of an algal-dominated Helikian succession on Northern Baffin Isand, N.W.T.: Geological Association of Canada, Memoir, v. 19, p. 99–126.

Gibson, T. M., Shih, P. M., Cumming, V. M., Fischer, W. W., Crockford, P. W., Hodgskiss, M. S. W., Wörndle, S., Creaser, R. A., Rainbird, R. H., Skulski, T. H., and Halverson, G. P., 2018, Precise age of *Bangiomorpha pubescens* dates the origin of eukaryotic photosynthesis: Geology, v. 46, p. 135-138.

Hahn, K.E. and Turner, E.C., 2013, Mesoproterozoic deep-water carbonate mound lithofacies, Borden Basin, Nunavut: Geological Survey of Canada, Current Research 2013-11, 14 p.

Hahn, K.E. and Turner, E.C., 2017, Composition and history of giant carbonate seep mounds, Mesoproterozoic Borden Basin, Arctic Canada: Precambrian Research, v. 293, p. 150–173.

Hahn, K. E., and Turner, E. C., 2017, Composition and history of giant carbonate seep mounds, Mesoproterozoic Borden Basin, Arctic Canada: Precambrian Research, v. 293, p. 150-173.

Hahn, K.E., Turner, E.C., Babechuk, M.G. and Kamber, B.S., 2015, Deep-water seep-related carbonate mounds in a Mesoproterozoic alkaline lake, Borden Basin (Nunavut, Canada): Precambrian Research, v. 271, p. 173–197.

Heaman, L.M., LeCheminant, A.N. and Rainbird, R.H., 1992, Nature and timing of Franklin igneous events, Canada: implications for a Late Proterozoic mantle plume and the break-up of Laurentia: Earth and Planetary Science Letters, v. 109, p. 117–131.

Hnatyshin, D., Kontak, D.J., Turner, E.C., Creaser, R.A., Morden, R. and Stern, R.A., 2016, Geochronologic (Re-Os) and fluid- chemical constraints on the formation of the

Mesoproterozoic-hosted Nanisivik Zn-Pb deposit, Nunavut, Canada: evidence for early diagenetic, low-temperature conditions of formation: Ore Geology Reviews, v. 79, p. 189–217.

Hofmann, H.J. and Jackson, G.D., 1991, Shelf-facies microfossils from the Uluksan Group (Proterozoic Bylot Supergroup), Baffin Island, Canada: Journal of Paleontology, v. 65, p. 361–382.

Hofmann, H.J. and Jackson, G.D., 1994, Shale-facies microfossils from the Proterozoic Bylot Supergroup, Baffin Island, Canada: The Paleontological Society Memoir, v. 65, p. 1–39.

Jackson, G.D. and Berman, R.G., 2000, Precambrian metamorphic and tectonic evolution of northern Baffin Island, Nunavut, Canada: The Canadian Mineralogist, v. 38, p. 399–421.

Jackson, G.D. and Cumming, L.M., 1981, Evaporites and folding in the Neohelikian Society Cliffs Formation, northeastern Bylot Island, Arctic Canada: in Current Research, Part C, Geological Survey of Canada, Paper 81-1C, p. 35–44.

Jackson, G.D., Iannelli, T.R. and Tilley, B.J., 1980, Rift-related late Proterozoic sedimentation and volcanism on northern Baffin and Bylot Islands, District of Franklin: in Current Re- search, Part A, Geological Survey of Canada, Paper 80-1A, p. 319–328.

Jackson, G.D. and Iannelli, T.R., 1981, Rift-related cyclic sedimentation in the Neohelikian Borden Basin, northern Baffin Island: in Proterozoic Basins of Canada, F.H.A. Campbell (ed.), p. 269– 302.

Jackson, G., Iannelli, T., Knight, R., and Lebel, D., 1985, Neohelikian Bylot Supergroup of Borden Rift Basin, northwestern Baffin Island, District of Franklin: Current research, part A. Geological Survey of Canada, Paper, p. 639-649.

Kah, L.C., 1997, Sedimentological, geochemical, and paleobiological interactions on a Mesoproterozoic carbonate platform: Society Cliffs Formation, northern Baffin Island, Arctic Canada: Ph.D. thesis, Harvard University, Cambridge, Massachusetts, 380 p.

Kah, L.C., 2000, Depositional d18O signatures in Proterozoic dolostones: constraints on seawater chemistry and early diagenesis: in Carbonate Sedimentation and Diagenesis in the Evolving Precambrian World, J.P. Grotzinger and N.P. James, editors: SEPM Special Publication, v. 67, p. 345–360.

Kah, L.C. and Knoll, A.H., 1996, Microbenthic distribution of Proterozoic tidal flats: environmental and taphonomic considerations: Geology, v. 24, p. 79–82.

Kah, L.C., Lyons, T.W. and Chesley, J.T., 2001, Geochemistry of a 1.2 Ga carbonate-evaporite succession, northern Baffin and Bylot Islands: implications for Mesoproterozoic marine evolution: Precambrian Research, v. 111, p. 203–234.

Kah, L.C., Sherman, A.G., Narbonne, G.M., Knoll, A.H. and Kaufman, A.J., 1999, d13C stratigraphy of the Proterozoic Bylot Supergroup, Baffin Island, Canada: implications for regional lithostratigraphic correlations: Canadian Journal of Earth Sciences, v. 36, p. 313–332.

Knight, R. D., and Jackson, G. D., 1994, Sedimentology and stratigraphy of the Mesoproterozoic Elwin Subgroup (Aqigilik and Sinasiuvik formations), uppermost Bylot Supergroup, Borden rift basin, northern Baffin Island: Bull. Canadian Geolical Survey.

Knoll, A.H., Wörndle, S. and Kah, L.C., 2013, Covariance of microfossil assemblages and microbialite textures across an upper Mesoproterozoic carbonate platform: Palaios, v. 28, p. 453–470.

LeCheminant, A.N. and Heaman, L.M., 1989, Mackenzie igneous events, Canada: Middle Proterozoic hotspot magmatism associated with ocean opening: Earth and Planetary Science Letters, v. 96, p. 38–48.

Manning-Berg, A.R. and Kah, L.C., 2016, Proterozoic microbial mats and their constraints on environments of silicification: Geobiology, v. 15, p. 469–483. doi:10.1111/gbi.1223

Narbonne, G.M. and James, N.P., 1996, Mesoproterozoic deep-water reefs from Borden Peninsula, Arctic Canada: Sedimentology, v. 43, p. 827–848.

North American Commission on Stratigraphic Nomenclature, 2005: North American stratigraphic code: AAPG Bulletin v. 89, p. 1547-1591.

Patterson, K.M. and Powis, K., 2002, Structural and stratigraphic controls on Zn-Pb-Ag mineralization at the Nanisivik Mississippi Valley-type deposit, northern Baffin Island, Nunavut: Geological Survey of Canada, Current Research 2003-C22, 12 p.

Pehrsson, S.J. and Buchan, K.L., 1999, Borden dykes of Baffin Island, Northwest Territories: a Franklin U-Pb baddeleyite age and a paleomagnetic reinterpretation: Canadian Journal of Earth Sciences, v. 36, p. 65–73.

Rainbird, R., Jefferson, C., and Young, G., 1996, The early Neoproterozoic sedimentary Succession B of northwestern Laurentia: Correlations and paleogeographic significance: Geological Society of America Bulletin, v. 108, p. 454-470.

Scott, D., and De Kemp, E., 1998, Bedrock Geology Compilation Northern Baffin Island and Northern Melville Peninsula, Northwest Territories, Geological Survey of Canada, Natural Resources Canada.

Sherman, A.G., James, N.P. and Narbonne, G.M., 2000, Sedimentology of a late Mesoproterozoic muddy carbonate ramp, northern Baffin Island, Arctic Canada: in Carbonate Sedimentation and Diagenesis in the Evolving Precambrian World, J.P. Grotzinger and N.P. James (ed.), SEPM Special Publication, v. 67, p. 275–294.

Sherlock, R.L., Lee, J.K.W. and Cousens, B.L., 2004, Geologic and geochronologic constraints on the timing of mineralization at the Nanisivik zinc-lead Mississippi Valley-type deposit, northern Baffin Island, Nunavut, Canada: Economic Geology, v. 99, p. 279–293.

Sherman, A.G., Narbonne, G.M. and James, N.P., 2001, Anatomy of a cyclically packaged Mesoproterozoic carbonate ramp in northern Canada: Sedimentary Geology, v. 139, p. 171–203.

Sherman, A.G., James, N.P. and Narbonne, G.M., 2002, Evidence for reversal of basin polarity during carbonate ramp development in the Mesoproterozoic Borden Basin, Baffin Island: Canadian Journal of Earth Sciences, v. 39, p. 519–538.

Thomson, D., Rainbird, R. H., and Krapez, B., 2015, Sequence and tectonostratigraphy of the Neoproterozoic (Tonian-Cryogenian) Amundsen Basin prior to supercontinent (Rodinia) breakup: Precambrian Research, v. 263, p. 246-259.

Trettin, H. P., 1969, Lower Palaeozoic Sediments of Northwestern Baffin Island, District of Franklin, Department of Energy, Mines and Resources.

Turner, E.C., 2003, New contributions to the stratigraphy of the Mesoproterozoic Society Cliffs Formation, northern Baffin Island, Nunavut: Geological Survey of Canada, Current Research 2003-B3, 13 p.

Turner, E.C., 2004, Stratigraphy of the Mesoproterozoic Society Cliffs Formation (Borden Basin, Nunavut): correlation between northwestern and southeastern areas of the Milne Inlet Graben: Geological Survey of Canada, Current Research 2004-B3, 11 p.

Turner, E.C., 2009, Mesoproterozoic carbonate systems in the Borden Basin, Nunavut: Canadian Journal of Earth Sciences, v. 46, p. 915–938.

Turner, E.C., 2011, Structural and stratigraphic controls on the carbonate-hosted base metal mineralization in the Mesoproterozoic Borden Basin (Nanisivik District), Nunavut: Economic Geology, v. 106, p. 1197–1223.

Turner, E.C. and Kamber, B.S., 2012, Arctic Bay Formation, Borden Basin, Nunavut (Canada): basin evolution, black shale and dissolved metal systematics in the Mesoproterozoic ocean: Precambrian Research, v. 208, p. 1–18.

Turner, E.C., Long, D.G.F., Rainbird, R.H., Petrus, J.A. and Rayner, N.M., 2016, Late Mesoproterozoic rifting in Arctic Canada during Rodinia assembly: impactogens, trans-continental far-field stress and zinc mineralisation: Terra Nova, v. 28, p. 188–194.

Preface to Chapter 3:

The previous chapter provides a synthesis of the sedimentology of the Bylot Supergroup and describes previously unrecognized aspects of its tectonostratigraphy. These insights provide critical depositional context for paleontological data from this succession and will inform future paleo-environmental reconstructions. Previous work has shown diverse and abundant microfossils from both carbonate (Hofmann and Jackson, 1991; Knoll et al., 2013) and shale facies (Hoffmann and Jackson, 1994) throughout the succession. Most notably, the multicellular filamentous fossil *Bangiomorpha pubescens* first occurs in early silicified peritidal carbonates from the correlative Hunting Formation in the Aston and Hunting Basin and Angmaat Formation in the Borden Basin (Butterfield et al., 1990; Kah and Knoll, 1996; Knoll et al., 2013).

Nearly thirty years after Butterfield *et al.*'s (1990) report of this Precambrian red alga, *Bangiomorpha pubescens* remains widely regarded as the most influential fossil for shaping our understanding of early eukaryotic evolution. As the oldest taxonomically resolved eukaryote, earliest example of eukaryotic photosynthesis, and first instance of sexual reproduction in the fossil record, *Bangiomorpha* is the fulcrum on which all interpretations of early evolution hinge (Butterfield et al., 2000). Despite its tremendous importance and wide citation in recent molecular clock work, this fossil's age was poorly constrained to between 1270 and 720 Ma. As a result, interpretations regarding the cadence of early eukaryotic evolution vary considerably. In the following chapter we have resolved this issue using Re-Os geochronology to significantly revise *Bangiomorpha's* first appearance age to between 1060 and 1030 Ma.

This new age constraint reconciles longstanding disparities between the fossil record and molecular clock estimates and serves as the basis for a much significantly enhanced molecular calibration of milestones in the early evolution of eukaryotes—namely primary plastid endosymbiosis ca. 1250 Ma. These results are the first step toward a robust chronological framework for the Bylot Supergroup, which hosts a critical record of late Proterozoic global change, including oxygenation of the atmosphere and oceans. Furthermore, they offer the much-needed temporal context for studies examining the impact of algae on Proterozoic biogeochemical cycles.

A larger aim of the following chapter is to capture the attention of a broad audience—from molecular evolutionary biologists to paleontologists and Earth scientists. By generating results

with broad implications, we hope our investigation of *Bangiomorpha pubescens* will successfully bring together these typically disparate fields through their common interests in the fields of paleobiology.

References

Butterfield, N.J., 2000, *Bangiomorpha pubescens* n. Gen., n. sp.: Implications for the evolution of sex, multicellularity, and the Mesoproterozoic/Neoproterozoic radiation of eukaryotes: Paleobiology, v. 26, p. 386–404.

Butterfield, N.J., Knoll, A.H., and Swett, K., 1990, A bangiophyte red alga from the Proterozoic of arctic Canada: Science, v. 250, p. 104–107.

Hofmann, H.J. and Jackson, G.D. 1991: Shelf-facies microfossils from the Uluksan Group (Proterozoic Bylot Supergroup), Baffin Island, Canada: Journal of Paleontology, v. 65, p. 361–382.

Hofmann, H.J. and Jackson, G.D. 1994: Shale-facies microfossils from the Proterozoic Bylot Supergroup, Baffin Island, Canada: The Paleontological Society Memoir, v. 65, p. 1–39.

Kah, L.C. and Knoll, A.H. 1996: Microbenthic distribution of Proterozoic tidal flats: environmental and taphonomic considerations: Geology, v. 24, p. 79–82.

Knoll, A.H., Wörndle, S. and Kah, L.C. 2013: Covariance of microfossil assemblages and microbialite textures across an upper Mesoproterozoic carbonate platform: Palaios, v. 28, p. 453–470.

Chapter 3

Precise age of *Bangiomorpha pubescens* dates the origin of eukaryotic photosynthesis[1]

[1] This chapter was published as: "Gibson, T.M., Shih, P.M., Cumming, V.M., Fischer, W.W., Crockford, P.W., Hodgskiss, M., Wörndle, S., Creaser, R.A., Rainbird R.H., Skulski, T.M., Halverson, G.P., 2018, Precise age of *Bangiomorpha pubescens* dates the origin of eukaryotic photosynthesis. In: *Geology*, v. 46, p., 135—138."

Abstract

Although the geological record indicates that eukaryotes evolved by 1900–1400 million years ago (Ma), their early evolution is poorly resolved taxonomically and chronologically. The fossil red alga *Bangiomorpha pubescens* is the only recognized crown-group eukaryote older than ca. 800 Ma and marks the earliest known expression of extant forms of multicellularity and eukaryotic photosynthesis. Because it postdates the divergence between the red and green algae and the prior endosymbiotic event that gave rise to the chloroplast, *Bangiomorpha pubescens* is uniquely important for calibrating eukaryotic evolution. However, molecular clock estimates for the divergence between the red and green algae are highly variable, and some analyses estimate this split to be younger than the widely inferred but poorly constrained first appearance age of 1200 Ma for *Bangiomorpha. pubescens*. As a result, many molecular clock studies reject this fossil ex post facto. Here we present new Re-Os isotopic ages from sedimentary rocks that stratigraphically bracket the occurrence of *Bangiomorpha pubescens* in the Bylot Supergroup of Baffin Island and revise its first appearance to 1047 +13/–17 Ma. This date is 150 million years younger than commonly held interpretations and permits more precise estimates of early eukaryotic evolution. Using cross-calibrated molecular clock analyses with the new fossil age, we calculate that photosynthesis within the Eukarya emerged ca. 1250 Ma. This date for primary plastid endosymbiosis serves as a benchmark for interpreting the fossil record of early eukaryotes and evaluating their role in the Proterozoic biosphere.

1. Introduction

Photosynthetic eukaryotes (i.e., plants and algae) are responsible for most global primary production, and their evolution and diversification set the stage for today's thriving biosphere. However, the timing and tempo of early eukaryotic evolution are unclear (Berney and Pawlowski, 2006; Parfrey et al., 2011; Shih and Matzke, 2013). While the origins of the Eukarya are debated, it is clear they became photosynthetic by engulfing a cyanobacterium in the primary endosymbiotic event that gave rise to the plastid, an organelle that houses photosynthetic machinery known as a chloroplast (Keeling, 2010). The fossil red alga *Bangiomorpha pubescens* provides the earliest unambiguous record of photosynthetic eukaryotic life and exhibits distinct morphological features of complex multicellularity and sexual reproduction (Butterfield et al., 1990; Butterfield, 2000). Therefore, this fossil is widely recognized as critical to calibrating the tempo of early eukaryotic diversification and constraining the acquisition of photosynthesis within the domain. Because concrete evidence for such evolutionary milestones is scarce, the appearance of *Bangiomorpha pubescens* in the fossil record presents a rare opportunity to anchor interpretations regarding early eukaryotic evolution. The timing for the origin of the Eukarya is unresolved, with estimates spanning over a billion years. (Roger and Hug, 2006). Isolated stem group eukaryotes may date as far back as ca. 3200 Ma (Javaux et al., 2010), whereas more widely occurring fossils with possible eukaryotic affinities, such as *Grypania*, occur in 1900–1800 Ma rocks (Han and Runnegar, 1992). Fossils from the Vindhyan Supergroup in India are suggested to represent ca. 1600 Ma algae (Bengtson et al., 2017), but their age (Ray, 2006) and taxonomic assignment are uncertain. The first fossils with robust age control that conclusively display both the large cell size and complex ultrastructure or surface ornamentation characteristic of eukaryotes are 1650–1400 Ma acanthomorphic acritarchs; i.e., *Tappania* and *Valeria* (Javaux et al., 2001; Lamb et al., 2009; Knoll, 2014; Adam et al., 2017).

Aside from *Bangiomorpha pubescens*, eukaryotic fossils remain taxonomically unresolvable until ca. 800 Ma (Knoll, 2014; Cohen and Macdonald, 2015). Accepting that the last eukaryotic common ancestor had evolved by 1650 Ma, the protracted early evolutionary history of stem group eukaryotes is poorly documented. While *Bangiomorpha pubescens* was long presumed to arise 1200 Ma (see Appendix), its true age was only loosely constrained by conventional radiometric ages to a >500 million-year interval. Here we present two new Re-Os

isochron ages that precisely date the first appearance of *Bangiomorpha. pubescens* in the Bylot Supergroup of Baffin Island. This revised fossil age helps resolve inconsistencies between molecular clocks and fossil evidence for early eukaryotic diversification (e.g., Berney and Pawlowski, 2006; Cavalier-Smith et al., 2006; Parfrey et al., 2011; Eme et al., 2014) and permits more precise calibration of primary plastid endosymbiosis and the split between the red and green algae.

2. Geological Background

Bangiomorpha pubescens was first was first described in chert from peritidal carbonate facies of the Hunting Formation on Somerset Island (Butterfield et al., 1990) and later in similar facies in the correlative Angmaat Formation of the Bylot Supergroup on Baffin Island, both in northeastern Canada (Knoll et al., 2013; **Fig. 1**). The Hunting and Angmaat formations occur within comparable stratigraphic sequences hypothesized to be remnants of previously interconnected basins in northeastern Canada and northwestern Greenland (known as the Bylot basins), the initial development of which was linked to emplacement of the ca. 1270 Ma Mackenzie large igneous province (LIP; LeCheminant and Heaman, 1989). Basalt flows with similar paleomagnetic poles to the Mackenzie LIP occur at the base of the Bylot Supergroup and provide a maximum depositional age for the overlying strata (Fahrig et al., 1981). Mafic dikes that intrude the succession provide a minimum depositional age of ca. 720 Ma (Heaman et al., 1992; Pehrsson and Buchan, 1999).

The Angmaat Formation records progradation and stabilization of a rimmed carbonate platform over black shale and siltstone of the underlying Arctic Bay Formation (**Fig. 1**; Turner, 2009). A regional subaerial unconformity developed above the Angmaat Formation and is overlain by black shale of the lower Victor Bay Formation, deposited during a subsequent marine transgression (Sherman et al., 2001). Chemostratigraphic data (Kah et al., 1999) and the absence of any discernable depositional hiatus in the lower Bylot Supergroup led to the inference that the Hunting and Angmaat Formations, and thus *Bangiomorpha pubescens*, are closer in age to 1270 Ma than 720 Ma. This interpretation has informed a critical constraint for studies of eukaryotic evolution (Berney and Pawlowski, 2006; Parfrey et al., 2011; Shih and Matzke, 2013; Knoll, 2014; Shih et al., 2017).

3. Re-Os Geochronology

Black shale samples were collected for Re-Os geochronology from stratigraphic sections of the middle Arctic Bay and lower Victor Bay Formations in the Milne Inlet graben of northern Baffin Island (Fig. 1). Regression of all Arctic Bay Formation samples yields a model 3 age of 1051 ± 31 Ma (2σ, *n* = 6, mean square of weighted deviates, MSWD = 4.5) with an initial $^{187}Os/^{188}Os$ (Osi) of 1.44 ± 0.27. Regression of all Victor Bay Formation samples yields a model 3 age of 1047 ± 32 Ma (2σ, *n* = 8, MSWD = 6.4, Os_i = 1.24 ± 0.17; Fig. A4; Table A1). Uncertainty in these ages owes largely to variation in the $^{187}Os/^{188}Os$ of basin waters throughout the depositional timespan recorded by the sampled stratigraphic intervals (Cohen et al., 1999; Creaser et al., 2002; Cohen, 2004) rather than open-system behavior of the Re-Os isotope system. This conclusion is based on (1) linear correlation between $^{187}Re/^{188}Os$ and $^{187}Os/^{188}Os$ within each sample set; (2) general agreement both between these ages and with existing age constraints; (3) lack of correlation between $^{187}Os/^{188}Os$ and $1/^{188}Os$ (Kendall et al., 2009; Rooney et al., 2010); and (4) Re and Os abundances and Os_i values similar to reported values for black shale (Dubin and Peucker-Ehrenbrink, 2015). Regression of samples from a narrow stratigraphic range yields statistically indistinguishable, but more precise (model 3) depositional ages than regressions using the full stratigraphic sampling ranges. Arctic Bay Formation samples from a 2.9 m stratigraphic range yield an age of 1048 ± 12 Ma (2σ, *n* = 5), and Victor Bay Formation samples from a 0.15 m stratigraphic range yield an age of 1046 ± 16 Ma (2σ, *n* = 6; **Fig. 2**). These depositional ages significantly improve chronostratigraphic constraints on the Bylot Supergroup and bracket the Angmaat Formation. We propose 1047 +13/–17 Ma as the first appearance age of *Bangiomorpha pubescens*.

4. Cross-Calibrated Molecular Clock Analyses

When combined with robust fossil data, molecular clocks offer an effective method to query the evolutionary history of eukaryotes (Hedges et al., 2004; Parfrey et al., 2011; Shih and Matzke, 2013). Although several potential sources of error exist in molecular clock analyses, one pivotal, geologically resolvable inconsistency is in the fossil ages required for calibration (Yoon et al., 2004; Berney and Pawlowski, 2006). As the first definitive fossil member of the red algae

and photosynthetic eukaryote (Butterfield, 2000), *Bangiomorpha pubescens* is the oldest eukaryotic fossil included in these analyses and provides minimum limits on the age of both primary plastid endosymbiosis and the divergence between the red (rhodophytes) and green (viridiplantae) algae. To reexamine models for early eukaryotic evolution in light of the refined age of *Bangiomorpha pubescens*, we conducted cross-calibrated molecular clock analyses (updated from Shih and Matzke, 2013), testing three different priors on the rhodophytes-viridiplantae divergence: (1) no constraint, (2) the previously reported age for *Bangiomorpha pubescens* of ca. 1200 Ma (Butterfield, 2000), and (3) the age from this study of ca. 1045 Ma (Table 1).

5. Discussion

Much diversity within the Eukarya derives from various forms of plastid acquisition (Delwiche, 1999), but dating the original endosymbiosis of an ancient photosynthetic cyanobacterium has been elusive. Our molecular clock analysis using the refined *Bangiomorpha pubescens* age of ca. 1045 Ma (run T09) suggests that primary plastid endosymbiosis occurred by ca. 1250 Ma (Fig. 3; Table 1). This analysis yields a decrease in the 95% confidence interval width for this event compared to the analysis using the previously accepted age of *Bangiomorpha pubescens* (run T08). The analysis with no age constraint for *Bangiomorpha pubescens* places the divergence between rhodophytes and viridiplantae at 1166 Ma, which is younger than the fossil's previously inferred age, but consistent with this study and many previous molecular clock estimates (Berney and Pawlowski, 2006; Cavalier-Smith et al., 2006; Parfrey et al., 2011; Shih and Matzke, 2013; Eme et al., 2014). Together these confirm that the new age constraint better fits the existing molecular data set. It is important to note that these analyses utilize the most conservative (i.e., oldest) placement of the *B. pubescens* constraint. Various morphological features of *B. pubescens* suggest that it might belong to the Bangiales lineage within the Rhodophyta (Butterfield, 2000), and thus our analyses provide a conservative minimum age limit on primary plastid endosymbiosis.

Although the algorithms employed in molecular clock studies differ, the age constraints they implement exert by far the greatest control on their results. Accordingly, results from this study are calibrated with and improved by the revised first appearance age of *B. pubescens*.

However, we note that these analyses differ from previous studies in other ways. Due to the paucity of available calibration points in deep time, Precambrian molecular clock studies often employ indirect or ambiguous constraints on the origins of key lineages (e.g., Archean lipid biomarkers and/or microfossils of uncertain taxonomic affinity) that affect their age estimates for evolutionary events. For example, Sánchez-Baracaldo et al. (2017) calculated, using controversial cyanobacterial microfossil calibrations (Butterfield, 2015), that both primary plastid endosymbiosis and the split between the red and green algae occurred ca. 1900 Ma. Because divergence calculations from molecular data are only as valuable as their geological tie points, this study employs less controversial constraints from the fossil record of algae and plants; and by using a cross-calibration approach (Shih and Matzke, 2013), the value of these constraints is effectively doubled.

Various other Proterozoic fossils have been suggested to represent ca. 1800–1600 Ma primitive eukaryotic algae (Han and Runnegar, 1992; Moczydłowska et al., 2011; Bengtson et al., 2017). The Vindhyan Supergroup of central India was interpreted to host ca. 1600 Ma crown-group rhodophyte fossils (Bengtson et al., 2017). Whereas *Rafatazmia chitrakootensis* and *Ramathallus lobatus* may have eukaryotic affinities, they are hundreds of millions of years older than most phylogenetic estimates (including those that exclude the age of *Bangiomorpha pubescens* as a constraint) for the rhodophytes-viridiplantae divergence, more than 500 million years older than *Bangiomorpha pubescens*, and almost one billion years older than the earliest green algae (Butterfield et al., 1988). Because early eukaryotic life was perhaps dominated by stem-group taxa (Javaux and Knoll, 2017), if the age assignment for these fossils is correct (see Appendix), they may represent eukaryotes that diverged long before the origins of red and green algae. In this case, convergent evolution may account for their similarities to extant algae. Considering that plastids have been acquired at least twice within the Eukarya (i.e., algae and *Paulinella*; Marin et al., 2005), these fossils could represent an early failed experimentation in photosynthesis. In addition, it is difficult to distinguish the primary morphology of these fossils from secondary taphonomic features from phosphatization that obscure their taxonomic assignment. However, if the interpretations of the taxonomic identity and age of these fossils are correct, then they are discordant with the results of this study.

6. Conclusions

Given the remarkable preservation of *B. pubescens* and its morphological similarities to modern *Bangia* red algae (Butterfield et al., 1990; Butterfield, 2000), a precise first appearance age of 1047 Ma cements its role as currently the most robust geological datum for reconstructing early eukaryotic evolution. This revised age narrows the window for when photosynthesis in crown eukaryotes first evolved and introduces a chronological framework for investigating the role this fundamental biological innovation played in shaping global biogeochemical cycles.

Acknowledgements

This research was supported by the Agouron Institute, as well as funding from the Geo-mapping for Energy and Minerals (GEM), GEM-2, Natural Sciences and Engineering Research Council of Canada, and Polar Continental Shelf Program. Gibson acknowledges funding from the Eric Mountjoy Legacy Fund (McGill University), Mountjoy Exchange Award (Geological Association of Canada), and a Graduate Student Research Grant (Geological Society of America). We thank E.J. Javaux, A.D. Rooney, and an anonymous reviewer for constructive comments.

Tables and Figures

Table 1: Effects of the new age for *Bangiomorpha pubescens* on molecular clock analyses.

Run	*Bangiomorpha* age prior for red-green divergence (Ma)	Red-Green Divergence ± 2σ (Ma)	95% CI width	Primary Plastid Endosymbiosis ± 2σ (Ma)	95% CI width
T07	omitted	1166 (1450–883)	567	1325 (1647–1029)	618
T08	1198 ± 24 (previous)	1194 (1242–1150)	92	1422 (1568–1291)	277
T09	1045 ± 15 (this study)	1046 (1046–1016)	58	1246 (1368–1142)	226

Note: Multiple analyses using a lognormal relaxed clock in BEAST2 utilized either no constraint for the age of *Bangiomorpha pubescens* (Run T07), its previously accepted age (Run T08), or its new reported age from this study (Run T09). The various analyses were compared based on the 95% Confidence Interval (CI) widths (in millions of years) of key nodes of interest, specifically the red-green divergence and plastid endosymbiosis. BEAST2 run outputs are presented in Figures A1–A3.

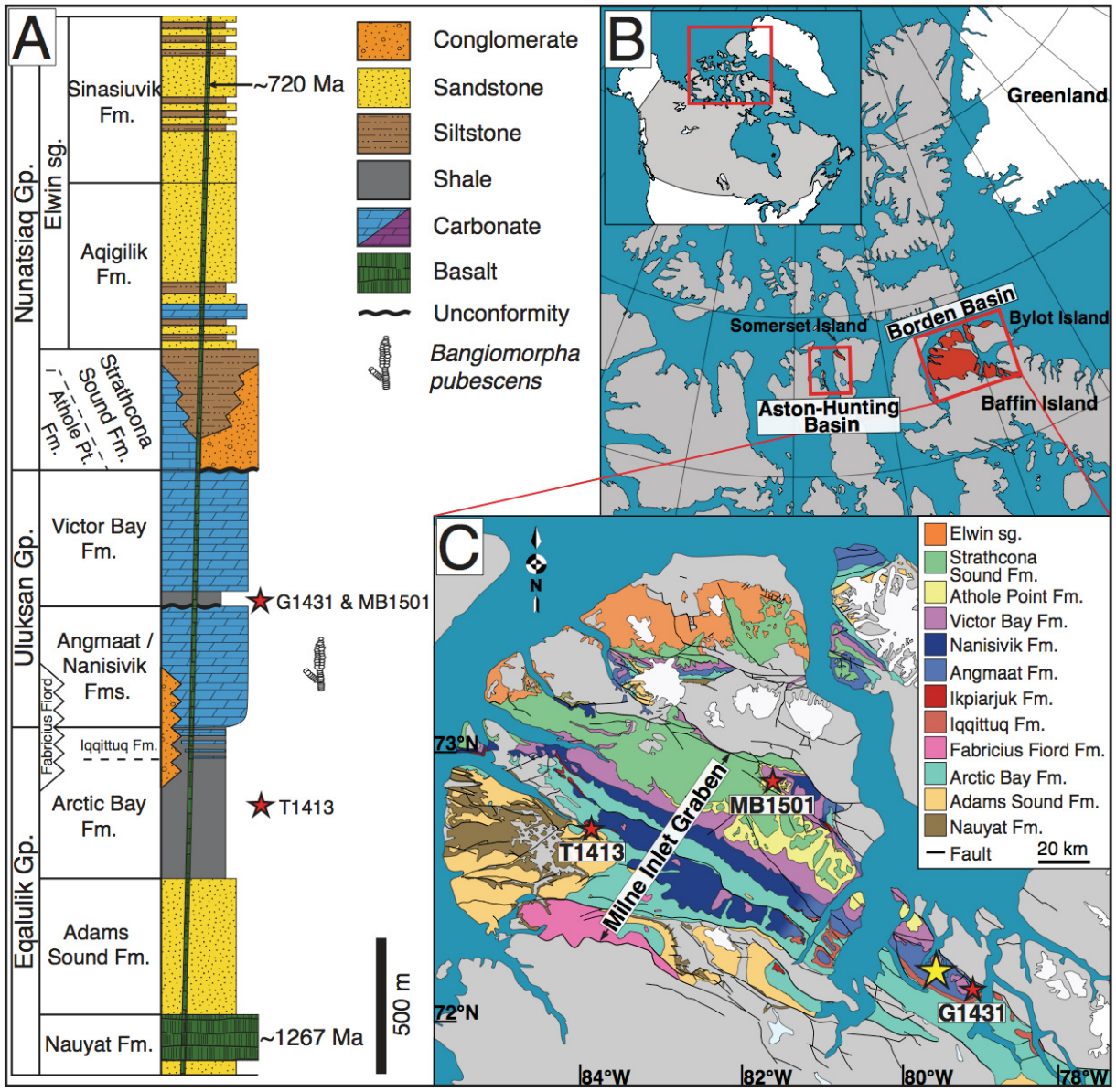

Figure 1: Location and geological context of the study area. (**A**) Schematic lithostratigraphy of the Bylot Supergroup in the Borden Basin (age constraints from LeCheminant and Heaman, 1989; Heaman et al., 1992; Pehrsson and Buchan, 1999). Gp.—Group; sg.—subgroup; Fm.—Formation; Pt.—Point. (B) Locations (red boxes) where *Bangiomorpha pubescens* occurs. (C) Map of the Borden Basin (adapted from Turner, 2009) showing Re-Os sample localities (red stars) and *Bangiomorpha. pubescens* fossil locality (yellow star; Knoll et al., 2013).

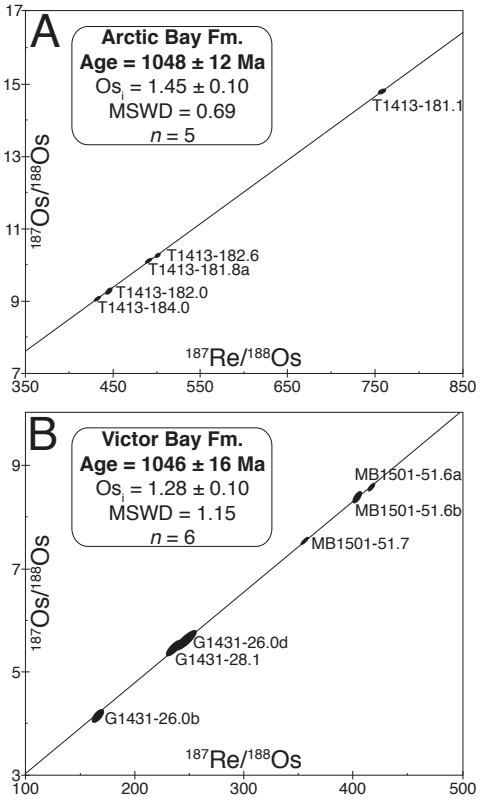

Figure 2: Re-Os isochron diagrams. (A) The Arctic Bay Formation. MSWD—mean square of weighted deviates. (B) The Victor Bay Formation. Data-point error ellipses represent 2σ uncertainty. Elemental abundances and isotopic compositions are presented in Table DR1.

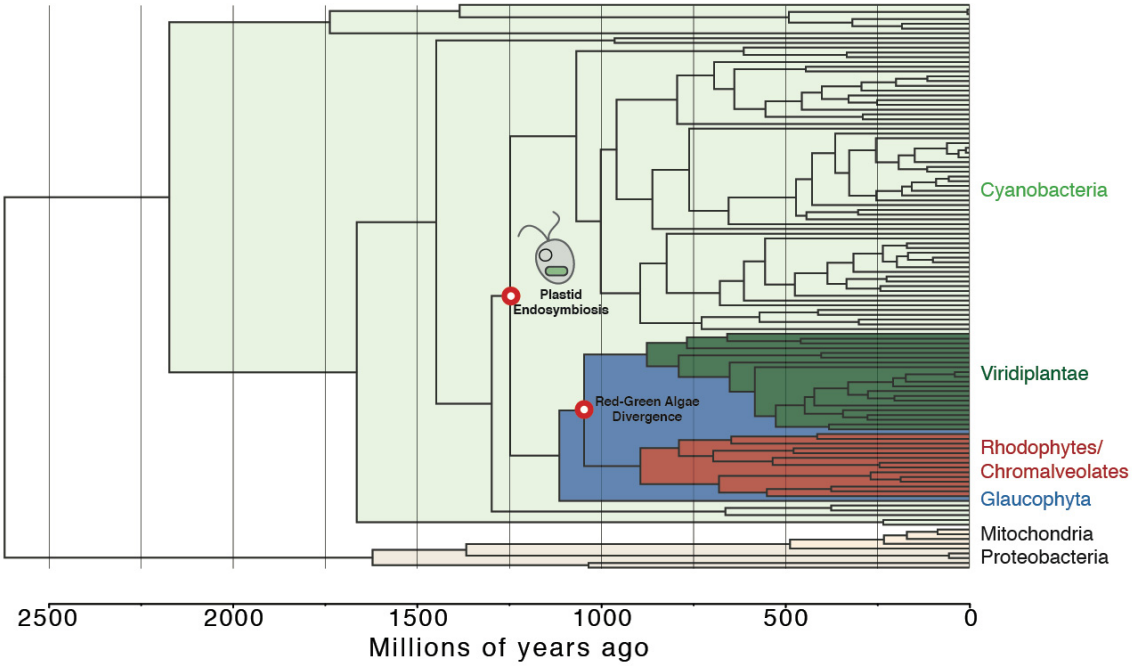

Figure 3: Schematic timeline of key evolutionary events. Dates are estimated from cross-calibrated BEAST2 run T09 based on the revised age of *Bangiomorpha pubescens* of ca. 1045 ± 15 Ma.

References

Adam, Z.R., Skidmore, M.L., Mogk, D.W., and Butterfield, N.J., 2017, A Laurentian record of the earliest fossil eukaryotes: Geology, v. 45, p. 387–390.

Bengtson, S., Sallstedt, T., Belivanova, V., and White- house, M., 2017, Three-dimensional preservation of cellular and subcellular structures suggests 1.6 billion-year-old crown-group red algae: PLoS Biology, v. 15, e2000735.

Berney, C., and Pawlowski, J., 2006, A molecular time-scale for eukaryote evolution recalibrated with the continuous microfossil record: Royal Society of London Philosophical Transactions, ser. B, v. 273, p. 1867–1872.

Butterfield, N.J., 2000, *Bangiomorpha pubescens* n. Gen., n. sp.: Implications for the evolution of sex, multicellularity, and the Mesoproterozoic/Neoproterozoic radiation of eukaryotes: Paleobiology, v. 26, p. 386–404.

Butterfield, N.J., 2015, Proterozoic photosynthesis—A critical review: Palaeontology, v. 58, p. 953–972.

Butterfield, N.J., Knoll, A.H., and Swett, K., 1988, Exceptional preservation of fossils in an upper Proterozoic shale: Nature, v. 334, p. 424–427.

Butterfield, N.J., Knoll, A.H., and Swett, K., 1990, A bangiophyte red alga from the Proterozoic of arctic Canada: Science, v. 250, p. 104–107.

Cavalier-Smith, T., Brasier, M., and Embley, T.M., 2006, Introduction: How and when did microbes change the world?: Royal Society of London Philosophical Transactions, ser. B, v. 361, p. 845– 850.

Cohen, A.S., 2004, The rhenium-osmium isotope system: Applications to geochronological and palaeoenvironmental problems: Journal of the Geological Society [London], v. 161, p. 729–734.

Cohen, A.S., Coe, A.L., Bartlett, J.M., and Hawkesworth, C.J., 1999, Precise Re-Os ages of organic-rich mudrocks and the Os isotope composition of Jurassic seawater: Earth and Planetary Science Letters, v. 167, p. 159–173.

Cohen, P.A., and Macdonald, F.A., 2015, The Proterozoic record of eukaryotes: Paleobiology, v. 41, p. 610–632.

Creaser, R.A., Sannigrahi, P., Chacko, T., and Selby, D., 2002, Further evaluation of the Re-Os

geo- chronometer in organic-rich sedimentary rocks: A test of hydrocarbon maturation effects in the Exshaw Formation, Western Canada Sedimentary Basin: Geochimica et Cosmochimica Acta, v. 66, p. 3441–3452.

Delwiche, C.F., 1999, Tracing the thread of plastid diversity through the tapestry of life: American Naturalist, v. 154, p. S164–S177.

Dubin, A., and Peucker-Ehrenbrink, B., 2015, The importance of organic-rich shales to the geochemical cycles of rhenium and osmium: Chemical Geology, v. 403, p. 111–120.

Eme, L., Sharpe, S.C., Brown, M.W., and Roger, A.J., 2014, On the age of eukaryotes: Evaluating evidence from fossils to molecular clocks: Cold Spring Harbor Perspectives in Biology, v. 6, a016139.

Fahrig, W.F., Christie, K.W., and Jones, D.J., 1981, Paleomagnetism of the Bylot Basins: Evidence for Mackenzie continental tensional tectonics: Geological Survey of Canada Paper 81-10, p. 303–312.

Han, T.M., and Runnegar, B., 1992, Megascopic eukaryotic algae from the 2.1-billion-year-old Naguanee iron-formation, Michigan: Science, v. 257, p. 232–235.

Heaman, L.M., LeCheminant, A.N., and Rainbird, R.H., 1992, Nature and timing of Franklin igneous events, Canada: Implications for a late Proterozoic mantle plume and the break-up of Laurentia: Earth and Planetary Science Letters, v. 109, p. 117–131.

Hedges, S.B., Blair, J.E., Venturi, M.L., and Shoe, J.L., 2004, A molecular timescale of eukaryote evolution and the rise of complex multicellular life: BMC Evolutionary Biology, v. 4, p. 2.

Javaux, E.J., and Knoll, A.H., 2017, Micropaleontology of the lower Mesoproterozoic Roper Group, Australia, and implications for early eukaryotic evolution: Journal of Paleontology, v. 91, p. 199– 229.

Javaux, E.J., Knoll, A.H., and Walter, M.R., 2001, Morphological and ecological complexity in early eukaryotic ecosystems: Nature, v. 412, p. 66–69.

Javaux, E.J., Marshall, C.P., and Bekker, A., 2010, Organic-walled microfossils in 3.2-billion-year- old shallow-marine siliciclastic deposits: Nature, v. 463, p. 934–938.

Kah, L.C., Sherman, A.G., Narbonne, G.M., Knoll, A.H., and Kaufman, A.J., 1999, δ13C stratigraphy of the Proterozoic Bylot Supergroup, Baffin Island, Canada: Implications for regional lithostratigraphic correlations: Canadian Journal of Earth Sciences, v. 36, p. 313–332.

Keeling, P.J., 2010, The endosymbiotic origin, diversification and fate of plastids: Royal Society of London Philosophical Transactions, ser. B, v. 365, p. 729–748.

Kendall, B., Creaser, R.A., and Selby, D., 2009, ^{187}Re-^{187}Os geochronology of Precambrian organic-rich sedimentary rocks, *in* Craig, J., et al., eds., Global Neoproterozoic petroleum systems: The emerging potential in North Africa: Geological Society of London Special Publication 326, p. 85–107.

Knoll, A.H., 2014, Paleobiological perspectives on early eukaryotic evolution: Cold Spring Harbor Perspectives in Biology, v. 6, a016121.

Knoll, A.H., Wörndle, S., and Kah, L.C., 2013, Covariance of microfossil assemblages and microbialite textures across an upper Mesoproterozoic carbonate platform: Palaios, v. 28, p. 453–470.

Lamb, D.M., Awramik, S.M., Chapman, D.J., and Zhu, S., 2009, Evidence for eukaryotic diversification in the ~1800 million-year-old Changzhougou Formation, north China: Precambrian Research, v. 173, p. 93–104.

LeCheminant, A.N., and Heaman, L.M., 1989, Mackenzie igneous events, Canada: Middle Proterozoic hotspot magmatism associated with ocean opening: Earth and Planetary Science Letters, v. 96, p. 38–48.

Marin, B., Nowack, E.C.M., and Melkonian, M., 2005, A plastid in the making: Evidence for a second primary endosymbiosis: Protist, v. 156, p. 425– 432.

Moczydłowska, M., Landing, E., Zang, W., and Palacios, T., 2011, Proterozoic phytoplankton and timing of chlorophyte algae origins: Palaeontology, v. 54, p. 721–733.

Parfrey, L.W., Lahr, D.J.G., Knoll, A.H., and Katz, L.A., 2011, Estimating the timing of early eukaryotic diversification with multigene molecular clocks: Proceedings of the National Academy of Sciences of the United States of America, v. 108, p. 13,624–13,629.

Pehrsson, S.J., and Buchan, K.L., 1999, Borden dykes of Baffin Island, Northwest Territories: A Franklin U-Pb baddeleyite age and paleomagnetic reinterpretation: Canadian Journal of Earth Sciences, v. 36, p. 65–73.

Ray, J.S., 2006, Age of the Vindhyan Supergroup: A review of recent findings: Journal of Earth System Science, v. 115, p. 149–160.

Roger, A.J., and Hug, L.A., 2006, The origin and diversification of eukaryotes: Problems with

molecular phylogenetics and molecular clock estimation: Royal Society of London Philosophical Transactions, ser. B, v. 361, p. 1039–1054.

Rooney, A.D., Selby, D., Houzay, J.-P., and Renne, P.R., 2010, Re-Os geochronology of a Mesoproterozoic sedimentary succession, Taoudeni basin, Mauritania: Implications for basin-wide correlations and Re-Os organic-rich sediments systematics: Earth and Planetary Science Letters, v. 289, p. 486–496.

Sánchez-Baracaldo, P., Raven, J.A., Pisani, D., and Knoll, A.H., 2017, Early photosynthetic eukaryotes inhabited low-salinity habitats: Proceedings of the National Academy of Sciences of the United States of America, v. 114, p. E7737– E7745.

Sherman, A.G., Narbonne, G.M., and James, N.P., 2001, Anatomy of a cyclically packaged Mesoproterozoic carbonate ramp in northern Canada: Sedimentary Geology, v. 139, p. 171–203.

Shih, P.M., and Matzke, N.J., 2013, Primary endosymbiosis events date to the later Proterozoic with cross-calibrated phylogenetic dating of duplicated ATPase proteins: Proceedings of the National Academy of Sciences of the United States of America, v. 110, p. 12,355–12,360.

Shih, P.M., Hemp, J., Ward, L.M., Matzke, N.J., and Fischer, W.W., 2017, Crown group Oxyphotobacteria postdate the rise of oxygen: Geobiology, v. 15, p. 19–29.

Turner, E.C., 2009, Mesoproterozoic carbonate systems in the Borden Basin, Nunavut: Canadian Journal of Earth Sciences, v. 46, p. 915–938.

Yoon, H.S., Hackett, J.D., Ciniglia, C., Pinto, G., and Bhattacharya, D., 2004, A molecular timeline for the origin of photosynthetic eukaryotes: Molecular Biology and Evolution, v. 21, p. 809–818.

7. Appendix

7.1. Supplemental Methods

7.1.1. Stratigraphy and Sampling

Shale samples were collected from outcrops that lack evidence for secondary mineralization from hydrothermal activity and weathered regions that may have experienced alteration were also avoided. Sample sets comprise several 100–200 g samples excavated 10–30 cm from the outcrop surface to target fresh material. Samples were collected along strike from a narrow stratigraphic range (<10 cm), as well as from a vertical profile (up to 5 m). The most organic-rich and least visibly-weathered samples were then chosen for digestion and isotopic analysis.

Arctic Bay Formation samples are from Shale Valley (N 72° 45' 04.8" W 83° 50' 39.2"), ca. 180 m above the base of section T1413 (Arctic Bay-Adams Sound formations contact not exposed in this locale) and ca. 170 m below the base of the Ikpiarjuk Formation (Angmaat Formation equivalent; Fig. 1). Victor Bay Formation samples are from sections G1431 at Angmaat Mountain (N 72° 09' 25.9" W 79° 02' 05.5") and MB1501 at Pingo Valley (N 72° 53' 48.3" W 81° 24' 45.02"). Both Victor Bay Formation sample sets are from within the same maximum flooding interval indicated by the finest-grained and most organic-rich horizon ca. 25 m above the contact with the Angmaat Formation.

7.1.2. Re-Os Geochronology Methods

Least-weathered samples from each sample set were selected and trimmed with a diamond-tipped lapidary saw blade to remove any weathered surfaces, then polished with a diamond pad to remove any metal contamination. After samples were dried at room temperature, 30–50 g aliquots were crushed to a fine powder (ca. 30 μm) using a SPEX #8506 zirconia ceramic puck and grinding container in a SPEX 8500 shatterbox to homogenize each sample (Kendall et al., 2009a). Analyses of Re and Os isotopic abundances and compositions were performed at the University of Alberta's Re-Os Crustal Geochronology Laboratory in the Department of Earth and Atmospheric Sciences

following methodologies developed by Creaser et al. (2002), Selby and (2003), Kendall et al. (2004), and Cumming et al. (2013).

Between 0.2 and 0.5 g of each sample was digested and equilibrated with 8 ml of Cr^{VI}-H_2SO_4 along with a known quantity of mixed $^{185}Re + ^{190}Os$ tracer solution (spike) in Carius tubes at 220 °C for 48 hrs. Digestion with Cr^{VI}-H_2SO_4 is known to preferentially liberate hydrogenous rather than detrital Re and Os in shale samples, resulting in more accurate and precise isochrons (Selby and Creaser, 2003; Kendall et al., 2004; Rooney et al., 2011). Osmium was isolated and purified by $CHCl_3$ solvent extraction and micro-distillation using HBr, and Re was purified using $(CH_3)_2CO$ solvent extraction and anion chromatography following protocols outlined by Selby and Creaser (2003) and Cumming et al. (2013). These Re and Os fractions were then loaded onto Ni and Pt filaments, respectively (Selby and Creaser, 2003; Selby et al., 2007), for analysis with a ThermoScientific TRITON instrument using negative thermal ionization mass spectrometry (NTIMS; Creaser et al., 1991). Re was analyzed via static Faraday collection and Os utilizing ion-counting with a secondary electron multiplier in peak-hopping mode.

Isochron ages were regressed using the Re and Os isotopic measurements, calculated 2σ uncertainties for $^{187}Re/^{188}Os$ and $^{187}Os/^{188}Os$, and the associated error correlation function (rho) using Isoplot V. 4.15 (Ludwig, 1980; Ludwig, 2011) with a ^{187}Re decay constant (λ) of $1.666 \times 10^{-11} year^{-1}$ (Table A1; Smoliar et al., 1996). A Re standard solution of normal isotopic composition was repeatedly analyzed to monitor long-term mass spectrometry reproducibility, using analysis amounts typical for shale samples (1–4 ng). For this solution, an average value for $^{185}Re/^{187}Re$ of 0.5973 ± 0.0007 (n = 52; 1σ) was obtained over the period of analysis, which overlaps the value of 0.5974 (Gramlich et al., 1973). A Johnson–Matthey Os solution is used as an in-house standard for Os, which yielded an average $^{187}Os/^{188}Os$ ratio of 0.10683 ± 0.00010 (n = 186; 1σ) by pulse-counting SEM measurement over the period of analysis, which is identical to values reported elsewhere (Li et al., 2010).

7.1.3. Cross-Calibrated Molecular Clock (BEAST2) Methods

In lieu of a complete fossil record, molecular clock analyses may be improved by increasing the amount of age data they incorporate. Cross-calibrated analyses leverage relative dating information using gene duplication events to increase the accuracy of divergence time

estimates (Shih and Matzke, 2013). Molecular clock analyses were run on a concatenated dataset of proteins: AtpA, AtpB, AtpE, AtpF, AtpH, AtpI, Rpl2, Rpl16, Rps3, Rps12, and EfTu, as well as 16S rDNA. To generate the dataset, sequences were aligned using MAFFT (Katoh et al., 2005), then partitioned into the concatenated protein sequences and 16S nucleotide sequences. The base set of age calibrations implemented are primarily from on the fossil records of plants and algae and the molecular clock analyses of Smith et al. (2010). A summary of the various constraints used can be found in Table A2. A uniform prior of 2400–3800 million years ago (Ma) was used as a constraint for the last common ancestor. The only constraint that differed between the three analyses was the prior set on the green-red divergence, representing the oldest possible node for which *Bangiomorpha pubescens* can provide a direct constraint based on its position either derived within the Bangiales or perhaps as a stem-group red alga (e.g., Butterfield, 2000; Yang et al., 2016). In these analyses (Table 1), three constraints were tested to compare their effect on different interpretations of plastid endosymbiosis: 1) no prior (Run T07; Fig. A1), 2) a prior based on the previously reported age for *Bangiomorpha pubescens* of 1198 Ma (Run T08; Fig. A2; Butterfield, 2000), and 3) a prior based on our geochronology data of 1045 Ma (Run T09; Fig. A3). As previously described (Shih et al., 2017), molecular clock analyses were estimated with the program BEAST2 (Drummond and Rambaut, 2007) using the CIPRES Science Gateway server (Miller et al., 2010). The CpREV model and the GTR + G model were used as the substitution model for the protein and nucleotide datasets, respectively. A lognormal relaxed molecular clock model was implemented. For all analyses, three separate MCMC chains for 40–50 million generations were generated, sampling every 10,000 generations. The initial 20 million generations were discarded as burn-in, and maximum clade credibility trees were generated using TreeAnnotator v1.7.5. The analyses and dates of interest are summarized in the main text and Table 1.

7.2. Supplemental Text

7.2.1. Re-Os Results

Re and Os data from this study (see Table A1) are within reported concentrations and isotopic ratios of other black shales and do not display evidence for post-depositional disturbance of the Re-Os system. Regression of Arctic Bay Formation samples excluding T1413-181.1 yields

a nearly identical age of 1054 ± 41 Ma and confirms that this sample does not disproportionally affect the isochron by "anchoring" its slope. Victor Bay Formation samples are from two correlative stratigraphic sections (G1431 and MB1501). Regression of G1431 Victor Bay Formation samples yield an imprecise Model 3 age of 1077 ± 28 Ma due to an insufficient spread in initial $^{187}Re/^{188}Os$ and too much variation in initial $^{187}Os/^{188}Os$ values (see Table DR1) necessary to develop a precise isochron (Selby and Creaser, 2005; Kendall et al., 2009a). Therefore, samples from section MB1501 of the same maximum flooding interval in the lower Victor Bay Formation were also incorporated. Regression of MB1501 samples yielded an imprecise, but indistinguishable to G1431 (within uncertainty), Model 3 age of 995 ± 320 Ma. A sharp transgressive surface directly above the basin-wide Angmaat-Victor Bay unconformity marks a regional flooding event in the Milne Inlet Graben, and offers an unequivocally synchronous datum (Sherman et al., 2001). Sample set G1431 was collected from 26–28.1 m above this unconformity, and sample set MB1501 is from a slightly deeper-water, but time-correlative horizon 21.3–21.6 m above this unconformity. Robust stratigraphic evidence for depositional synchronicity and the similarity of their model ages enable regression of these samples as a combined data set to produce a significantly more precise age (Fig. A4; Geboy et al., 2013). Combining these data sets is further supported by the relative precision and lower variance in the composite isochron, as well as its agreement with the Re-Os age for the Arctic Bay Formation reported herein (Fig. 2).

Initial $^{187}Os/^{188}Os$ values for all Arctic Bay and Victor Bay samples range from 1.17–1.45 (average modern continental runoff $^{187}Os/^{188}Os$ = 1.5; Levasseur et al., 1999), consistent with a highly radiogenic Os flux dominated by evolved, continentally derived sediment and waters (Xu et al., 2009; Cumming et al., 2012; Cumming et al., 2013; Rooney et al., 2014). These data demonstrate that the Borden Basin had minimal communication with the global ocean during deposition of the sampled black shale units from the middle Arctic Bay (Turner and Kamber, 2012; Hahn et al., 2015) and lower Victor Bay formations and was strongly influenced chemically by runoff from the surrounding highly-evolved Archean to Paleoproterozoic orthogneiss and metasedimentary successions of the Rae Province (Crocker et al., 1993). However, abundant sulfate evaporite deposits, marine C, S, and Sr isotopic signatures, and evidence for tidal influence indicate that the Borden Basin was connected to a large ocean basin during deposition of the Angmaat Formation and other intervals of carbonate deposition (i.e. upper Victor Bay and Athole Point formations; Kah et al., 1999; Kah et al., 2001). Together these data demonstrate that the

Borden Basin was periodically restricted from the open ocean and that the degree of restriction influenced sedimentation patterns, perhaps due to changes in the geochemical stratification of its basin waters. These interpretations may help characterize the environment in which *Bangiomorpha pubescens* evolved.

Precise Re-Os isochrons require samples of the same (or similar) age and with similar initial $^{187}Os/^{188}Os$ (Cohen et al., 1999; Creaser et al., 2002; Cohen, 2004). Sediment in restricted basins are known to exhibit highly variable $^{187}Os/^{188}Os$ as they are sensitive to short-term variability in weathering sources and runoff (McArthur et al., 2008; Cumming et al., 2012; Cumming et al., 2013; Tripathy et al., 2015). Therefore, on the condition that a sufficient spread in $^{187}Re/^{188}Os$ is maintained, utilizing samples from a reduced stratigraphic interval, especially from restricted basins, can minimize age uncertainty by limiting the depositional timescale over which samples were deposited and thus stratigraphic variation in initial $^{187}Os/^{188}Os$ (Os_i; Xu et al., 2009; Cumming et al., 2012; Xu et al., 2014).

7.2.2. Previous Geochronology from the Bylot Supergroup

Pyrite Re-Os geochronology from the carbonate-hosted Nanisivik Pb-Zn deposit (Angmaat Formation equivalent; see Fig. 1) suggest approximately syn-depositional mineralization ca. 1100 Ma, though the data span 1151–1013 Ma (Hnatyshin et al., 2016), which is broadly consistent with depositional ages presented from this study. Turner and Kamber (2012) conducted whole-rock U-Th-Pb analyses of Arctic Bay Formation black shales and calculated an age of 1092 ± 59 Ma from the weighted mean of a ^{206}Pb-^{207}Pb isochron and ^{238}U-^{206}Pb and ^{232}Th-^{208}Pb errorchrons; however, a total of nine outlying samples were excluded in these calculations and stratigraphic heights are not reported.

Unpublished whole-rock, carbonate Pb-Pb geochronology of Angmaat Formation samples were reported to produce an age of 1199 ± 24 Ma, and combined data from Angmaat, Victor Bay, and Athole Point formations samples an age of 1204 ± 22 Ma (Kah et al., 2001). While these dates were often cited as the age of *Bangiomorpha* pubescens (ca. 1200 Ma), they are older than and therefore incompatible with the calculated age of the underlying Arctic Bay Formation from Turner and Kamber (2012). Furthermore, Pb-Pb carbonate ages can overestimate depositional ages due to incorporation of basement-derived Pb during diagenesis (i.e., dolomitization), meteoric

alteration, and metamorphism (e.g., Babinski et al., 2007). These incongruent ages highlight obstacles associated with the application of whole-rock U-Th-Pb and Pb-Pb geochronology to typical Precambrian samples. The utility of the black shale Re-Os geochronometer for yielding precise and accurate ages of Precambrian sedimentary successions, on the other hand, is corroborated by numerous recent studies (e.g., Selby and Creaser, 2003; Kendall et al., 2009b; Cumming et al., 2013; van Acken et al., 2013; Rooney et al., 2014; Rooney et al., 2015).

7.2.3. Age of the Chitrakoot Taxa

The Vindhyan Supergroup in central India has long been the center of debate regarding fossil discoveries and their ages (see Ray, 2006 for overview). This up-to 4-km-thick sedimentary succession primarily outcrops in the Son Valley and Rajasthan. The lower Vindhyan Semri Group has largely been studied in the Son Valley region where multiple interbedded volcanic tuffs offer robust U-Pb zircon depositional age constraints of ca. 1600 Ma (Rasmussen et al., 2002; Ray et al., 2002; Bengtson et al., 2009). These ages are broadly consistent with the occurrence of microfossils such as *Grypania* (Kumar, 1995) which occur globally in strata of similar ages (Adam et al., 2017).

The Chitrakoot Formation occurs as a stratigraphic outlier in the Jankikund-Chitrakoot region to the north of the Son Valley and is interpreted to record deposition within an isolated sub-basin that was disconnected from the main Vindhyan basin (Bose et al., 2015); however, discontinuous lateral exposure renders robust correlations, even within the Chitrakoot region, tenuous. The Chitrakoot Formation has been dated using whole-rock geochronological techniques, with whole-rock Rb-Sr ages from lower glauconitic facies spanning ca. 1500–1400 Ma (Kumar et al., 2001), and a whole-rock Pb-Pb age of 1650 ± 89 Ma from the uppermost phosphatic Tirohan Dolomite (Bengtson et al., 2009). While these dates broadly support correlation between the Tirohan Dolomite of the Chitrakoot Formation and the Rohtas Limestone of the Semri Group (Bengtson et al., 2017), robust stratigraphic correlations between the Chitrakoot outlier and principal Vindhyan sections in the Son Valley are complicated by inconclusive chemostratigraphic signatures (Ray et al., 2003) and significant lithological and thickness differences between these successions (Chakraborty, 2006). Alternately, if the Tirohan Dolomite is equivalent to the next younger unit that directly overlies the Rohtas Limestone, it would belong to the upper Vindhyan

Kaimur Group which could be as young as ca. 1070 Ma (Gregory et al., 2006)—similar to the age of the Angmaat Formation. Thus, the ca. 1600 Ma age of the phosphatized fossils from the Tirohan Dolomite is primarily based on the internally inconsistent dates for the Chitrakoot Formation, and so further corroboration of the anomalously old age of these fossils requires the application of reliable, high precision geochronology to the Chitrakoot sections themselves.

Supplemental Tables and Figures

Table A1: Re and Os abundances and isotopic compositions.

Sample*	Formation	Re (ppb)	±2σ	Os (ppt)	±2σ	$^{187}Re/^{188}Os$	±2σ	$^{187}Os/^{188}Os$	±2σ	Rho	Os_i
T1413-181.1	Arctic Bay	67.31	0.25	1247.38	8.16	757.68	3.48	14.80	0.06	0.54	1.42
T1413-181.8	Arctic Bay	21.62	0.08	488.94	3.55	490.77	2.97	10.12	0.05	0.73	1.45
T1413-182.0	Arctic Bay	22.10	0.09	524.52	4.69	445.38	2.98	9.28	0.07	0.62	1.41
T1413-182.6	Arctic Bay	48.49	0.18	1082.97	7.36	501.16	2.37	10.27	0.05	0.48	1.41
T1413-184.0	Arctic Bay	16.76	0.07	404.74	3.11	432.12	2.94	9.07	0.06	0.76	1.43
T1413-185.0	Arctic Bay	50.76	0.19	1145.79	8.71	485.80	2.41	9.91	0.05	0.48	1.33
G1431-26.0b	Victor Bay	0.76	0.01	33.38	0.49	166.36	4.32	4.15	0.10	0.66	1.22
G1431-26.0d	Victor Bay	0.72	0.01	24.25	0.39	246.74	7.93	5.61	0.16	0.84	1.27
G1431-28.1	Victor Bay	0.94	0.01	32.57	0.48	236.08	5.78	5.46	0.12	0.79	1.31
G1431-28.2	Victor Bay	0.94	0.01	32.79	0.43	229.48	5.36	5.21	0.10	0.83	1.18
MB1501-51.6a	Victor Bay	16.73	0.04	406.59	3.41	416.96	2.52	8.58	0.06	0.75	1.24
MB1501-51.6b	Victor Bay	15.52	0.04	384.67	4.13	403.94	3.25	8.39	0.09	0.69	1.28
MB1501-51.7	Victor Bay	7.04	0.02	187.46	1.58	355.79	2.82	7.54	0.06	0.86	1.28
MB1501-51.9	Victor Bay	12.89	0.03	316.92	2.33	404.81	2.12	8.29	0.05	0.78	1.17

Note: Total procedural blanks analyzed during this study were 11 ± 3 pg Re and 0.25 ± 0.3 pg Os and $^{187}Os/^{188}Os$ of 1.3 ± 0.8 (1σ, *n*=5).

*Samples in **bold** are included in the isochrons that utilized a limited stratigraphic range (Fig. 2).

Os_i = Initial $^{187}Os/^{188}Os$ isotope composition calculated from $\lambda^{187}Re$ and isochron ages that utilize all samples (1051 Ma for Arctic Bay samples and 1047 Ma for Victor Bay formations samples; Figure A4).

Rho = associated error correlation (Ludwig, 1980).

Table A2: Summary of calibration constraints used in this study.

Divergence event	Type of Distribution	Age Constraint (Ma)
Angiospermae	Normal	217 ± 40 (1σ)
Land Plants	Normal	477 ± 70 (1σ)
Bangiomorpha pubescens	Uniform	1174–1222
"Rise of Oxygen"	Uniform	2400–3000
Last Common Ancestor	Uniform	2400–3800

Note: Angiospermae and land plant age constraints from Smith et al. (2010).

Table A3: Abbreviations for species names used in Figures A1-3.

Species Name	Clade	Abbreviation
Gloeobacter violaceus PCC 7421	Cyanobacteria	PCC7421
Gloeobacter kilaueensis JS1	Cyanobacteria	GLOJS1
Synechococcus sp. PCC 7336	Cyanobacteria	PCC7336
Synechococcus sp. JA-3-3Ab	Cyanobacteria	JA33A
Pseudanabaena sp. PCC 7367	Cyanobacteria	PCC7367
Pseudanabaena sp. PCC 6802	Cyanobacteria	PCC6802
Synechococcus sp. PCC 7502	Cyanobacteria	PCC7502
Acaryochloris marina MBIC11017	Cyanobacteria	MB11017
Cyanothece sp. PCC 7425	Cyanobacteria	PCC7425
Thermosynechococcus elongatus BP-1	Cyanobacteria	BP1
Geitlerinema sp. PCC 7407	Cyanobacteria	PCC7407
Leptolyngbya sp. PCC 7375	Cyanobacteria	PCC7375
Prochlorothrix hollandica PCC 9006	Cyanobacteria	PCC9006
Synechococcus elongatus PCC 7942	Cyanobacteria	PCC7942
Cyanobium sp. PCC 7001	Cyanobacteria	PCC7001
Cyanobium gracile PCC 6307	Cyanobacteria	PCC6307
Synechococcus sp. WH 5701	Cyanobacteria	WH5701
Synechococcus sp. RS 9916	Cyanobacteria	RS9916
Synechococcus sp. CC 9311	Cyanobacteria	CC9311
Synechococcus sp. WH 7805	Cyanobacteria	WH7805
Synechococcus sp. BL 107	Cyanobacteria	BL107
Synechococcus sp. CC 9605	Cyanobacteria	CC9605
Synechococcus sp. WH 8102	Cyanobacteria	WH8102
Prochlorococcus marinus MIT 9313	Cyanobacteria	MIT9313
Prochlorococcus marinus, subsp. marinus CCMP 1375	Cyanobacteria	CCMP1375
Prochlorococcus marinus MIT 9211	Cyanobacteria	MIT9211
Prochlorococcus marinus MIT 9312	Cyanobacteria	MIT9312
Prochlorococcus marinus MIT 9215	Cyanobacteria	MIT9215
Prochlorococcus marinus AS 9601	Cyanobacteria	AS9601
Prochlorococcus marinus, subsp. pastoris CCMP 1986	Cyanobacteria	MED4
Prochlorococcus marinus NATL 2A	Cyanobacteria	NATL2A
Synechococcus sp. RCC307	Cyanobacteria	RCC307
Crinalium epipsammum PCC 9333	Cyanobacteria	PCC9333
Microcoleus sp. PCC 7113	Cyanobacteria	PCC7113
Chroococcidiopsis sp. PCC 6712	Cyanobacteria	PCC6712
Stanieria cyanosphaera PCC 7437	Cyanobacteria	PCC7437
Cyanobacterium stanieri PCC 7202	Cyanobacteria	PCC7202
Synechococcus sp. PCC 7002	Cyanobacteria	PCC7002
Gloeocapsa sp. PCC 73106	Cyanobacteria	PCC73106
Cyanothece sp. PCC 7424	Cyanobacteria	PCC7424
Microcystis aeruginosa NIES-843	Cyanobacteria	NIES843
Pleurocapsa sp. PCC 7327	Cyanobacteria	PCC7327
Synechocystis sp. PCC 6803	Cyanobacteria	PCC6803
Cyanothece sp. PCC 8801	Cyanobacteria	PCC8801
Crocosphaera watsonii WH 8501	Cyanobacteria	PCC8501
Cyanothece sp. ATCC 51142	Cyanobacteria	ATCC51142
Unidentified cyanobacterium UCYN-A	Cyanobacteria	UCYNA
Halothece sp. PCC 7418	Cyanobacteria	PCC7418
Chroococcidiopsis thermalis PCC 7203	Cyanobacteria	PCC7203
Synechocystis sp. PCC 7509	Cyanobacteria	PCC7509
Rivularia sp. PCC 7116	Cyanobacteria	PCC7116
Nostoc punctiforme PCC 73102	Cyanobacteria	PCC73102
Calothrix sp. PCC 7507	Cyanobacteria	PCC7507
Nostoc azollae 0708	Cyanobacteria	az0708
Raphidiopsis brookii D9	Cyanobacteria	RaphD9
Nostoc sp. PCC 7107	Cyanobacteria	PCC7107
Nostoc sp. PCC 7120	Cyanobacteria	PCC7120
Calothrix sp. PCC 6303	Cyanobacteria	PCC6303
Mastigocladopsis repens PCC 10914	Cyanobacteria	PCC10914
unidentified cyanobacterium PCC 7702	Cyanobacteria	PCC7702
Fischerella sp. PCC 9605	Cyanobacteria	PCC9605

Oscillatoria acuminata PCC 6304	Cyanobacteria	PCC6304
Oscillatoria sp. PCC 6506	Cyanobacteria	PCC6506
Microcoleus vaginatus FGP-2	Cyanobacteria	FGP2
Arthrospira maxima CS-328	Cyanobacteria	CS328
Trichodesmium erythraeum IMS 101	Cyanobacteria	IMS101
Gloeomargarita lithophora	Cyanobacteria	GLITH
MEL.A1	Melainabacteria	MELA1
MEL.B1	Melainabacteria	MELB1
MEL.B2	Melainabacteria	MELB2
MEL.C1	Melainabacteria	MELC1
MEL.C2	Melainabacteria	MELC2
Rickettsia prowazekii strain, Madrid E	α-proteobacteria	RICPR
Rickettsia typhi strain ATCC VR-144	α-proteobacteria	ATPA_RICTY
Caulobacter crescentus strain ATCC 19089	α-proteobacteria	ATPA_CAUCR
Agrobacterium tumefaciens strain C58	α-proteobacteria	ATPA_AGRTU
Arabidopsis thaliana	Plastid	ARATH
Oryza sativa subsp. Japonica	Plastid	ORYSJ
Zea mays	Plastid	ZMAYS
Amborella trichopoda	Plastid	AMBTC
Pinus thunbergii	Plastid	PINTH
Cycas taitungensis	Plastid	CYCTA
Gnetum parvifolium	Plastid	GNETU
Psilotum nudum	Plastid	PSINU
Anthoceros formosae	Plastid	ANTFO
Marchantia polymorpha	Plastid	MARPO
Physcomitrella patens subsp. patens	Plastid	PHYPA
Zygnema circumcarinatum	Plastid	ZYGCR
Staurastrum punctulatum	Plastid	STAPU
Chaetosphaeridium globosum	Plastid	CHAGL
Chara vulgaris	Plastid	CHAVU
Chlamydomonas reinhardtii	Plastid	CHLRE
Chlorella vulgaris	Plastid	CHLVU
Nephroselmis olivacea	Plastid	NEPOL
Euglena gracilis	Plastid	EUGLE
Mesostigma viride	Plastid	MESVI
Chlorokybus atmophyticus	Plastid	CHLAT
Verdigellas peltata	Plastid	VPELT
Cyanophora paradoxa	Plastid	CYAPA
Cyanidioschyzon merolae	Plastid	CYAME
Cyanidium caldarium	Plastid	CYACA
Gracilaria tenuistipitata	Plastid	GRATL
Porphyridium purpureum	Plastid	PORPH
Galdieria sulphuraria	Plastid	GALSU
Thalassiosira pseudonana	Plastid	THAPS
Ectocarpus siliculosus	Plastid	ECTSI
Phaeodactylum tricornutum	Plastid	PHATC
Guillardia theta	Plastid	GUITH
Rhodomonas salina	Plastid	RHDSA
Vaucheria litorea	Plastid	VAULI
Heterosigma akashiwo NIES-293	Plastid	HETAK
Odontella sinensis	Plastid	ODONT
Emiliania huxleyi	Plastid	EMIHU
Paulinella chromatophora	Plastid	PAUCH
Arabidopsis thaliana	Mitochondria	ARATH
Zea mays	Mitochondria	ZMAYS
Oryza sativa	Mitochondria	ORYSJ
Amborella trichopoda	Mitochondria	AMBTC
Physcomitrella patens subsp. patens	Mitochondria	PHYPA

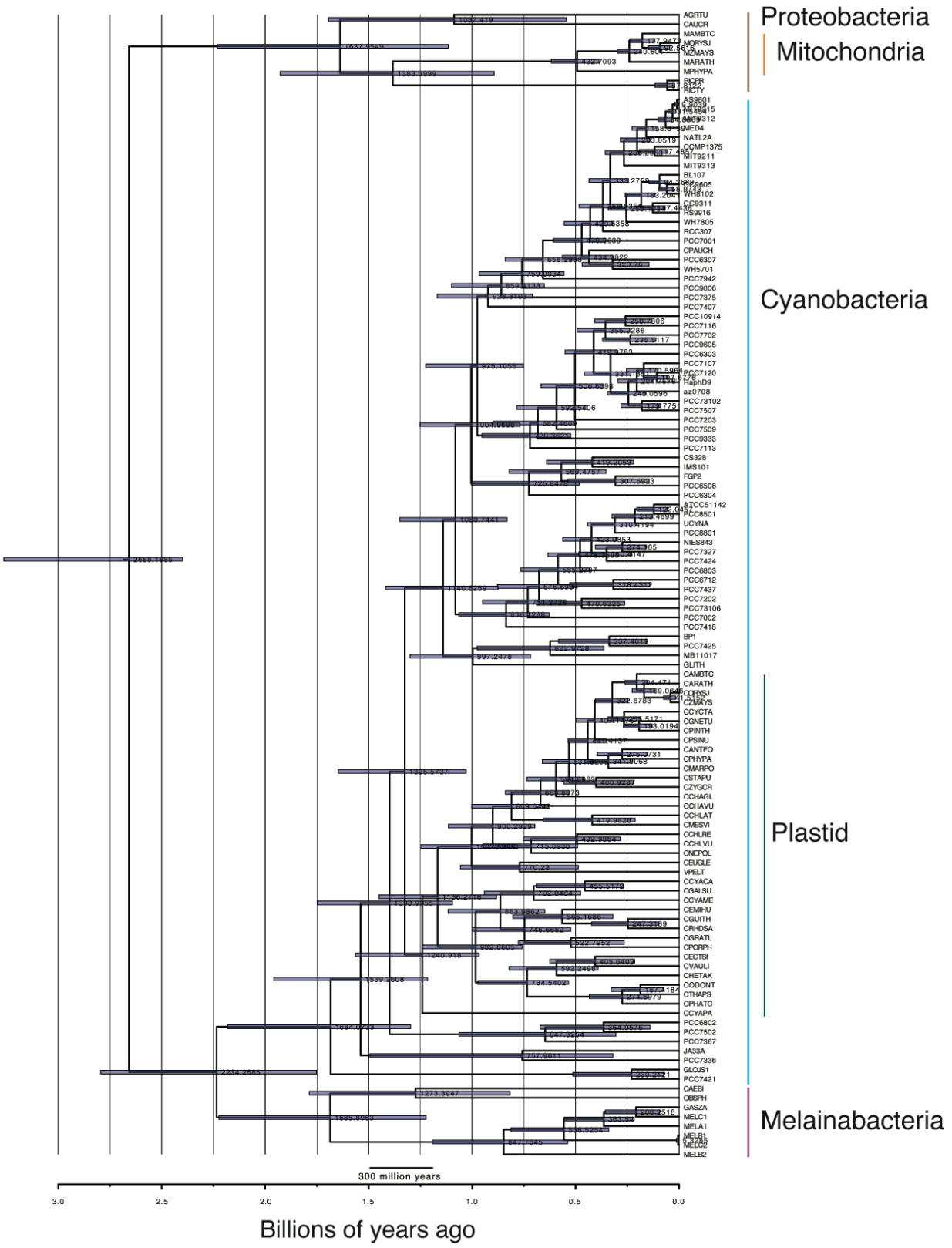

Figure A1: Divergence time estimates from T07 cross-calibrated BEAST2 run. All land plant constraints were used; however, no *Bangiomorpha pubescens* constraint was utilized. Abbreviations are summarized in Table A3.

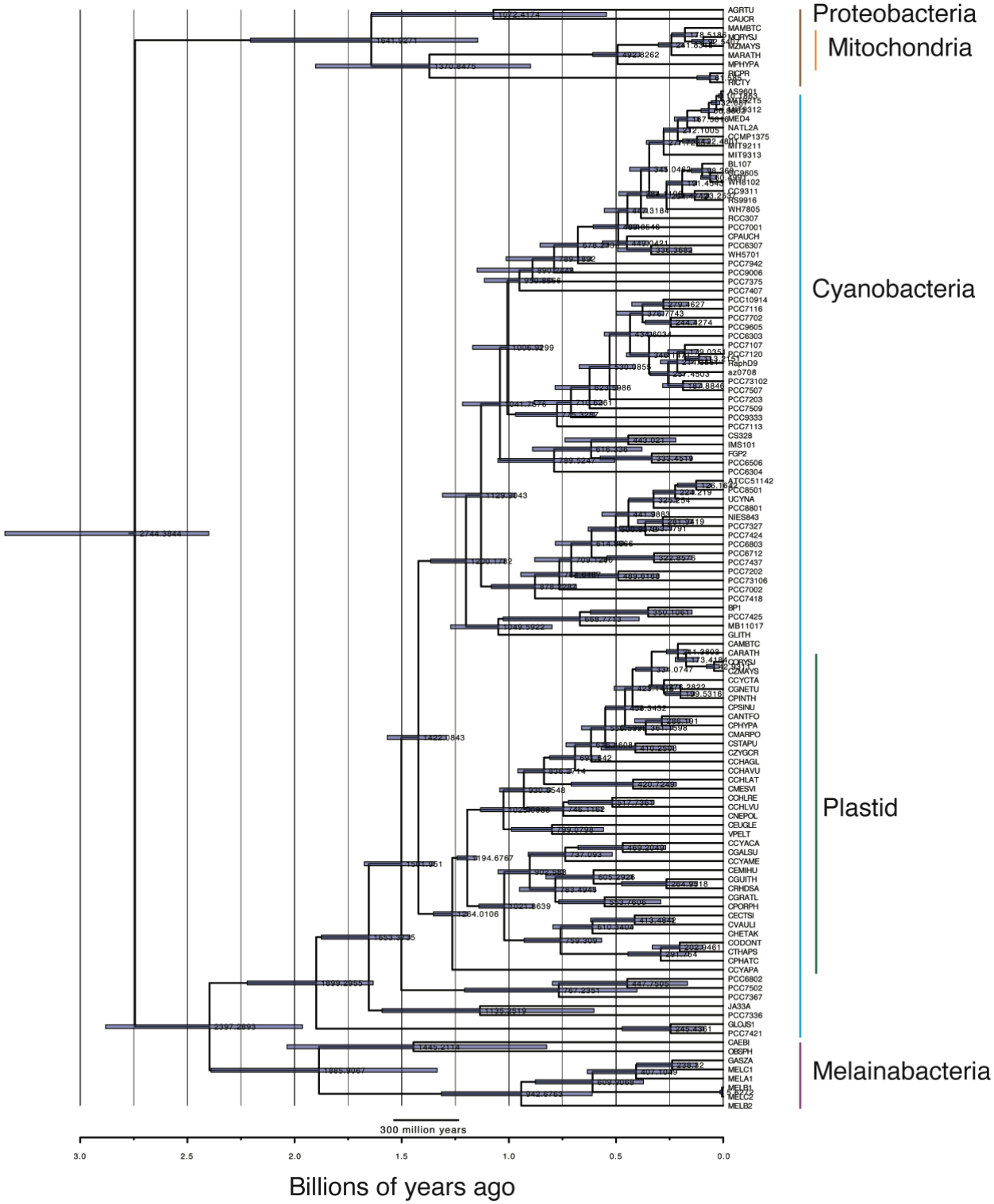

Figure A2: Divergence time estimates from T08 cross-calibrated BEAST2 run. All land plant constraints were used. *Bangiomorpha pubescens* was constrained to the green-red divergence using the older and previously inferred age of 1200 Ma. Abbreviations are summarized in Table A3.

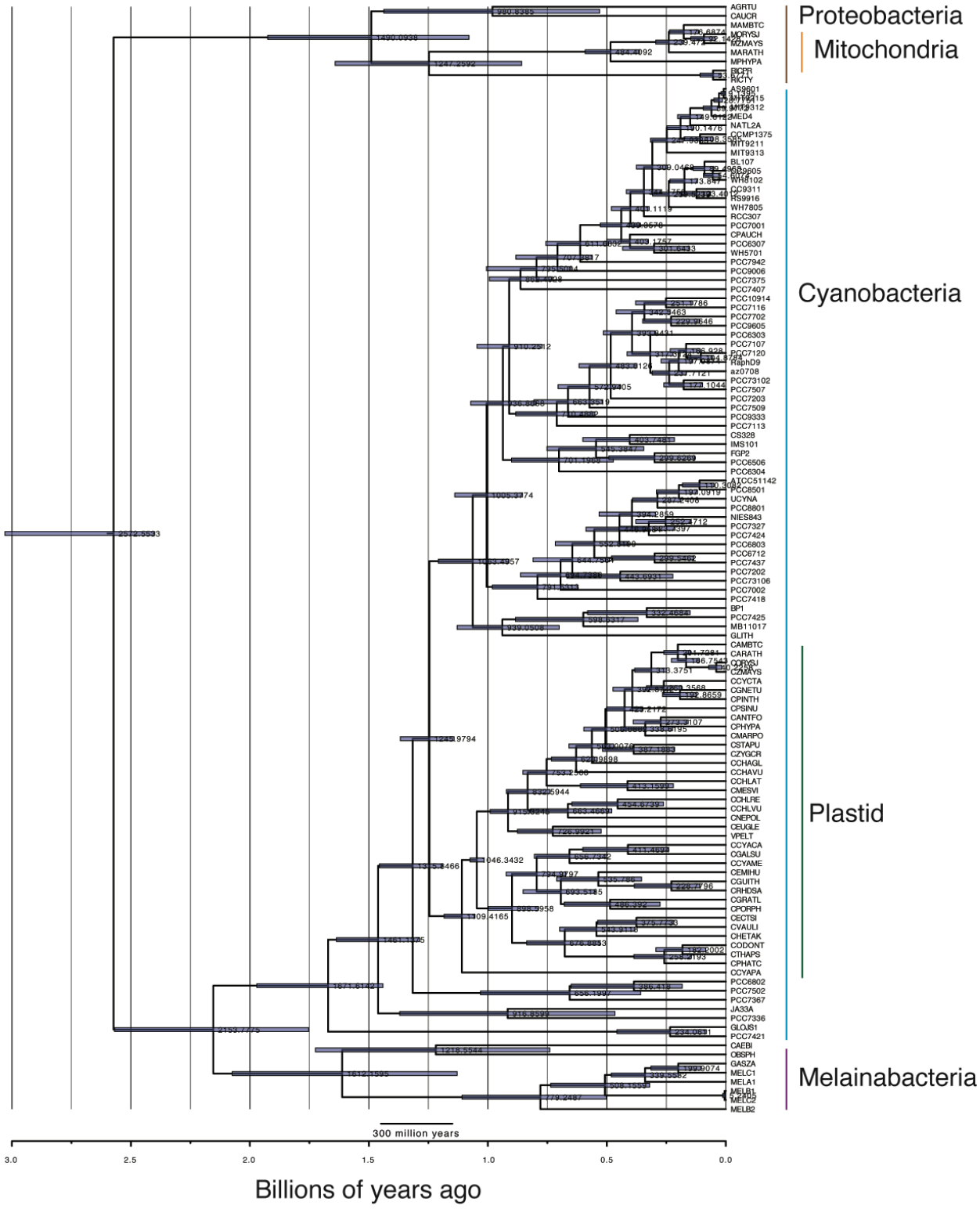

Figure A3: Divergence time estimates from T09 cross-calibrated BEAST2 run. All land plant constraints were used. *Bangiomorpha pubescens* was constrained to the green-red divergence using the younger, revised age of 1045 Ma. Abbreviations are summarized in Table A3.

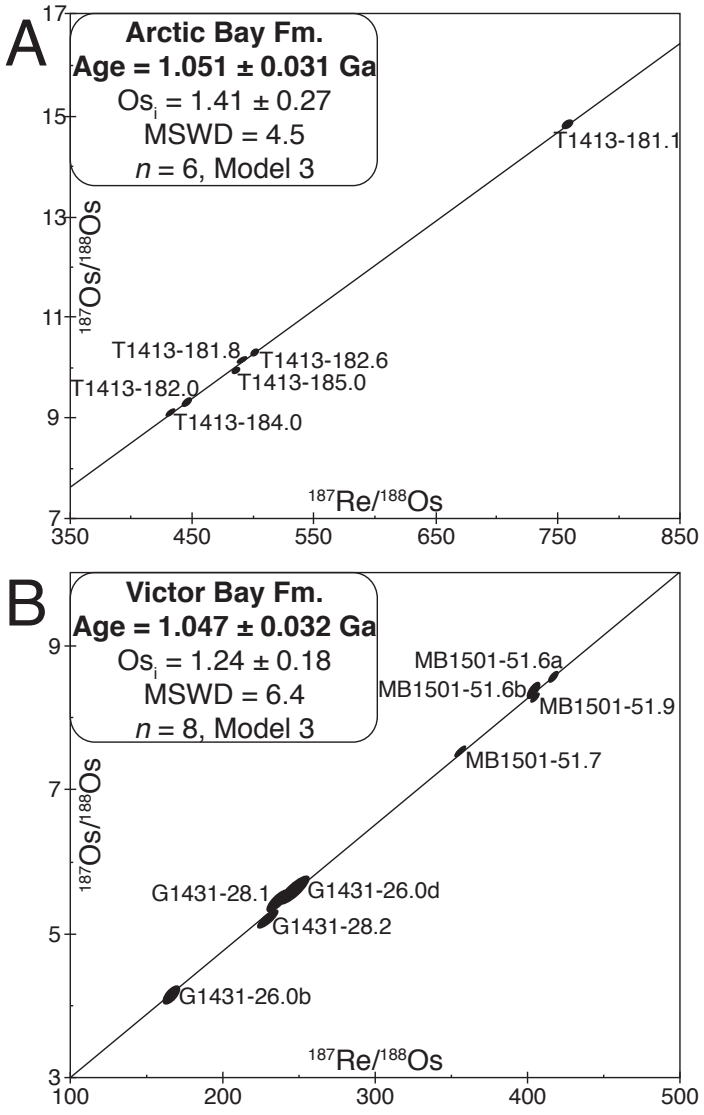

Figure A4: Re-Os geochronological data and isochron diagrams for all Arctic Bay (A) and Victor Bay (B) formations samples. Mean square of weighted deviation (MSWD) values greater than unity (i.e., 1) indicate that geological factors rather than analytical error are responsible for scatter about the isochron (Mahon, 1996). Data-point error ellipses represent 2σ uncertainty. Elemental abundances and isotopic compositions are presented in Table A1.

Supplementary References

Adam, Z.R., Skidmore, M.L., Mogk, D.W., and Butterfield, N.J., 2017, A Laurentian record of the earliest fossil eukaryotes: Geology, v. 45, p. 387–390.

Babinski, M., Vieira, L.C., Trindade, R.I.F., 2007, Direct dating of the Sete Lagoas cap carbonate (Bambuí Group, Brazil) and implications for the Neoproterozoic glacial events: Terra Nova, v. 19, p. 401–406.

Bengtson, S., Belivanova, V., Rasmussen, B., and Whitehouse, M., 2009, The controversial "Cambrian" fossils of the Vindhyan are real but more than a billion years older: Proceedings of the National Academy of Sciences, v. 106, p. 7729–7734.

Bengtson, S., Sallstedt, T., Belivanova, V., and Whitehouse, M., 2017, Three-dimensional preservation of cellular and subcellular structures suggests 1.6 billion-year-old crown-group red algae: PLoS Biology, v. 15, e2000735.

Bose, P.K., Sarkar, S., Das, N.G., Banerjee, S., Mandal, A., and Chakraborty, N., 2015, Proterozoic Vindhyan Basin: Configuration and evolution: Geological Society, London, Memoirs, v. 43, p. 85–102.

Butterfield, N.J., 2000, *Bangiomorpha pubescens* n. Gen., n. sp.: Implications for the evolution of sex, multicellularity, and the Mesoproterozoic/ Neoproterozoic radiation of eukaryotes: Paleobiology: Paleobiology, v. 26, p. 386–404.

Chakraborty, C., 2006, Proterozoic intracontinental basin: The Vindhyan example: Journal of Earth System Science, v. 115, p. 3–22.

Cohen, A.S., Coe, A.L., Bartlett, J.M., and Hawkesworth, C.J., 1999, Precise Re–Os ages of organic-rich mudrocks and the Os isotope composition of Jurassic seawater: Earth and Planetary Science Letters, v. 167, p. 159–173.

Cohen, A.S., 2004, The rhenium–osmium isotope system: applications to geochronological and palaeoenvironmental problems: Journal of the Geological Society of London, v. 161, p. 729–734.

Creaser, R. A., Papanastassiou, D. A., and Wasserburg, G. J., 1991, Negative thermal ion mass spectrometry of osmium, rhenium and iridium: Geochimica et Cosmochimica Acta, v. 55, p. 397-401.

Creaser, R.A., Sannigrahi, P., Chacko, T., and Selby, D., 2002. Further evaluation of the Re–Os

geochronometer in organic-rich sedimentary rocks: a test of hydrocarbon maturation effects in the Exshaw Formation, Western Canada Sedimentary Basin: Geochimica et Cosmochimica Acta, v. 66, p. 3441–3452.

Crocker, C.H., Collerson, K.D., Lewry, J.F. and Bickford, M.E., 1992, Sm-Nd, U-Pb and Rb-Sr geochronology and lithostructural relationships in the southwestern Rae province: constraints on crustal assembly in the western Canadian shield: Precambrian Research, v. 61, p. 27–50.

Cumming, V.M., Selby, D., and Lillis, P.G., 2012, Re-Os geochronology of the lacustrine Green River Formation: Insights into direct depositional dating of lacustrine successions, Re-Os systematics, and paleocontinental weathering: Earth and Planetary Science Letters, v. 359-360, p. 194–205.

Cumming, V.M., Poulton, S.W., Rooney, A.D., and Selby, D., 2013, Anoxia in the terrestrial environment during the late Mesoproterozoic: Geology, v. 41, p. 583–586.

Drummond, A.J., and Rambaut, A., 2007, BEAST: Bayesian evolutionary analysis by sampling trees: BMC Evolutionary Biology, v. 7, p. 214.

Geboy, N.J., Kaufman, A.J., Walker, R.J., Misi, A., de Oliviera, T.F., Miller, K.E., Azmy, K., Kendall, B., and Poulton, S.W., 2013, Re-Os age constraints and new observations of Proterozoic glacial deposits in the Vazante Group, Brazil: Precambrian Research, v. 238, p. 199–213.

Gramlich, J.W., Murphy, T.J., Garner, E.L., and Shields, W.R., 1973, Absolute isotopic abundance ratio and atomic weight of a reference sample of Rhenium: Journal of Research of the National Bureau of Standards, v. 77A, p. 691–698.

Gregory, L.C., Meert, J.G., Pradhan, V., Pandit, M.K., Tamrat, E., and Malone, S.J., 2006, A paleomagnetic and geochronologic study of the Majhgawan kimberlite, India: Implications for the age of the Upper Vindhyan Supergroup: Precambrian Research, v. 149, p. 65–75.

Hahn, K.E., Turner, E.C., Babechuk, M.G., and Kamber, B.S., 2015, Deep-water seep-related carbonate mounds in a Mesoproterozoic alkaline lake, Borden Basin (Nunavut, Canada): Precambrian Research, v. 271, p. 173–197.

Hnatyshin, D., Kontak, D.J., Turner, E.C., Creaser, R.A., Morden, R., and Stern, R.A., 2016, Geochronologic (Re–Os) and fluid-chemical constraints on the formation of the Mesoproterozoic-hosted Nanisivik Zn–Pb deposit, Nunavut, Canada: Evidence for early

diagenetic, low-temperature conditions of formation: Ore Geology Reviews, v. 79, p. 189–217.

Kah, L.C., Sherman, A.G., Narbonne, G.M., Knoll, A.H., and Kaufman, A.J., 1999, $\delta^{13}C$ stratigraphy of the Proterozoic Bylot Supergroup, Baffin Island, Canada: Implications for regional lithostratigraphic correlations: Canadian Journal of Earth Sciences, v.36, p. 313–332.

Kah, L.C., Lyons, T.W., and Chesley, J.T., 2001, Geochemistry of a 1.2 Ga carbonate-evaporite succession, northern Baffin and Bylot Islands: implications for Mesoproterozoic marine evolution: Precambrian Research, v. 111, p. 1–32.

Katoh, K., Kuma, K.-i., Toh, H., and Miyata, T., 2005, MAFFT version 5: Improvement in accuracy of multiple sequence alignment: Nucleic Acids Research, v. 33, p. 511–518.

Kendall, B.S., Creaser, R.A., Ross, G.M., and Selby, D., 2004. Constraints on the timing of Marinoan 'Snowball Earth' glaciation by 187Re–187Os dating of a Neoproterozoic post-glacial black shale in Western Canada: Earth and Planetary Science Letters, v. 222, p. 729–740.

Kendall, B., Creaser, R.A., Gordon, G.W., and Anbar, A.D., 2009a, Re-Os and Mo isotope systematics of black shales from the Middle Proterozoic Velkerri and Wollogorang Formations, McArthur Basin, northern Australia: Geochimica Cosmochimica Acta, v. 73, p. 2534-2558.

Kendall, B., Creaser, R.A., and Selby, D., 2009b, 187Re-187Os geochronology of Precambrian organic-rich sedimentary rocks: Geological Society of London Special Publications, v. 326, p. 85–107.

Kumar, S., 1995, Megafossils from the Mesoproterozoic Rohtas Formation (the Vindhyan Supergroup), Katni area, central India: Precambrian Research, v. 72, p. 171–184.

Kumar, A., Gopalan, K., and Rajagopalan, G., 2001, Age of the Lower Vindhyan sediments, Central India: Current Science–Bangalore, v. 81, p. 806–809.

Levasseur, S., Birck, J.L., and Allegre, C.J., 1999, The osmium riverine flux and the oceanic mass balance of osmium: Earth and Planetary Science Letters, v. 174, p. 7–23.

Li, J., Liang, X.-R., Xu, J.-F., Suzuki, K., and Dong, Y.-H., 2010, Simplified technique for themeasurements of Re-Os isotope by multicollector inductively coupled plasma mass spectrometry (MC-ICP-MS): Geochemical Journal, v. 44, p. p. 73-80.

Ludwig, K. R., 1980, Calculation of uncertainties of U-Pb isotope data: Earth and Planetary Science Letters, v. 46, p. 212-220.

Ludwig, K.R., 2011, Isoplot/Ex, Version 4.15: A geochronological toolkit for Microsoft Excel: Geochronology Center Berkeley, v. 4, p.1-70.

Mahon, K.I., 1996, The new "York" Regression: Application of an improved statistical method to geochemistry: International Geology Reviews, v. 38, p. 293–303.

McArthur, J.M., Algeo, T.J., van de Schootbrugge, B., Li, Q., and Howarth, R.J., 2008, Basinal restriction, black shales, Re-Os dating, and the Early Toarcian (Jurassic) oceanic anoxic event: Paleoceanography, v. 23, p. p. 1–22.

Miller, M.A., Pfeiffer, W., and Schwartz, T., 2010, Creating the CIPRES Science Gateway for inference of large phylogenetic trees: In Gateway Computing Environments Workshop (GCE), p. 1–8.

Rasmussen, B., Bose, P.K., Sarkar, S., Banerjee, S., Fletcher, I.R., and McNaughton, N.J., 2002, 1.6 Ga U-Pb zircon age for the Chorhat Sandstone, lower Vindhyan, India: Possible implications for the early evolution of animals: Geology, v. 30, p. 103–106.

Ray, J.S., Martin, M.W., Veizer, J., and Bowring, S.A., 2002, U-Pb zircon dating and Sr isotope systematics of the Vindhyan Supergroup, India: Geology, v. 30, p. 131–134.

Ray, J.S., Veizer, J., and Davis, W.J., 2003, C, O, Sr and Pb isotope systematics of carbonate sequences of the Vindhyan Supergroup, India: age, diagenesis, correlations and implications for global events: Precambrian Research, v. 121, p. 103–140.

Ray, J.S., 2006, Age of the Vindhyan Supergroup: a review of recent findings: Journal of Earth System Science, v. 115, p. 149–160.

Rooney, A.D., Chew, D.M., and Selby, D., 2011, Re-Os geochronology of the Neoproterozoic-Cambrian Dalradian Supergroup of Scotland and Ireland: Implications for Neoproterozoic stratigraphy, glaciations, and Re-Os systematics: Precambrian Research, v. 185, p. 202–214.

Rooney, A.D., Macdonald, F.A., Strauss, J.V., Dudas, F.O., Hallman, C., and Selby, D., 2014, Re-Os geochronology and coupled Os-Sr isotope constraints on the Sturtian Snowball Earth: Proceedings of the National Academy of Sciences, v. 111, p. 51–56.

Rooney, A.D., Strauss, J.V., Brandon, A.D., and Macdonald, F.A., 2015, A Cryogenian

chronology: Two long-lasting synchronous Neoproterozoic glaciations: Geology, v. 43, p. 459–462.

Selby, D., and Creaser, R.A., 2003. Re–Os geochronology of organic rich sediments: an evaluation of organic matter analysis methods: Chemical Geology, v. 200, p. 225–240.

Selby, D., and Creaser, R.A., 2005, Direct radiometric dating of the Devonian-Mississippian time-scale boundary using the Re-Os black shale geochronometer: Geology v. 33, p. 545–548.

Selby, D., Creaser, R.A., Stein, H.J., Markey, R.J., and Hannah, J.L., 2007, Assessment of the ^{187}Re decay constant by cross calibration of Re–Os molybdenite and U–Pb zircon chronometers in magmatic ore systems: Geochimica et Cosmochimica Acta, v. 71, p. 1999–2013.

Sherman, A.G., Narbonne, G.M., and James, N.P., 2001, Anatomy of a cyclically packaged Mesoproterozoic carbonate ramp in northern Canada: Sedimentary Geology, v. 139, p. 171–203.

Shih, P.M., and Matzke, N.J., 2013, Primary endosymbiosis events date to the later Proterozoic with cross-calibrated phylogenetic dating of duplicated ATPase proteins: Proceedings of the National Academy of Sciences, v. 110, p. 12355–12360.

Shih, P.M., Hemp., J., Ward, L.M., Matzke, N.J., and Fischer, W.W., 2017, Crown group Oxyphotobacteria postdate the rise of oxygen: Geobiology, v. 15, p. 19–20.

Smoliar, M.I., Walker, R.J., and Morgan, J.W., 1996, Re-Os ages of Group IIA, IIIA, IVA and IVB iron meteorites: Science, v. 271, p. 1099–1102, doi: 10.1126/science.271.5252.1099.

Smith, S.A., Beaulieu, J.M., and Donoghue, M.J., 2010, An uncorrelated relaxed-clock analysis suggests an earlier origin for flowering plants: Proceedings of the National Academy of Sciences, v. 107, p. 5897–5902.

Tripathy, G.R., and Singh, S.K., 2015, Re–Os depositional age for black shales from the Kaimur Group, Upper Vindhyan, India: Chemical Geology, v. 4.13, p. 63–72.

Turner, E.C., and Kamber, B.S., 2012, Arctic Bay Formation, Borden Basin, Nunavut (Canada): Basin evolution, black shale, and dissolved metal systematics in the Mesoproterozoic ocean: Precambrian Research, v. 208, p. 1–18.

van Acken, D., Thomson, D., Rainbird, R.H., and Creaser, R.A., 2013, Constraining the

depositional history of the Neoproterozoic Shaler Supergroup, Amundsen Basin, NW Canada: Rhenium-osmium dating of black shales from the Wynniatt and Boot Inlet Formations: Precambrian Research, v. 236, p. 124–131.

Xu, G., Hannah, J.L., Stein, H.J., Bingen, B., Yang, B., Zimmerman, A., Weitschat, W., Mork A., and Weiss, H., 2009, Re-Os Geochronology of Arctic black shales to evaluate the Anisian-Ladinian boundary and global faunal correlations: Earth and Planetary Science Letters, v. 288, p. 581–587.

Xu, G., Hannah, J.L., Stein, H.J., Mork A., Vigran, J.O., Bingen, B., Schutt, D.L., and Lundschien, B.A., 2014, Cause of Upper Triassic climate crisis revealed by Re–Os geochemistry of Boreal black shales: Palaeogeography, Palaeoclimatology, Palaeoecology, v. 395, p. 222–232.

Yang, E.C., Boo, S.M., Battacharya, D., Saunders, G.W., Knoll, A.H., Fredericq, S., Graf, L., and Yoon, H.S., 2016, Divergence time estimates and the evolution of major lineages in the florideophyte red algae: Nature, v. 6, p. 21361.

Preface to Chapter 4:

In the previous chapter, we provide Re-Os geochronology from the Bylot Supergroup showing that it is significantly younger than previously assumed. This revised timeframe demonstrates that deposition of the Bylot Supergroup in the terminal Mesoproterozoic Era coincided with the consolidation of Rodinia as a supercontinent (Evans, 2009; Hynes and Rivers, 2010). Considering silicate weathering's central role in the global carbon cycle and supply of nutrients to the ocean, supercontinent cycles have likely played an influential role in the evolution of Earth's surface environment. Late Proterozoic Sr isotopic datasets reveal a transition in the global chemical weathering regime, from predominantly seafloor alteration through the Mesoproterozoic Era to pervasive continental weathering in the early to middle Neoproterozoic Era (Cox et al., 2016). A wholesale shift in the style of silicate weathering across the Meso-Neoproterozoic transition has critical implications for the biogeochemical cycling of carbon and nutrients—and by extension, Earth's climate and biology.

Indeed, the lifespan of Rodinia bridges the transition from relative environmental and evolutionary stasis in the Mesoproterozoic to early Neoproterozoic eras (1600 to 800 Ma) to climatic extremes and biological innovation later in the Neoproterozoic Era. Whereas early Neoproterozoic emplacement of continental flood basalts and the breakup of Rodinia in low latitudes (Goddéris et al., 2003; Donnadieu et al., 2004; Cox et al., 2016; Goddéris et al., 2017), or a nadir in arc magmatism (McKenzie et al., 2014 and 2016) are thought to have caused some of these changes, few data exist spanning Rodinia's amalgamation and residence. Sr isotopic data from the Bylot Supergroup presented in the following chapter fill in this record and display a steep rise in $^{87}Sr/^{86}Sr$ ratios from ~0.705 to 0.706 ca. 1050 Ma, concurrent with peak continental collision of the Ottawan phase of the Grenville orogeny (Hynes and Rivers, 2013). Similar peaks in global marine $^{87}Sr/^{86}Sr$ ratios occurred during the Pan African orogeny, which assembled Gondwana (Goddéris et al., 2017), and the onset of the Himalayan orogeny Edmond (1992).

The formation and configuration of Rodinia may have also affected global biogeochemical cycles more directly through changes in ecological landscapes. Many late Mesoproterozoic epicratonic sedimentary basins indicate that global highstand sea level produced widespread shallow epeiric seaways within Rodinia. These environments likely experienced heterogeneous redox conditions (Gilleaudeau and Kah, 2013a; Gilleaudeau and Kah, 2015) and nutrient

availability (Gilleaudeau and Kah, 2013b). Marginal marine or lacustrine environments that had minimal communication with the open ocean were also prevalent within Rodinia. These settings were likely replete with nutrients delivered by continental weathering. Highly variable local environments within Mesoproterozoic epeiric seaways may have exerted unique selective pressures that governed early eukaryotic evolution (Mukherjee et al., 2018). In fact, some molecular clock studies suggest that early photosynthetic eukaryotes inhabited or even evolved in non-marine, freshwater environments (Blank, 2013; Ponce-Toledo et al., 2017; Sánchez-Baracaldo et al., 2017).

The Borden Basin has been variably interpreted as marine (Kah et al., 2001), temporarily restricted from the open ocean (Turner and Kamber, 2012; Gibson et al., 2018), or entirely lacustrine (Hahn et al., 2015). Furthermore, as presented in the previous chapter, the Bylot Supergroup preserves the earliest known multicellular and photosynthetic eukaryote. Therefore, this sedimentary succession can be studied to decipher the role of various ecological niches on eukaryotic evolution. In the following chapter, we characterize the complex hydrologic history of the Borden Basin and demonstrate that tectonically driven hydrographic modifications affected the circulatory patterns of the basin's water mass. In addition to providing critical context for future paleontological studies aimed at reconstructing paleoecological-fossil assemblage associations, this study also outlines a novel combination of geochemical proxies that are well-suited for deciphering between marine and non-marine environments in ancient sedimentary basins.

References

Blank, C. E., 2013, Origin and early evolution of photosynthetic eukaryotes in freshwater environments: Reinterpreting Proterozoic paleobiology and biogeochemical processes in light of trait evolution: Journal of Phycology, p. 1-16.

Cox, G. M., Halverson, G. P., Stevenson, R. K., Vokaty, M., Poirier, A., Kunzmann, M., Li, Z.-X., Denyszyn, S. W., Strauss, J. V., and Macdonald, F. A., 2016, Continental flood basalt weathering as a trigger for Neoproterozoic Snowball Earth: Earth and Planetary Science Letters, v. 446, p. 89-99.

Donnadieu, Y., Goddéris, Y., Ramstein, G., Nedelec, A., and Meert, J. G., 2004, A 'snowball Earth' climate triggered by continental break-up through changes in runoff: Nature, p. 1-4.

Edmond, J.M., 1992. Himalayan tectonics, weathering processes, and the strontium isotope record in marine limestones: Science, v. 258, p. 1594-1597.

Evans, D. A. D., 2009, The palaeomagnetically viable, long-lived and all-inclusive Rodinia supercontinent reconstruction: Geological Society, London, Special Publications, v. 327, p. 371-404.

Gibson, T. M., Shih, P. M., Cumming, V. M., Fischer, W. W., Crockford, P. W., Hodgskiss, M. S. W., Wörndle, S., Creaser, R. A., Rainbird, R. H., Skulski, T. H., and Halverson, G. P., 2018, Precise age of *Bangiomorpha pubescens* dates the origin of eukaryotic photosynthesis: Geology, v. 46, p. 135-138.

Gilleaudeau, G. J., and Kah, L. C., 2013a, Carbon isotope records in a Mesoproterozoic epicratonic sea: Carbon cycling in a low-oxygen world: Precambrian Research, v. 228, p. 85-101.

Gilleaudeau, G. J., and Kah, L. C., 2013b, Oceanic molybdenum drawdown by epeiric sea expansion in the Mesoproterozoic: Chemical Geology, v. 356, p. 21-37.

Gilleaudeau, G. J., and Kah, L. C., 2015, Heterogeneous redox conditions and a shallow chemocline in the Mesoproterozoic ocean: Evidence from carbon-sulfur-iron relationships: Precambrian Research, v. 257, p. 94-108.

Goddéris, Y., Donnadieu, Y., Nedelec, A., Dupré, B., Dessert, C., Grard, A., Ramstein, G., and Francois, L. M., 2003, The Sturtian 'snowball' glaciation: fire and ice: Earth and Planetary Science Letters, v. 211, p. 1-12.

Goddéris, Y., Le Hir, G., Macouin, M., Donnadieu, Y., Hubert-Théou, L., Dera, G., Aretz, M., Fluteau, F., Li, Z.-X., and Halverson, G. P., 2017, Paleogeographic forcing of the strontium isotopic cycle in the Neoproterozoic: Gondwana Research, v. 42, p. 151-162.

Hahn, K.E., Turner, E.C., Babechuk, M.G., and Kamber, B.S., 2015, Deep-water seep-related carbonate mounds in a Mesoproterozoic alkaline lake, Borden Basin (Nunavut, Canada): Precambrian Research, v. 271, p. 173–197.

Hynes, A., and Rivers, T., 2010, Protracted continental collision—Evidence from the Grenville orogen: Canadian Journal of Earth Sciences, v. 47, p. 591-620.

Kah, L.C., Lyons, T.W. and Chesley, J.T. 2001: Geochemistry of a 1.2 Ga carbonate-evaporite succession, northern Baffin and Bylot Islands: implications for Mesoproterozoic marine evolution: Precambrian Research, v. 111, p. 203–234.

McKenzie, N. R., Horton, B. K., Loomis, S. E., Stockli, D. F., Planavsky, N. J., and Lee, C.-T. A., 2016, Continental arc volcanism as the principaldriver of icehouse-greenhouse variability: Science, p. 1-5.

Mukherjee, I., Large, R. R., Corkrey, R., and Danyushevsky, L. V., 2018, The Boring Billion, a slingshot for Complex Life on Earth: Scientific reports, v. 8, p. 4432.

Ponce-Toledo, R. I., Deschamps, P., Lopez-Garcia, P., Zivanovic, Y., Benzerara, K., and Moreira, D., 2017, An Early-Branching Freshwater Cyanobacterium at the Origin of Plastids: Current Biology, v. 27, p. 386-391.

Sánchez-Baracaldo, P., Raven, J. A., Pisani, D., and Knoll, A. H., 2017, Early photosynthetic eukaryotes inhabited low-salinity habitats: Proceedings of the National Academy of Sciences, v. 7, p. 201620089-201620089.

Turner, E.C., and Kamber, B.S., 2012, Arctic Bay Formation, Borden Basin, Nunavut (Canada): Basin evolution, black shale, and dissolved metal systematics in the Mesoproterozoic ocean: Precambrian Research, v. 208, p. 1–18.

Chapter 4

Radiogenic isotope (Sr, Os, Nd) evidence for episodic hydrologic restriction in the latest Mesoproterozoic Borden Basin, Arctic Canada[1]

[1] This chapter has been submitted as: "Gibson, T.M., Wörndle, S., Crockford, P.W., Bui, T.H., Creaser, R.A., and Halverson, G.P., Paleoecology of the episodically restricted late Mesoproterozoic Borden Basin, arctic Canada. To: *Geological Society of American Bulletin*."

Abstract

The ca. 1050 Ma Bylot Supergroup in Arctic Canada is one of the best-preserved archives of late Mesoproterozoic geochemistry and biology and offers evidence that this period of Earth history may have been more dynamic than previously appreciated. The Bylot Supergroup was deposited in the Borden Basin and is the most thoroughly studied stratigraphic succession from a series of broadly contemporaneous late Mesoproterozoic intracratonic basins known as the Bylot basins. This ~6 km-thick mixed carbonate-siliciclastic succession has undergone minimal post-depositional deformation and is now exposed on Baffin and Bylot islands, Nunavut, Canada. Deep-water and tidally-influenced carbonate facies, traditionally interpreted as marine, have yielded important insights into the evolution of Proterozoic seawater chemistry; however, more recent studies indicate the Borden Basin was restricted or entirely non-marine for portions of its depositional history. Here, we present new radiogenic isotope chemostratigraphic data spanning the Bylot Supergroup. Coupled radiogenic isotopic compositions of hydrogenous (black shale $^{187}Os/^{188}Os$ and limestone $^{87}Sr/^{86}Sr$) and detrital (mudrock $^{143}Nd/^{144}Nd$) sedimentary phases elucidate the complex hydrologic history of the Borden Basin and reconcile these disparate interpretations.

These data indicate that the Borden Basin experienced fluctuating open marine, restricted, and non-marine conditions and that the red algal fossil *Bangiomorpha pubescens* evolved in highly variable environments. Episodically restricted epeiric basins similar to the Borden Basin were relatively widespread within Rodinia and may have exerted unique selective pressures on eukaryotic evolution in the Mesoproterozoic Era. Coupled hydrogenous and detrital radiogenic

isotope chemostratigraphy, as implemented in this study, may provide the key paleo-ecological framework for future paleontological studies aimed at testing the role of freshwater environments in eukaryotic evolution. Additionally, eighty-one new $^{87}Sr/^{86}Sr$ compositions from unaltered, middle Bylot Supergroup marine limestone samples, calibrated by recent Re-Os geochronology, contribute to the terminal Mesoproterozoic marine $^{87}Sr/^{86}Sr$ curve. These data display a rise from ~0.705 to 0.706 that reflects weathering of the active Grenville orogenic belt and demonstrate a global increase in silicate weathering during the amalgamation of Rodinia.

1. Introduction

The Bylot Supergroup in arctic Canada (Fig. 1) serves as an extraordinary archive of latest Mesoproterozoic biology and geochemistry. Diverse microfossil assemblages are preserved within various facies throughout the succession, including early silicified peritidal carbonate that host the early red alga, *Bangiomorpha pubescens* (Hofmann and Jackson, 1991, 1994; Knoll et al., 2013). Sedimentological and geochemical studies of this facies yield key insight into the early diagenetic history of Proterozoic tidal environments (Kah, 2000; Kah et al., 2001; Manning-Berg and Kah, 2017) and support a shift in the style of carbonate deposition through the Proterozoic Eon (Kah and Knoll, 1996; Narbonne and James, 1996; Sherman et al., 2000; Kah and Riding, 2007). Chemostratigraphic data from the Bylot Supergroup are incorporated into reconstructions of the secular $\delta^{13}C$ and $\delta^{34}S$ evolution of seawater (Kah et al., 1999; Kah et al., 2001) despite evidence that the Borden Basin was restricted or non-marine during deposition of the remarkably organic-rich (up to ~20 weight % total organic carbon) Arctic Bay and lower Victor Bay formations (Hahn et al., 2015; Gibson et al., 2018). This sedimentary record is now constrained by Re-Os geochronology (Gibson et al., 2018) to have coincided with the Grenville orogeny (ca. 1090-1020 Ma; Hynes and Rivers, 2010) and the peak assembly of Rodinia (ca. 1100-1050 Ma; Evans, 2009).

Here, we present Sr, Os, and Nd isotope chemostratigraphic data from the Bylot Supergroup that demonstrate episodic, tectonically driven changes to the degree of water mass restriction in the Borden Basin. Identifying stratigraphic intervals that are non-marine presents a useful framework for future studies aimed at reconstructing the paleo-environments that certain microfossil assemblages inhabited. Furthermore, global, age-calibrated radiogenic isotopic data sets are sparse from this time period and Sr isotopes from stratigraphic intervals of the Bylot

Supergroup that reflect marine deposition provide a record of global chemical weathering during the amalgamation of Rodinia and the Grenville orogeny.

2. Background

2.1. Geological Setting

The Bylot Supergroup consists of up to 6 km of predominantly carbonate and siliciclastic sediment with minor volcanic and evaporite lithologies exposed within a series of northwest trending grabens in northern Baffin and Bylot islands, Nunavut, Canada. This succession occupies the Borden Basin, which is one of a series of late Mesoproterozoic basins within Archean to Paleoproterozoic Rae Province crust in the Canadian Arctic Archipelago and western Greenland known as the Bylot basins (Fig. 1). Putative correlation between Bylot basins indicate that they formed either as contemporaneous but distinct epicratonic basins or that they are remnants of a larger previously interconnected seaway (Jackson and Iannelli, 1981); however, their relation to one another is speculative due to a paucity of depositional ages from all but the Borden Basin. Although multiple models have been proposed, the tectonic setting responsible for the formation and evolution of the Bylot basins remains enigmatic.

The Borden and other Bylot basins were initially interpreted as aulacogens formed during ca. 1270 Ma emplacement of the Mackenzie Large Igneous Province (LIP; Jackson and Iannelli, 1981; Dostal et al., 1989; LeCheminant and Heaman, 1989). However, the absence of fault-controlled sedimentation patterns in the lowermost Bylot Supergroup (Nauyat and Adams Sound formations) led Turner et al. (2016) to propose that the Borden Basin formed as an intracratonic sag basin from far-field deformation. Pulses of normal faulting, largely accommodated along graben-bounding faults, accompanied by gentle subsidence during deposition of the middle Bylot Supergroup (Arctic Bay through Victor Bay formations) are punctuated by uplift that reversed/inverted the Borden Basin's bathymetric polarity (Sherman et al., 2002). This compressional event marks an abrupt change from the carbonate-dominated Uluksan Group to the siliciclastic-dominated Eqalulik Group (Fig. 1), interpreted as the transition from rift to foreland basin due to collision along Laurentia's northern margin (Geldsetzer, 1973; Hoffman, 1989; Sherman et al., 2002) or from far-field lithospheric deformation related to the Grenville orogeny

~2000 km to the southeast (Turner et al., 2016). In any case, it is clear that the Borden Basin experienced a complex geodynamic history associated with various stress regimes.

The Bylot Supergroup was long considered ca. 1200 Ma because paleomagnetic poles from basal Nauyat Formation basalt overlap with those of the Mackenzie LIP (Fahrig et al., 1981), and no evidence for a prolonged depositional hiatus was observed throughout the succession (Jackson and Iannelli, 1981). Baddeleyite from Savage Point diabase sills that intrude the basal Aston Group in the nearby Aston and Hunting Basin (Fig. 1) have been dated to 1268 Ma (Dixon et al., 1971), and correlation to the Nauyat Formation supports this timeframe (see Chapter 3 Appendix for discussion on other geochronology from the Bylot Supergroup). Franklin dykes that cross-cut the entire Bylot Supergroup provide a 723 Ma minimum age limit (Heaman et al., 1992; Pehrsson and Buchan, 1999), although chemostratigraphy suggests it is >800 Ma (Kah et al., 1999). An unconventional whole-rock shale Pb-Pb age of 1092 ± 59 Ma (Turner and Kamber, 2012), and subsequent shale Re-Os dates of 1048 ± 12 Ma for the middle Arctic Bay Formation and 1046 ± 16 Ma for the lower Victor Bay Formation (Gibson et al., 2018) indicate that the middle to upper Bylot Supergroup is younger than previously thought.

These depositional ages require that either the inferred age of ca. 1270 Ma for the Nauyat Formation basalt is incorrect or that an unrecognized ~200 Myr depositional hiatus exists between deposition of the Nauyat and Arctic Bay formations. Considering the close association and gradational contact between shallow marine Nauyat and Adams Sound formations sandstone facies (Long and Turner, 2012), the only plausible position for such a hiatus in the lower Bylot Supergroup is the sharp contact between Adams Sound Formation sandstone and Arctic Bay Formation shale; however, due to the contrasting resistance to weathering between these lithologies, this contact is exposed and an unconformity at this level has not been verified. Chemostratigraphic data from this study are from the Arctic Bay and overlying formations and are unaffected by this age uncertainty.

2.2. Radiogenic Isotope Proxies

The ^{87}Rb-^{87}Sr and ^{187}Re-^{187}Os radiogenic isotopic systems in hydrogenous sedimentary components function as paleo-weathering proxies by tracking the relative contributions of radiogenic (evolved) versus non-radiogenic (primitive or juvenile) sources to the water mass from

which the sediment formed. The parent elements in both systems (Rb and Re) are incompatible relative to their daughter products, so they accumulate in partial melts. Therefore, crust formed by partial melting contains high Rb and Re relative to Sr and Os, respectively (Taylor and Mclennan, 1995). Following the *in situ* radioactive decay of the parent isotopes (^{87}Rb and ^{87}Re), the ratio between the radiogenic daughters (^{87}Sr and ^{187}Os) and their stable counterparts (^{86}Sr and ^{188}Os) in a given rock is governed by a balance between the degree of partial melting (e.g., high in continental crust and low in tholeiitic basalt) and the amount of time the decay products have accumulated (i.e., the age of the rocks).

The residence times of Sr (~ 4 Myr; Lecuyer, 2016) and Os (~10-50 kyr; Peucker-Ehrenbrink and Ravizza, 2000 and references therein) are long relative to the ca. 1–2 kyr mixing time for the global ocean (Banner, 2004). Therefore, Sr and Os are well-mixed in the ocean (Veizer, 1989; Ravizza and Turekian, 1992), and the Sr and Os isotopic composition of marine sediment reveal the globally averaged contributions from weathering of relatively radiogenic continental crust versus juvenile contributions from hydrothermal fluids and alteration of oceanic crust (Fig. 2). Since the Sr and Os isotope compositions of continental runoff and seawater are distinct throughout Earth history and they do not undergo fractionation during evapo-concentration, these proxies serve as a valuable tool for recognizing marine versus non-marine signatures in ancient sedimentary basins (e.g., Cumming et al., 2013; Rooney et al., 2017; Stüeken et al., 2017; Xu et al., 2017). Additionally, the contrasting residence times between Sr and Os in the modern ocean enable coupled Sr-Os isotopic data to resolve geological processes that operate across a range of temporal scales.

Unlike Sr and Os isotopes measured in hydrogenous sedimentary phases, ^{143}Nd/^{144}Nd ratios were measured in detrital minerals whose distribution is limited by sediment transport processes. Therefore, ^{143}Nd-^{144}Nd chemostratigraphy here provides a record of sediment provenance within the catchment basin. In the ^{147}Sm-^{143}Nd radiogenic system, the parent (Sm) is more compatible than the daughter (Nd), so Nd accumulates in partial melts relative to Sm. As a result, ^{143}Nd is enriched in juvenile crust relative to stable ^{144}Nd due to *in situ* ^{147}Sm decay, and evolved lithologies are have lower ^{143}Nd/^{144}Nd ratios. By combining hydrogenous (Sr and Os) and detrital (Nd) paleo-weathering proxies in this study, we are able to compare the geochemistry of basin waters to the local weathering regime to disentangle regional from global affects.

3. Materials and Methods

Samples included in this study were collected from 12 locations in the Milne Inlet Graben and Eclipse Trough of the Borden Basin (Fig. 1) over the course of four field seasons while logging and measuring stratigraphic sections at a decimeter to meter scale. Sr isotope analyses were conducted on limestone samples, Os isotopes on organic-rich shale, and Nd isotopes on mudstones. Methods used for this study are summarized below. See chapter 2 for stratigraphic sections and sedimentological context for samples used in this study.

3.1. Limestone Sample Preparation and Elemental Concentrations

Approximately 15 mg of powder was drilled from freshly cut limestone hand samples to avoid fractures, veins, and weathered surfaces. Sample powders were agitated with methanol to remove the insoluble clay fraction, which was discarded, and then rinsed with MQ H_2O three times. Samples were then leached twice in 0.2 M ammonium acetate to remove loosely bound ^{87}Sr that is likely to reside in detrital phases, with MQ H_2O rinses between each leach. The remaining sample was then allowed to react in 0.5 M acetic acid for two hours to dissolve the calcite fraction, which was centrifuged to separate it from the residual insoluble fraction. This step was repeated as necessary to dissolve all calcite within the sample. Samples dissolved in acetic acid were then dried down and taken up in 3 N HNO_3. Half of this solution was analyzed via Inductively Coupled Plasma Optical Emission (ICP-OES) on a Thermo Scientific iCAP 6000^{TM} series instrument at McGill University for major and minor element concentrations (Table A1). Final concentrations in the carbonate fraction for each sample were corrected based on the mass of the insoluble residue after dissolution.

These data were used to screen for alteration and possible radiogenic ingrowth on the basis of Sr, Rb, and Fe concentrations and Mg/Ca, Mn/Sr, and Rb/Sr ratios. Because diagenetic alteration of carbonates almost always increases $^{87}Sr/^{86}Sr$ ratios (Banner and Hanson, 1990) and the degree of overprinting is modulated by Sr concentrations, $^{87}Sr/^{86}Sr$ plotted against these parameters provides a qualitative basis for identifying the cut-offs for diagenetically overprinted samples (Edwards et al., 2015). These geochemical relationships are plotted in Figure 3, which

also shows samples excluded from the Bylot Supergroup $^{87}Sr/^{86}Sr$ curve (in red) on the basis of the following criteria: Sr < 400 ppm; Mg/Ca > 0.1; Mn/Sr > 1; Rb/Sr > 0.2.

3.2. Sr Isotopes ($^{87}Sr/^{86}Sr$)

Strontium was separated and purified from the other aliquot of limestone sample solution following standard Sr chromatography procedures using EICHROM Sr Spec™ resin. Strontium isotope ratios were measured on purified Sr fractions using a a Thermo Scientific TRITON™ thermal ionization mass spectrometer (TIMS) at the Université de Québec à Montréal/Geotop. Internal mass bias was corrected based on the ratio $^{86}Sr/^{88}Sr = 0.1194$. Analyses of NBS SRM 987 yielded a long-term average of 0.710273 (Std. Err. = 1.14 X 10^{-5}; $2\sigma = 0.032$), compared to the accepted value of 0.710250. No correction was made to sample data. No age correction was made to this data. All Sr isotope data from this study are presented in Table 1.

3.3. Os Isotopes ($^{187}Os/^{188}Os$)

Black shale samples were trimmed with a diamond-tipped lapidary saw blade to remove any weathered surfaces, and polished with a diamond pad to remove metal contamination. Samples were then dried at room temperature. Between 30–50 g aliquots of each sample were crushed to a fine powder (ca. 30 μm) using a SPEX #8506 zirconia ceramic puck and grinding container in a SPEX 8500 shatterbox to homogenize each sample (Kendall et al., 2009a). Re and Os isotopic analyses were performed at the University of Alberta's Re-Os Crustal Geochronology Laboratory in the Department of Earth and Atmospheric Sciences following methodologies developed by Creaser et al. (2002), Selby and (2003), Kendall et al. (2004), and Cumming et al. (2013).

Both Re and Os were isolated and purified following the protocol outlined in Creaser et al. (2002); Selby and Creaser (2003); Kendall et al. (2004); Cumming et al. (2013) and hydrogenous Re and Os were preferentially liberated by Cr^{IV}-H_2SO_4 digestion in Carius tubes to avoid detrital Re and Os phases. Isotopic ratios were analyzed with a Thermo Scientific TRITON™ instrument using negative thermal ionization mass spectrometry (NTIMS; Creaser et al., 1991) by ion-counting with a secondary electron multiplier in peak-hopping mode at the University of Alberta.

Initial $^{187}Os/^{188}Os$ (Os_i) was calculated from the isochron age of 1048 Ma for the Arctic Bay Formation (Table 2; Gibson et al., 2018) and the ^{187}Re decay constant (Smoliar et al., 1996).

3.4. Nd Isotopes ($^{143}Nd/^{144}Nd$)

Refer to Cox et al. (2016) and Macdonald et al. (2017) for detailed methods. Mudstone samples were trimmed with a lapidary to remove weathered surfaced followed by homogenization with a SPEX 8500 shatterbox using a tungsten carbide grinding container. Resulting sample powders were then heated to ~1000° C in order to remove volatiles and combust organic matter. Between 0.2 and 0.4 g of powder from each sample was spiked with enriched ^{150}Nd-^{149}Sm tracer, then dissolved in a concentrated mixture of HF (~29N) and HNO_3 (~16N). Sample solutions were evaporated and re-dissolved twice—first in aqua-regia (3:1, 6N HCl:7N HNO_3), and again in 6N HCl in cases where organic matter persisted. Purified Sm and Nd extracts were isolated in columns using the following three-stage chromatography process. Iron was first removed with 200-400 mesh AG1X8 ion exchange resin. Then, rare earth elements were concentrated with EICHROM TRU™ Resin SPS 50-100. Last, Sm and Nd were purified with with 600 mg of EICHROM LN™ Resin 100-150.

Reported $^{143}Nd/^{144}Nd$ and $^{147}Sm/^{144}Nd$ ratios from this study were measured using both a Thermo Scientific TRITON™ thermal ionization mass spectrometer (TIMS) and a Nu Plasma II™ multi-collector inductively coupled plasma mass spectrometer (MC-ICP-MS) in the Geotop laboratories at Université de Québec à Montréal. For TIMS analyses, Nd extracts were loaded onto outgassed Re filaments and set facing outgassed Re ionization filaments, in a double filament array. Isotopic ratios were measured in dynamic mode on the TIMS, and the total combined blank for Sm and Nd was less than 150 pg. Resulting $^{146}Nd/^{144}Nd$ values were normalized to 0.7219 to correct for internal mass fractionation. For MC-ICPMS analyses, Nd extracts were dissolved into 2% HNO_3 to produce solutions with ~20-40 ppb Nd and samples were run between 2 and 20V. Repeated measurements of the Nd isotopic reference JNdi-1 yielded Nd isotopic values within error of the value obtained by Tanaka et al. (2000) during the study period, and repeat measurements of BHVO-2 also yielded Nd isotopic values within error of the accepted value of Jochum et al., (2005). Results are presented in epsilon notation, or parts per 10,000, where:

$$\varepsilon Nd = [(^{143}Nd/^{144}Nd)_{sample}\ C\ (^{143}Nd/^{144}Nd)_{CHUR}] / (^{143}Nd/^{144}Nd)_{CHUR} \times 10000.$$

Chondritic meteorites serve as a reference for the isotopic ratio of undifferentiated bulk-Earth (or Chondritic Uniform Reservoir; CHUR; Jacobsen and Wasserburg, 1984). The reference value for CHUR used for εNd calculations is:

$$^{143}Nd/^{144}Nd_{CHUR} = 0.512638,\ ^{147}Sm/^{144}Nd_{CHUR} = 0.1966,$$

and the decay constant used for ^{147}Sm is 6.54 x 10^{12} a^{-1} from Goldstein et al. (1984).

Reported Nd and Sm concentrations and $^{147}Sm/^{144}Nd$ ratios have < 0.5% error. These correspond to an error of < 0.5 εNd units on individual samples, with most of the reported εNd values having an error of < 0.2 εNd units. Initial εNd (εNd_i) values were calculated from an age model based on depositional ages of Gibson et al. (2018) and presented in Table 3.

4. Results

Eighty-nine Sr, 13 Os, and 50 Nd isotopic data points are plotted stratigraphically in Figure 4. $^{87}Sr/^{86}Sr$ values range from 0.7051 to 0.7061 and display a steady decrease from 0.7060 to 0.7053 through the Iqqittuq Formation and into the Nanisivik Formation, which is the distal slope facies equivalent of the Angmaat Formation. Angmaat Formation carbonates have high Mg/Ca ratios and no reliable Sr isotope data have been generated from these facies. $^{87}Sr/^{86}Sr$ values from the lower half of the Victor Bay Formation are consistently low, between 0.7051 to 0.7053, and then rise towards the base of the Athole Point Formation where they become higher and more variable (0.7053 to 0.7063).

Initial $^{187}Os/^{188}Os$ ratios from the Arctic Bay Formation are highly radiogenic (1.56 to 0.97), but a sample near the top of the Arctic Bay Formation with an Os_i composition of 0.71 indicates a trend to more intermediate values. Two Re-Os isochron ages provide additional highly radiogenic Os_i values, 1.45 from the middle Arctic Bay Formation and 1.25 for the basal Victor Bay Formation (Gibson et al., 2018).

Sedimentary εNd_i values from the lower Bylot Supergroup (Arctic Bay through Angmaat formations) are unradiogenic, between –18 and –11. Samples from the lower Victor Bay Formation

display a shift to more juvenile εNd_i values with a steady increase from –13.5 and –2. While upper Bylot εNd_i data are sparse, available data define a trend from juvenile (0.38) to intermediate-evolved (–13.5 to –10) compositions through the Nunatsiaq Group. Together, these proxies appear to be coupled through the Arctic Bay Formation before decoupling in the uppermost Arctic Bay to Iqqittuq formations. They remain decoupled into the Angmaat Formation before again converging in the basal Victor Bay Formation. A trend to less radiogenic εNd_i values through the lower Victor Bay Formation is then followed by a steady interval of low $^{87}Sr/^{86}Sr$.

Nauyat Formation basalt yields an εNd_i of –5.60 calculated from its putative age of 1267 Ma (Fahrig et al., 1981; LeCheminant and Heaman, 1989). This is within the –6.6 to –0.4 range for previously published whole rock compositions of the ca. 1267 Ma Muskox layered intrusion (Day et al., 2008), which is an early expression of the Mackenzie LIP (LeCheminant and Heaman, 1989). However, the εNd_i composition of Nauyat Formation basalt is more negative than the estimated –3 to +1 εNd composition of the parental magma for the Makenzie LIP (Stewart and DePaolo, 1996; Day et al., 2008). Initial $^{143}Nd/^{144}Nd$ chemostratigraphic data from the Bylot Supergroup are consistently < –11 in the Arctic Bay, Iqqittuq, and Angmaat formations and are inconsistent with a dominant local Nauyat Formation contribution to the weathering regime in the Borden Basin's catchment area during of the Ikpiarjuk and Arctic Bay formation as suggested by Hahn et al. (2015).

5. Discussion

5.1. Hydrologic Restriction

Even though the Bylot Supergroup is commonly cited as providing key insights into late Mesoproterozoic marine environments (Narbonne and James, 1996; Kah et al., 1999, 2001; Sherman et al., 2000, 2001), the Borden Basin has also been interpreted to have been hydrologically restricted from the open ocean. However, these interpretations are based almost entirely on Os_i data from the Arctic Bay Formation (Gibson et al., 2018) and rare earth element + Yttrium patterns from contemporaneous seep-related carbonate mounds (Ikpiarjuk Formation; Turner and Kamber, 2012; Hahn et al., 2015). The highly radiogenic Os_i of the Victor Bay Formation Re-Os isochron from Gibson et al. (2018) is the only data indicating restriction at

another time during the basin's depositional history. Combined $^{87}Sr/^{86}Sr$, Os_i, and εNd_i isotope chemostratigraphic data herein from samples throughout most of the Bylot Supergroup reconcile these seemingly contradictory accounts of the Borden Basin.

Initial $^{187}Os/^{188}Os$ ratios through the Arctic Bay Formation are between 0.97 and 1.5, until the top of the formation where one sample records an Os_i value of 0.71, and the Os_i of the Victor Bay Formation is 1.25 (Fig. 4; Gibson et al., 2018). The consistency in $^{187}Os/^{188}Os$ ratios from this study and the coherent Re-Os isochron generated from the same Arctic Bay Formation stratigraphic section in Shale Valley (Fig. 1) indicate that the Re-Os system here remained undisturbed. These values are higher than any previously reported Mesoproterozoic to early Neoproterozoic marine deposits in which the Re-Os system was undisturbed (Osi <0.8; Creaser and Stasiuk, 2007; Azmy et al., 2008; Kendall et al., 2009a; Rooney et al., 2010; Geboy et al., 2013; van Acken et al., 2013; Rooney et al., 2014; Sperling et al., 2014; Strauss et al., 2014; Cohen et al., 2017; Rooney et al., 2017); however, they are similar to compositions from restricted marginal marine to lacustrine basins of this age (Osi >0.8; Cumming et al., 2013; Tripathy and Singh, 2015; Rooney et al., 2017).

Based on Os_i calculated from precise isochrons from the Taoudeni Basin in Mauritania and São Francisco Basin in Brazil the marine $^{187}Os/^{188}Os$ composition was between ~0.3 and 0.7 ca. 1100–1000 Ma (Azmy et al., 2008; Rooney et al., 2010; Geboy et al., 2013). Restricted continental basin waters of any age may be more radiogenic than contemporaneous marine waters due to a combination of increased influence from runoff and decreased influence from seafloor weathering and hydrothermal input (Poirier and Hillaire-Marcel, 2011; Cumming et al., 2012; Xu et al., 2017). Previous investigations of select modern rivers, drainage areas, and restricted basins identified sediment with less radiogenic $^{187}Os/^{188}Os$ than seawater (Ravizza et al., 1991; Martin et al., 2000; Poirier, 2006). While most of these data are from bulk sediment, which tends to yield higher $^{187}Os/^{188}Os$ because most detrital minerals contain less radiogenic Os than hydrogenous phases, attempts to isolate the hydrogenous component suggest that waters are, in fact, less radiogenic that seawater. Although it is possible for water from specific continental settings to be less radiogenic than the ocean, continental influence is the only known mechanism to drive basin waters more radiogenic. Therefore, the Os_i data points with values between 1.0 and 1.5 for the Arctic Bay and lowermost Victor Bay formations offer very strong evidence that the Os flux to the basin was

dominated by evolved, continental sources and that the basin had minimal communication with the open ocean at these times.

These Os_i data are also consistent with εNd_i values between –16 to –11 in the Arctic Bay and Iqqittuq formations (Fig. 4) that establish a highly evolved local weathering regime in the vicinity of the Borden Basin. Runoff from the surrounding Archean to Paleoproterozoic granite orthogneiss and metasedimentary units of the Rae Province (Crocker et al., 1993) likely dominated the input to the basin, and so this Os isotope record reflects local signals with no discernably marine influence. Compared to $Os_i \approx 0.3$ from the broadly coeval ca. 1100 Ma epicratonic Taoudeni Basin (Rooney et al., 2010; Kah et al., 2012; Gilleaudeau and Kah, 2013a, b), which is also surrounded by Archean to Paleoproterozoic felsic basement, highly radiogenic Os_i compositions (~1–1.5) from this study indicate the Borden Basin was hydrologically restricted from the open ocean during deposition of the Arctic Bay and basal Victor Bay formations.

There is little overlap between data that inform interpretations from this study for open marine versus restricted conditions in the Borden Basin because Sr and Os isotopes are measured in separate lithologies. This dichotomy poses a potential problem for reconciling these datasets. Because the residence times for Sr and Os in the ocean differ, so do the timescales on which each isotopic system is sensitive to change. The residence time of Sr in the ocean is ~3–5 Myr. The residence of Os is less constrained, but is on the order of 10–50 kyr (reviewed in Peucker-Ehrenbrink and Ravizza, 2000). Both are long relative to the mixing time of the ocean and therefore homogenous with respect to $^{87}Sr/^{86}Sr$ and $^{187}Os/^{188}Os$; however, the marine $^{187}Os/^{188}Os$ composition is sensitive to processes that result in shorter-term fluctuations than $^{87}Sr/^{86}Sr$. The size of the marine Os reservoir reflects a balance between sources of Os, namely oxidative weathering, and sinks, namely the areal extent of organic-rich sediment deposition (i.e., bottom water anoxia; Ravizza and Turekian, 1992; Peucker-Ehrenbrink and Ravizza, 2000). Therefore, the reservoir size of Os was probably smaller and its residence time shorter in Proterozoic oceans than today. These factors could potentially result in $^{187}Os/^{188}Os$ heterogeneity in the Proterozoic ocean, as was suggested by (Kendall et al., 2009a; Kendall et al., 2009b).

If the marine Os isotopic composition was not homogenous in the ocean, the $^{187}Os/^{188}Os$ of marginal marine basin waters may largely reflect local, continental runoff; however, low Os_i values (~0.3) from the Taoudeni Basin demonstrate that epicratonic basins surrounded by old, evolved continental crust still preserved marine Os signatures, with minimal influence from local

weathering. The highly radiogenic Os_i values in the Borden Basin record periods in which abundant organic carbon burial in a restricted setting would have reduced the residence time of Os in the basin drastically. The transition to less radiogenic Os_i and $^{87}Sr/^{86}Sr$ from the upper Arctic Bay Formation through the Iqqittuq Formation at a time when εNd_i values indicate that the local weathering flux into the basin remained consistently radiogenic suggest that marine incursion significantly lowered the $^{187}Os/^{188}Os$ of basin waters. A reduction in organic carbon burial at this time also would have increased the residence time of Os in the basin. Thus, the Os_i composition of 0.71 in the uppermost Arctic Bay Formation represents some mixture of locally-derived runoff and seawater and provides an upper limit for the $^{187}Os/^{188}Os$ composition of the ocean at ca. 1050 Ma.

5.2. Marine Incursion

Rare earth element (REE) patterns from Arctic Bay Formation black shale and coeval Ikpiarjuk Formation seep-related carbonate mounds were interpreted to represent deposition in a restricted setting based on their negative slope (Turner and Kamber, 2012) and absence of positive La and Gd anomalies (Hahn et al., 2015), respectively. Conversely, Uluksan Group (the middle Bylot Supergroup) also exhibits various evidence for deposition in a marine environment. The Angmaat Formation contains diverse peritidal facies and extensive sulfate evaporite deposits, which requires a source of sulfate. Furthermore, $\delta^{13}C$ of carbonates and $\delta^{34}S$ and $^{87}Sr/^{86}Sr$ of evaporites through the Uluksan Group are within expected ranges for late Mesoproterozoic marine compositions (Kah and Knoll, 1996; Kah et al., 1999; Kah et al., 2001). Additionally, the Angmaat and Victor Bay formations both exhibit decimeter-scale cyclicity that have been interpreted to reflect high-amplitude eustatic sea level change (Sherman et al., 2001; Turner, 2009).

The Os_i of the uppermost Arctic Bay Formation declines to 0.71, following highly radiogenic Os_i values between ~1–1.5 through most of the formation. A steady, up-section decline in $^{87}Sr/^{86}Sr$ ratios from 0.70599 to 0.70552 through the Iqqittuq Formation continues this secular trend toward more juvenile signatures in the basin—closer to those expected for latest Mesoproterozoic seawater. Through the same interval, εNd_i remains highly evolved, between –17 and –13 (Fig. 4). This transition, in which water mass proxies decouple from the detrital input to the basin (evolved εNd_i) coincides with a significant sedimentological transition in the Bylot

Supergroup. The Iqqittuq Formation marks the development of a mixed carbonate-siliciclastic ramp and contains facies assemblages that are transitional between the Arctic Bay and Angmaat Formations (Turner, 2009). The shallow-water Angmaat Formation and deep-water correlative carbonate slope of the Nanisivik Formation mark the development of a stable, rimmed carbonate platform and the onset of widespread carbonate deposition in the Borden Basin. Laterally continuous, bedded sulfate evaporite facies were deposited in back-barrier lagoonal settings at this time.

An increase in carbonate saturation in the basin concurrent with distinct shifts in $^{87}Sr/^{86}Sr$ and $^{187}Os/^{188}Os$ that are decoupled from the local weathering input reflect a marine incursion into the Borden Basin. Nanisivik Formation limestone rhythmites display very low $^{87}Sr/^{86}Sr$ compositions, between 0.70528 and 0.70537, which almost certainly track coeval seawater. Thus, the Iqqittuq Formation records a gradual increase in marine influence, and the Borden Basin was in full communication with the open ocean during Angmaat-Nanisivik time. These interpretations suggest that marine influence and the degree of water mass-restriction controlled water chemistry and sedimentation patterns in the basin. Hence, we infer that the organic-rich (up to 20% TOC) Arctic Bay Formation black shales were deposited when the Borden Basin was cut off from the global ocean and was fed by runoff from the surrounding, highly-evolved Archean to Paleoproterozoic basement of the Rae Province. Conversely, middle Bylot Supergroup carbonates were deposited while the Borden Basin was connected to the open ocean in all but shallow, lagoonal environments during Angmaat Formation deposition.

Kah et al. (2001) previously published $^{87}Sr/^{86}Sr$ data from Angmaat Formation evaporites. These data range from 0.70540 to 0.70858 (Fig. 4), and values below ~0.707 were interpreted to reflect marine Sr isotopic compositions and a few higher values derive from variable degrees of influence from continental runoff in evaporative environments (Kah et al., 2001). The facies architectural reconstruction of the Angmaat Formation carbonate platform by Turner (2009) elucidates a probable mechanism for the development of thick evaporite deposits in the shallowest portions of the basin. During Angmaat-Nanisivik formations time, the Borden Basin deepened roughly to the west-northwest, and shallow, peritidal facies comprising much of the Angmaat Formation were separated from Nanisivik Formation carbonate slope facies by ooid grainstone barrier shoals between White Bay and Tremblay Peninsula (Fig. 1; Turner, 2009; Gibson et al., 2017). Evaporites only occur at Angmaat Mountain and Bylot Island, which are in the

southwestern extremes of the Milne Inlet Graben and Eclipse Trough, respectively (Fig. 1). The up-to 1.5 m-thick evaporite beds in these locations require that the shallow environments in which they formed were hydrologically restricted from the open ocean to some degree, but also that their sulfate reservoir was periodically replenished by seawater.

Kah et al. (2001) interpreted the $\delta^{34}S$ of evaporite minerals to reflect the composition of Mesoproterozoic seawater sulfate. However, $^{87}Sr/^{86}Sr$ compositions in the evaporites are as high as 0.70858, whereas all limestone samples from this study have $^{87}Sr/^{86}Sr < 0.706$ and broadly coeval data from the Nanisivik Formation are lower than the least radiogenic evaporate deposits. These data reflect an increasing proportion of continental influence due to progressive hydrologic restriction of an internal platform lagoon. The highest values from Angmaat evaporites likely reflect some degree of mixing between local runoff and marine waters, and so they offer only a minimum $^{87}Sr/^{86}Sr$ ratio derived from local weathering. Intervals of relative sea-level fall, as indicated by shallowing-upward cycles in the ooid grainstone barrier sections in the southeastern Milne Inlet Graben (Fig. 1), led to progressively restricted circulation to Angmaat lagoonal environments, triggering evaporite deposition even as the deep-water slope environments (Nanisivik Formation) remained connected to the open ocean.

5.3. Tectonic Adjustment to Stable Marine Configuration

After deposition of the Angmaat and Nanisivik formations, the Milne Inlet Graben was uplifted and tilted to the northeast (present coordinates; Turner, 2011). As a result, the contact between the Angmaat/Nanisivik and Victor Bay formations varies from paraconformable in the southeastern Milne Inlet Graben to erosional in the center of the graben and angular and erosional in the northwest (Fig. 1; Turner, 2009; Turner, 2011). The lower Victor Bay shale member blankets this unconformity throughout the Milne Inlet Graben but is absent in Eclipse Trough, where the Victor Bay Formation appears to overlie the Angmaat Formation conformably. The basal Victor Bay Formation shale has been interpreted to record a rapid marine transgression in the Borden basin due to tectonic subsidence in the Milne Inlet Graben (Jackson and Iannelli, 1981; Sherman et al., 2001). However, this interpretation is inconsistent with the radiogenic $Os_i = 1.25$ in the basal Victor Bay shale, which instead suggests renewed restriction at this time, perhaps due to the differential uplift and subsidence at this time.

Any interpretation for depositional history of the basal Victor Bay Formation shale must reconcile the seemingly contradictory phenomena of simultaneous basin foundering and hydrologic restriction. Northeast-side down half graben rotation of the Milne Block (Fig. 1) could have down-dropped a portion of the basin along the White Bay Fault Zone while a seaward block was uplifted above level, temporarily forming a barrier from the open ocean that restricted circulation to the Milne Inlet Graben. In fact, Nanisivik Formation carbonate slope facies in the northwestern Milne Inlet Graben, near the hamlet of Arctic Bay, were uplifted prior to deposition of the lower Victor Bay Formation (Turner, 2011), and this uplift could have been responsible for isolation of the basin.

Neodymium data also reveal tectonically-driven modifications to the Borden Basin through changes in sediment provenance. Initial $^{143}Nd/^{144}Nd$ values remained between –18 and –11 through the Arctic Bay, Iqqittuq, and Angmaat formations despite fluctuating $^{87}Sr/^{86}Sr$ and Os_i through this interval (Fig. 4). However, a sharp rise in εNd_i from –13.5 to –2.0 through the lower Victor Bay Formation indicates a significant change in provenance towards more juvenile compositions. Tectonic activity at this time is further indicated by a shift in depositional environment from shallow water carbonates and evaporites of the Angmaat Formation to slope facies in lower Victor Bay carbonates. In the absence of other known lithologies with juvenile εNd_i signatures, we infer that block faulting at this time uplifted the Nauyat Formation (or other cogenetic mafic rocks) and that erosion of these basalts was at least locally a major source of detritus to the basin. The subsequent return towards more evolved (–13.5 to –10) compositions in the Nunatsiaq Group (Fig. 4) records the removal of this mafic source, possibly combined with uplift of older, felsic basement.

Up to 300 m of thin, rhythmically bedded limestone overlie the basal Victor Bay Formation shale member. This facies was deposited on a storm-dominated, muddy carbonate ramp (Sherman et al., 2000; Sherman et al., 2001) with a well-developed reef tract composed of large stromatolite build-ups (Narbonne and James, 1996). The $^{87}Sr/^{86}Sr$ composition of Victor Bay Formation outer ramp rhythmite facies are consistently unradiogenic: 0.70511 to 0.70558 (Fig. 4). The transition from organic-rich black shale of the basal Victor Bay Formation with a highly radiogenic Os_i composition to the development of a carbonate ramp with stromatolitic bioherms with unradiogenic $^{87}Sr/^{86}Sr$ composition through the lower Victor Bay Formation once again marks a return to open marine conditions in the Borden Basin.

The timing of this lithological and geochemical transition coincides with the shift in sediment provenance recorded by increasing εNd_i (Fig. 4). Thus, further tectonic reconfiguration of the Borden Basin likely opened the basin to the ocean and triggered the onset of stable marine conditions throughout deposition of the Victor Bay Formation carbonate ramp. Except for localized evaporite deposition in sabkha environments in the shallowest portions of the basin, there is no evidence that the Borden Basin was restricted at any point during deposition of the Victor Bay or Athole Point formations. Although $^{87}Sr/^{86}Sr$ compositions of Athole Point Formation limestone are somewhat more radiogenic (0.70542–0.70597), these are still consistent with marine compositions for the latest Mesoproterozoic ocean (Bartley et al., 2001).

5.4. Regional Tectonics

After deposition of the Victor Bay Formation, the eastern Milne Inlet Graben subsided, creating accommodation space for Athole Point carbonates, which conformably overlie the Victor Bay Formation (Jackson and Iannelli, 1981). At the same time, uplift along the central axis of the basin near the inlet to Strathcona Sound, produced an erosional unconformity between the Victor Bay and Strathcona Sound formations in the west and throughout Eclipse Trough (Fig. 1; Sherman et al., 2002). Sherman et al. (2002) interpret this reversal in the polarity of the Borden Basin to result from a novel tectonic regime that could not explained by continued extension. They attributed the differential subsidence and uplift at this time to forebulge migration and distal foreland subsidence related to east-directed compression.

However, the angular and erosional unconformity beneath the sub-Victor Bay unconformity in the northwestern Borden Basin near the hamlet of Arctic Bay indicates pronounced uplift of the Nanisivik Formation in what was the deepest portion of the basin at the time (Turner, 2011), similar to the subsequent uplift of the Victor Bay Formation at Strathcona River (Fig. 1). Furthermore, the Angmaat-Nanisivik carbonate platform and distal slope consistently deepened to the present west-northwest—a bathymetric trend that had persisted since deposition of the Arctic Bay Formation (Turner, 2009). Then, the well-developed Victor Bay Formation reef tract and facies distribution in the Milne Inlet Graben clearly define south-southwest deepening (in present coordinates) carbonate ramp (Sherman et al., 2000).

Together, these previously documented observations imply that differential uplift between Uluksan and Nunatsiaq Group deposition need not represent a novel stage in the basin's tectonic evolution, but rather can be explained by extensional reactivation of older, basin-controlling faults. In fact, northeast-side down half graben rotation of the Milne Block (Fig. 1) could have also produced the concurrent uplift in the vicinity of Strathcona Sound and subsidence along the White Bay Fault Zone (i.e., Mala River, Pingo Valley and White Bay as observed by Sherman et al., 2002) during both early Victor Bay and early Nunatsiaq Group times. Hence, Victor Bay deformation may simply reflect renewed half graben rotation of the Milne Block that was kinematically similar to the rotation that restricted the basin during early Victor Bay time. Although we cannot rule out contractional tectonics during the evolution of the Borden Basin, they are not required to explain its depositional evolution.

5.5. Global Implications

5.5.1. Role of Episodically Restricted Environments in Eukaryotic Evolution

Several phylogenetic studies indicate that early photosynthetic eukaryotes (i.e., relatives of plants and algae) inhabited low-salinity waters and may have evolved in non-marine, freshwater environments (Blank, 2013; Ponce-Toledo et al., 2017; Sánchez-Baracaldo et al., 2017). These investigations provide a potentially testable hypothesis that requires the ability to recognize such environments in ancient, fossiliferous basins. Strother et al. (2011) identified acritarchs from the ca. 1200 Ma Stoer Group in Scotland and interpreted them as the first known freshwater eukaryotes based on sedimentary structures (Stewart, 2002), high Mo (Parnell et al., 2015), and low B concentrations in illite (Stewart and Parker, 1979). On the other hand, Stüeken et al. (2017) presented Mo isotopes from the Stoer Group that are consistent with the composition of coeval marine shales, and interpret Sr isotopes to reflect mixing of continental runoff and seawater. They therefore posit that the Stoer Group was deposited in a marginal marine environment and attribute earlier observations to evapo-concentration in a partially restricted, marginal marine environment—much like that of the Angmaat Formation.

Bangiomorpha pubescens is a multicellular eukaryotic fossil that has been recovered from the Angmaat Formation in the Borden Basin (Knoll et al., 2013) and the putatively correlative

Hunting Formation in the Aston and Hunting Basin on Somerset Island (Fig. 1; Butterfield et al., 1990). Due to its morphological similarity to modern bangiophyte red algae, it is also the oldest unambiguously photosynthetic and crown group eukaryote (Butterfield, 2000). Although this study cannot definitively resolve the timescale of hydrologic restriction in the Borden Basin, episodically restricted epeiric seaways were widespread across Rodinia (Kah et al., 2012; Gilleaudeau and Kah, 2013b; Gilleaudeau and Kah, 2015; Cox et al., 2016). Thus, a preponderance of spatio-temporally heterogeneous late Mesoproterozoic environments may have exerted unique selective pressure that drove eukaryotic evolution and diversification.

Evidence presented herein demonstrates *Bangiomorpha* emerged in an environment that fluctuated between marine and non-marine and by extension varied from saline to freshwater conditions. Furthermore, the lagoonal, evaporative facies of the Angmaat Formation that preserve *Bangiomorpha*, were likely hypersaline. Together, these datasets and interpretations for the hydrographic evolution of the Borden Basin support the hypothesis that non-marine environments provided important ecological niches for eukaryotic evolution, additional paleontological datasets must be integrated with detailed hydrologic histories of their fossil-bearing basins in order to determine if this is a global phenomenon. Here, we demonstrate that coupled $^{87}Sr/^{86}Sr$, $^{187}Os/^{188}Os$, and $^{143}Nd/^{144}Nd$ data can elucidate the hydrologic evolutionary history of ancient sedimentary basins, with potential application to other Proterozoic sedimentary basins.

5.5.2. Terminal Mesoproterozoic Age-Calibrated $^{87}Sr/^{86}Sr$ Curve

Limestone from the Nanisivik, Victor Bay, and Athole Point formations are interpreted to record precipitation from seawater. Calibrated by Re-Os depositional ages from Gibson et al. (2018), $^{87}Sr/^{86}Sr$ compositions from these units contribute to the sparsely populated late Mesoproterozoic global marine $^{87}Sr/^{86}Sr$ curve (Fig. 5). Inferred marine $^{87}Sr/^{86}Sr$ data rise from 0.70511 to 0.70597 through the Victor Bay Formation into the Athole Point Formation where they become more variable. Values from ca. 1050 Ma middle Bylot Supergroup limestone are similar in composition, though somewhat more primitive than filtered data ($^{87}Sr/^{86}Sr$ between 0.70560–0.70613) from the ca. 1050–1000 Ma Sukhayu Tunguska Formation of the Turukhansk Uplift in Siberia (Bartley et al., 2001; Semikhatov et al., 2002; Cox et al., 2016). Combined, these data indicate a rise in seawater $^{87}Sr/^{86}Sr$ from ~0.705 to 0.706. Considering the timing of this rise

coincided with peak metamorphism of Grenville orogeny during the Ottawan Phase (Fig. 5; Hynes and Rivers, 2010), this trend is most simply interpreted as a result of the chemical weathering of orogens formed during the amalgamation of Rodinia. This pattern, along with a subsequent fall towards less radiogenic values, mirrors the $^{87}Sr/^{86}Sr$ trend in the late Neoproterozoic to Paleozoic eras, where peak values correspond to the assembly of Gondwana during the Pan-African orogeny (Goddéris et al., 2017).

6. Conclusions

Coupled $^{87}Sr/^{86}Sr$ limestone, $^{187}Os/^{188}Os$ black shale, and $^{143}Nd/^{144}Nd$ mudstone chemostratigraphy of the Bylot Supergroup elucidate the hydrologic evolution of the late Mesoproterozoic Borden Basin. Black shale from the Arctic Bay Formation exhibit highly radiogenic initial $^{187}Os/^{188}Os$ (Os_i; ~1–1.5) and initial $^{143}Nd/^{144}Nd$ (εNd_i; to –18 to –11) compositions, consistent with a principal flux of evolved, local continental weathering products to the basin. These data require that the Borden Basin was hydrologically restricted from the open ocean at this time. Both Os_i and $^{87}Sr/^{86}Sr$ values trend toward more intermediate to juvenile compositions (Os_i ~ 0.7 and $^{87}Sr/^{86}Sr$ from ~0.706 to 0.705) at the transition to the carbonate-dominated Uluksan Group, while εNd_i values remain low (–10 to –15). This decoupling between hydrogenous (Sr and Os) and detrital (Nd) radio-isotope proxies and trends signifies a marine incursion to the basin. This transition also indicates that marine influence and the degree of water mass-restriction controlled chemistry and sedimentation patterns in the basin. Previously published $^{87}Sr/^{86}Sr$ evaporite compositions from the Angmaat Formation show a trend of increasing radiogenic input up-section, consistent with deposition in a restricted, back-barrier environment. Highly radiogenic Os_i in overlying black shale of the Victor Bay Formation also implies deposition in a restricted environment.

A rapid increase in εNd_i through the lower Victor Bay Formation reflects local uplift of Nauyat Formation basalt in the Borden Basin. Well-preserved limestone facies through the Victor Bay and Athole Point Formations consistently display low $^{87}Sr/^{86}Sr$ values, indicative of stable marine conditions. These trends in εNd_i and $^{87}Sr/^{86}Sr$ data, as well as sedimentological and stratigraphic evidence, indicate that regional tectonic activity modified the geometry of the Borden Basin so that it was exposed to the open ocean throughout the remainder of Victor Bay and Athole

Point deposition. Limestone facies of the Victor Bay and Athole Point formations limestone record the $^{87}Sr/^{86}Sr$ composition of terminal Mesoproterozoic seawater.

These data along with some from Nanisivik Formation slope facies provide 89 new, age-calibrated $^{87}Sr/^{86}Sr$ data points from samples filtered for post-depositional alteration. A rise from ~0.705 to 0.706 coincides with peak metamorphism of the Ottawan Phase of the Grenville orogeny and may be a product of increased continental weathering during the amalgamation of Rodinia. These data fill in a critical gap in the late Proterozoic marine $^{87}Sr/^{86}Sr$ curve and imply that a transformation in global silicate weathering may have begun just prior to the Mesoproterozoic-Neoproterozoic boundary.

Another tectonic event at the end of Victor Bay Formation time was previously interpreted to be a result of novel compressional stresses acting on the basin; however, northeast-side down half-graben rotation of the Milne Block in the Milne Inlet Graben can explain simultaneous uplift and subsidence, as well as facies trends both at this time and during early Victor Bay Formation transgression. Therefore, these deformation events in the Borden Basin do not require a novel extensional stress regime, as previously suggested, but can be explained by continued extension through the middle Bylot Supergroup.

In summary, Sr, Os, and Nd radiogenic isotope chemostratigraphy from the Bylot Supergroup records the complex hydrologic and depositional history of the Borden Basin. Coupled hydrogenous and detrital radio-isotope chemostratigraphy offers unique insights into periods of marine versus non-marine conditions in ancient basins with complex hydrologic histories, like the Borden Basin, which may have been important loci for early eukaryotic evolution. Paleo-environmental interpretations from this study provides a backdrop for future work correlating fossil assemblages and/or diversity from the Bylot Supergroup and add to a growing database from epeiric seaways within Rodinia that may have influenced global biogeochemical cycles.

Acknowledgments

This research was supported by Geomapping for Energy and Minerals (GEM-2) and Polar Continental Shelf Program of Natural Resources Canada, the Natural Sciences and Engineering Research Council of Canada, and the Agouron Institute. TMG further acknowledges funding from the Eric Mountjoy Legacy Fund (McGill University), Mountjoy Exchange Award (Geological

Association of Canada), and Graduate Student Research Grant (Geological Society of America). We thank Vivien Cumming, Malcolm Hodgskiss, Marcus Kunzmann, Kelsey Lamothe, Rob Rainbird, Tom Skulski, and Heda Agiç for their contributions to fieldwork and sample preparation.

Table and Figures

Table 1: $^{87}Sr/^{86}Sr$ data from this study and Kah et al. (2001).

Formation	Section	Height (m)	Composite (m)	$^{87}Sr/^{86}Sr$*
Athole Point	R1609	192.0	4329	**0.70566**
Athole Point	R1609	183.0	4311	**0.70550**
Athole Point	R1609	182.0	4294	**0.70546**
Athole Point	R1609	176.0	4277	**0.70550**
Athole Point	R1609	175.0	4260	**0.70550**
Athole Point	R1609	174.0	4243	**0.70550**
Athole Point	R1609	171.0	4226	**0.70549**
Athole Point	R1609	167.0	4209	**0.70549**
Athole Point	T1509	423.0	4191	**0.70576**
Athole Point	T1509	404.2	4174	**0.70584**
Athole Point	T1509	292.5	4157	**0.70558**
Athole Point	T1509	289.0	4140	**0.70563**
Athole Point	T1509	242.9	4123	**0.70561**
Athole Point	T1509	234.0	4106	**0.70547**
Athole Point	T1509	232.2	4089	**0.70568**
Athole Point	T1509	214.5	4071	**0.70563**
Athole Point	T1509	210.0	4054	**0.70588**
Athole Point	T1509	202.5	4037	**0.70584**
Athole Point	T1509	180.0	4020	**0.70597**
Athole Point	T1509	170.0	4003	**0.70555**
Athole Point	T1509	165.8	3986	**0.70563**
Athole Point	SW1602	130.5	3969	**0.70543**
Athole Point	SW1602	128.7	3951	**0.70553**
Athole Point	SW1602	126.0	3934	**0.70547**
Athole Point	SW1602	125.6	3917	**0.70549**
Athole Point	SW1601	199.6	3900	**0.70545**
Athole Point	SW1601	195.4	3883	**0.70551**
Athole Point	SW1601	192.6	3866	**0.70550**
Athole Point	SW1601	187.3	3849	**0.70559**
Athole Point	SW1601	170.8	3831	**0.70563**
Athole Point	SW1601	168.2	3814	**0.70577**
Athole Point	SW1601	149.4	3797	**0.70589**
Athole Point	T1509	159.8	3686	**0.70582**
Athole Point	T1509	155.1	3780	**0.70589**
Athole Point	T1509	133.7	3763	**0.70581**
Athole Point	T1509	3.4	3643	**0.70568**
Athole Point	SW1602	6.4	3634	**0.70552**
Athole Point	SW1602	5.8	3626	**0.70542**
Athole Point	SW1602	3.2	3617	**0.70571**
Athole Point	SW1602	0.4	3609	**0.70561**
Victor Bay	SW1603	111.6	3557	**0.70558**

Victor Bay	SW1603	102.1	3514	**0.70546**
Victor Bay	SW1603	92.5	3471	**0.70544**
Victor Bay	SW1603	89.3	3429	**0.70545**
Victor Bay	SW1603	74.8	3386	**0.70548**
Victor Bay	T1508	193.0	3300	**0.70543**
Victor Bay	T1508	179.1	3257	**0.70538**
Victor Bay	T1508	135.6	3214	**0.70526**
Victor Bay	T1508	63.5	3171	**0.70528**
Victor Bay	T1508	47.8	3129	**0.70538**
Victor Bay	T1707	290.0	3086	**0.70519**
Victor Bay	T1707	286.5	3000	**0.70521**
Victor Bay	T1707	123.1	2929	**0.70517**
Victor Bay	T1707	113.8	2909	**0.70519**
Victor Bay	T1707	110.2	2889	**0.70518**
Victor Bay	T1707	107.1	2869	**0.70515**
Victor Bay	T1707	105.7	2849	**0.70527**
Victor Bay	T1707	103.8	2829	**0.70530**
Victor Bay	T1707	101.0	2809	**0.70516**
Victor Bay	T1707	100.6	2789	**0.70516**
Victor Bay	T1707	97.0	2769	**0.70519**
Victor Bay	T1707	93.5	2749	**0.70518**
Victor Bay	T1707	90.5	2729	**0.70526**
Victor Bay	T1707	89.1	2709	**0.70522**
Victor Bay	T1707	87.7	2689	**0.70521**
Victor Bay	T1707	74.6	2669	**0.70520**
Victor Bay	T1707	72.6	2649	**0.70516**
Victor Bay	T1707	54.9	2629	**0.70517**
Victor Bay	T1707	51.9	2609	**0.70534**
Victor Bay	T1707	48.9	2589	**0.70517**
Victor Bay	T1707	47.0	2569	**0.70516**
Victor Bay	T1707	43.3	2549	**0.70522**
Victor Bay	T1707	41.4	2529	**0.70530**
Victor Bay	T1707	31.3	2500	**0.70511**
Victor Bay	T1707	24.1	2490	**0.70519**
Victor Bay	T1707	21.4	2480	**0.70512**
Victor Bay	T1707	17.3	2470	**0.70516**
Victor Bay	T1707	14.3	2460	**0.70522**
Nanisivik	T1602	20.6	1714	**0.70528**
Nanisivik	T1602	10.0	1629	**0.70531**
Nanisivik	T1602	5.0	1543	**0.70537**
Iqqittuq	SW1605	2.1	1500	0.70552
Iqqittuq	SW1605	0.4	1491	0.70558
Iqqittuq	SW1604	193.5	1457	0.70554
Iqqittuq	SW1604	112.3	1440	0.70568
Iqqittuq	T1410	138.0	1423	0.70545
Iqqittuq	T1410	136.7	1414	0.70550
Iqqittuq	T1410	116.0	1371	0.70579
Iqqittuq	T1410	96.8	1329	0.70599
Iqqittuq	T1410	84.0	1286	0.70589
Angmaat	*Kah et al. (2001)*	BY97-2957	2417	0.70659
Angmaat	*Kah et al. (2001)*	BY97-2910	2394	0.70663
Angmaat	*Kah et al. (2001)*	TH97-G9	2371	0.70790
Angmaat	*Kah et al. (2001)*	TH97-G8	2348	0.70703
Angmaat	*Kah et al. (2001)*	TH97-G7	2325	0.70706
Angmaat	*Kah et al. (2001)*	BY97-2891	2302	0.70677
Angmaat	*Kah et al. (2001)*	TH97-G6	2279	0.70676
Angmaat	*Kah et al. (2001)*	BY97-1731	2256	0.70619

Angmaat	*Kah et al. (2001)*	BY97-1643	2233	0.70612
Angmaat	*Kah et al. (2001)*	BY97-1554	2210	0.70578
Angmaat	*Kah et al. (2001)*	TH97-G5	2187	0.70637
Angmaat	*Kah et al. (2001)*	BY97-1422	2164	0.70587
Angmaat	*Kah et al. (2001)*	BY97-1337	2141	0.70557
Angmaat	*Kah et al. (2001)*	BY97-1237	2118	0.70573
Angmaat	*Kah et al. (2001)*	BY97-1231	2095	0.70554
Angmaat	*Kah et al. (2001)*	TH97-G4	2072	0.70631
Angmaat	*Kah et al. (2001)*	BY97-998	2049	0.70548
Angmaat	*Kah et al. (2001)*	BY97-946	2026	0.70565
Angmaat	*Kah et al. (2001)*	TH97-G3	2003	0.70612
Angmaat	*Kah et al. (2001)*	BY97-664	1980	0.70540
Angmaat	*Kah et al. (2001)*	BY97-658	1957	0.70542
Angmaat	*Kah et al. (2001)*	TH97-G2	1934	0.70603
Angmaat	*Kah et al. (2001)*	BY97-597	1911	0.70575
Angmaat	*Kah et al. (2001)*	BY97-426	1888	0.70607
Angmaat	*Kah et al. (2001)*	TH97-G1	1865	0.70610
Angmaat	*Kah et al. (2001)*	BY97-238	1842	0.70777
Angmaat	*Kah et al. (2001)*	BY97-223	1819	0.70665
Angmaat	*Kah et al. (2001)*	BY97-290	1796	0.70578
Angmaat	*Kah et al. (2001)*	BY97-96	1773	0.70594
Angmaat	*Kah et al. (2001)*	BY97-59	1750	0.70580

* Only $^{87}Sr/^{86}Sr$ values in **bold** are interpreted to record marine compositions and are included in the global $^{87}Sr/^{86}Sr$ seawater curve in Figure 4.

Table 2: Re and Os abundances and isotopic compositions from this study and Gibson et al., (2018).

Formation	Section	Height (m)	Composite (m)	Re (ppb)	Os (ppt)	$^{187}Re/^{188}Os$	2σ	$^{187}Os/^{188}Os$	2σ	Os_i*
Victor Bay	Gibson et al. (2018)	-	2450							1.25
Arctic Bay	T1413	310.3	1200	2.41	67.18	308.68	3.83	6.15	0.07	0.71
Arctic Bay	T1413	282.8	1150	8.41	183.72	525.14	4.82	10.71	0.10	1.47
Arctic Bay	T1413	259.6	1080	21.27	557.45	367.89	1.61	7.80	0.03	1.32
Arctic Bay	T1413	226.5	1000	24.69	601.73	423.12	1.91	8.87	0.05	1.42
Arctic Bay	T1413	192.5	930	31.04	722.20	458.09	1.72	9.42	0.04	1.35
Arctic Bay	Gibson et al. (2018)	-	910							1.45
Arctic Bay	T1413	154.7	850	10.82	304.36	324.41	1.87	6.99	0.03	1.27
Arctic Bay	T1413	145.1	830	5.16	143.14	334.86	2.76	7.23	0.05	1.33
Arctic Bay	T1413	140	820	12.86	335.99	379.54	3.04	8.24	0.08	1.56
Arctic Bay	T1413	130.8	800	7.17	243.19	237.44	2.99	5.28	0.11	1.10
Arctic Bay	T1413	126.5	790	15.71	449.54	309.85	1.55	6.57	0.03	1.11
Arctic Bay	T1413	107.8	770	36.57	851.67	437.96	1.48	8.69	0.03	0.97
Arctic Bay	T1413	86.5	730	23.93	516.56	526.42	2.71	10.54	0.06	1.27
Arctic Bay	T1413	71.5	700	21.05	506.04	438.70	2.16	9.24	0.05	1.51

*Os_i = Initial $^{187}Os/^{188}Os$ isotope composition calculated from $\lambda^{187}Re$ and an age of 1048 Ma from Gibson et al. (2018).

Table 3: Sm and Nd abundances and isotopic compositions. Initial $^{143}Nd/^{144}Nd$ ratios (εNd_i) are calculated from age model based on depositional ages from Gibson et al. (2018).

Formation	Section	Height (m)	Nd (ppm)	Sm (ppm)	$^{147}Sm/^{144}Nd$	$^{143}Nd/^{144}Nd$	2σ	Age Model (Ma)	εNdi
Sinasiuvik	PC1505	66	51.9	8.7	0.1011	0.5114	5.87E-06	1035	-11.4
Sinasiuvik	PC1505	33.6	63.6	9.9	0.0937	0.5114	5.87E-06	1035	-10.4
Sinasiuvik	PC1505	27.1	92.7	24.2	0.1581	0.5119	5.87E-06	1035	-9.8
Sinasiuvik	T1510	174.2	38.8	6.8	0.1054	0.5114	5.87E-06	1035	-12.3
Sinasiuvik	T1510	107	44.7	7.8	0.1060	0.5114	5.87E-06	1035	-11.9
Sinasiuvik	T1510	35.3	29.1	5.6	0.1173	0.5114	5.87E-06	1035	-13.4
Aqigilik	T1607	27.5	21.9	4.3	0.1181	0.5116	5.87E-06	1038	-9.7
Aqigilik	T1606	100.4	45.0	9.0	0.1204	0.5116	5.87E-06	1038	-11.0
Strathcona	T1606	14	30.5	6.0	0.1188	0.5116	5.87E-06	1040	-9.0
Strathcona	T1605	4.2	28.4	6.1	0.1295	0.5119	5.87E-06	1040	-5.7
Athole Point	SW1602	121.95	9.5	2.8	0.1810	0.5126	4.49E-06	1045	0.4
Victor Bay	MB1501	107.3	33.0	3.8	0.0692	0.5115	5.87E-06	1046	-4.3
Victor Bay	MB1501	85.9	58.2	3.3	0.0345	0.5114	5.87E-06	1046	-2.0
Victor Bay	MB1501	77.8	16.2	2.9	0.1098	0.5115	5.87E-06	1046	-10.5
Victor Bay	MB1501	52.1	43.7	5.3	0.0733	0.5113	5.87E-06	1046	-9.0
Victor Bay	MB1501	51.7	28.3	5.0	0.1065	0.5113	5.87E-06	1046	-13.9
Victor Bay	G1431	36.8	25.3	5.5	0.1310	0.5116	5.87E-06	1046	-10.7
Victor Bay	G1431	10	28.2	5.2	0.1107	0.5114	5.87E-06	1046	-13.5
Angmaat	M1406	177.1	21.7	1.9	0.0518	0.5117	5.87E-06	1047	-18.2
Angmaat	M1406	48.6	19.0	3.3	0.1034	0.5112	5.86E-06	1047	-15.9
Iqqittuq	T1409	267.5	40.3	7.5	0.1122	0.5112	5.86E-06	1047	-17.1
Iqqittuq	T1409	174	33.6	6.1	0.1105	0.5113	5.87E-06	1047	-15.2
Iqqittuq	T1409	22	36.3	6.5	0.1081	0.5112	5.86E-06	1047	-17.0
Iqqittuq	T1409	13.5	27.3	4.1	0.0903	0.5111	5.86E-06	1047	-15.6
Iqqittuq	T1409	7	31.8	5.6	0.1059	0.5112	5.87E-06	1047	-15.8
Iqqittuq	T1412	194.3	28.7	4.6	0.0961	0.5111	5.86E-06	1047	-15.9
Iqqittuq	T1412	153.7	91.1	21.8	0.1446	0.5116	5.87E-06	1047	-13.4
Iqqittuq	T1412	139	39.4	8.2	0.1261	0.5114	5.87E-06	1047	-15.0
Arctic Bay	T1413	342.6	20.5	3.4	0.0998	0.5112	5.87E-06	1048	-14.4
Arctic Bay	T1413	282.8	20.5	4.2	0.1228	0.5115	5.87E-06	1048	-12.9
Arctic Bay	T1413	226.5	25.1	4.7	0.1135	0.5114	5.87E-06	1048	-12.6
Arctic Bay	T1413	192.5	23.7	4.3	0.1090	0.5113	5.87E-06	1048	-14.6
Arctic Bay	T1413	154.7	16.4	2.9	0.1078	0.5113	5.87E-06	1048	-15.1
Arctic Bay	T1413	149.4	43.3	7.6	0.1057	0.5112	5.86E-06	1048	-16.4
Arctic Bay	T1413	129.7	53.4	10.2	0.1152	0.5113	5.87E-06	1048	-15.4
Arctic Bay	T1413	105.7	43.1	8.8	0.1230	0.5115	5.87E-06	1048	-12.7
Arctic Bay	T1413	90.6	35.2	6.1	0.1054	0.5113	5.87E-06	1048	-13.3
Arctic Bay	T1413	67.2	61.9	11.4	0.1118	0.5114	5.87E-06	1048	-12.1
Arctic Bay	MB1401	441.5	46.3	7.9	0.1031	0.5112	5.87E-06	1048	-14.9
Arctic Bay	MB1401	150	48.0	8.3	0.1048	0.5113	5.87E-06	1048	-13.9
Arctic Bay	MB1401	61.9	33.0	6.4	0.1177	0.5114	5.87E-06	1048	-14.2
Arctic Bay	MB1401	6.4	64.3	14.0	0.1321	0.5114	5.87E-06	1048	-15.8
Arctic Bay	PWC1405	636.5	35.1	6.1	0.1042	0.5112	5.87E-06	1048	-14.8
Arctic Bay	PWC1405	600.5	33.4	5.3	0.0964	0.5112	5.87E-06	1048	-14.5
Arctic Bay	PWC1405	388	56.4	11.9	0.1278	0.5116	5.87E-06	1048	-11.6
Arctic Bay	PWC1405	257.5	41.9	7.3	0.1051	0.5114	5.87E-06	1048	-11.3
Arctic Bay	PWC1405	74	48.5	8.1	0.1006	0.5113	5.87E-06	1048	-12.8
Arctic Bay	PWC1405	23.1	46.7	7.8	0.1014	0.5113	5.87E-06	1048	-13.4
Arctic Bay	T1412	126.5	46.8	8.3	0.1070	0.5112	5.87E-06	1048	-16.1
Nauyat	R1607	116.4	11.2	2.9	0.1572	0.5120	3.07E-06	1276	-5.6

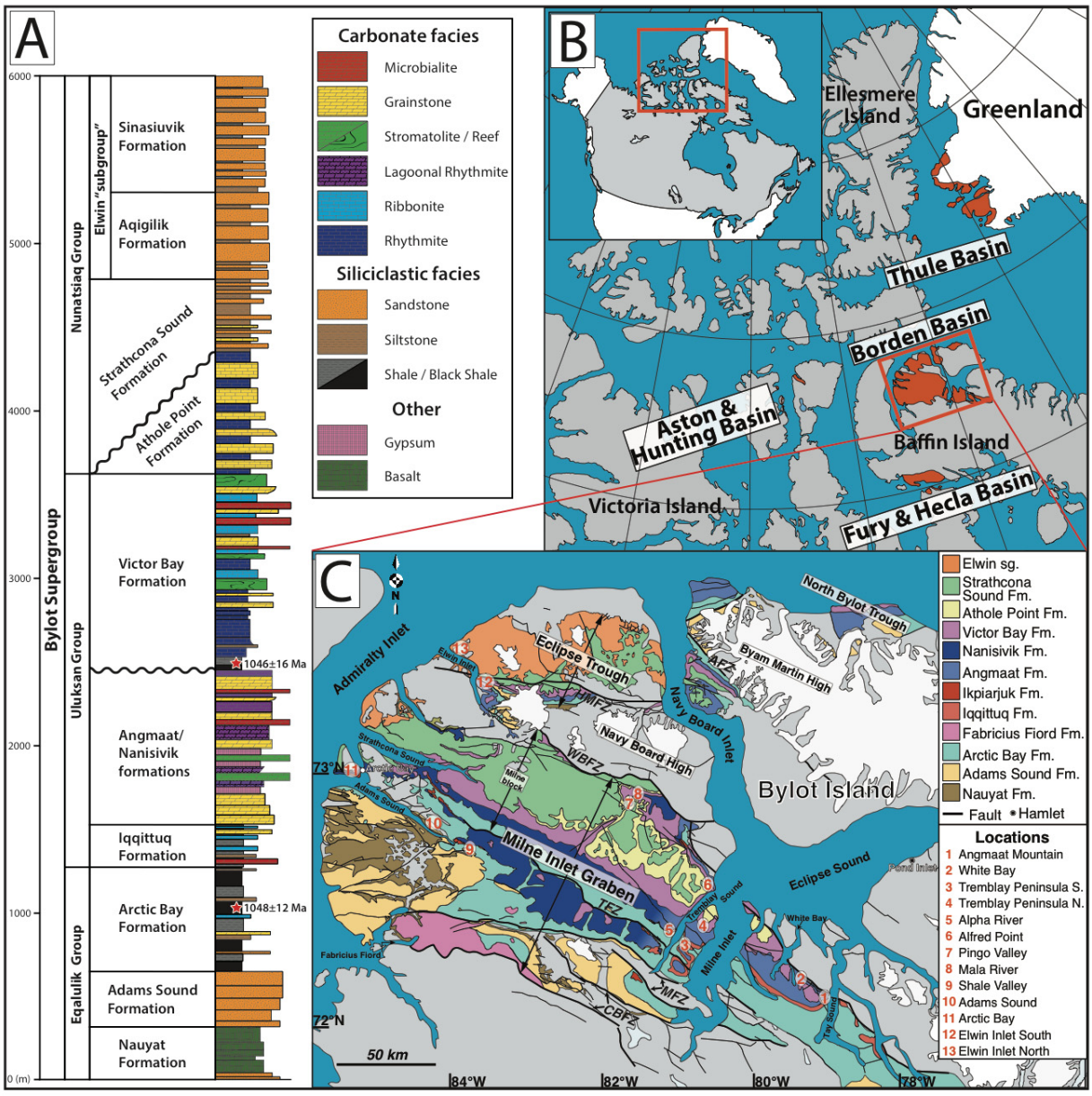

Figure 1: Location and geological context of the study area. (A) Schematic stratigraphy of the Bylot Supergroup in the Borden Basin. (B) Location of the Bylot basins in Arctic Canada and eastern Greenland. Re-Os ages from Gibson et al. (2018). (C) Geological map showing the Bylot Supergroup in the Borden Basin (adapted from Scott and deKemp, 1998 and Turner et al., 2009) showing sample locations. Abbreviations for structural features: CBFZ—Central Borden Fault Zone; MFZ—Magda Fault Zone; TFZ—Tikirarjuaq Fault Zone; WBFZ—White Bay Fault Zone; HMFZ—Hartz Mountain Fault Zone; AFZ—Actineq Fault Zone.

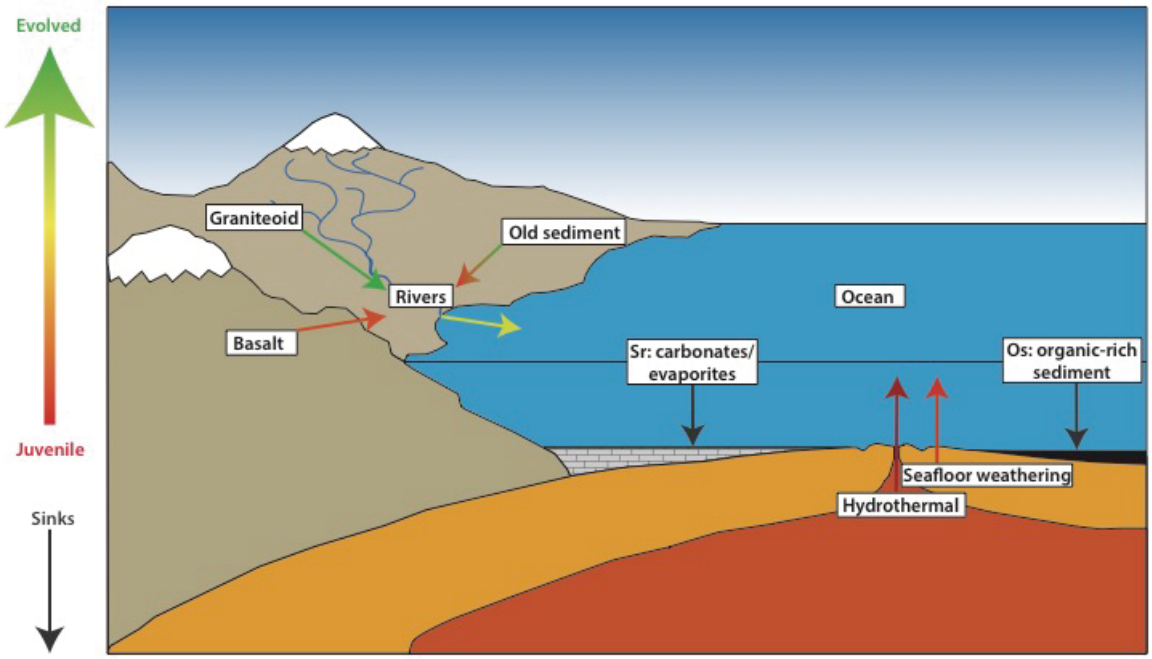

Figure 2: Schematic model of marine $^{87}Sr/^{86}Sr$ and $^{187}Os/^{188}Os$ systematics.

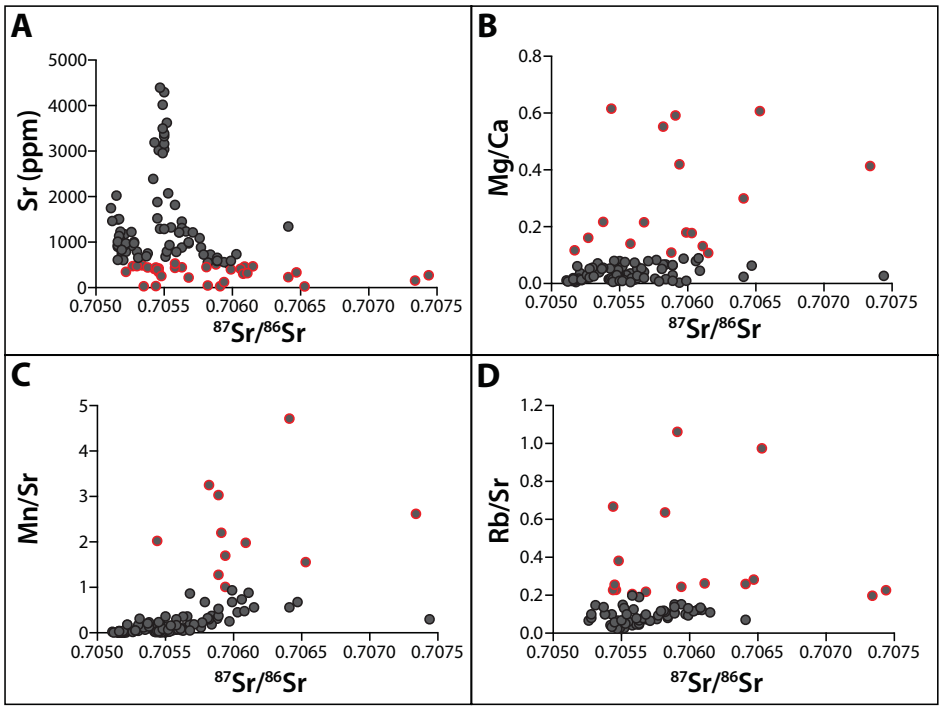

Figure 3: Geochemical data from limestone samples used to screen for post-depositional alteration. Samples outlined in red show geochemical evidence for post-depositional alteration are excluded from this study. (A) $^{87}Sr/^{86}Sr$ versus Sr concentration (ppm). (B) $^{87}Sr/^{86}Sr$ versus Mg/Ca ratios (ppm/ppm). (C) $^{87}Sr/^{86}Sr$ versus Mn/Sr ratios (ppm/ppm). (D) $^{87}Sr/^{86}Sr$ versus Rb/Sr ratios (ppm/ppm).

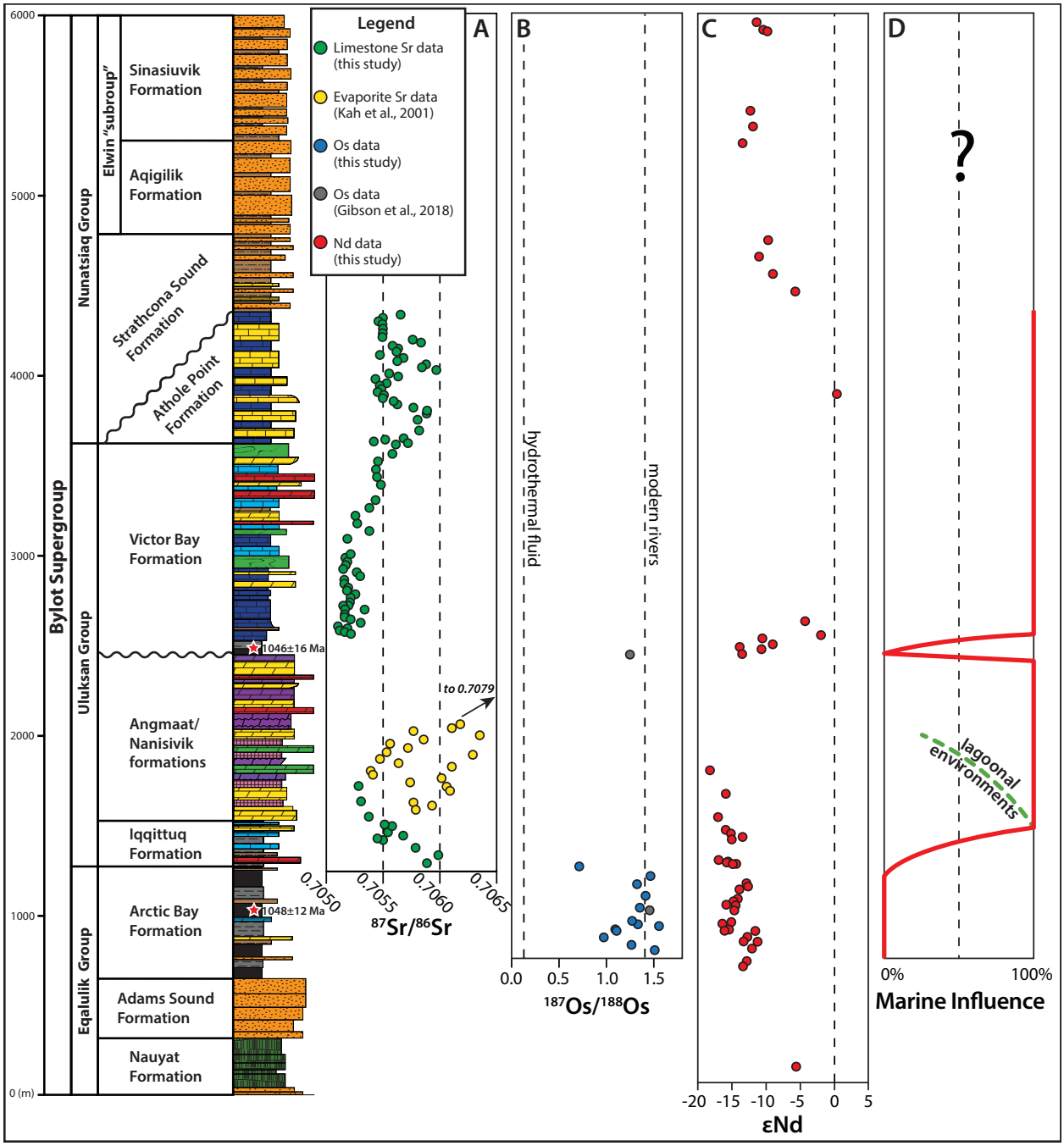

Figure 4: Isotopic data plotted along a schematic diagram of the Bylot Supergroup stratigraphy. (A) Filtered $^{87}Sr/^{86}Sr$ compositions of limestone (green; this study) and evaporite samples (yellow; Kah et al., 2001). (B) Initial $^{187}Os/^{188}Os$ (Os_i) composition of black shale calculated from a depositional age of 1048 Ma. Gray circles are Os_i of Re-Os isochrons from Gibson et al. (2018). Hydrothermal input and modern riverine values from Peucker-Ehrenbrink and Ravizza (2000). (C) Initial $^{143}Nd/^{144}Nd$ (εNd_i) composition of mudstone samples from this study. (D) Degree of marine influence in the Borden Basin as interpreted from radiogenic chemostratigraphic data.

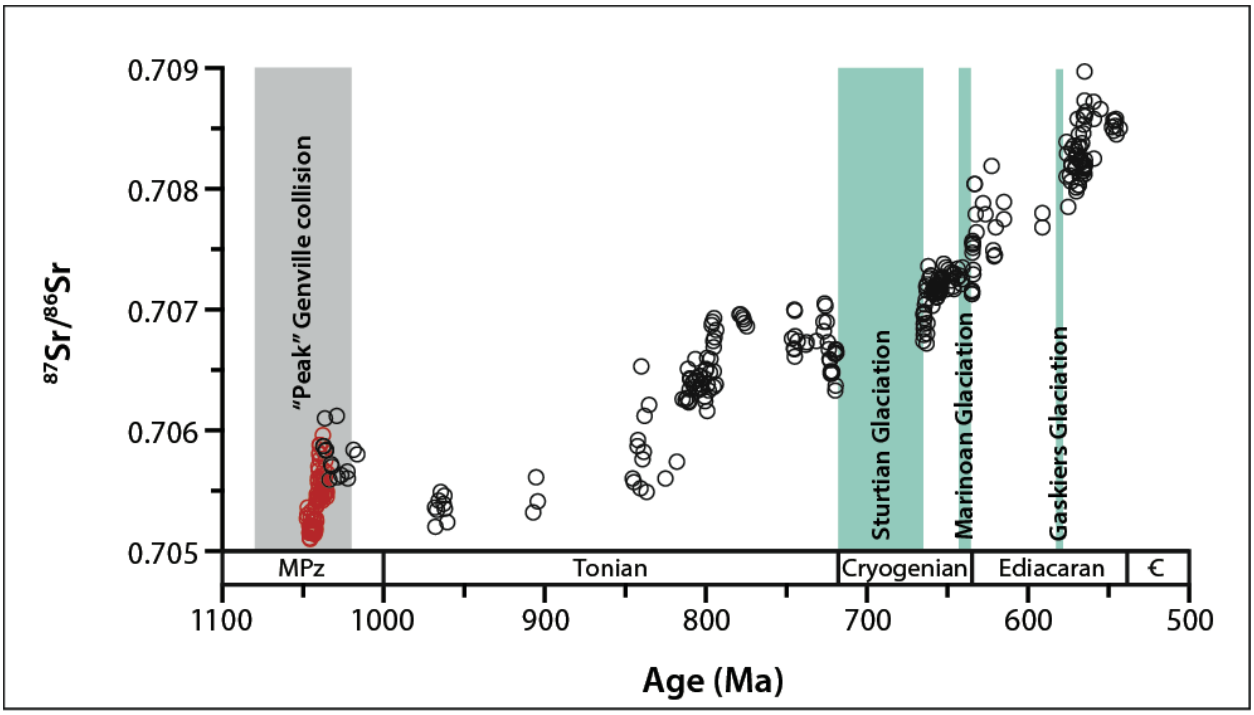

Figure 5: Updated global seawater $^{87}Sr/^{86}Sr$ curve from 1100 to 500 Ma. Age-calibrated $^{87}Sr/^{86}Sr$ composition of marine limestone samples from the Bylot Supergroup are plotted in red (this study) on the global seawater curve of Cox et al. (2016), which is compiled from references therein. Timing of "Peak" Grenville collision from Hynes and Rivers (2010).

References

Azmy, K., Kendall, B. S., Creaser, R. A., Heaman, L. M., and de Oliviera, T. F., 2008, Global correlation of the Vazante Group, São Francisco Basin, Brazil: Re–Os and U–Pb radiometric age constraints: Precambrian Research, v. 164, p. 160-172.

Banner, J. L., 2004, Radiogenic isotopes: systematics and applications to earth surface processes and chemical stratigraphy: Earth Science Reviews, v. 65, p. 1-54.

Banner, J. L., and Hanson, G. N., 1990, Calculation of simultaneous isotopic and trace element variations during water-rock interaction with applications to carbonate diagenesis: Geochimica et Cosmochimica Acta, v. 54, p. 3123-3137.

Bartley, J. K., Semikhatov, M. A., Kaufman, A. J., Knoll, A. H., Pope, M. C., and Jacobsen, S. B., 2001, Global events across the Mesoproterozoic–Neoproterozoic boundary: C and Sr isotopic evidence from Siberia: Precambrian Research, v. 111, p. 165-202.

Blank, C. E., 2013, Origin and early evolution of photosynthetic eukaryotes in freshwater environments: Reinterpreting Proterozoic paleobiology and biogeochemical processes in light of trait evolution: Journal of Phycology, v. 49, p. 1040-1055.

Butterfield, N. J., 2000, Bangiomorpha pubescens n. Gen., n. sp.: Implications for the evolution of sex, multicellularity, and the Mesoproterozoic/ Neoproterozoic Radiation of Eukaryotes: Paleobiology, v. 26, p. 386-404.

Butterfield, N. J., Knoll, A. H., and Swett, K., 1990, A Bangiophyte Red Alga from the Proterozoic of Arctic Canada: Science, v. 250, p. 104-107.

Cohen, P. A., Strauss, J. V., Rooney, A. D., Sharma, M., and Tosca, N., 2017, Controlled hydroxyapatite biomineralization in an 810 million-year-old unicellular eukaryote: Science Advances, v. 3, p. e1700095.

Cox, G. M., Halverson, G. P., Stevenson, R. K., Vokaty, M., Poirier, A., Kunzmann, M., Li, Z.-X., Denyszyn, S. W., Strauss, J. V., and Macdonald, F. A., 2016, Continental flood basalt weathering as a trigger for Neoproterozoic Snowball Earth: Earth and Planetary Science Letters, v. 446, p. 89-99.

Cox, G.M., Jarrett, A., Edwards, D., Crockford, P.W., Halverson, G.P., Collins, A.S., Poirier, A., and Li, Z-X., 2016, Basin redox and primary productivity within the Mesoproterozoic Roper Seaway: Chemical Geology, v. 440, p. 101-114.

Creaser, R., and Stasiuk, L., 2007, Depositional age of the Douglas Formation, northern Saskatchewan, determined by Re-Os geochronology: Bulletin-Geological Survey of Canada, v. 588, p. 341.

Creaser, R. A., Papanastassiou, D. A., and Wasserburg, G. J., 1991, Negative thermal ion mass spectrometry of osmium, rhenium, and iridium: Geochimica et Cosmochimica Acta, v. 55, p. 397-401.

Creaser, R. A., Sannigrahi, P., Chacko, T., and Selby, D., 2002, Further evaluation of the Re-Os geochronometer in organic-rich sedimentary rocks: A test of hydrocarbon maturation effects on the Exshaw Formation, Western Canada Sedimentary Basin: Geochimica et Cosmochimica Acta, v. 66, p. 3441-3452.

Crocker, C. H., Collerson, K. D., Lewry, J. F., and Bickford, M. E., 1993, Sm-Nd, U-Pb, and Rb-Sr geochronology and lithostructural relationships in the southwestern Rae province:

constraints on crustal assembly in the western Canadian shield: Precambrian Research, v. 61, p. 27-50.

Cumming, V. M., Poulton, S. W., Rooney, A. D., and Selby, D., 2013, Anoxia in the terrestrial environment during the late Mesoproterozoic: Geology, v. 41, p. 583-586.

Cumming, V. M., Selby, D., and Lillis, P. G., 2012, Re-Os geochronology of the lacustrine Green River Formation: Insights into direct depositional dating of lacustrine successions, Re-Os systematics and paleocontinental weathering: Earth and Planetary Science Letters, v. 359-360, p. 194-205.

Day, J. M. D., Pearson, D. G., and Hulbert, L. J., 2008, Rhenium-osmium isotope and platinum-group element constraints on the origin and evolution of the 1.27 Ga Muskox layered intrusion: Journal of Petrology, v. 49, p. 1255-1295.

Dixon, O. A., Williams, S. R., and Dixon, J., 1971, The Aston Formation (? Proterozoic) on Prince of Wales Island, Arctic Canada: Canadian Journal of Earth Sciences, v. 8, p. 1-11.

Dostal, J., Jackson, G. D., and Galley, A., 1989, Geochemistry of Neohelikian Nauyat plateau basalts, Borden rift basin, northwestern Baffin Island, Canada: Canadian Journal of Earth Sciences, v. 26, p. 2214-2223.

Edwards, C. T., Saltzman, M. R., Leslie, S. A., Bergstrom, S. M., Sedlacek, A. R. C., Howard, A., Bauer, J. A., Sweet, W. C., and Young, S. A., 2015, Strontium isotope (Sr-87/Sr-86) stratigraphy of Ordovician bulk carbonate: Implications for preservation of primary seawater values: Geological Society of America Bulletin, v. 127, p. 1275-1289.

Evans, D. A. D., 2009, The palaeomagnetically viable, long-lived and all-inclusive Rodinia supercontinent reconstruction: Geological Society, London, Special Publications, v. 327, p. 371-404.

Fahrig, W. F., Christie, K. W., and Jones, D. J., 1981, Paleomagnetism of the Bylot Basins: Evidence for Mackenzie Continental Tensional Tectonics: Geological Survey of Canada Contribution, v. 81-10, p. 303-312.

Geboy, N. J., Kaufman, A. J., Walker, R. J., Misi, A., de Oliviera, T. F., Miller, K. E., Azmy, K., Kendall, B. S., and Poulton, S. W., 2013, Re–Os age constraints and new observations of Proterozoic glacial deposits in the Vazante Group, Brazil: Precambrian Research, v. 238, p. 199-213.

Geldsetzer, H., 1973, The tectono-sedimentary development of an algal-dominated Helikian succession on northern Baffin Island, N.W.T., *in* Proceedings Symposium on the Geology of the Canadian Arctic, University of Saskatchewan 1973, Volume 19, Canadian Society of Petroleum Geologists, p. 99-126.

Gibson, T. M., Shih, P. M., Cumming, V. M., Fischer, W. W., Crockford, P. W., Hodgskiss, M. S. W., Wörndle, S., Creaser, R. A., Rainbird, R. H., Skulski, T. H., and Halverson, G. P., 2018, Precise age of *Bangiomorpha pubescens* dates the origin of eukaryotic photosynthesis: Geology, v. 46, p. 135-138.

Gibson, T. M., Wörndle, S., Halverson, G. P., Agić, H., Lamothe, K. G., Rainbird, R. H., and Skulski, T. H., 2017, Composite Stratigraphic section of exceptionally exposed middle Bylot Supergroup carbonate rocks along Tremblay Sound, northwestern Baffin Island, Nunavut: Canada-Nunavut Geoscience Office Summary of Activities, p. 81-91.

Gilleaudeau, G. J., and Kah, L. C., 2013a, Carbon isotope records in a Mesoproterozoic epicratonic sea: Carbon cycling in a low-oxygen world: Precambrian Research, v. 228, p. 85-101.

Gilleaudeau, G. J., and Kah, L. C., 2013b, Oceanic molybdenum drawdown by epeiric sea expansion in the Mesoproterozoic: Chemical Geology, v. 356, p. 21-37.

Gilleaudeau, G. J., and Kah, L. C., 2015, Heterogeneous redox conditions and a shallow chemocline in the Mesoproterozoic ocean: Evidence from carbon-sulfur-iron relationships: Precambrian Research, v. 257, p. 94-108.

Goddéris, Y., Le Hir, G., Macouin, M., Donnadieu, Y., Hubert-Théou, L., Dera, G., Aretz, M., Fluteau, F., Li, Z.-X., and Halverson, G. P., 2017, Paleogeographic forcing of the strontium isotopic cycle in the Neoproterozoic: Gondwana Research, v. 42, p. 151-162.

Goldstein, S. L., Onions, R. K., and Hamilton, P. J., 1984, A Sm-Nd Isotopic Study of Atmospheric Dusts and Particulates from Major River Systems: Earth and Planetary Science Letters, v. 70, p. 221-236.

Hahn, K. E., Turner, E. C., Babechuk, M. G., and Kamber, B. S., 2015, Deep-water seep-related carbonate mounds in a Mesoproterozoic alkaline lake, Borden Basin (Nunavut, Canada): Precambrian Research, v. 271, p. 173-197.

Heaman, L. M., LeCheminant, A. N., and Rainbird, R. H., 1992, Nature and timing of Franklin igneous events, Canada: Implications for a Late Proterozoic mantle plume and the break-up of Laurentia: Earth and Planetary Science Letters, v. 109, p. 117-131.

Hoffman, P. F., 1989, Precambrian geology and tectonic history of North America *in* Bally, A. W., and Palmer, A. R., eds., The geology of North America - an overview: Boulder, Co, Geological Society of America, p. 21.

Hofmann, H. J., and Jackson, G. D., 1991, Shelf-facies microfossils from the Uluksan Group (Proterozoic Bylot Supergroup), Baffin Island, Canada: Journal of Paleontology, v. 65, p. 361-382.

Hofmann, H. J., and Jackson, G. D., 1994, Shale-Facies Microfossils from the Proterozoic Bylot Supergroup, Baffin Island, Canada: The Paleontological Society, v. 68, p. 1-35.

Hynes, A., and Rivers, T., 2010, Protracted continental collision—Evidence from the Grenville orogen: Canadian Journal of Earth Sciences, v. 47, p. 591-620.

Jackson, G. D., and Iannelli, T. R., 1981, Rift-related cyclic sedimentation in the Neohelikian Borden Basin, northern Baffin Island: Proterozoic Basins of Canada, v. 81-10, p. 269-302.

Jacobsen, S., and Wasserburg, G., 1984, Sm-Nd isotopic evolution of chondrites and achondrites, II: Earth and Planetary Science Letters, v. 67, p. 137-150.

Jochum, K. P., Willbold, M., Raczek, I., Stoll, B., and Herwig, K., 2005, Chemical characterisation of the USGS reference glasses GSA-1G, GSC-1G, GSD-1G, GSE-1G, BCR-2G, BHVO-2G and BIR-1G using EPMA, ID-TIMS, ID-ICP-MS and LA-ICP-MS: Geostandards and Geoanalytical Research, v. 29, p. 285-302.

Kah, L. C., 2000, Depositional $\delta^{18}O$ signatures in Proterozoic dolostones: constraints on seawater chemistry and early diagenesis: SEPM Special Publication, p. 1-17.

Kah, L. C., Bartley, J. K., and Teal, D. A., 2012, Chemostratigraphy of the Late Mesoproterozoic Atar Group, Taoudeni Basin, Mauritania: Muted isotopic variability, facies correlation, and global isotopic trends: Precambrian Research, v. 200-203, p. 82-103.

Kah, L. C., and Knoll, A. H., 1996, Microbenthic distribution of Proterozoic tidal flats: Environmental and taphonomic considerations: Geology, v. 24, p. 79-82.

Kah, L. C., Lyons, T. W., and Chesley, J. T., 2001, Geochemistry of a 1.2 Ga carbonate-evaporite succession, northern Baffin and Bylot Islands: implications for Mesoproterozoic marine evolution: Precambrian Research, v. 111, p. 203-234.

Kah, L. C., and Riding, R., 2007, Mesoproterozoic carbon dioxide levels inferred from calcified cyanobacteria: Geology, v. 35, p. 799-802.

Kah, L. C., Sherman, A. G., Narbonne, G. M., Knoll, A. H., and Kaufman, A. J., 1999, $\delta^{13}C$ stratigraphy of the Proterozoic Bylot Supergroup, Baffin Island, Canada: implications for regional lithostratigraphic correlations: Canadian Journal of Earth Sciences, v. 36, p. 313-332.

Kendall, B. S., Creaser, R. A., Gordon, G. W., and Anbar, A. D., 2009a, Re–Os and Mo isotope systematics of black shales from the Middle Proterozoic Velkerri and Wollogorang Formations, McArthur Basin, northern Australia: Geochimica et Cosmochimica Acta, v. 73, p. 2534-2558.

Kendall, B. S., Creaser, R. A., Ross, G. M., and Selby, D., 2004, Constraints on the timing of Marinoan "Snowball Earth" glaciation by 187Re–187Os dating of a Neoproterozoic, post-glacial black shale in Western Canada: Earth and Planetary Science Letters, v. 222, p. 729-740.

Kendall, B. S., Creaser, R. A., and Selby, D., 2009b, ^{187}Re-^{187}Os geochronology of Precambrian organic-rich sedimentary rocks: Geological Society, London, Special Publications, v. 326, p. 85-107.

Knoll, A. H., Worndle, S., and Kah, L. C., 2013, Covariance of microfossil assemblages and microbialite textures across an upper Mesoproterozoic carbonate platform: *Palaios*, v. 28, p. 453-470.

LeCheminant, A. N., and Heaman, L. M., 1989, Mackenzie igneous events, Canada: Middle Proterozoic hotspot magmatism associated with ocean opening: Earth and Planetary Science Letters, v. 96, p. 1-11.

Lecuyer, C., 2016, Seawater residence times of some elements of geochemical interest and the salinity of the oceans: Bulletin De La Societe Geologique De France, v. 187, p. 245-259.

Long, D. G. F., and Turner, E. C., 2012, Tectonic, sedimentary and metallogenic re-evaluation of basal strata in the Mesoproterozoic Bylot basins, Nunavut, Canada: Are unconformity-type uranium concentrations a realistic expectation?: Precambrian Research, v. 214-215, p. 192-209.

Macdonald, F.A., Karabinos, P.M., Crowley, J.L., Hodgin, E.B., Crockford, P.W. and Delano, J.W., 2017, Bridging the gap between the foreland and hinterland II: Geochronology and tectonic setting of Ordovician magmatism and basin formation on the Laurentian margin of New England and Newfoundland: American Journal of Science, v. 317, p.555-596.

Manning-Berg, A. R., and Kah, L. C., 2017, Proterozoic microbial mats and their constraints on environments of silicification: Geobiology, v. 15, p. 469-483.

Martin, C. E., Peucker-Ehrenbrink, B., Brunskill, G. J., and Szymczak, R., 2000, Sources and sinks of unradiogenic osmium runoff from Papua New Guinea: Earth and Planetary Science Letters, v. 183, p. 261-274.

Narbonne, G. M., and James, N. P., 1996, Mesoproterozoic deep-water reefs from Borden Peninsula, Arctic Canada, v. 43, p. 827-848.

Parnell, J., Spinks, S., Andrews, S., Thayalan, W., and Bowden, S., 2015, High Molybdenum availability for evolution in a Mesoproterozoic lacustrine environment: Nature Communications, v. 6, p.6996.

Pehrsson, S. J., and Buchan, K. L., 1999, Borden dykes of Baffin Island, Northwest Territories: a Franklin U-Pb baddeleyite age and paleomagnetic reinterpretation: Canadian Journal of Earth Sciences, v. 36, p. 1-9.

Peucker-Ehrenbrink, B., and Ravizza, G., 2000, The marine osmium isotope record: Terra Nova, v. 12, p. 205-219.

Poirier, A., 2006, Re-Os and Pb isotope systematics in reduced fjord sediments from Saanich Inlet (Western Canada): Earth and Planetary Science Letters, v. 249, p. 119-131.

Poirier, A., and Hillaire-Marcel, C., 2011, Improved Os-isotope stratigraphy of the Arctic Ocean: Geophysical Research Letters, v. 38, L467.

Ponce-Toledo, R. I., Deschamps, P., Lopez-Garcia, P., Zivanovic, Y., Benzerara, K., and Moreira, D., 2017, An Early-Branching Freshwater Cyanobacterium at the Origin of Plastids: Current Biology, v. 27, p. 386-391.

Ravizza, G., and Turekian, K. K., 1992, The osmium isotopic composition of organic-rich marine sediments: Earth and Planetary Science Letters, v. 110, p. 1-6.

Ravizza, G., Turekian, K. K., and Hay, B. J., 1991, The Geochemistry of Rhenium and Osmium in Recent Sediments from the Black-Sea: Geochimica et Cosmochimica Acta, v. 55, p. 3741-3752.

Rooney, A. D., Austermann, J., Smith, E. F., Li, Y., Selby, D., Dehler, C. M., Schmitz, M. D., Karlstrom, K. E., and Macdonald, F. A., 2017, Coupled Re-Os and U-Pb geochronology of the Tonian Chuar Group, Grand Canyon: Geological Society of America Bulletin, *in press.*

Rooney, A. D., Macdonald, F. A., Strauss, J. V., Dudás, F. Ö., Hallman, C., and Selby, D., 2014, Re-Os geochronology and coupled Os-Sr isotope constraints on the Sturtian snowball Earth: Proceedings of the National Academy of Sciences, v. 111, p. 51-56.

Rooney, A. D., Selby, D., Houzay, J.-P., and Renne, P. R., 2010, Re–Os geochronology of a Mesoproterozoic sedimentary succession, Taoudeni basin, Mauritania: Implications for basin-wide correlations and Re–Os organic-rich sediments systematics: Earth and Planetary Science Letters, v. 289, p. 486-496.

Sánchez-Baracaldo, P., Raven, J. A., Pisani, D., and Knoll, A. H., 2017, Early photosynthetic eukaryotes inhabited low-salinity habitats: Proceedings of the National Academy of Sciences, v. 7, p. 201620089-201620089.

Selby, D., and Creaser, R. A., 2003, Re–Os geochronology of organic rich sediments: an evaluation of organic matter analysis methods: Chemical Geology, v. 200, p. 225-240.

Semikhatov, M., Kuznetsov, A., Gorokhov, I., Konstantinova, G., Melnikov, N., Podkovyrov, V., and Kutyavin, E., 2002, Low $^{87}Sr/^{86}Sr$ ratios in seawater of the Grenville and post-Grenville time: determining factors: Stratigraphy and Geological Correlation, v. 10, p. 1-41.

Sherman, A. G., James, N. P., and Narbonne, G. M., 2002, Evidence for reversal of basin polarity during carbonate ramp development in the Mesoproterozoic Borden Basin, Baffin Island: Canadian Journal of Earth Sciences, v. 39, p. 519-538.

Sherman, A. G., Narbonne, G. M., and James, N. P., 2001, Anatomy of a cyclically packaged Mesoproterozoic carbonate ramp in northern Canada, p. 1-29.

Sherman, A. G., Sherman, James, N. P., and Narbonne, G. M., 2000, Sedimentology of a late Mesoproterozoic muddy carbonate ramp, northern Baffin Island, arctic Canada: SEPM Special Publication, p. 1-20.

Smoliar, M. I., Walker, R. J., and Morgan, J. W., 1996, Re-Os ages of group IIA, IIIA, IVA, and IVB iron meteorites: Science, v. 271, p. 1099-1102.

Sperling, E. A., Rooney, A. D., Hays, L., Sergeev, V. N., Vorob'eva, N. G., Sergeeva, N. D., Selby, D., Johnston, D. T., and Knoll, A. H., 2014, Redox heterogeneity of subsurface waters in the Mesoproterozoic ocean: Geobiology, v. 12, p. 373-386.

Stewart, A., and Parker, A., 1979, Palaeosalinity and environmental interpretation of red beds from the late Precambrian (‘Torridonian’) of Scotland: Sedimentary Geology, v. 22, p. 229-241.

Stewart, A. D., The later Proterozoic Torridonian rocks of Scotland: their sedimentology, geochemistry and origin, 2002, Geological Society of London.

Stewart, B. W., and DePaolo, D. J., 1996, Isotopic Studies of Processes in Mafic Magma Chambers: III. the Muskox Intrusion, Northwest Territories, Canada, Earth Processes: Reading the Isotopic Code, American Geophysical Union, v. 104, p. 277-292.

Strauss, J. V., Rooney, A. D., Macdonald, F. A., Brandon, A., and Knoll, A. H., 2014, 740 Ma vase-shaped microfossils from Yukon, Canada: Implications for Neoproterozoic chronology and biostratigraphy: Geology, v. 42, p. 659.

Strother, P. K., Battison, L., Brasier, M. D., and Wellman, C. H., 2011, Earth's earliest non-marine eukaryotes: Nature, v. 473, p. 505-509.

Stüeken, E. E., Bellefroid, E. J., Prave, A. R., Asael, D., Planavsky, N. J., and Lyons, T. W., 2017, Not so non-marine? Revisiting the Stoer Group and the Mesoproterozoic biosphere: Geochemical Perspectives Letters, v. 3, p. 221-229.

Tanaka, T., Togashi, S., Kamioka, H., Amakawa, H., Kagami, H., Hamamoto, T., Yuhara, M., Orihashi, Y., Yoneda, S., Shimizu, H., Kunimaru, T., Takahashi, K., Yanagi, T., Nakano, T., Fujimaki, H., Shinjo, R., Asahara, Y., Tanimizu, M., and Dragusanu, C., 2000, JNdi-1: a neodymium isotopic reference in consistency with LaJolla neodymium: Chemical Geology, v. 168, p. 279-281.

Taylor, S. R., and McLennan, S. M., 1995, The Geochemical Evolution of the Continental-Crust: Reviews of Geophysics, v. 33, p. 241-265.

Tripathy, G. R., and Singh, S. K., 2015, Re–Os depositional age for black shales from the Kaimur Group, Upper Vindhyan, India: Chemical Geology, v. 413, p. 63-72.

Turner, E. C., 2009, Mesoproterozoic carbonate systems in the Borden Basin, Nunavut: Canadian Journal of Earth Sciences, v. 46, p. 915-938.

Turner, E. C., 2011, Structural and stratigraphic controls on carbonate-hosted base metal mineralization in the Mesoproterozoic Borden Basin (Nanisivik District), Nunavut: Economic Geology, v. 106, p. 1197-1223.

Turner, E. C., and Kamber, B. S., 2012, Arctic Bay Formation, Borden Basin, Nunavut (Canada): Basin evolution, black shale, and dissolved metal systematics in the Mesoproterozoic ocean: Precambrian Research, v. 208-211, p. 1-18.

Turner, E. C., Long, D. G. F., Rainbird, R. H., Petrus, J. A., and Rayner, N. M., 2016, Late Mesoproterozoic rifting in Arctic Canada during Rodinia assembly: impactogens, trans-continental far-field stress and zinc mineralisation: Terra Nova, v. 28, p. 188-194.

van Acken, D., Thomson, D., Rainbird, R. H., and Creaser, R. A., 2013, Constraining the depositional history of the Neoproterozoic Shaler Supergroup, Amundsen Basin, NW Canada: Rhenium-osmium dating of black shales from the Wynniatt and Boot Inlet Formations: Precambrian Research, v. 236, p. 124-131.

Veizer, J., 1989, Strontium isotopes in seawater through time: Annual Review in Earth Planetary Sciences, v. 17, p. 141-167.

Xu, W. M., Ruhl, M., Jenkyns, H. C., Hesselbo, S. P., Riding, J. B., Selby, D., Naafs, B. D. A., Weijers, J. H., Pancost, R. D., Tegelaar, E., and Idiz, E. F., 2017, Carbon sequestration in an expanded lake system during the Toarcian oceanic anoxic event: Nature Geoscience, v. 10, p. 129-134.

7. Appendix

Supplemental Table

Table A1: Limestone elemental abundance data used to screen samples for diagenetic alteration. $^{87}Sr/^{86}Sr$ data in **bold** are deemed unaltered and included in the Bylot Supergroup compilation in Figure 4.

Sample	Fm.	Ca (ppm)	Fe (ppm)	Mg (ppm)	Mn (ppm)	Rb (ppm)	Sr (ppm)	Mg/Ca	Mn/Sr	Rb/Sr	$^{87}Sr/^{86}Sr^*$	2σ
T1509-605.2	AP	259545	2293	6267	1099	60	233	0.024	4.715	0.259	0.70641	0.087
T1509-468	AP	304203	5201	9116	1940	70	640	0.030	3.031	0.110	0.70589	0.024
T1509-443.5	AP	247594	4749	11075	923	57	466	0.045	1.982	0.122	0.70609	0.024
T1509-423	AP	349763	2001	5878	131	81	1091	0.017	0.120	0.074	**0.70576**	0.018
T1509-404.2	AP	232635	1195	3808	249	54	670	0.016	0.372	0.080	**0.70584**	0.034
T1509-292.5	AP	322054	1618	11486	125	74	1820	0.036	0.069	0.041	**0.70558**	0.017
T1509-289	AP	281380	2598	16508	174	65	1454	0.059	0.119	0.045	**0.70563**	0.016
T1509-285.5	AP	220891	2887	23805	263	51	467	0.108	0.562	0.109	0.70615	0.022
T1509-242.9	AP	242385	10971	3296	77	56	1213	0.014	0.064	0.046	**0.70561**	0.059
T1509-234	AP	368054	273	3244	31	85	1295	0.009	0.024	0.066	**0.70547**	0.017
T1509-232.2	AP	307443	2546	12529	186	71	973	0.041	0.191	0.073	**0.70568**	0.017
T1509-214.5	AP	287912	1859	14772	99	66	1310	0.051	0.076	0.051	**0.70563**	0.016
T1509-210	AP	238165	3609	26060	158	55	511	0.109	0.309	0.108	**0.70588**	0.026
T1509-202.5	AP	279621	2974	18630	134	65	725	0.067	0.185	0.089	**0.70584**	0.019
T1509-180	AP	231790	2836	20378	135	53	533	0.088	0.253	0.100	**0.70597**	0.028
T1509-170	AP	345143	1049	10278	66	80	1322	0.030	0.050	0.060	**0.70555**	0.024
T1509-165.8	AP	253110	796	4889	42	59	882	0.019	0.047	0.067	**0.70563**	0.028
T1509-159.8	AP	266560	2458	17873	164	62	550	0.067	0.298	0.112	**0.70582**	0.024
T1509-155.1	AP	265591	2412	17027	217	61	585	0.064	0.371	0.104	**0.70589**	0.024

T1509-147.1	AP	161587	3367	29039	270	37	400	0.180	0.675	0.093	0.70599	0.015
T1509-133.7	AP	235165	1799	12142	146	54	454	0.052	0.321	0.119	**0.70581**	0.041
T1509-123	AP	221325	3596	17376	304	51	414	0.079	0.734	0.123	0.70606	0.050
T1509-115.8	AP	257344	3519	23155	226	59	388	0.090	0.581	0.153	-	
T1509-84.3	AP	131723	6999	54581	407	31	156	0.414	2.618	0.197	0.70734	0.062
T1509-76.8	AP	76756	3891	39253	271	17	65	0.511	4.195	0.270	-	
T1509-47.7	AP	113323	7103	56765	510	26	66	0.501	7.754	0.398	-	
T1509-14.2	AP	120561	6323	41902	286	28	84	0.348	3.417	0.330	-	
T1509-3.4	AP	211185	3666	45572	194	49	224	0.216	0.865	0.218	**0.70568**	0.022
R1609-192	AP	388820	5728	20417	444	98	1235	0.053	0.360	0.079	**0.70566**	0.022
R1609-186	AP	376051	19146	112730	753	94	1344	0.300	0.560	0.070	0.70641	0.027
R1609-183	AP	395813	2974	13311	168	99	3038	0.034	0.055	0.033	**0.70550**	0.024
R1609-182	AP	399230	1631	5721	44	100	3020	0.014	0.015	0.033	**0.70546**	0.028
R1609-176	AP	407549	1441	5979	53	103	3162	0.015	0.017	0.032	**0.70550**	0.026
R1609-175	AP	377765	1589	9017	71	95	4293	0.024	0.017	0.022	**0.70550**	0.021
R1609-174	AP	392343	1120	6675	43	99	3328	0.017	0.013	0.030	**0.70550**	0.040
R1609-171	AP	403156	1207	6444	44	101	2957	0.016	0.015	0.034	**0.70549**	0.030
R1609-167	AP	376617	2786	16746	100	95	4019	0.044	0.025	0.024	**0.70549**	0.021
SW1601-199.6	AP	402495	267	4304	24	101	1881	0.011	0.013	0.054	**0.70545**	0.031
SW1601-195.4	AP	404335	434	5978	96	101	682	0.015	0.141	0.149	**0.70551**	0.014
SW1601-192.6	AP	472002	3485	37388	119	118	3384	0.079	0.035	0.035	**0.70550**	0.021
SW1601-187.3	AP	391199	964	7428	63	98	786	0.019	0.081	0.125	**0.70559**	0.024
SW1601-170.8	AP	338383	2754	9630	159	85	447	0.028	0.356	0.190	**0.70563**	0.029
SW1601-168.2	AP	330160	3772	27551	203	83	886	0.083	0.229	0.093	**0.70577**	0.020
SW1601-160.1	AP	337982	6973	60194	332	84	735	0.178	0.451	0.115	0.70603	0.019
SW1601-149.4	AP	395208	6152	25847	347	99	658	0.065	0.527	0.151	**0.70589**	0.030
SW1602-130.5	AP	413503	601	6366	44	104	3191	0.015	0.014	0.033	**0.70543**	0.033
SW1602-128.7	AP	413528	1786	5560	53	104	2071	0.013	0.025	0.050	**0.70553**	0.026
SW1602-126	AP	403614	1064	8195	41	101	4392	0.020	0.009	0.023	**0.70547**	0.028
SW1602-125.6	AP	393900	1913	18805	84	99	3497	0.048	0.024	0.028	**0.70549**	0.020
SW1602-6.4	AP	380428	2700	22330	88	96	3622	0.059	0.024	0.026	**0.70552**	0.019
SW1602-5.8	AP	401812	974	6080	58	101	2388	0.015	0.024	0.042	**0.70542**	0.033
SW1602-3.2	AP	315119	6708	24786	224	79	1215	0.079	0.184	0.065	**0.70571**	0.021
SW1602-0.4	AP	377770	3214	27859	109	95	1213	0.074	0.090	0.078	**0.70561**	0.022
SW1603-111.6	VB	359513	1914	50198	129	90	434	0.140	0.296	0.207	**0.70558**	0.024
SW1603-105.2	VB	227477	260	129031	30	57	67	0.567	0.443	0.853	-	
SW1603-102.1	VB	386423	152	5859	15	97	424	0.015	0.034	0.228	**0.70546**	0.086
SW1603-92.5	VB	402831	177	7961	16	101	443	0.020	0.035	0.227	**0.70544**	0.024
SW1603-89.3	VB	404520	139	6415	14	101	397	0.016	0.035	0.255	**0.70545**	0.026
SW1603-85.3	VB	230795	314	127861	116	58	65	0.554	1.773	0.883	-	
SW1603-81.6	VB	228490	344	124446	54	57	71	0.545	0.755	0.804	-	
SW1603-74.8	VB	392124	360	11632	22	98	258	0.030	0.084	0.381	**0.70548**	0.035
SW1603-68.2	VB	247430	6972	147697	370	62	127	0.597	2.905	0.485	-	
SW1603-2.6	VB	229723	560	126681	187	57	79	0.551	2.367	0.726	-	
SW1603-1.3	VB	230790	261	127423	70	58	84	0.552	0.829	0.688	-	
T1508-197.3	VB	191865	1205	65058	136	44	255	0.339	0.534	0.174	-	
T1508-193	VB	175715	285	9376	40	41	411	0.053	0.098	0.099	**0.70543**	0.043
T1508-187.1	VB	291913	1062	38744	120	67	143	0.133	0.836	0.470	-	
T1508-179.1	VB	327661	931	18236	106	76	752	0.056	0.141	0.102	**0.70538**	0.015
T1508-171.5	VB	180044	1512	15994	145	41	306	0.089	0.475	0.134	0.70608	0.028
T1508-154.5	VB	161819	1227	13236	192	37	198	0.082	0.969	0.187	-	
T1508-150.1	VB	266565	581	7221	81	62	272	0.027	0.298	0.226	0.70744	0.075
T1508-144.5	VB	376977	154	3296	20	88	659	0.009	0.030	0.133	-	
T1508-139.2	VB	275517	895	42887	32	64	423	0.156	0.075	0.151	-	
T1508-135.6	VB	347171	241	10246	25	80	1221	0.030	0.020	0.066	**0.70526**	0.018
T1508-130.4	VB	181286	888	107891	43	44	27	0.595	1.614	1.629	-	
T1508-129	VB	182994	825	108410	38	44	27	0.592	1.400	1.607	-	

T1508-120.8	VB	103175	968	63590	72	24	36	0.616	2.022	0.667	0.70544	0.096
T1508-117.8	VB	183929	847	110216	54	45	43	0.599	1.258	1.040	-	
T1508-98.9	VB	167463	1432	102290	81	40	33	0.611	2.442	1.221	-	
T1508-97.2	VB	146016	1189	86385	70	34	32	0.592	2.202	1.061	0.70591	0.086
T1508-94.2	VB	157652	1566	88576	97	38	64	0.562	1.521	0.596	-	
T1508-73.7	VB	159892	1963	93836	99	38	50	0.587	1.982	0.773	-	
T1508-72	VB	154697	1170	95301	84	37	41	0.616	2.042	0.902	-	
T1508-66.8	VB	156141	1900	82827	89	37	79	0.530	1.134	0.475	-	
T1508-63.5	VB	336535	400	17625	47	81	1002	0.052	0.046	0.080	**0.70528**	0.018
T1508-59.2	VB	182427	1551	68408	135	44	119	0.375	1.134	0.367	-	
T1508-51.5	VB	127589	1848	53606	122	30	121	0.420	1.010	0.244	0.70594	0.126
T1508-47.8	VB	187473	1138	40716	102	44	443	0.217	0.231	0.099	**0.70538**	0.048
T1508-45.5	VB	178559	2345	100613	91	43	32	0.563	2.838	1.335	-	
T1508-43.5	VB	161925	1565	96378	66	39	44	0.595	1.520	0.891	-	
T1508-38.8	VB	166220	1138	98092	50	40	46	0.590	1.080	0.870	-	
T1508-36.5	VB	164609	904	102416	60	40	37	0.622	1.611	1.063	-	
T1508-29.7	VB	151346	1410	91208	120	36	43	0.603	2.797	0.842	-	
T1508-25.8	VB	126614	1290	69947	150	29	46	0.552	3.250	0.636	0.70582	0.108
T1508-9	VB	161323	1219	100042	82	39	45	0.620	1.795	0.850	-	
T1508-4.8	VB	123728	1156	75095	46	29	29	0.607	1.556	0.974	0.70653	0.181
T1507-429	VB	135342	168	82527	44	-	32	0.610	1.384	-	-	
T1507-425.5	VB	143959	69	87251	36	-	41	0.606	0.885	-	-	
T1507-421.4	VB	152770	109	92054	40	-	42	0.603	0.935	-	-	
T1507-415.1	VB	124903	220	76646	73	-	34	0.614	2.114	-	-	
T1507-414.2	VB	155856	201	95196	43	-	31	0.611	1.377	-	-	
T1507-409.8	VB	155018	150	92989	33	-	44	0.600	0.767	-	-	
T1507-405.5	VB	14863	12	8959	3	-	4	0.603	0.893	-	-	
T1507-402.9	VB	146450	103	88243	28	-	52	0.603	0.534	-	-	
T1507-399.5	VB	157618	53	93630	19	-	52	0.594	0.371	-	-	
T1507-395.1	VB	157950	329	94835	53	-	58	0.600	0.913	-	-	
T1507-386.1	VB	146363	84	88535	30	-	45	0.605	0.676	-	-	
T1507-379.8	VB	143787	113	88778	37	-	30	0.617	1.226	-	-	
T1507-378.2	VB	119325	61	73224	17	-	33	0.614	0.513	-	-	
T1507-376	VB	144606	68	87990	18	-	30	0.608	0.590	-	-	
T1507-376	VB	147535	49	89290	12	-	36	0.605	0.341	-	-	
T1507-373.2	VB	133181	52	81332	14	-	33	0.611	0.415	-	-	
T1507-371.2	VB	122197	187	73883	57	-	45	0.605	1.260	-	-	
T1507-367.2	VB	109858	47	66527	13	-	33	0.606	0.408	-	-	
T1507-364.3	VB	122994	57	73724	18	-	43	0.599	0.423	-	-	
T1507-356.5	VB	131906	68	81768	32	-	34	0.620	0.953	-	-	
T1507-355	VB	152443	89	92023	25	-	45	0.604	0.560	-	-	
T1507-352.2	VB	117666	35	70906	16	-	36	0.603	0.450	-	-	
T1507-348.7	VB	131761	59	80247	23	-	38	0.609	0.615	-	-	
T1507-347.2	VB	139751	54	85045	24	-	49	0.609	0.484	-	-	
T1507-343.9	VB	127918	109	78056	34	-	34	0.610	1.000	-	-	
T1507-342	VB	136767	59	84310	29	-	39	0.616	0.749	-	-	
T1507-290	VB	362936	55	6235	8	-	1061	0.017	0.008	-	**0.70519**	0.033
T1507-286.5	VB	344479	57	11307	9	-	1173	0.033	0.008	-	**0.70521**	0.023
T1507-285	VB	144784	51	87916	17	-	42	0.607	0.394	-	-	
T1507-279.6	VB	115698	195	70490	79	-	46	0.609	1.723	-	-	
T1507-278.1	VB	142658	274	86601	86	-	51	0.607	1.674	-	-	
T1507-273.8	VB	122114	150	74411	69	-	38	0.609	1.840	-	-	
T1507-271.3	VB	132279	117	80159	39	-	51	0.606	0.761	-	-	
T1507-269.3	VB	132791	133	80717	32	-	36	0.608	0.882	-	-	
T1507-265.5	VB	235651	199	42545	27	-	318	0.181	0.085	-	-	
T1507-200.2	VB	124522	147	75336	71	-	46	0.605	1.556	-	-	
T1507-197.2	VB	104709	191	64211	84	-	39	0.613	2.143	-	-	

T1507-187.2	VB	129017	77	78352	31	-	42	0.607	0.739	-	-	
T1507-182.1	VB	125019	94	76269	42	-	44	0.610	0.946	-	-	
T1507-177	VB	124045	134	77229	66	-	29	0.623	2.250	-	-	
T1507-171	VB	123308	96	75899	52	-	36	0.616	1.416	-	-	
T1507-166.3	VB	120012	97	74515	42	-	34	0.621	1.222	-	-	
T1507-163.1	VB	127102	102	78216	50	-	36	0.615	1.407	-	-	
T1507-160.1	VB	130897	83	81415	46	-	37	0.622	1.245	-	-	
T1507-157.1	VB	107505	268	66598	97	-	29	0.619	3.380	-	-	
T1507-136	VB	119809	426	74247	165	-	37	0.620	4.525	-	-	
T1507-131	VB	122011	177	76006	75	-	35	0.623	2.172	-	-	
T1507-126.2	VB	127227	159	77856	67	-	32	0.612	2.122	-	-	
T1507-123.1	VB	276212	96	32371	10	-	932	0.117	0.010	-	**0.70517**	0.036
T1507-113.8	VB	350880	93	4939	11	-	701	0.014	0.015	-	**0.70519**	0.051
T1507-110.2	VB	345518	0	1568	5	-	1233	0.005	0.004	-	**0.70518**	0.023
T1507-107.1	VB	341894	8	2943	5	-	2024	0.009	0.003	-	**0.70515**	0.019
T1507-105.7	VB	225966	378	36380	24	-	471	0.161	0.050	-	**0.70527**	0.029
T1507-103.8	VB	294189	257	15684	34	-	793	0.053	0.043	-	**0.70530**	0.030
T1507-102.5	VB	26185	20	1050	2	-	31	0.040	0.067	-	0.70535	0.036
T1507-101	VB	322194	447	5989	55	-	1497	0.019	0.037	-	**0.70516**	0.018
T1507-100.6	VB	331130	48	4527	10	-	898	0.014	0.011	-	**0.70516**	0.030
T1507-97	VB	359050	36	4879	17	-	783	0.014	0.022	-	**0.70519**	0.029
T1507-93.5	VB	348950	57	5071	11	-	1048	0.015	0.010	-	**0.70518**	0.024
T1507-90.5	VB	345042	140	6755	27	-	918	0.020	0.030	-	**0.70526**	0.022
T1507-89.1	VB	336918	105	8011	36	-	791	0.024	0.046	-	**0.70522**	0.023
T1507-87.7	VB	308191	245	11486	41	-	930	0.037	0.044	-	**0.70521**	0.037
T1507-74.6	VB	324113	162	5789	16	-	607	0.018	0.026	-	**0.70520**	0.043
T1507-72.6	VB	338743	70	6079	11	-	930	0.018	0.012	-	**0.70516**	0.027
T1507-54.9	VB	353556	76	3438	19	-	1134	0.010	0.017	-	**0.70517**	0.037
T1507-51.9	VB	248548	673	17603	59	-	488	0.071	0.120	-	**0.70534**	0.047
T1507-48.9	VB	333977	521	4929	51	-	1505	0.015	0.034	-	**0.70517**	0.029
T1507-47	VB	340388	295	5150	38	-	1012	0.015	0.038	-	**0.70516**	0.029
T1507-43.3	VB	341872	260	3997	166	-	975	0.012	0.171	-	**0.70522**	0.046
T1507-41.4	VB	290272	739	16301	81	-	471	0.056	0.173	-	**0.70530**	0.043
T1507-39.4	VB	238181	771	18980	79	-	344	0.080	0.228	-	0.70546	0.043
T1507-33.5	VB	112989	1274	51135	59	-	98	0.453	0.599	-	-	
T1507-31.3	VB	326742	40	3715	37	-	1749	0.011	0.021	-	**0.70511**	0.031
T1507-27.1	VB	133425	856	52964	54	-	115	0.397	0.468	-	-	
T1507-24.5	VB	127339	60	78425	34	-	30	0.616	1.123	-	-	
T1507-24.1	VB	304974	252	18540	33	-	831	0.061	0.040	-	**0.70519**	0.027
T1507-21.4	VB	362087	40	2435	10	-	1463	0.007	0.007	-	**0.70512**	0.015
T1507-17.3	VB	356075	44	5167	20	-	612	0.015	0.033	-	**0.70516**	0.035
T1507-14.3	VB	323431	16	4578	63	-	348	0.014	0.180	-	**0.70522**	0.037
T1507-10.2	VB	182033	1648	43637	179	-	140	0.240	1.275	-	-	
T1507-7.6	VB	138198	5790	63059	638	-	82	0.456	7.816	-	-	
T1602-149.5	NA	224195	5498	127147	715	56	34	0.567	21.238	1.675	-	
T1602-147.2	NA	241983	4015	140434	613	61	37	0.580	16.394	1.636	-	
T1602-147	NA	229709	3813	128705	563	58	39	0.560	14.448	1.483	-	
T1602-119	NA	247309	17216	138895	951	62	56	0.562	17.092	1.118	-	
T1602-103	NA	223248	7555	121712	565	56	54	0.545	10.405	1.039	-	
T1602-92.8	NA	218398	6390	121643	583	55	40	0.557	14.702	1.384	-	
T1602-84.5	NA	222742	9367	117804	483	56	43	0.529	11.185	1.303	-	
T1602-75.3	NA	257211	11811	133457	419	65	89	0.519	4.690	0.727	-	
T1602-73.5	NA	249960	14877	127481	511	63	78	0.510	6.537	0.801	-	
T1602-72	NA	249049	9931	128711	362	62	67	0.517	5.379	0.927	-	
T1602-56	NA	214239	1245	120348	213	54	32	0.562	6.742	1.716	-	
T1602-54.5	NA	222321	1242	125285	212	56	35	0.564	6.126	1.619	-	
T1602-20.6	NA	383980	239	7886	53	97	978	0.021	0.054	0.099	**0.70528**	0.016

T1602-15	NA	239658	6196	126580	342	60	150	0.528	2.285	0.402	-	0.000
T1602-10	NA	380093	488	9857	203	96	655	0.026	0.310	0.147	**0.70531**	0.040
T1602-5	NA	373855	744	19415	144	94	690	0.052	0.208	0.137	**0.70537**	0.030
T1602-0	NA	210294	439	121213	299	53	39	0.576	7.648	1.360	-	
SW1605-40.6	IQ	241069	676	133953	129	61	63	0.556	2.062	0.967	-	
SW1605-36.9	IQ	240823	1032	133148	109	61	38	0.553	2.902	1.612	-	
SW1605-33.7	IQ	234602	2194	130585	178	59	34	0.557	5.217	1.727	-	
SW1605-30.7	IQ	239112	2570	133046	135	60	46	0.556	2.938	1.310	-	
SW1605-15.1	IQ	266508	45684	68590	1102	67	171	0.257	6.461	0.392	-	
SW1605-12.1	IQ	240257	48102	95928	1119	60	51	0.399	22.020	1.188	-	
SW1605-4.4	IQ	378941	7336	23974	227	95	335	0.063	0.678	0.283	0.70647	0.034
SW1605-2.1	IQ	415892	1406	3866	54	104	792	0.009	0.068	0.132	**0.70552**	0.017
SW1605-0.4	IQ	417220	746	2037	90	105	530	0.005	0.169	0.198	**0.70558**	0.022
SW1604-193.5	IQ	367057	4814	27976	152	92	936	0.076	0.162	0.099	**0.70554**	0.024
SW1604-186.3	IQ	332003	13298	43956	281	83	319	0.132	0.882	0.262	0.70611	0.036
SW1604-183.8	IQ	402310	5493	8531	344	101	338	0.021	1.018	0.300	-	
SW1604-112.3	IQ	386229	1707	7791	50	97	996	0.020	0.051	0.098	**0.70568**	0.026
SW1604-85.3	IQ	358884	2025	35339	225	90	290	0.098	0.775	0.311	-	
SW1604-47.8	IQ	257786	60518	102660	2466	65	175	0.398	14.088	0.370	-	
SW1604-39.6	IQ	231824	55012	83494	3627	58	96	0.360	37.763	0.608	-	
T1410-174	IQ	200392	12008	74988	2017	48	95	0.374	21.255	0.504	-	
T1410-170	IQ	356006	1359	1159	949	85	559	0.003	1.697	0.152	0.70594	0.020
T1410-138	IQ	364809	420	2235	356	87	1523	0.006	0.234	0.057	**0.70545**	0.022
T1410-136.7	IQ	364539	680	3614	463	87	1290	0.010	0.359	0.067	**0.70550**	0.021
T1410-116	IQ	354947	688	3000	493	84	728	0.008	0.676	0.116	**0.70579**	0.019
T1410-96.8	IQ	323548	1218	3121	549	77	588	0.010	0.934	0.131	**0.70599**	0.016
T1410-84	IQ	345641	1103	3558	758	82	594	0.010	1.276	0.138	**0.70589**	0.016
T1409-323	IQ	166488	8035	94573	499	39	59	0.568	8.406	0.660	-	
T1409-318	IQ	181713	6879	106136	420	43	53	0.584	7.986	0.811	-	
T1409-274.5	IQ	174245	31404	67866	1513	41	102	0.389	14.837	0.402	-	
T1409-246	IQ	175939	13527	82118	820	41	195	0.467	4.196	0.210	-	
T1409-116.5	IQ	150432	8387	85444	745	35	57	0.568	13.172	0.622	-	
T1409-63	IQ	150975	9828	82190	1284	35	67	0.544	19.238	0.528	-	
T1409-17	IQ	286714	2652	10581	2684	67	212	0.037	12.641	0.314	0.71248	0.055

Fm.—Formation; AP—Athole Point; VB—Victor Bay; NA—Nanisivik; IQ—Iqqittuq.

*$^{87}Sr/^{86}Sr$ data in **bold** are deemed unaltered and included in the Bylot Supergroup compilation in Figure 4.

Preface to Chapter 5:

This thesis has thus far focused on the Bylot Supergroup in the Borden Basin in order to characterize critical late Mesoproterozoic eukaryotic evolutionary environments. In previous chapters we establish the complex evolution of the Borden Basin throughout deposition of the Bylot Supergroup and relate its history to the Proterozoic global change. Whereas Earth's environment through the interval between ca. 1600 to 800 Ma was previously considered stagnant, our studies illuminate dynamic interactions between tectonics, ecology, biology, and geochemistry directly preceding the Mesoproterozoic-Neoproterozoic boundary. Perturbations to these systems may have disrupted biogeochemical cycles earlier than previously appreciated. For instance, widespread burial of extraordinarily organic-rich (up to 20% by weight) black shale of the Arctic Bay Formation would have effectively released a globally significant mass of oxygen into the atmosphere ca. 1050 Ma.

Exactly when oxic marine environments expanded in the late Proterozoic Eon remains contentious. However, many proxies suggest that continental shelves were at least episodically oxygenated by 800 Ma, coincidental with the emergence of numerous crown group eukaryotic clades (Cohen and Macdonald, 2015). The first of a series of dramatic Neoproterozoic negative carbon isotope excursions also occurred around this time (Halverson et al., 2007). Together, these phenomena, which are generally presumed to be linked, mark the end of what has colloquially been referred to as the 'boring billion.'

In the following chapter, we investigate shale intervals from the ca. 850 to 800 Ma Reefal assemblage in Yukon that were deposited during successive marine transgressions. While it was previously established that the surface waters of this basin were oxygenated (Sperling et al., 2013), the sequence stratigraphic context afforded by previous studies (Halverson et al., 2012, Macdonald et al., 2012) enabled a comprehensive investigation of various redox proxies in light of changing sea level. Much of our current state of knowledge concerning Earth's oxygenation history derives from iron-based proxies. Yet, fundamental aspects of the Precambrian biogeochemical cycles are poorly understood. This study explores the mechanisms that controlled the distribution of iron and other redox-sensitive proxies in a partially restricted rift basin with a strong redox gradient during relative sea level changes.

References

Cohen, P. A., and Macdonald, F. A., 2015, The Proterozoic Record of Eukaryotes: Paleobiology, v. 41, p. 610-632.

Halverson, G. P., Maloof, A. C., Schrag, D. P., Dudas, F. O., and Hurtgen, M., 2007, Stratigraphy and geochemistry of a ca 800 Ma negative carbon isotope interval in northeastern Svalbard: Chemical Geology, v. 237, p. 5-27.

Halverson, G. P., Macdonald, F. A., Strauss, J. V., Cox, G. M., and Hubert-Theou, L., 2012, Updated definition and correlation of the lower Fifteenmile Group in the central and eastern Ogilvie Mountains: Yukon Exploration and Geology, p. 1-16.

Macdonald, F. A., Halverson, G. P., Strauss, J. V., Smith, E. F., Cox, G., Sperling, E. A., and Roots, C. F., 2012, Early Neoproterozoic Basin Formation in Yukon, Canada: Implications for the make-up and break-up of Rodinia: Geoscience Canada, v. 39, p. 77-99.

Chapter 5

Redox boundary fluctuations kick-started a vigorous benthic particulate shuttle in the 811 Ma upper Fifteenmile Group, Yukon[1]

[1] This chapter will be submitted as: "Gibson, T.M., Kunzmann, M., Poirier, A., Schumann, D., Tosca, N.J., Redox boundary fluctuations kick-started a vigorous benthic particulate shuttle in the 811 Ma upper Fifteenmile Group, Yukon. To: *Geochimica et Cosmochimica Acta*.

Abstract

Despite iron and trace element proxies providing much of our insight into Earth's oxygenation history, the processes that controlled these proxies in Proterozoic sedimentary basins are not yet fully understood. Here, we present a multi-proxy study to investigate sedimentary iron cycling and redox sensitive element delivery directly preceding major perturbations to the global carbon cycle in the ca. 811 Ma Reefal assemblage in the upper Fifteenmile Group, Yukon, Canada. Coherent stratigraphic trends in bulk-rock iron isotope, iron speciation, and redox-sensitive element (RSE) abundance data across three shale intervals reflect complex interactions between relative sea-level change, hydrographic restriction, and redox fluctuations during high relative sea-level within a basin with a redox-stratified water column. Short-term chemical fluctuations superimposed on relative sea-level change produced variable redox conditions as the boundary between oxygenated waters and anoxic waters migrated across the seafloor. The strong redox gradient promoted dissimilatory iron reduction (DIR) within the sediment, which released isotopically light Fe(II) into the water column where it was rapidly oxidized to iron oxy(hydr)oxide species that both accumulated locally and shuttled downslope. Accumulation of abundant bio-available iron oxy(hydr)oxide in the vicinity of the redox boundary further stimulated DIR, lowering the sediment Fe_T/Al (rendering it Fe-depleted) and isotopically enriched in ^{56}Fe.

Drawdown during water-mass restriction depleted the S and various RSE reservoirs of the basin throughout deposition of most samples from this study; however, intermittent deep-water renewal replenished the basin's RSE reservoirs and ushered in ephemeral euxinic conditions that,

along with fluctuations of the redox boundary, enabled Mo to be adsorbed and co-shuttled along with abundant Fe and Mn oxy(hydr)oxide particles in the water column. This mechanism created extraordinary Mo (up to 726 ppm) and other RSE (Cr and Ni) enrichments. These enrichments were short-lived because Mo and S were quickly depleted from the restricted water column. Enhanced Mo delivery owing to Fe-Mn oxy(hydr)oxide shuttling, termed the "Mo-pump", has been identified in modern and Phanerozoic sedimentary environments. While multiple local factors are responsible for the unique efficiency of particulate shuttling in the Reefal assemblage, expansion of global RSE inventories due to the onset of early Neoproterozoic oxygenation may have also contributed to these extreme enrichments.

1. Introduction

The interim redox state of the global ocean between oxygenation events that bracket the Proterozoic Eon (2500–541 Ma) is poorly constrained beyond being predominantly ferruginous (anoxic and Fe(II)-rich) with punctuated and locally restricted periods of euxinia (anoxic and H_2S-rich; Canfield et al., 2008; Planavsky et al., 2011; Poulton and Canfield, 2011; Guilbaud et al., 2015; Sperling et al., 2015). As a bio-essential nutrient and geologically abundant element with multiple oxidation states, iron is intimately connected to Earth's oxygenation history through biogeochemical redox cycling. Consequently, current models for marine redox evolution rely heavily on iron-based sedimentary proxies, such as iron speciation, which can differentiate sediment deposited within oxic, euxinic, or ferruginous water columns (Raiswell and Canfield, 1998). Sedimentary iron isotope compositions also record marine redox cycling processes (Johnson et al., 2002; Johnson and Beard, 2005; Anbar and Rouxel, 2007), as well as secular global oxygenation (Rouxel et al., 2005; Anbar and Rouxel, 2007; Johnson et al., 2008b; Bekker et al., 2010; Planavsky et al., 2012a). A recent compilation of bulk-shale iron isotope and iron speciation data demonstrates a state-shift ca. 660 Ma (Kunzmann et al., 2017b) that corroborates evidence for changes in global iron cycling in the mid-Neoproterozoic (Fan et al., 2014; Zhang et al., 2015) potentially related to some degree of oxygenation of the ocean-atmosphere system. These studies confirm the utility of iron isotopes in conjunction with iron speciation in marine shale for interrogating ancient marine redox conditions but also highlight the necessity for detailed

investigations into the mechanisms that fueled Neoproterozoic iron cycling to improve future interpretations of this proxy.

Unlike the ca. 2460–2240 Ma Great Oxidation Event (GOE; Bekker et al., 2004), the timing and magnitude of late Proterozoic oxygenation remains vague. Following a spike to between ~0.1–1% PAL (present atmospheric levels) during the GOE (Farquhar et al., 2000; Pavlov and Kasting, 2004; Canfield, 2005; Rouxel et al., 2005; Holland, 2006; Gumsley et al., 2017) and subsequent decline ca. 2000–1800 Ma (Frei et al., 2009; Bekker and Holland, 2012; Planavsky et al., 2012b; Partin et al., 2013a; Scott et al., 2014), oxygen concentrations may have remained persistently low (<0.1 to 1% PAL) for up to a billion years (Planavsky et al., 2014; Cole et al., 2016). On the other hand, trace metal patterns in ca. 1400 Ma organic-rich strata have been interpreted to reflect at least a transient increase in oxygen to >4% PAL (Zhang et al., 2016a). However, this interpretation is contentious (Planavsky et al., 2016; Zhang et al., 2016b; Diamond et al., 2018) and chromium isotope fractionation preserved in marine authigenic sediment, thought to require >1% PAL, is not observed in carbonate rocks predating ca. 1100 Ma (Gilleaudeau et al., 2016) and in shale and ironstone predating ca. 800 Ma (Planavsky et al., 2014; Cole et al., 2016). Similarly, measurement of ca. 815 Ga gas inclusions in halite thought to be direct relicts of the Neoproterozoic atmosphere and interpreted to indicate a pO_2 content of 10.9% (i.e., ~50% PAL; Blamey et al., 2016) contradict most conceptual models for Proterozoic oxygenation, but the validity of these data and conclusions has been challenged (Yeung, 2017).

Global compilations of various sedimentary authigenic trace elements (e.g., Mo, U, Zn) display step-wise changes in the Neoproterozoic, which support expansion of deep marine oxygenated environments (Scott et al., 2008; Partin et al., 2013b; Liu et al., 2016). Although transient oxygenation of deep marine environments is recognized following both the Sturtian (ca. 650 Ma; Kunzmann et al., 2015; Zhang et al., 2015; Lau et al., 2017) and Marinoan (Sahoo et al., 2012; Kunzmann et al., 2015; Sahoo et al., 2016; ca. 635 Ma; Kunzmann et al., 2017a) Snowball glaciations, permanent oxygenation of the deep ocean may not have occurred until the terminal Ediacaran Period (Fike et al., 2006; Canfield et al., 2007; Scott et al., 2008), early Paleozoic Era (Sperling et al., 2015), or even middle Paleozoic Era (Dahl et al., 2010; Wallace et al., 2017).

Despite these discrepancies in the timing and pace of late Proterozoic oxygenation and long-lasting deep ocean ventilation, most evidence supports a scenario in which shallow marine environments have been oxygenated since at least ca. 800 Ma and deep marine environments

remained occasionally anoxic until at least 580 Ma (Canfield et al., 2007). Major eukaryotic diversification and perhaps emergent metazoan evolution took place in an ocean with a significant redox gradient and therefore heterogeneous distribution of aqueous iron and trace metal concentrations (Sperling et al., 2013; Knoll, 2014; Cohen and Macdonald, 2015). Thus, establishing the specific mechanisms controlling sedimentary iron and trace metal proxies is necessary to both accurately reconstruct Earth's secular redox evolution and to provide a more nuanced perspective into the environments in which these key evolutionary events took place. Furthermore, assessing how and to what extent modern oxidative weathering has affected these proxies (e.g., Ahm et al., 2017) is necessary to confidently interpret them in the context of ancient sedimentary or early diagenetic processes.

A previous study of the ca. 850 Ma upper Fifteenmile Group reconstructed paleo-redox conditions from seven stratigraphic sections across a ~30 km-long basin transect of the Fifteenmile basin in Yukon, Canada. Results revealed a stratified water column whereby largely ferruginous deep waters were overlain by sufficiently oxygenated shallow waters to support early metazoan metabolisms in shelf environments (>1% PAL; Sperling et al., 2013). The current study provides an investigation of high-resolution stratigraphic trends in iron and trace metal paleoredox proxies from shale intervals of the upper Fifteenmile Group to evaluate the role of relative sea-level fluctuations on sedimentary redox-sensitive element (RSE) enrichments and iron cycle systematics. Contrasting solubility trends (i.e., mobilization vs. sequestration) with respect to marine redox conditions between iron and trace metals enables cross-calibration between these proxies.

Here, we integrate sequence stratigraphic data with bulk-rock RSE concentrations, iron isotopes, iron speciation, and XRD data for 43 shale samples, supported by SEM-EDS element maps, spanning transgressive shale intervals. This work provides an in-depth assessment of the dynamics of this basin's redox structure and iron cycling just prior to major perturbations in global carbon cycling indicated by the ca. 810–790 Ma Bitter Springs carbon isotope stage (e.g., Halverson et al., 2005; Swanson-Hysell et al., 2015), eukaryotic diversification and emergence of the Metazoa (Berney and Pawlowski, 2006; Erwin et al., 2011; Parfrey et al., 2011; Dohrmann and Worheide, 2017). This study highlights various processes that have previously been ignored as mechanisms of redox cycling in Neoproterozoic sedimentary basins and demonstrates the importance of considering samples' sequence stratigraphic context and specific enrichment

pathways when interpreting various redox proxies. These insights provide a useful template from which to determine whether RSE enrichments record global or local processes.

2. Geological Setting

The lower Neoproterozoic (ca. 850–800 Ma) Fifteenmile Group was deposited within a tectonically-active series of sub-basins in response to crustal attenuation and thermal subsidence in northwest Laurentia, perhaps during the early stages of the breakup of Rodinia (Macdonald et al., 2012). These strata outcrop in three erosional inliers from central Yukon, Canada to eastern Alaska, USA and correlate with the Little Dal Group of the Mackenzie Mountains Supergroup in the Wernecke and Mackenzie Mountains to the east (Fig. 1; Macdonald and Roots, 2010). This study investigates the Fifteenmile Group in the Coal Creek inlier which lies within the central Ogilvie Mountains, Yukon. The Fifteenmile Group is separated into lower and upper subgroups which are further subdivided into four units (Macdonald et al., 2011; Halverson et al., 2012). The age of the lower Fifteenmile Group, comprising the Gibben and Chandindu formations (Halverson et al., 2012; Kunzmann et al., 2014), is younger than ca. 1000 Ma as constrained by detrital zircon U-Pb ages from the Hart River inlier (Rainbird et al., 1997). Laterally-variable, mixed siliciclastic and carbonate units of the basal Gibben formation unconformably overlie the < ca. 1380 Ma Pinguicula Group (Medig et al., 2012) and shoal upward into carbonate-dominated facies (Halverson et al., 2012; Macdonald et al., 2012). A prominent, mud-cracked exposure surface marks the contact with the Chandindu Formation, which contains numerous fine-grained siliciclastic and dolostone cycles with locally abundant bioherms (Kunzmann et al., 2014). Crustal extension and normal faulting through lower Fifteenmile Group deposition generated topographic relief and, at least locally, NNW-deepening (in present coordinates) basin geometry (Macdonald et al., 2012).

The contact with the upper Fifteenmile Group is marked by a ubiquitous flooding surface at the transition from heterolithic facies of the Chandindu Formation to thick shale and dolostone packages of the Reefal assemblage (Halverson et al., 2012; Kunzmann et al., 2014). The 500–1700 m-thick Reefal assemblage contains peritidal facies that grade distally into basinal shale, representing the NNW-progradation of reefs into a shale basin (Halverson et al., 2012). Thick platform to slope carbonate successions are interbedded with prominent black to gray shale and

siltstone intervals representing transgressive and highstand systems tract deposits (Halverson et al., 2012; Macdonald et al., 2012; Sperling et al., 2013). Primary magmatic zircon collected from an ash bed in the upper Reefal assemblage yields a U-Pb depositional age of 811.5 ± 0.1 Ma (Macdonald et al., 2010). Negative carbonate carbon isotope excursions directly above this ash bed in the upper Reefal assemblage record initiation of the globally synchronous Bitter Springs carbon isotope stage (Halverson et al., 2005; Halverson et al., 2007; Macdonald et al., 2012; Swanson-Hysell et al., 2015). Given the lack of any discernable depositional hiatus, the entire Reefal assemblage is likely younger than 850 Ma (Macdonald et al., 2010). The Fifteenmile Group culminates with the Craggy dolostone, which comprises massive, regionally extensive, silicified dolograinstone, coarse, intra-formational conglomerate, and floatstone with minor microbialite and low-relief stromatolite facies overlying the uppermost black shale unit of the Reefal assemblage (Macdonald and Roots, 2010; Macdonald et al., 2011). The Craggy dolostone records renewed extension in the Fifteenmile basin and establishment of isolated carbonate platforms adjacent to topographic lows that accumulated coarse carbonate debris from platform margins. The top of the Fifteenmile Group is variably truncated by the sub-Callison Lake Formation unconformity, above which a Re-Os age of 751.2 ± 5.1 Ma provides a minimum age for Fifteenmile Group (Rooney et al., 2015; Strauss et al., 2015).

3. Interpretive Framework

3.1. Iron Speciation

Sequential extraction methods provide an operational definition for various sedimentary iron pools based on their reactivity (Raiswell and Canfield, 1998; Poulton and Canfield, 2005). A highly-reactive pool (Fe_{HR}) is defined as iron in pyrite (Fe_{Py}) plus iron that is reactive to H_2S on early diagenetic timescales, which includes iron carbonates (Fe_{Carb}; such as siderite, ankerite, and ferrous dolomite), Fe(III)-oxy(hydr)oxides (Fe_{Ox}; mainly hematite, goethite, ferrihydrite, lepidocrosite) and magnetite (Fe_{Mag}). The remaining iron is considered biogeochemically unreactive (Fe_U) and consists mainly of sheet silicate minerals. Together, these pools comprise the total iron (Fe_T) within sedimentary rocks. In basins with an oxygenated water column, Fe_{HR}/Fe_T ratios of the sediment mimic that of the incoming detrital flux. Sediment deposited in modern oxic

environments have Fe_{HR}/Fe_T ratios between 0.06 and 0.38, with an average value of 0.26 (Raiswell and Canfield, 1998). Therefore, sediment with Fe_{HR}/Fe_T ratios > 0.38 are indicative of mobilization, transport, and scavenging of reactive iron, which are processes exclusive to redox cycling within an anoxic water column. Such enrichments are seen in elevated Fe_T relative to the siliciclastic input, typically characterized by approximately crustal Fe_T/Al ratios (~0.4–0.5), although the crustal baseline for a given basin varies depending on provenance (Lyons and Severmann, 2006; Raiswell et al., 2018).

Here we implement the conservative limit of Fe_{HR}/Fe_T ratios < 0.22 to identify samples deposited within an oxic water column (Poulton and Canfield, 2011). This value is based on the average ratio for "oxic" Phanerozoic samples (Poulton and Raiswell, 2002; 0.14 ± 0.08; 1σ; Canfield et al., 2007; Poulton and Canfield, 2011; Sperling et al., 2013), leaving the depositional redox conditions for samples with Fe_{HR}/Fe_T ratios between 0.22 and 0.38 ambiguous. Samples deemed "anoxic" can then be further distinguished by their Fe_{Py}/Fe_{HR} ratios. Those with Fe_{Py}/Fe_{HR} > 0.80 were deposited in euxinic waters, and those with Fe_{Py}/Fe_{HR} < 0.8 in ferruginous waters (Andersen and Raiswell, 2004; Lyons and Severmann, 2006; Lyons et al., 2009; Poulton and Canfield, 2011). Various sedimentary processes, such as sediment gravity flows, can influence iron speciation through rapid burial of detrital sediment, thereby precluding the requisite communication with the overlying water column to accumulate excess Fe_{HR}. Raiswell et al. (2018) and Slotznick et al. (2017) also highlight the importance of petrological examination for post-depositional Fe and S mobilization (e.g., pyrite weathering) or metamorphic modification (e.g., reactive pyrite altered unreactive pyrrhotite) in order to confirm iron speciation data represent valid, primary signals.

3.2. Redox-Sensitive Elements

The solubility of the trace metals uranium (U), vanadium (V), molybdenum (Mo), and chromium (Cr) varies according to their oxidation state and is therefore a function of the redox conditions of their environment (Emerson and Huested, 1991; Tribovillard et al., 2006). In general, the solubility of these redox-sensitive elements (RSEs) increases in oxidizing conditions and decreases in reducing conditions. Due to their relatively low crustal abundances, riverine fluxes of U, V, Mo, and Cr are also relatively small, so their enrichment in marine sediment is predominantly

controlled by seawater redox cycling. In fully oxygenated basins, the long residence times of these elements promote accumulation of their aqueous species within the water column, while the sediment remains unenriched. Conversely, RSEs are efficiently sequestered within sediment underlying anoxic bottom waters via diffusion and scavenging across the sediment-water interface, such that they may be depleted in anoxic basin waters (e.g., Algeo, 2004; Algeo and Lyons, 2006). Thus, authigenic enrichment of these elements requires both a substantial inventory within the water column (expansive oxic conditions) sourced by oxidative continental weathering and an effective mechanism for their removal (anoxic bottom waters), hence reflecting the proportion of oxidizing and reducing bottom water conditions within a given basin (or the global ocean for open marine settings; Emerson and Huested, 1991; Reinhard et al., 2013). These conditions are maximized in modern sub-oxic to anoxic environments that are connected to the global ocean, such as oxygen minimum zones (OMZs) or redox stratified basins (Brumsack, 2006), such as were common through much of the Proterozoic (Canfield et al., 2008; Johnston et al., 2010; Poulton et al., 2010; Sperling et al., 2013; Ader et al., 2014; Hardisty et al., 2014; Sperling et al., 2014; Gilleaudeau and Kah, 2015; Cox et al., 2016).

Molybdenum enrichments are specifically associated with euxinic environments, because H_2S or HS^- converts unreactive aqueous molybdate (MoO_4^{2-}) to particle-reactive thiomolybdate ($MoO_xS_{(4-x)}^{2-}$, x = 0 to 3) (Helz et al., 1996; Erickson and Helz, 2000; Zheng et al., 2000; Sundby et al., 2004; Vorlicek et al., 2004; Scott and Lyons, 2012). Although Mo enrichments require a critical activity of H_2S (>~11 μM), peaks in porewater Mo concentrations often to not correspond to peaks in H_2S (Sundby et al., 2004). Additional mechanisms are required to "fix" these enrichments permanently in the sedimentary record. In restricted (e.g., silled) basins, prolonged Mo burial is maximized in weakly sulfidic conditions and decreases with higher H_2S concentrations. This relationship is due to the "basin reservoir effect" whereby Mo is consistently depleted within strongly sulfidic basins (e.g., the Black Sea or Framvaren Fjord) because it is efficiently delivered to the sediment (Algeo and Lyons, 2006). Thus, Mo concentrations do not simply scale with dissolved H_2S concentrations, but rather H_2S may simply serve as "geochemical toggle" (Helz et al., 1996). Temporary enrichments can occur at a specific activation point, but other mechanisms are required to preserve exceptional sedimentary Mo accumulations. Recent work has highlighted the role of organic matter in Mo removal pathways and fixation in sediment (Dahl et al., 2017; Wagner et al., 2017).

Although specific sequestration mechanisms vary between U, V, Mo, and Cr, authigenic enrichments of these elements are maximized in organic-rich sediment underlying anoxic bottom waters (Emerson and Huested, 1991; Tribovillard et al., 2006). Additionally, changes in provenance can influence elemental abundances in the detrital flux of these elements, so concentrations are often normalized to either total organic carbon (TOC) or conservative elements, such as Ti or Al, to demonstrate authigenic enrichments relative to crustal abundances (e.g., Calvert and Pedersen, 1993; Algeo and Lyons, 2006). Although normalization presents certain drawbacks (Van der Weijden, 2002; Tribovillard et al., 2006; Cole et al., 2017), calculating authigenic enrichments or enrichment factors is useful for assessing relative enrichments between large numbers of samples (Algeo and Tribovillard, 2009; Scott et al., 2017).

3.3. Iron Isotopes in Marine Sediment

The iron isotopic budget of the global ocean is dictated by the isotopic composition of the fluxes of iron to the open ocean, its sinks, and the isotopic fractionation associated with those sinks. Iron from deep-sea hydrothermal vents has an isotopic composition (reported here as δ^{56}Fe relative to the IRMM-14 standard) between –0.9‰ and +0.1‰ (Severmann et al., 2004; Rouxel et al., 2008; Bennett et al., 2009; Klar et al., 2017). While continental crust has an average iron isotopic composition of +0.09±0.05‰ (Beard et al., 2003a; Dauphas and Rouxel, 2006; Anbar and Rouxel, 2007; Johnson et al., 2008b; Asael et al., 2013), dissolution during continental weathering results in riverine fluxes to the ocean that are fractionated to different degrees from crustal values (Fantle and DePaolo, 2004). Dissolved, suspended and colloidal iron in rivers has an isotopic composition between –1.0 to +0.3‰, with the majority between –0.1 to +0.3‰, closely approximating continental crust (Beard et al., 2003b; Bergquist and Boyle, 2006; Ingri et al., 2006). Although much of the iron delivered to the ocean by rivers is removed in nearshore environments and so does not reach the open ocean (Poulton and Raiswell, 2002; Raiswell, 2011b), the flux of dissolved riverine iron was likely greater in the early Precambrian under a reducing atmosphere (Yamaguchi et al., 2005; Johnson et al., 2008b) and may have been a more significant source to the deep ocean than at present.

Bioavailable nanoparticulate iron oxy(hydr)oxide sourced from rivers undergo vigorous redox cycling (and thus isotopic fractionation) in continental shelves, ultimately enabling export

to deeper-water, open marine environments via iron-shuttling (see section 2.2.5; Lyons and Severmann, 2006; Raiswell, 2011b). Iron within shelf sediment pore-waters, which can account for a large component of the iron delivered to distal settings (Elrod et al., 2008; Lohan and Bruland, 2008; Cullen et al., 2009; Dale et al., 2015), is typically isotopically light with compositions ranging from –3.5‰ to –0.5‰ (Bergquist and Boyle, 2006; Severmann et al., 2006; Staubwasser et al., 2006; Severmann et al., 2008; Homoky et al., 2009; Severmann et al., 2010; Tangalos et al., 2010; John et al., 2012; Chever et al., 2015). Icebergs and wind-blown dust also provide bioavailable iron oxy(hydr)oxide particulates to the ocean (Duce and Tindale, 1991; Fung et al., 2000; Raiswell, 2011a; Conway and John, 2014) with isotopic compositions near 0‰ (Beard et al., 2003b), though these sources are highly geographically and temporally variable (Zhu et al., 2000; Homoky et al., 2013).

3.4. Iron Isotope Fractionation

Sedimentary iron isotopes reflect fractionation from both biological (Beard et al., 1999; Beard et al., 2003a; Johnson et al., 2003; Johnson et al., 2004; Matthews et al., 2004; Johnson et al., 2008b) and abiotic (Bullen et al., 2001; Johnson et al., 2002; Beard et al., 2003b; Anderson et al., 2004; Wiesli et al., 2004) redox processes. If these redox chemical reactions do not proceed to completion (i.e., are not quantitative), then the reacted iron will be isotopically distinct from its precursor phase. Therefore, sedimentary iron isotopes may preserve information on the modes of iron cycling in their depositional environments (Johnson et al., 2008b). While theoretical, experimental and observational studies of iron isotopes in recent decades have elucidated many fractionation pathways and their corresponding fractionation factors, there is much overlap in the range of isotopic values resulting from each mechanism. Therefore, discriminating between specific fractionation processes from the sedimentary record poses significant challenges (Beard and Johnson, 2004). However, the "direction" of fractionation is generally consistent with the "direction" of oxidation state change regardless of whether fractionation is microbially or abiotically mediated. In both cases the heavier isotopes (^{56}Fe and ^{57}Fe) are preferentially oxidized and the light isotope (^{54}Fe) is preferentially reduced. Therefore, while it may not be possible to conclusively differentiate biological versus abiotic isotopic fingerprints, sedimentary iron isotopes provide a valuable record of redox cycling within depositional environments.

A particular challenge to interpreting sedimentary iron isotopes is determining whether fractionation occurred in the water column or in sediment pore-water during diagenesis. Importantly, water column fractionation processes are directly related to oceanic redox conditions while diagenetic processes reflect microbial processes that may be partially decoupled from the redox environment of the overlying water column (Kunzmann et al., 2017b). Discriminating between water column and diagenetic processes is essential to make informative interpretations using iron isotopes and can be realized utilizing pyrite morphology (Wilkin et al., 1996) and complementary geochemical data sets such as Fe_T/Al and iron speciation .

Dissimilatory iron reduction (DIR) of reactive particulate Fe(III) to aqueous Fe(II) is associated with a fractionation factor ($\Delta^{56}Fe_{Fe(II)—Fe(III)}$) of –3‰ in both microbially (Beard et al., 1999; Icopini et al., 2004; Crosby et al., 2005; Crosby et al., 2007) and abiotically mediated (Johnson et al., 2002; Welch et al., 2003; Anbar et al., 2005) reactions. Thus, fractionation associated with Fe(III) reduction produces an isotopically-depleted aqueous Fe(II) pool. The most abundant reactive iron-bearing minerals available for DIR are oxy(hydr)oxides. Depending on the proportion of Fe(III) that is reduced by DIR, the iron isotopic composition of the resulting aqueous Fe(II) is generally between 1‰ to 3‰ lower than the Fe(III) substrate (Dauphas et al., 2017), though modelling suggests that when all steps are accounted for (i.e., sorption, etc.) the net isotopic fractionation of the Fe_{HR} pool from diagenetic iron cycling is at most 1‰ (Kunzmann et al., 2017b).

Iron also undergoes isotopic fractionation when oxidized from Fe(II) to Fe(III), a process most-common in the water column (Chever et al., 2015) but that can be either biologically or abiotically mediated. Biological oxidation is associated with a fractionation factor ($\Delta^{56}Fe_{Fe(II)—Fe(III)}$) of ca. –1.5‰ (Croal et al., 2004) and abiotic oxidation an equilibrium fractionation factor of –3‰ (Bullen et al., 2001)—both result in an isotopically heavier Fe(III) product relative to the Fe(II) reactant. In this case, the isotopic composition of the Fe(III) produced is dictated both by the proportion and the initial composition of the Fe(II) that is oxidized. Because Fe(II) is rapidly oxidized to Fe(III) in oxygenated waters, aqueous Fe(II) in modern environments is limited to anoxic waters, such as in restricted basins, oxygen minimum zones (OMZs), and sediment pore-waters. Most of the Fe(II) in these environments is produced by DIR and is therefore isotopically light (Dauphas et al., 2017). Hydrothermal plumes also introduce Fe(II) to the ocean (Toner, 2009; Saito, 2013; Conway and John, 2014), and as stated above, hydrothermal activity likely sourced a

larger proportion of iron in the Proterozoic ocean than it does today. However, modern mid-ocean ridge hydrothermal fluids express a range in isotopic values between –0.8‰ to –0.1‰, though the mass-average is closer to –0.1‰ because the iron is generally leached from unfractionated basalts and neither high nor low temperature hydrothermal process impart large iron isotope fractionations (Beard et al., 2003b; Severmann et al., 2004; Johnson et al., 2008a; Rouxel et al., 2008; Klar et al., 2017). Finally, oxidation by photoferrotrophic bacteria is associated with an experimentally determined net fractionation factor ($\Delta^{56}Fe_{Fe(II)—Fe(III)}$) of ca. –1‰, from combined kinetic (binding of Fe(II) to organic ligands) and equilibrium (precipitation of Fe(III)) processes. Thus, the ~1‰ enrichment of the Fe(III) phase following photoferrotrophic oxidation is overwhelmed by the ~3‰ from abiotic Fe(II) oxidation and is therefore untraceable in the sedimentary record with iron isotopes alone (Balci et al., 2006; Swanner et al., 2015).

Finally, fractionation factors associated with the precipitation of many iron minerals have been identified. In most cases these involve equilibrium fractionation between aqueous Fe(II) species and precipitated (ppt) iron oxy(hydr)oxide ($\Delta^{56}Fe_{Fe(II)—Fe(III)ppt}$) and are –1.2‰ to –1‰ for goethite (FeO(OH); Beard et al., 2010; Frierdich et al., 2014a), –1.6‰ to –1.3‰ for magnetite (Fe3O4; Johnson et al., 2005; Frierdich et al., 2014b), and –3.2‰ for hematite (Fe_2O_3) (Skulan et al., 2002; Welch et al., 2003; Beard et al., 2010). While equilibrium fractionation from pyrite formation has yet to be determined experimentally, the fractionation between Fe(II) and mackinawite (FeS) is –0.32‰ (Guilbaud et al., 2010; Wu et al., 2012), and is likely small for pyrite. Conversely, the formation of iron carbonates, such as siderite ($FeCO_3$), produces isotopically-enriched minerals with an experimentally-determined fractionation factor of 0.48‰ (Wiesli et al., 2004); however, other experiments show no fractionation or up to 0.9‰ for Ca-substituted siderite (Johnson et al., 2005). In sum, sedimentary iron isotopes effectively track the "direction" of redox transformations during marine iron cycling. When used in conjunction with other proxies that help differentiate between water column versus diagenetic processes, these data can be used as a marine redox proxy.

3.5. Benthic Iron Shuttling

Hydrothermal activity was likely the primary source of iron to the Precambrian ocean (Isley, 1995; Bau et al., 1997; Krapez et al., 2003; Bekker et al., 2010), and lower oxygen levels

potentially enabled iron to accumulate to higher concentrations than in the modern ocean when SO_4^{2-} levels were low. Iron-based metabolisms emerged early in Earth's evolutionary history to utilize this abundant metabolite, and so microbial iron reduction and oxidation played a significant role in ancient marine iron cycling (Widdel et al., 1993; Konhauser et al., 2002; Kappler et al., 2005; Konhauser et al., 2005; Crowe et al., 2008; Fischer and Knoll, 2009). Consequently, benthic shuttling was central component of the Proterozoic iron cycle, especially in redox-stratified basins. This process operates by dissimilatory iron reduction within anoxic shelf sediment to produce aqueous Fe(II) or amorphous oxy(hydr)oxide, which are then transported, predominantly down-slope, and subsequently removed through the formation of various syngenetic phases, such as pyrite or iron oxy(hydr)oxide. Benthic iron shuttling has been observed in modern euxinic basins (e.g., Black Sea) and oxygen minimum zones (OMZ; e.g., Cariaco basin), by the mobilization of isotopically light, reactive iron from sediments underlying oxic to suboxic shelf settings to the water column and subsequent transported and removal in distal anoxic basin waters (Severmann et al., 2006; Severmann et al., 2008; Severmann et al., 2010; Scholz et al., 2014)

4. Materials and Methods

4.1. Samples

Black and gray shale to silty shale samples were excavated from the outcrop every ~50 cm across three shale intervals through the course of measuring and logging an almost entirely exposed stratigraphic section (M103) of the Chandindu Formation and Reefal assemblage in the Coal Creek inlier, Yukon, Canada (Fig. 1; N64°45'17.0", W139°32' 13.7"). Sampling targeted the finest-grained material, avoiding coarser-grained horizons, turbidite beds, and regions that show evidence for structural or hydrothermal alteration. This study presents new iron speciation, iron isotope, and major and trace elemental abundance data from 18 shale samples along with their stratigraphic context, as well as new major and trace elemental abundance and stratigraphic data from an additional 27 samples with previously published iron speciation, iron isotope, and major (Fe and Al) elemental abundance data (Kunzmann et al., 2017b). Although some data were previously published as part of a global Fe isotope data set for the Neoproterozoic (Kunzmann et al., 2017b), this is the first time these data are discussed in a detailed stratigraphic framework.

Samples span three intervals described in stratigraphic order: (1) the first spans 18.5 m (284.0-302.5 m) and comprises 16 samples (M103-380.3 to M103-398.9); (2) the second spans 9.0 m (354.0-363.0 m) and comprises 19 samples (M103-450.0 to M103-459.3); (3) and the third interval spans 4.5 m (378.9-383.4 m) and contains 10 samples (M103-475.2 to M103-479.7).

4.2. Bulk Shale Iron Speciation and Isotopes

Iron speciation analyses follow protocols outlined in Poulton and Canfield (2005), and total organic carbon (TOC), major and trace elemental concentration determination follows protocols outlined in Kunzmann et al. (2015). Iron isotope analyses follow protocols outlined in Kunzmann et al. (2017b). Iron was purified using ion exchange column chromatography in the clean laboratory (Sossi et al., 2015), and the isotopic measurements were carried out using a *NuPlasma II* MC-ICP-MS with a high-resolution slit (>7000) to resolve interferences (e.g., ArO) in classic standard bracketing analytical scheme. The use of an *Aridus* II desolvating membrane permitted enhance sensitivity. Typical external reproducibility of triplicate measurements of a sample was 0.05 permil during the course of this study. NIST SRM 3126a was used for standard bracketing due to the limitation of IRMM-14 availability. All analyses are reported in delta (δ) notation in relation to IRMM-14 (Dauphas and Rouxel, 2006), renormalizing from NIST SRM 3126a measurement as determined by Rouxel and Auro (2010):

$$\delta^{56}Fe = [(^{56}Fe/^{54}Fe)_{sample}/ (^{56}Fe/^{54}Fe)_{IRMM\text{-}14} - 1] X 1000$$

$$\delta^{56}Fe = ([(^{56}Fe/^{54}Fe)_{sample}/ (^{56}Fe/^{54}Fe)_{NIST\ SRM\ 3126a} - 1] X 1000) - 0.4$$

Using the conversion equation from Craig (1957):

$$\delta^{56}Fe_{(sample–SRM\ 3126a)} = \delta^{56}Fe_{(sample–\ IRMM\text{-}14)} + \delta^{56}Fe_{(IRMM\text{-}14–SRM\ 3126a)} + 10^{-3}\ \delta^{56}Fe_{(sample–\ IRMM\text{-}14)}\ X\ \delta^{56}Fe_{(IRMM\text{-}14–SRM\ 3126a)}$$

Here, (sample–SRM 3126a) and (sample– IRMM-14) are analyses of a sample relative to SRM 3126a and IRMM-14 standards, and (IRMM-14–SRM 3126a) is the analysis of IRMM-14 relative to SRM 3126a.

4.3. X-Ray Diffraction (XRD)

To determine mineralogical composition, powder X-ray diffraction (XRD) was performed at the University of Oxford on bulk powdered shale samples. Powder X-ray diffraction was performed on sample powders by grinding by hand in an agate mortar and pestle. Samples were mounted as a slurry mixed with anhydrous ethanol on a low background scattering silicon crystal substrate and analyzed using a Panalytical Empyrean Series 2 diffractometer operating at 40 kV and 40 mA with a Co Kα source. Samples were analyzed while continuously rotated and data were acquired from 5-85 degrees 2-theta using a step size of 0.026 degrees. Sample height displacement corrections were performed using the positions of quartz reflections as internal standards. Peaks were identified and matched against the Powder Diffraction File-4+ database (International Center for Diffraction Data), using the reference intensity ratio method (Snyder and Bish, 1989). In addition, clay mineral speciation and polytype identification was performed by scanning from 69-75 degrees 2-theta using a step size of 0.026 degrees and count rates of 200 seconds per step. In this way, mineral-specific 060 reflections were quantified, and clay mineral abundances expressed as a relative fraction of the total clay content, because the area of these reflections has been shown to correspond in a linear fashion to clay mineral abundance (Srodon et al., 2001).

4.4. Light Microscopy and Scanning Electron Microscopy (SEM)

Samples M103-458.3 and M103-475.2 were embedded in 25 mm diameter epoxy molts and polished on a TECHPREP^{TM} polishing system. The final polish was done with 0.05 μm colloidal silica solution. Sample M103-475.2 was additionally ion polished in a Leica EM TIC 3X large area ion polisher. Large-area reflected-light microscopy image mosaics were acquired from the sample M103-475.2 using a Zeiss AXIO Zoom.V16 light microscope. The mosaics were acquired with the software "ZEN Pro" using the Plan Apo Z 1.0/0.25 objective (FWD 60 mm) at a resolution of 410 nm/pixel with reflected-light from a LED light ring mounted on the microscope objective. The entire light microscopy image mosaic of M103-475.2 consists of 218 images. The principal purpose of acquiring the large-area image mosaics was to understand the mineralogy, the mineral associations, and textures of the entire sample. Large-area SEM image mosaics of the

samples M103-458.3 and M103-475.2 were acquired with the ZEISS Atlas 5 software by using a ZEISS SIGMA HDVP FE-SEM at Fibics Incorporated (Ottawa, Canada). See appendix for online access to full Atlas 5 datasets.

4.5. Energy-Dispersive X-Ray Spectroscopy (EDS)

Energy-dispersive spectroscopic (EDS) analyses on sample M103-475.2 were carried out on a Zeiss EVO MA 15 tungsten filament SEM to evaluate the effects of pyrite wreathing on sample mineralogy and elemental distribution. This instrument was equipped with two Bruker XFlash 6/30 EDS detectors and controlled using the Esprit 1.9 software. An accelerating voltage of 20 kV and a 3.7 nA probe current were used for the acquisition of EDS element maps and point analyses. The acquired element maps and point analyses were exported from the Bruker Esprit software are linked with their respective location of acquisition in the Atlas 5 Browser-Based Viewer (BBV) data sets (see appendix).

5. Results

Total organic carbon (TOC), major elemental (Sc/Th and Fe_T/Al), iron speciation, iron isotopic, RSE abundance and authigenic enrichment, and clay mineralogical data are presented in Table 1 and along with their samples' stratigraphic context in Figure 2. Samples range from 0.1% to 3.8% TOC. Sc/Th ratios fluctuate between 0.61 and 1.14 with no apparent stratigraphic structure. Fe_T/Al ratios span 0.15 to 1.3 and display systematic stratigraphic trends within each shale interval. Fe_T/Al ratios are generally low (most <0.4), but consistent with Reefal assemblage data sampled throughout the basin by Sperling et al. (2013). Of the 45 samples analyzed for iron speciation, 25 (56%) have Fe_{HR}/Fe_T values greater than 0.38 (anoxic), 8 (18%) are less than 0.22 (oxic), and 12 (27%) are between 0.22 and 0.38 (ambiguous). These data display coherent stratigraphic trends from "oxic" to "anoxic" and, in some cases back to "oxic" values across each shale interval that closely mimic those of Fe_T/Al ratios. In the second sampled interval, Fe_T/Al and Fe_{HR}/Fe_T ratios demonstrate two, symmetrical peaks. All samples from this study have Fe_{Py}/Fe_{HR} ratios less than 0.1 (from below detection limit to 0.084) and total S concentrations less than 1% by weight, with the majority less than 0.1% by weight (Table 1). Iron oxy(hydr)oxide comprise

the majority of all reactive iron as demonstrated by Fe_{Oxy}/Fe_{HR} ratios between 0.58 and 0.98 and a mean of 0.88. Iron isotopic compositions are nearly all positive, ranging from –0.02‰ to 0.83‰. Over the first and second sampled intervals, $\delta^{56}Fe$ data demonstrate similar but inverse stratigraphic structures to Fe_T/Al and Fe_{HR}/FeT, where low Fe_T/Al and Fe_{HR}/FeT ratios correspond to heavy $\delta^{56}Fe$ values and high Fe_T/Al and Fe_{HR}/FeT ratios to light $\delta^{56}Fe$ values. However, this pattern is not expressed in the third interval, where $\delta^{56}Fe$ fluctuations are muted. Relationships between Fe_T/Al, Fe_{HR}/Fe_T, and $\delta^{56}Fe$ are shown in Figs. 3 and 4. Fe_T/Al ratios are positively correlated with Fe_{HR}/Fe_T, and both Fe_T/Al and Fe_{HR}/Fe_T are weakly negatively correlated with $\delta^{56}Fe$.

Concentrations and authigenic enrichments of U, V, Mo, and Cr are highly variable and exhibit minimal stratigraphic trends (Fig. 2; Table 1). Some samples are remarkably enriched in Mo (up to 726 ppm) relative to the upper crustal average of 1.5 ppm and in Cr (up to 5792 ppm) relative to the upper crustal average of 83 ppm. However, most samples contain between 1 and 5 ppm Mo and 64 and 100 ppm Cr (McLennan, 2001). Both U and V are enriched to a much lesser degree than Mo or Cr, with a maximum of 8 ppm U (upper crustal average is 2.8 ppm) and 225 ppm V (upper crustal average is 107 ppm; McLennan, 2001). Trace element concentrations (normalized to Al) are plotted against TOC in Figure 5. There is no apparent correlation between Mo/Al and TOC (r^2=0.15) nor between Cr/Al and TOC (r^2=0.14), though there is weak positive correlation between V/Al and TOC (r^2=0.36), and slightly more substantial positive correlation between U/Al and TOC (r^2=0.49). Furthermore, Mo versus U authigenic enrichment factors (EFs) display two distinct populations (Fig. 6). One of these groups clusters around crustal Mo and U concentrations and falls below 0.1 times the ratio of Mo to U in the modern ocean. The second group is significantly more-enriched in Mo relative to U and lies above 0.3 times the modern marine Mo to U enrichments ratio, with some samples greater than 3 times this ratio. Samples with Mo concentrations exceeding 200 ppm also contain comparable Mn concentrations (Fig. 7). In cross-plots of Mo versus Cr and Mo versus Ni (nickel) concentration, two trends also emerge (Fig. 8). Samples with low Mo concentrations (<10ppm) do not appear to co-vary with Cr or Ni concentrations, while there is a strong, linear covariation (r^2=0.99) between samples with high Mo and their Cr and Ni abundances. Ratios of S/TOC are generally lower than the Holocene “normal” marine ratio of 1:3 (Fig. 8; Raiswell and Berner, 1986).

XRD analyses reveal that samples contain quartz, 2M1 illite (i.e., detrital muscovite) and 1M illite (diagenetic illite), and that glauconite accounts for a significant proportion of the illite polymorphs. Glauconite to total illite ratios range from 0.004 to 0.31, with an average of 0.9 and minimal stratigraphic patterns in all but the second interval, where it mimics the Fe_T/Al, Fe_{HR}/Fe_T, Fe_{Oxy}/Fe_T, and the inverse of $\delta^{56}Fe$ data (Fig. 2).

The Atlas 5 large-area BSE image mosaics demonstrate the texture and mineralogy of samples M103-475.2 (Fig. A1) and M103-358.3 (see appendix). Elemental maps from SEM-EDS reveal framboidal and subhedral pyrite "ghosts" ranging from ~5–20 μm diameter altered to iron oxy(hydr)oxide in both samples (Fig. 10 and Fig. A1E, F, G, and J). Sample M103-475.2 also contains diagenetic monazite grains, altered rutile grains, and zircon (Fig. A1B–D; Fig. A2A–C). In sample M103-475.2, EDS point analyses of the iron oxide minerals that replaced the former pyrite crystals reveal Cr, V, Ti, Ni, and Mo (detection limit is ~0.5 weight % for long runs) in the structure of the iron oxide minerals (Fig. A1E–J; Fig. A1D, E, F and H); however, the presence of Mo is difficult to confirm since the Lα Mo peak is overlapping with the Kα peak of S. This sample also contains lead phosphate phase (possibly corkite) that occurs as secondary euhedral crystals within secondary pore spaces (Fig. A1J–M; Fig. A2K, L, N).

6. Discussion

6.1. Sequence Stratigraphy

Here, as in previous studies (e.g., Halverson et al., 2012; Macdonald et al., 2012), the Reefal assemblage is interpreted to record a series of basin-wide transgressive-regressive (T-R) sequences where sequences boundaries are marked by maximum regressive surfaces (MGS; Fig. 2). For each of these sequences, stromatolite reefs that nucleated on basement highs were drowned by rapid flooding events during the transgressive systems tract (TST) that resulted in deposition of shale intervals. These reefs then began to prograde to the NNW into adjacent shale basins during the subsequent highstand systems tract (HST). Shale intervals are characterized by very fine-grained and finely-laminated mudstones with elevated TOC contents, low Fe_T/Al ratios, and spikes in RSE concentrations, providing strong sedimentological, geochemical, and sequence stratigraphic evidence for high relative sea level. They record both the TST and in some cases

early HST. The absence of significant falling stage systems tract (FSST) or lowstand systems tract (LST) deposits in the Reefal assemblage indicates that these base-level changes resulted primarily from rapid subsidence rather than eustatic sea-level changes, perhaps due to crustal attenuation through the rift-to-drift transition during early rifting of Rodinia (Macdonald et al., 2012).

Geochemical data across the three sampled intervals display distinct stratigraphic trends (Fig. 2) interpreted to represent chemocline fluctuations during small-scale transgressive-regressive sequences. Iron speciation data (Fe_{HR}/Fe_T and Fe_{Oxy}/Fe_T) effectively track transitions from an oxic to anoxic environment from flooding during the TST. The coherency of these trends and their similarity to data from throughout the basin (Sperling et al., 2013) support interpretation of these data as primary depositional signals. In all cases, the initial transition from oxic ($Fe_{HR}/Fe_T<0.22$) to anoxic ($Fe_{HR}/Fe_T>0.38$) conditions corresponds to an increase in Fe_T/Al ratios and spikes in RSE enrichments. TOC levels peak directly prior to these transitions and then sharply decline. Peaks in Fe_{HR}/Fe_T and Fe_T/Al ratios are interpreted to represent maximum flooding surfaces (MFSs), and the steady decline in these proxies following each MFS reflect shoaling at the start of the HST. Two-such sequences exist in the second interval.

6.2. Post-Depositional Alteration

The presence of framboidal pyrite "ghosts" (Fig. 10) indicate that outcrops from this study experienced some degree of post-depositional alteration. A comparative study between fresh drill core and weathered outcrop samples by Ahm et al. (2017) provides a template for assessing and predicting trends in iron speciation data from modern oxidative weathering. In that study, some iron from pyrite dissolution is transformed to iron oxy(hydr)oxide, as illustrated by excess Fe_{Oxy}/Fe_{HR} ratios in outcrop samples where Fe_{Py}/Fe_{HR} ratios were lower than core samples from the same stratigraphic horizon. While Fe_{HR}/Fe_T ratios decreased by up to ~30%, Fe_T/Al ratios were unaffected, so the mobilized Fe_{HR} was transformed to unreactive phases (Ahm et al., 2017). Similar to metamorphism (Lyons and Severmann, 2006; Slotznick et al., 2015; Slotznick et al., 2016), oxidative weathering can obscure primary iron speciation signals. However, as long as iron is neither lost nor gained, whole-rock iron proxies (i.e., Fe_T/Al and iron isotopes) are unaffected (Ahm et al., 2017). Both of these post-depositional processes also affect iron speciation in the same way—Fe_{Py} is altered to Fe_{Oxy} and Fe_{HR} is altered to Fe_U. This means that for samples where

oxidative weathering is suspected, euxinic versus ferruginous signals may be obscured. These alteration trends may also produce false "oxic" signals, but samples with $Fe_{HR}/Fe_T > 0.38$ can confidently be interpreted to reflect deposition within anoxic waters since there is no mechanism to generate new reactive iron.

A basin-wide iron speciation study by Sperling et al. (2013) from seven stratigraphic sections of the Fifteenmile Group display stratigraphic intervals in deeper-water facies hundreds of meters thick with Fe_{Py}/Fe_{HR} ratios between 0.2–0.8 and other similarly thick intervals in shallower water facies with almost no pyrite. Oxidative weathering is unlikely to produce such systematic stratigraphic trends across the basin, and the iron speciation data indicate that, while basin waters were anoxic, ferruginous rather than euxinic conditions are indicated. Therefore, low Fe_{Py}/Fe_{HR} ratios from "anoxic" samples do not necessarily indicate oxidative pyrite dissolution in all samples, but rather could arise from deposition within a restricted basin with a depleted S reservoir. Additionally, because section M103 from this study is from the shallowest portion of the basin (Macdonald et al., 2012; Sperling et al., 2013), the high proportion of "oxic" samples (~25%) are consistent with previous interpretations of the basin architecture and redox stratification. Therefore, we do not interpret Fe_{HR}/Fe_T values < 0.22 as false "oxic" signals.

Framboidal pyrite "ghosts" were observed in two out of the four samples imaged and pyrite framboids were preserved in the other two. The framboids are of variable sizes > 5 μm, indicating formation within sediment pore-waters underlying a non-euxinic water column (Wilkin et al., 1996; Wilkin and Barnes, 1997). Similar to (Sperling et al., 2013), we interpret that while iron speciation data indicate ferruginous conditions during anoxia, brief periods of euxinia likely occurred, but did not persist long enough for the sediment to accumulate substantial pyrite content. Although sample M103-475.2, which contains ~7 ppm Mo shows evidence for pyrite alteration and mineralization (Figs. 10 and A1), sample M103-450.8 has ~40 ppm Mo but shows unaltered pyrite framboids. Although the few samples with extreme Mo enrichments may have experienced post depositional alteration, samples with moderate Mo enrichments require free H_2S. Therefore, we use Mo enrichments >30 ppm as a proxy for transient euxinic conditions (Lyons et al., 2009). Furthermore, there is no correlation between Fe_{Py}/Fe_{HR} and Fe_{HR}/Fe_T either from this study (Fig. 11; $r^2=0.005$) or Sperling et al. (2013) ($r^2=0.02$), which indicates that whatever iron was liberated during pyrite dissolution was likely quantitatively transformed to other Fe_{HR} species locally (most likely Fe_{Oxy}; Fig. 12).

Data from (Sperling et al., 2013) display stratigraphic intervals with consistently low Fe_T/Al ratios (~0.2) in Reefal assemblage shale similar to samples from this study. Again, such basin-wide trends are unlikely to occur from post depositional alteration, and particularly not from oxidative weathering considering Fe_T/Al ratios from Ahm et al. (2017) were statistically indistinguishable between weathered and un-weathered samples and data from this study show coherent stratigraphic trends in Fe_T/Al. Pyrite weathering would more likely affect samples in no coherent fashion with regard to stratigraphy. Therefore, since it appears that Fe_T is retained as Fe_{Oxy} following pyrite, whole-rock iron isotopic values should also be unaffected by outcrop weathering. The range in iron isotopic values from this study are similar to those of samples of similar age from Svalbard (Kunzmann et al., 2017b). Finally, Ahm et al. (2017) observed no loss of trace elements in weathered versus un-weathered samples, indicating that if these elements were mobilized, they were subsequently captured in oxide or other secondary minerals.

6.3. Vigorous Benthic Iron Shuttling

Isotopic modeling of the diagenetic iron cycle by Kunzmann et al. (2017b) suggests that water column processes, i.e., the delivery of iron oxy(hydr)oxide particles, control the $\delta^{56}Fe$ composition of both Fe_{HR}, and therefore bulk shale. Therefore, the expected relationships between $\delta^{56}Fe$ and Fe_T/Al are characterized by varying enrichments of Fe_T/Al (set by the net enrichment from seawater) and corresponding ^{56}Fe enrichments controlled by the degree of oxidation of the Fe(II) seawater iron pool. However, Kunzmann et al. (2017b) noted an overall weak negative relationship between $\delta^{56}Fe$ and Fe_T/Al, Fe_{HR}/Fe_T, and Fe_{Oxy}/Fe_T in their Neoproterozoic sample set. This relationship was most strongly developed in samples from the Reefal assemblage, a trend further bolstered by new data reported herein. This trend suggests that although water column iron cycling often controls the iron isotopic composition of bulk shale, diagenetic iron cycling played a role in the isotopic composition through benthic iron shuttling in the Fifteenmile basin. This phenomenon is well-documented in the Black Sea (Severmann et al., 2008) and the OMZ off the coast of Peru (Scholz et al., 2014), though it should be noted OMZs likely did not exist in Proterozoic oceans.

Reefal assemblage samples from this study, Sperling et al. (2013), and Kunzmann et al. (2017b) all exhibit Fe_T/Al ratios consistently below crustal values. Slightly below average crustal

Fe_T/Al ratios may occur in a restricted basin with a relatively small catchment area dominated by relatively iron-poor lithologies. However, significantly depleted sedimentary Fe_T/Al ratios as we see in data from this study require an additional biogeochemical mechanism to facilitate iron mobilization, namely DIR, which can lower Fe_T/Al ratios by mobilizing Fe_{HR} (Noffke et al., 2012; Scholz et al., 2014). The positive relationship between Fe_T/Al and Fe_{HR}/Fe_T (Fig. 3) and that Fe_{Oxy} account for the majority of reactive iron species demonstrates that highly reactive iron oxy(hydr)oxide species account for the majority of iron enrichments and that such enrichments occurred primarily under an anoxic water column. Inverse correlations between $\delta^{56}Fe$ and both Fe_T/Al and Fe_{HR}/Fe_T, most pronounced in the first and second intervals (Fig. 4), reveal that samples deposited under an oxic or "redox-ambiguous" water column and those depleted in total iron are isotopically heavy.

It is important to note that the isotopic composition of Fe_{HR} in sediment is controlled not only by the degree of oxidation of the Fe(II) seawater inventory, but also its initial composition. The main source of iron oxy(hydr)oxide in the Proterozoic is generally thought to have been hydrothermal activity, and so its isotopic composition would have been ~–0.1‰ (Derry and Jacobsen, 1990). However, basins with a strong redox gradient that weren't well-mixed with the open ocean (like the Black Sea) may have contained a high proportion of isotopically light Fe_{HR} sourced by DIR. The benthic iron shuttle in the Black Sea can be identified by a negative relationship between $\delta^{56}Fe$ and Fe_T/Al because diagenetic reactions such as DIR mobilize isotopically light reactive iron in suboxic shelf sediments, which is subsequently transported to the euxinic basin where it is trapped by syngenetic pyrite formation and buried in sediments (Wijsman et al., 2001; Andersen and Raiswell, 2004; Lyons and Severmann, 2006; Severmann et al., 2008). In contrast, the $\delta^{56}Fe$-Fe_T/Al relationship in the OMZ off the coast of Peru is more complex and the benthic iron shuttle in open marine, non-euxinic settings leads to complex $\delta^{56}Fe$-Fe_T/Al relationships. In areas where the OMZ impinges on the seafloor, DIR mobilizes isotopically light iron, which is transported laterally within the OMZ or downslope and thus removed from the initial depositional site. This leaves behind a sediment with depleted Fe_T/Al and heavy $\delta^{56}Fe$ values (Scholz et al., 2014), much like the trend in data from this study. Although iron mobilized from the OMZ is isotopically light, partial precipitation below the OMZ as iron oxy(hydr)oxide imparts a positive fractionation, and so basinal sediment is characterized by elevated Fe_T/Al and heavy $\delta^{56}Fe$ (Scholz et al., 2014).

We interpret the negative relationship between $\delta^{56}Fe$ and Fe_T/Al and the stratigraphic patterns from the Reefal assemblage to record enhanced redox cycling during transgression in a strongly redox-stratified basin. Bio-reactive iron oxy(hydr)oxide is known to accumulate from oxidation of Fe(II) released from pore-waters where the redox boundary impinges the sediment-water interface (van Cappellen et al., 1998; Lyons and Severmann, 2006; Noffke et al., 2012; Scholz et al., 2014). Sediment that was deposited in oxic water above the redox boundary and was therefore replete with Fe(III) species, would at some point have been impinged by the shoaling redox boundary during initial transgression. The transgressing redox boundary introduced anoxic or suboxic water to the Fe(III)-replete sediment and promoted DIR, which preferentially removed ^{56}Fe-depleted, highly reactive iron, rendering it both residually ^{56}Fe-enriched and Fe_T/Al depleted (Fig. 4; e.g., Staubwasser et al., 2006; Homoky et al., 2009; Scholz et al., 2014). The ^{56}Fe-depleted Fe(II) would have been quickly and quantitatively oxidized across the redox boundary during subsequent shoaling and deposited nearby as highly reactive, iron oxy(hydr)oxide and perhaps minor pyrite. Then, as the redox boundary continued to shoal, this recently deposited bio-available iron would have been easily re-reduced and readily removed to the overlying anoxic water column where it could be transported downslope and permanently removed from the sediment. Thus, peaks in $\delta^{56}Fe$ values and minima in Fe_T/Al and Fe_{HR}/Fe_T correspond to maximum removal of isotopically-light iron in the vicinity of the redox boundary during transgression. Importantly, while DIR would have needed to reduce a significant amount of iron to drive these signals is, values from this study are within the upper limits of model predictions for the extent DIR can influence $\delta^{56}Fe_{HR}$ compositions (up to ~1‰), which require high fluxes of reducible iron (Kunzmann et al., 2017b). Here, we interpret extreme Fe_T/Al depletion coupled with $\delta^{56}Fe$ enrichment to represent unusually vigorous DIR stimulated by short-term fluctuations of the basin's redox boundary.

The subsequent, gradual return to lighter $\delta^{56}Fe$ values and enrichment in Fe_T and Fe_{HR} then reflects accumulation of iron oxy(hydr)oxide particles as the redox boundary continued to shoal during the HST when high relative sea level and low sedimentation rates promoted elevated organic carbon flux and expansion of basin anoxia below the redox boundary. The return to lighter isotopic compositions at this time may reflect quantitative oxidation of isotopically light Fe_{HR} across the redox boundary in sediment that was previously leached of its ^{56}Fe. Therefore, the accumulation of isotopically light iron would simply return the sediment to a "crustal" baseline.

Alternately, partial oxidation of an isotopically light Fe_{HR} pool from DIR would result in accumulation of Fe_{HR} with "crustal" compositions. In the latter case, the degree of partial Fe(II) oxidation may be responsible for the scatter in what would otherwise be strong negative linear correlation between $\delta^{56}Fe$ and both Fe_T/Al and Fe_{HR}/Fe_T. This scenario predicts that a reciprocal isotopically light reactive iron pool was sequestered elsewhere in the basin and would have elevated Fe_T/Al as seen in other studies where benthic iron shuttling was driven by DIR (Severmann et al., 2008; Scholz et al., 2014). Either way shuttling and accumulation of isotopically-light iron oxy(hydr)oxide below the redox boundary was maximized during maximum flooding, and so $\delta^{56}Fe$ minima (~0 to +0.1‰) and corresponding peaks in Fe_{HR}/Fe_T, Fe_{Oxy}/Fe_T, and Fe_T/Al mark the MFSs.

Iron speciation data from across the basin generally display a transition from predominantly anoxic to oxic depositional conditions in the middle Reefal assemblage just prior to the establishment of stromatolite reefs (Sperling et al., 2013) and approximately correlative to the shale intervals from this study. This transition approximately corresponds to an increase in Fe_T/Al from ~0.2–0.5 in sections ~15 km to the west (near Mount Harper). Together, these proxies indicate that this transition records a deepening of the redox boundary and deposition within the oxygenated surface layer where there was less abundant iron cycling. Deepening of the redox boundary could result from marine regression, changes in the depth of the pycnocline, or perhaps global increase in pO_2.

6.4. Exceptional Redox-Sensitive Element Enrichments

Assuming trace metal concentrations in samples from this study are represent primary, depositional signals, except for sample M103-475.2, an additional mechanism is required to explain Mo enrichment under predominantly non-euxinic conditions. Covariation between Mo-EF and U-EF (Fig. 6), display two distinct populations. Most samples are unenriched in U with respect to average upper continental crust (U-EF ~ 1; McLennan, 2001), but one population is highly enriched in Mo (Mo-EF > 1) and another depleted in Mo (Mo-EF < 1). The population enriched in Mo but unenriched in U has Mo-EF/U-EF ratios up to three times the molar ratio of modern seawater, indicative that Mo was periodically delivered to the sediment with remarkable efficiency. Low Mo/TOC (Fig. 5) and S/TOC ratios (Fig. 9) and the population depleted in Mo

(Fig. 6) suggest that the basin's Mo and S reservoirs were consistently depleted by a "basin reservoir" effect (Algeo, 2004; Algeo and Lyons, 2006; Algeo and Tribovillard, 2009; Tribovillard et al., 2012) considering that the Fifteenmile Group was deposited in a restricted rift basin (Macdonald et al., 2012). However, the extraordinary, but short-lived authigenic Mo enrichments demonstrate intermittent episodes of exceptional Mo delivery to the sediment from basin waters replete with Mo and S. These coincidental phenomena may be explained by periodically active particulate shuttling within a weakly restricted basin.

Authigenic Mo enrichment in modern sediment (>100 ppm) is typically associated with stable euxinic conditions (Scott and Lyons, 2012); however, delivery of Mo to sediment can be enhanced by active Fe (and possibly Mn) redox cycling via oxy(hydr)oxide particulate shuttling within weakly restricted water masses that experience variable redox conditions (Murray, 1975; Magyar et al., 1993; Crusius et al., 1996; Adelson et al., 2001; Dellwig et al., 2010). Within systems with an oscillating redox boundary (such as from seasonal chemical and density changes; Sundby, 2006), dynamic Fe-Mn redox cycling can promote extraordinarily large fluxes of Mo to the sediment through what has been termed the "Mo-pump" by Algeo and Lyons (2006) and Algeo and Tribovillard (2009), similar to the PO_4^{3-} pump in the Black Sea described by Shaffer (1986). This process operates by Fe-Mn-oxy(hydr)oxide particles adsorbing molybdate ions under suboxic bottom water conditions and converting it to particle-reactive molybdite (MoO_3) which is then shuttled to the sediment upon sinking (Tribovillard et al., 2012). Reductive dissolution of these particles during the reappearance of anoxic conditions releases the molybdite ions into the sediment where, given sufficient H_2S present, they can be reduced to thiomolybdate and be scavenged by organic carbon. Additionally, clay mineral surfaces catalyze hydrolysis and sulfidization of thiomolybdates (Erickson and Helz, 2000; Vorlicek and Helz, 2002), and may have the ability to enhance sedimentary Mo enrichments.

Molybdenum enrichments due to this particulate shuttle can result in distinctively high Mo/TOC (Algeo and Lyons, 2006) and Mo-EF/U-EF ratios (Algeo and Tribovillard, 2009; Tribovillard et al., 2012), as are observed in some samples from this data set. Conversely, low Mo/TOC, Mo-EF/U-EF, and S/TOC ratios are indicative of deposition within strongly restricted, euxinic to weakly sulfidic basins due to the "basin reservoir effect" whereby Mo burial outpaces deepwater renewal (Tribovillard et al., 2006; Algeo et al., 2007; Rowe et al., 2008; Algeo and Tribovillard, 2009; Bura-Nakić et al., 2018). Considering the evidence for vigorous iron

oxy(hydr)oxide shuttling in the vicinity of the redox boundary throughout deposition of the sampled shale intervals, occasional deepwater renewal that replenished the basin's Mo and S inventories would have activated the "Mo-pump" and enriched sediment until these reservoirs became depleted from to this mechanism. Extreme co-enrichments of Mo and Mn within high Mo samples (Fig. 7) support that Mn was also involved in the redox cycling and particulate shuttling in this basin, as documented elsewhere that a "Mo pump" has been observed. In this case, samples with low Mo/TOC, Mo-EF/U-EF, and S/TOC ratios from this data set result from consistent drawdown of the Mo and S reservoirs due to their efficient removal from the water column following intermittent euxinic conditions that did not persist long enough to produce significant pyrite enrichment in most samples (Berner and Raiswell, 1983; Berner and Raiswell, 1984; Raiswell and Berner, 1985, 1986; Algeo and Tribovillard, 2009; Tribovillard et al., 2012).

Since glauconite is a redox-sensitive mixed valence iron silicate, the high proportion of glauconite to total illite in samples near the transition from "oxic" ($Fe_{HR}/Fe_T < 0.22$) to "anoxic" ($Fe_{HR}/Fe_T > 0.38$) is indicative of fluctuating redox conditions in the vicinity of the redox boundary during transgressions (Obrien et al., 1990). That Mo enrichments are only observed in samples at or near the first oxic-anoxic transition for each flooding interval also suggest that oscillations of the redox boundary may have driven sedimentary authigenic Mo enrichments where it impinged the sediment water interface during short-lived euxinic conditions, perhaps driven by during intermittent deep-water renewal (Fig. 2). However, the "reservoir effect" depleted the basin's Mo reservoir and precluded its prolonged accumulation. The strong correlation between Mo, Cr, and Ni, in highly enriched samples (Fig. 8) could be interpreted as mineralization or weathering of an ultramafic ore body; however, there are no corresponding shifts in Sc/Th ratios to indicate changes in provenance (Fig. 2). Therefore, these co-enrichments indicate this shuttle also incorporated Cr and Ni, and that these reservoirs became similarly depleted during water mass restriction.

Remarkable Mo enrichments from this stratigraphic section but only subdued enrichments in other sections (up to 34 ppm; Sperling et al., 2013) may be due to the position within the basin during deposition. The M103 section may correspond to the position on the seafloor where the redox boundary commonly intersected the sediment-water interface during HST, and Fe-Mn particulate shuttling left a Mo, Cr, and Ni "bathtub ring" in this location during periods of intermittent euxinia (Force and Cannon, 1988; Adelson et al., 2001). Furthermore, particularly

steep slopes within this tectonically active basin may have further promoted down-slope benthic particulate shuttling.

6.5. Implications for Early Neoproterozoic Oxygenation

Coherent stratigraphic trends in iron speciation data from low to high Fe_{HR}/Fe_T ratios are interpreted to reflect transgression and regression of a strong redox boundary layer within a redox-stratified basin during relative sea-level change, confirming that the surface layer in the Fifteenmile basin was oxic while deep waters were anoxic and predominantly ferruginous. Whereas extraordinary Mo, Cr, and Ni enrichments may mark an expansion in their marine reservoirs due to the onset of Neoproterozoic oxygenation, unique mechanisms at work in this basin during transgressive events may have driven short-lived enrichments without significant changes in the global seawater inventory of these elements. Furthermore, global oxygenation would be expected to result in concomitant U and V enrichments, as well. Thus, identifying changes in global marine conditions should rely on sustained enrichments of multiple RSEs over significant depositional timespans. However, because an expansion of global marine Mo inventories from oxygenation would be expected to enhance sedimentary enrichments from particulate shuttling, this scenario cannot be ruled out. Although the coeval Wynniatt Formation from the Shaler Supergroup differs from the Reefal assemblage in that its iron speciation indicates euxinic rather than ferruginous conditions, Mo concentrations and Mo/TOC ratios are similarly intermediate between mid-Proterozoic and Phanerozoic levels (Thomson et al., 2015). Additional data is required from samples of this age worldwide to evaluate global oxygenation from RSE enrichments.

7. Conclusions

Results and interpretations from this study elucidate the central role of particulate shuttling within the weakly restricted and strongly redox stratified waters of the Fifteenmile rift basin. Fluctuations in relative sea level under these conditions generated large variations in redox proxies

which do not directly reflect changes in the redox state of the global ocean. Specifically, short-term oscillations in the position of the redox boundary invigorated a benthic Fe-Mn oxy(hydr)oxide particulate shuttle driven by DIR, and co-shuttling of various RSEs (Mo, Cr, Ni). This mechanism for trace element delivery to sediment can generate extraordinary Mo, Cr, and Ni sedimentary enrichments and may have been an important component of trace element cycling in Proterozoic basins; however, additional work is required to confirm that all of these signals are primary. Results from this study inform future investigations implementing iron and trace metal proxies in Proterozoic shale and highlight the importance of considering sequence stratigraphic context when making interpretations regarding global changes in marine oxidation state. Whereas these mechanisms do not directly reflect global oxygenation, the expansion of global oxic conditions may have contributed to the unique depositional setting required to produce this data set.

Acknowledgements

The Yukon Geological Survey, NSERC, and PCSP provided logistical and financial support. We thank Eric Bellefroid for help in the field. TMG acknowledges the Eric Mountjoy Legacy Scholarship and the Yukon Foundation for support. Discussions with Boswell Wing, Erik Sperling, Austin Miller, Malcolm Hodgskiss, Noah Planavsky and Silke Severmann improved this work. MK acknowledges support through various scholarships awarded by the Department of Earth and Planetary Sciences, McGill University and Geotop. MK publishes with permission of the Executive Director of the Northern Territory Geological Survey.

Table 1: Shale total organic carbon (TOC), major and minor elemental concentration, iron speciation, glauconite to illite ratio, and iron isotope data. Redox-sensitive element (Mo, V, U, and Cr) concentrations are shown alone, normalized to TOC, and as calculated authigenic components. Authigenic fractions were calculated by subtracting the detrital fraction from the bulk concentration. The detrital fraction is calculated as:

Sample	height	TOC	Al	Fe	Fe_T/Al	Sc	Th	Sc/Th	FeCarb	FeOxy	FeMag	FePy	FeHR/FeT	FePy/FeHR	glauc/ill	$\delta^{56}Fe$	1 SE	$\delta^{57}Fe$	1SE	Mo	Mo/TOC	auth Mo	V	V/TOC	auth V	U	U/TOC	auth U	Cr	Cr/TOC	auth Cr
	(m)	(%)	(wt. %)	(wt. %)		(ppm)	(ppm)	(ppm/ppm)	(%)	(%)	(%)	(%)				(‰)	(‰)	(‰)	(‰)	(ppm)	(ppm/%)	(ppm)	(ppm)	(ppm/%)	(ppm)	(ppm)	(ppm/%)	(ppm)	(ppm)	(ppm/%)	(ppm)
479.7	383.4	1.08	8.01	2.30	0.29	15.49	18.81	0.82	0.01	1.11	0.05	0.00	0.51	0.00	0.11	0.0541	0.1151	0.1063	0.1151	15.22	14.08	14.12	98.91	91.49	0.00	4.11	3.80	1.34	177.20	164.40	94.52
479.2	382.9	0.95	9.61	2.68	0.28	18.34	15.54	1.18	0.05	2.22	0.09	0.00	0.88	0.00	0.09	0.4301	0.0382	0.6428	0.0382	1.94	2.05	0.62	137.01	144.55	0.00	2.75	2.91	0.00	99.53	124.52	0.30
478.7	382.4	2.61	8.09	5.17	0.64	16.51	18.81	0.88	0.05	3.93	0.08	0.02	0.79	0.01	0.31	0.0467	0.0383	0.0887	0.0383	3.46	1.33	2.35	147.78	56.62	23.38	3.93	1.51	1.14	83.54	46.05	0.07
478.2	381.9	1.16	-	-	-	-	-	-	0.01	0.91	0.03	0.00	0.06	0.00	-	-	-	-	-	-	-	-	-	-	-	-	-	-	-	-	-
477.7	381.4	0.60	8.25	10.77	1.31	17.81	20.63	0.86	0.01	9.72	0.81	0.00	0.98	0.00	0.10	-	-	-	-	4.38	7.33	3.24	118.79	198.92	0.00	4.64	7.78	1.79	80.80	262.96	0.00
477.2	380.9	1.41	9.01	5.57	0.62	18.88	18.02	1.05	0.02	0.13	0.02	0.00	0.03	0.01	0.03	0.3466	0.0566	0.5636	0.0566	3.92	2.78	2.69	167.04	118.12	28.49	3.71	2.63	0.60	98.25	97.55	5.28
476.7	380.4	1.36	9.36	4.08	0.44	16.93	21.77	0.78	0.01	3.13	0.11	0.00	0.80	0.00	0.05	-0.0187	0.0365	-0.0586	0.0365	2.58	1.90	1.30	142.02	104.56	0.00	5.58	4.11	2.34	86.27	87.88	0.00
476.2	379.9	1.78	8.67	2.42	0.28	14.59	14.82	0.98	0.03	1.10	0.03	0.00	0.48	0.00	0.11	0.2323	0.0407	0.3036	0.0407	3.03	1.70	1.83	141.70	79.72	8.24	3.38	1.90	0.37	84.95	60.38	-4.60
475.7	379.4	1.29	6.32	1.09	0.17	10.78	17.74	0.61	0.01	0.26	0.02	0.00	0.26	0.01	0.09	0.2829	0.0471	0.4511	0.0471	2.85	2.21	1.98	78.30	60.89	0.00	3.96	3.08	1.77	64.74	52.81	0.00
475.2	378.9	3.85	8.04	3.67	0.46	14.05	16.53	0.85	0.00	0.15	0.02	0.00	0.05	0.00	0.09	0.1510	0.1052	0.2252	0.1052	726.45	188.52	725.34	225.26	58.46	101.49	7.19	1.87	4.41	5792.00	1516.16	5708.95
459.3	363.0		9.11	5.79	0.64	15.87	15.33	1.04	0.01	4.87	0.49	0.00	0.93	0.00	0.11	0.0835	0.0336	0.0831	0.0336	5.07	-	3.82	90.33	-	0.00	3.74	-	0.59	85.06	-	0.00
458.8	362.5	1.05	9.14	1.53	0.17	14.19	14.25	1.00	0.01	0.29	0.02	0.00	0.21	0.00	0.05	0.3178	0.1464	0.4536	0.1464	0.99	0.95	0.00	109.70	104.54	0.00	4.00	3.81	0.84	82.57	83.76	0.00
458.3	362.0	2.07	11.41	3.43	0.30	18.75	20.13	0.93	0.01	1.65	0.07	0.00	0.50	0.00	0.11	-0.0086	0.0317	-0.1206	0.0317	3.01	1.45	1.44	179.08	86.47	3.53	5.67	2.74	1.72	128.17	72.31	10.37
457.8	361.5	2.63	8.99	2.72	0.30	14.91	18.91	0.79	0.01	1.28	0.08	0.13	0.55	0.08	0.10	0.4664	0.0738	0.6939	0.0738	2.53	0.96	1.29	157.62	59.98	19.27	7.90	3.01	4.79	92.16	43.28	0.00
457.3	361.0	1.25	7.75	2.03	0.26	15.80	15.83	1.00	0.02	0.78	0.08	0.00	0.43	0.01	0.07	0.3625	0.0289	0.5697	0.0289	3.97	3.17	2.91	150.55	120.15	31.25	4.80	3.83	2.11	82.32	77.64	2.27
456.8	360.5	-	-	1.77	-	-	-	-	0.03	0.56	0.11	0.00	0.40	0.01	0.04	-	-	-	-	-	-	-	-	-	-	-	-	-	-	-	-
456.3	360.0	0.78	10.12	1.66	0.16	16.05	15.91	1.01	0.02	0.17	0.04	0.00	0.14	0.01	0.04	0.3222	0.0605	0.5327	0.0605	2.37	3.05	0.98	125.84	162.09	0.00	2.82	3.64	0.00	99.29	143.35	0.00
455.8	359.5	0.72	17.34	2.94	0.17	23.30	22.00	1.06	0.02	0.26	0.05	0.00	0.11	0.00	0.02	0.7050	0.1254	1.0333	0.1254	3.19	4.41	0.81	201.33	278.50	0.00	3.28	4.54	0.00	157.33	246.66	0.00
455.3	359.0	1.32	9.99	1.53	0.15	16.42	16.92	0.97	0.01	0.23	0.02	0.00	0.17	0.01	0.01	0.7356	0.0079	1.0976	0.0097	1.79	1.36	0.42	119.10	90.55	0.00	3.44	2.62	0.00	89.05	75.88	0.00
454.8	358.5	0.83	10.74	2.04	0.19	17.50	21.55	0.81	0.01	0.50	0.06	0.00	0.28	0.00	0.02	0.6634	0.0093	0.9887	0.0093	2.34	2.84	0.87	152.48	184.72	0.00	3.94	4.77	0.22	111.17	151.20	0.31
454.3	358.0	1.05	8.91	2.23	0.25	17.95	19.58	0.92	0.02	1.10	0.06	0.00	0.53	0.00	0.08	0.5316	0.1256	0.6813	0.0401	2.42	2.31	1.20	122.24	116.56	0.00	4.12	3.93	1.03	94.20	105.53	2.21
453.8	357.5	-	9.98	9.60	0.96	21.51	22.17	0.97	0.01	9.18	0.16	0.00	0.98	0.00	0.10	0.3137	0.0184	0.3965	0.0191	2.91	-	1.54	143.47	-	0.00	4.27	-	0.81	92.71	-	0.00
453.3	357.0	-	10.13	2.06	0.20	16.99	14.87	1.14	0.02	0.61	0.04	0.00	0.32	0.00	0.08	0.4265	0.0321	0.5905	0.0115	2.36	-	0.96	139.16	-	0.00	3.40	-	0.00	89.48	-	0.00
452.8	356.5	1.04	12.48	5.28	0.42	19.31	22.71	0.85	0.02	3.35	0.07	0.00	0.65	0.00	0.15	0.1059	0.1032	0.1042	0.0171	3.14	3.02	1.43	175.36	168.46	0.00	4.62	4.43	0.30	115.31	139.11	0.00
452.3	356.0	2.45	9.75	2.25	0.23	17.51	20.34	0.86	0.02	0.96	0.05	0.00	0.46	0.00	0.07	0.2149	0.0931	0.3249	0.0931	1.50	0.61	0.16	170.39	69.51	20.42	5.21	2.13	1.84	96.19	43.89	0.00
451.8	355.5	-	10.19	2.47	0.24	17.04	20.84	0.82	0.02	0.85	0.06	0.00	0.38	0.00	0.03	0.3883	0.0779	0.5506	0.0179	5.56	-	4.16	157.15	-	0.35	4.38	-	0.85	107.16	-	1.95
451.3	355.0	2.26	6.54	1.14	0.17	11.93	15.26	0.78	0.01	0.18	0.03	0.00	0.20	0.01	0.00	0.4723	0.0398	0.7054	0.0398	1.81	0.80	0.92	89.18	39.50	0.00	4.13	1.83	1.87	64.69	31.23	0.00
450.8	354.5	2.73	9.81	2.01	0.20	15.09	17.06	0.88	0.00	0.42	0.05	0.00	0.23	0.00	0.16	0.7493	0.0922	1.1231	0.0922	40.31	14.78	38.96	164.16	60.18	13.26	5.82	2.13	2.43	433.16	158.29	331.90
450.3	354.0	1.49	9.54	1.53	0.16	14.31	16.21	0.88	0.01	0.24	0.03	0.00	0.18	0.00	0.05	0.5077	0.0448	0.7465	0.0448	1.72	1.16	0.41	93.52	62.92	0.00	3.65	2.45	0.35	95.63	71.37	0.00
398.8	302.5	0.13	10.43	4.62	0.44	18.37	19.24	0.96	0.04	3.12	0.12	0.00	0.71	0.00	0.06	0.4056	0.0151	0.5706	0.0151	1.83	14.42	0.39	154.96	1223.36	0.00	2.90	22.88	0.00	89.51	975.12	0.00
397.8	301.5	0.10	9.84	5.53	0.56	17.18	22.02	0.78	0.02	3.92	0.20	0.00	0.75	0.00	0.09	0.1116	0.0265	0.2695	0.0355	42.18	410.77	40.83	148.86	1449.59	0.00	3.23	31.41	0.00	407.73	4160.55	306.15
394.4	298.1	0.14	11.08	4.04	0.36	17.89	18.25	0.98	0.01	2.47	0.22	0.00	0.67	0.00	0.12	0.2141	0.0399	0.2486	0.0489	1.38	9.91	0.00	164.98	1181.87	0.00	2.67	19.14	0.00	94.97	861.26	0.00
393.9	297.6	0.12	10.87	6.09	0.56	18.93	23.66	0.80	0.00	3.15	0.34	0.00	0.57	0.00	0.12	0.4414	0.0229	0.6287	0.0229	326.45	2642.06	324.96	181.77	1471.13	14.59	3.46	27.98	0.00	2845.29	23838.68	2733.11
393.4	297.1	0.19	10.48	5.03	0.48	18.82	18.53	1.02	0.01	3.62	0.15	0.00	0.75	0.00	0.17	0.1776	0.0406	0.1990	0.0334	2.30	11.85	0.86	167.94	864.43	6.75	2.87	14.75	0.00	91.61	663.30	0.00
392.9	296.6	0.17	11.03	4.31	0.39	18.18	21.41	0.85	0.01	2.60	0.14	0.00	0.64	0.00	0.06	0.3073	0.0391	0.2721	0.0367	38.82	225.51	37.31	164.47	955.38	0.00	3.23	18.79	0.00	414.03	2475.40	300.18
392.4	296.1	0.14	11.29	1.75	0.15	19.03	19.00	1.00	0.04	0.17	0.04	0.00	0.15	0.01	0.12	0.8384	0.0317	1.0499	0.0268	1.88	13.05	0.33	171.10	1185.70	0.00	2.88	19.93	0.00	98.12	773.00	0.00
391.9	295.6	0.71	7.98	1.36	0.17	13.12	17.38	0.75	0.00	0.32	0.03	0.00	0.25	0.00	-	0.5259	0.0552	0.6729	0.0469	60.45	85.58	59.36	91.55	129.60	0.00	3.63	5.14	0.87	573.93	788.43	491.60
391.4	295.1	1.20	10.02	1.63	0.16	17.79	17.98	0.99	0.00	0.64	0.03	0.00	0.42	0.00	0.14	0.3689	0.0367	0.5255	0.0226	1.33	1.10	0.00	165.89	138.04	11.67	3.53	2.94	0.06	106.40	95.75	2.91
390.9	294.6	0.41	9.32	1.55	0.17	15.20	17.67	0.86	0.02	0.38	0.08	0.00	0.31	0.00	0.08	0.5744	0.0424	0.7565	0.0406	0.68	1.69	0.00	129.06	318.30	0.00	3.67	9.05	0.44	80.87	213.08	0.00
390.4	294.1	0.15	7.31	0.77	0.11	12.06	14.55	0.83	0.02	0.06	0.02	0.00	0.14	0.00	0.07	0.6500	0.1660	1.0501	0.1660	2.11	14.12	1.10	72.88	488.06	0.00	3.13	20.98	0.60	70.88	467.23	0.00
389.9	293.6	0.39	9.19	1.91	0.21	15.83	18.52	0.85	0.00	0.19	0.04	0.00	0.12	0.01	0.17	0.7606	0.1444	1.1326	0.0240	221.91	562.80	220.65	150.95	382.82	9.53	3.90	9.90	0.72	2012.23	4927.67	1917.34
389.4	293.1	0.32	8.41	1.51	0.18	12.84	15.55	0.83	0.02	0.44	0.07	0.00	0.35	0.00	0.09	0.8067	0.0256	1.1918	0.0856	3.56	11.15	2.41	90.03	281.79	0.00	3.26	10.19	0.35	86.12	318.86	0.00
386	289.7	0.17	13.60	3.30	0.24	27.83	25.91	1.07	0.03	0.28	0.10	0.00	0.13	0.00	0.09	0.5687	0.0533	0.8442	0.0177	1.58	9.47	0.00	147.00	878.08	0.00	5.69	34.00	0.99	132.35	890.29	0.00
381	284.7	0.23	7.63	2.99	0.39	14.16	14.95	0.95	0.04	1.32	0.21	0.00	0.52	0.00	-	0.1984	0.1283	0.3018	0.0292	2.57	11.02	1.52	84.39	361.82	0.00	3.78	16.19	1.13	71.77	417.37	0.00
380.3	284.0	0.26	7.84	2.13	0.27	12.14	15.73	0.77	0.02	0.35	0.09	0.00	0.22	0.00	-	0.3902	0.0427	0.5450	0.0173	1.07	4.19	0.00	89.86	352.34	0.00	4.13	16.20	1.42	79.19	330.74	0.00

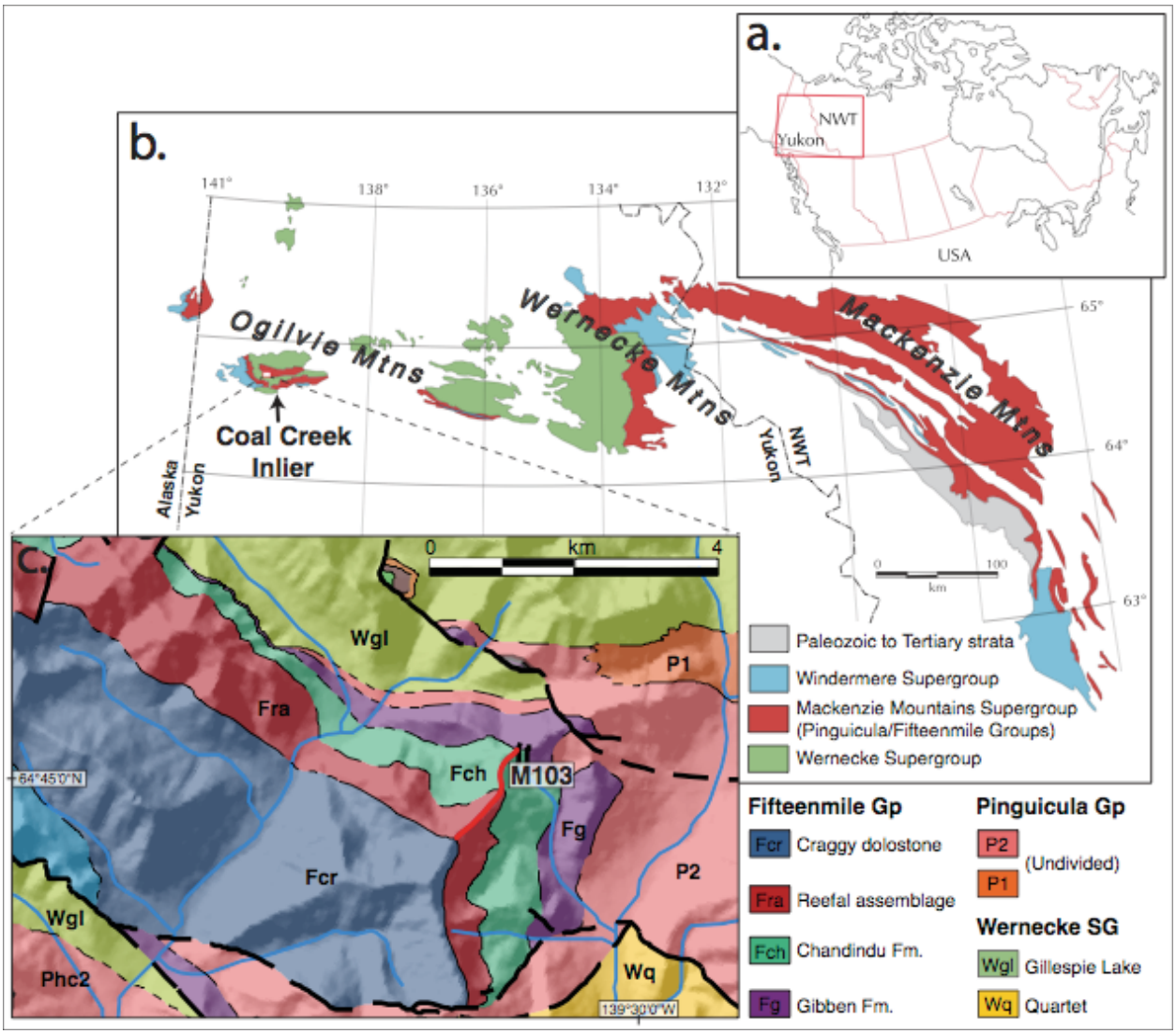

Figure 1: Overview of the study area. (A) Location map showing the area in (B) outlined in red. (B) Exposures of Proterozoic strata in the Ogilvie, Wernecke, and Mackenzie mountains in Yukon and the Northwest Territories (NWT) modified from Macdonald et al. (2012). C: Geological map showing the location of stratigraphic section M103 (red) modified from Strauss et al. (2014). Abbreviations for map units are described to the right. Thin lines are stratigraphic contacts, bold lines are faults and dashed lines are inferred contacts or faults.

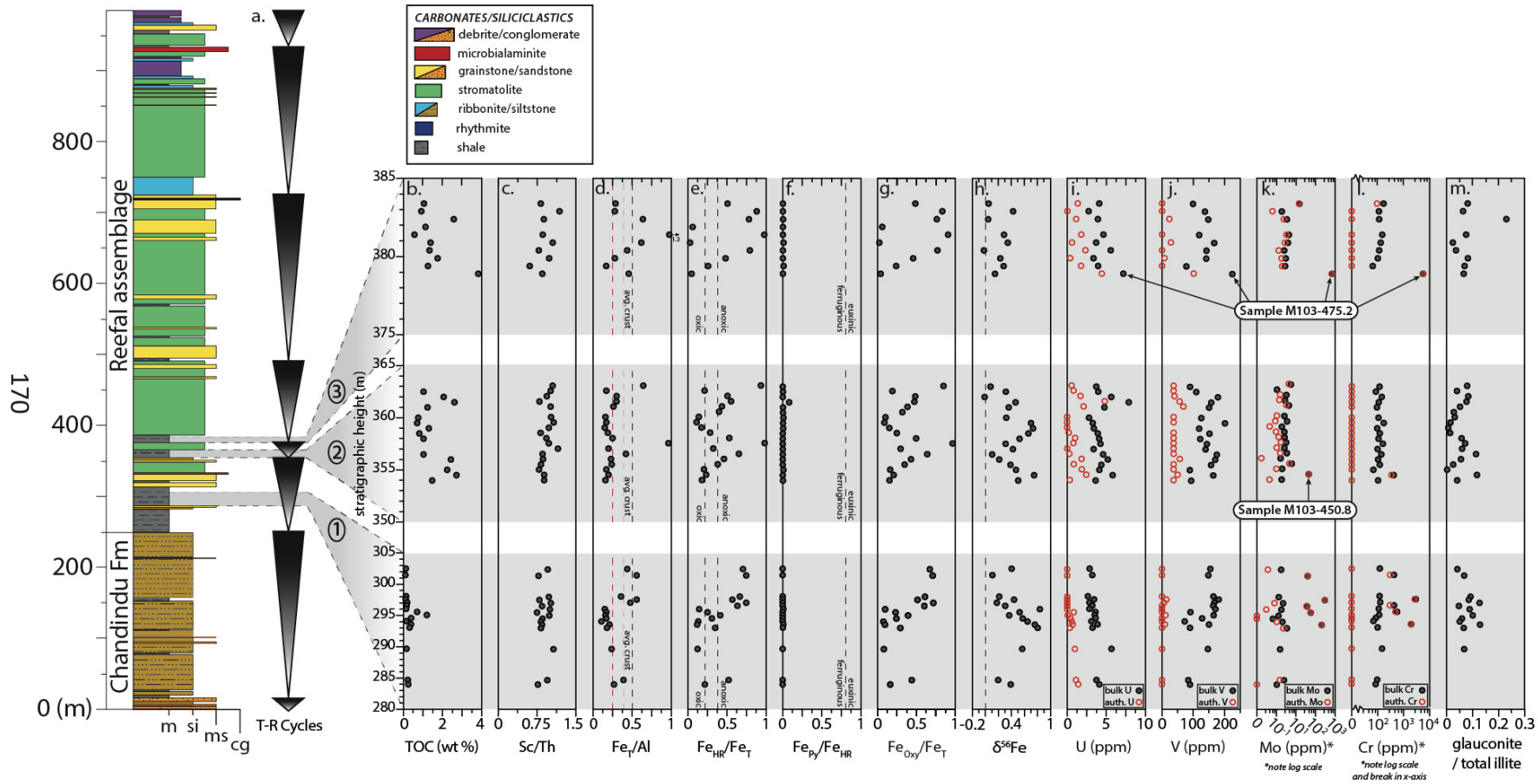
CARBONATES/SILICICLASTICS
debrite/conglomerate
microbialaminite
grainstone/sandstone
stromatolite
ribbonite/siltstone
rhythmite
shale
Reefal assemblage
Chandindu Fm
0 (m)
200
400
600
800
m si ms cg
T-R Cycles
a.
stratigraphic height (m)
Sample M103-475.2
Sample M103-450.8
TOC (wt %)
Sc/Th
Fe_T/Al
Fe_HR/Fe_T
Fe_Py/Fe_HR
Fe_Oxy/Fe_T
δ56Fe
U (ppm)
V (ppm)
Mo (ppm)*
*note log scale
Cr (ppm)*
*note log scale and break in x-axis
glauconite / total illite
bulk U
auth. U
bulk V
auth. V
bulk Mo
auth. Mo
bulk Cr
auth. Cr

Figure 2. Stratigraphic column and geochemical data from the three shale intervals (1–3) of the Reefal assemblage, upper Fifteenmile Group. (A) Sequence stratigraphic interpretation for the Chandindu Formation and Reefal assemblage showing transgressive-regressive (T-R) cycles as inverted triangles. (B) Total organic carbon content (% TOC). (C) Ratio of Scandium to Thorium (Sc/Th). (D) Ratio of total iron to aluminum (Fe_T/Al). Dashed lines (0.4 and 0.5) represent the average upper continental crust (UCC; McLennan et al., 2001). Red dashed line is the interpreted baseline for this basin (0.25). (E) Ratio of highly reactive iron to total iron (Fe_{HR}/Fe_T). Vertical dashed lines delineate samples deposited under oxic conditions ($Fe_{HR}/Fe_T < 0.22$) and those deposited under anoxic conditions ($Fe_{HR}/Fe_T > 0.38$) (Raiswell and Canfield, 1998; Poulton and Raiswell, 2002). The area between 0.22 and 0.38 is equivocal—samples within this range may have been deposited under oxic or anoxic conditions (Poulton and Canfield, 2011; Sperling et al., 2013). (F) Ratio of pyrite iron to highly reactive iron (Fe_{Py}/Fe_{HR}). Samples with ratios > 0.8 reflect deposition within a euxinic water column (Andersen and Raiswell, 2004). (G) Ratio of iron oxy(hydr)oxide to total iron (Fe_{Oxy}/Fe_T). (H) Bulk shale iron isotopic composition ($\delta^{56}Fe$) in ‰. (I–L) Bulk U, V, Mo, and Cr contents and calculated authigenic enrichments. Authigenic fractions were calculated by subtracting the detrital fraction from the bulk concentration. The detrital fraction is calculated as: detrital trace metal = $(\text{trace metal}/Al)_{UCC} \times Al_{sample}$. (M) Ratio of glauconite to total illite.

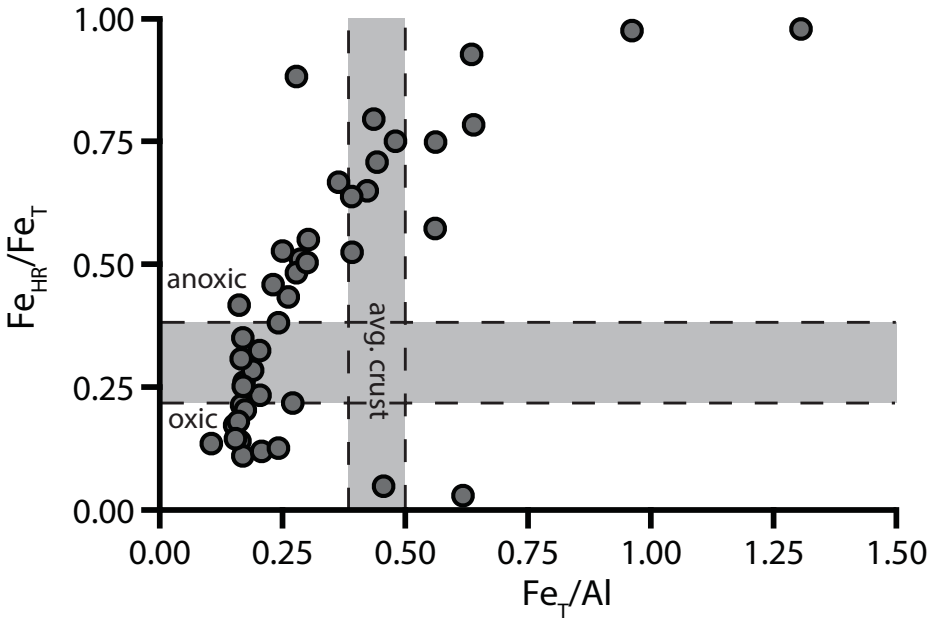

Figure 3: Cross-plot of Fe_T/Al and Fe_{HR}/Fe_T. Vertical shaded area ($Fe_T/Al = 0.4–0.5$) represents the average upper continental crust (McLennan, 2001). Horizontal dashed lines delineate samples deposited under oxic conditions ($Fe_{HR}/Fe_T < 0.22$) and those deposited under anoxic conditions ($Fe_{HR}/Fe_T > 0.38$) (Raiswell and Canfield, 1998; Poulton and Raiswell, 2002). The shaded area ($Fe_{HR}/Fe_T = 0.22–0.38$) is equivocal—samples within this range may have been deposited under oxic or anoxic conditions (Poulton and Canfield, 2011; Sperling et al., 2013).

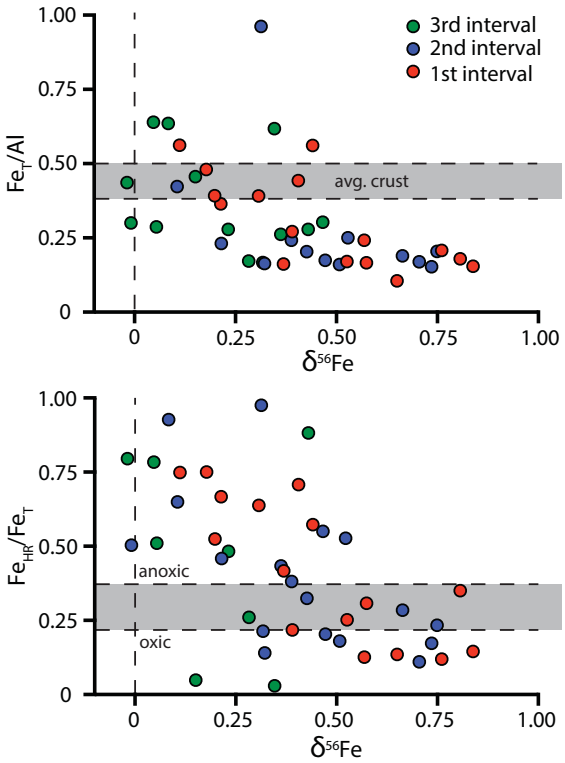

Figure 4: Cross-plots of Fe_T/Al (top) and Fe_{HR}/Fe_T (bottom) versus $\delta^{56}Fe$ color-coded from each flooding interval.

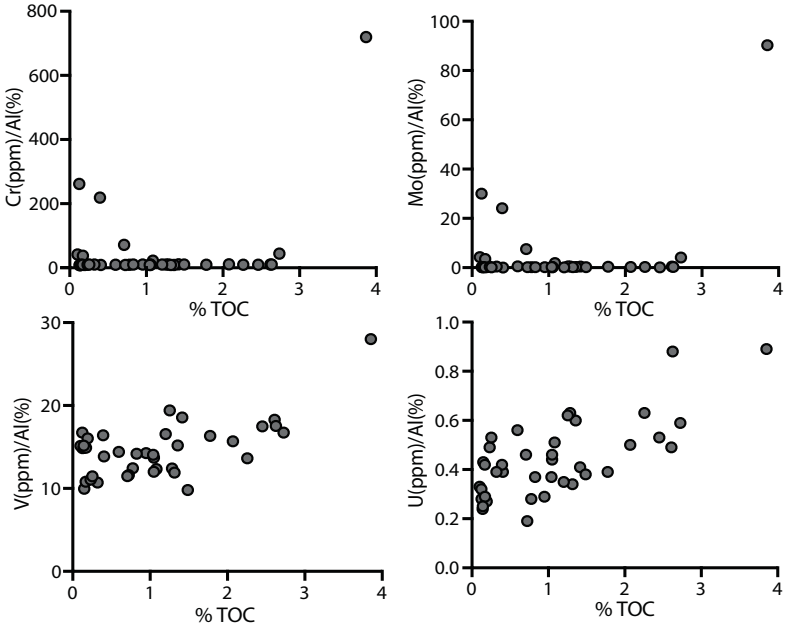

Figure 5: Cross-plots of redox-sensitive trace element concentrations versus TOC contents. All concentrations (Cr, Mo, V, and U; ppm) are normalized to Al (weight %). TOC is in weight %.

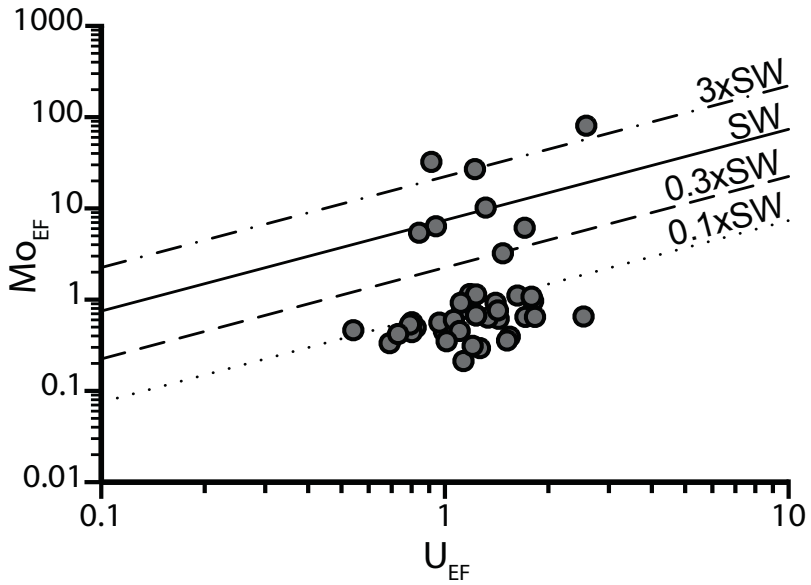

Figure 6: Cross-plot of the U enrichment factor (U_{EF}) and Mo enrichment factor (Mo_{EF}) for each sample. Dashed lines represent the Mo/U molar ratio of modern seawater (SW; ~7.5–7.9; Algeo and Tribovillard, 2009) and ratios of the modern Mo/U molar ratios (0.1xSW; 0.3xSW; 3xSW). Enrichment factors were calculated as; $X_{EF} = (X/Al)_{sample} / (X/Al)_{UCC}$, where X and Al stand for the concentrations (ppm) of element X and Al, respectively, and UCC is upper continental crust (McLennan, 2001).

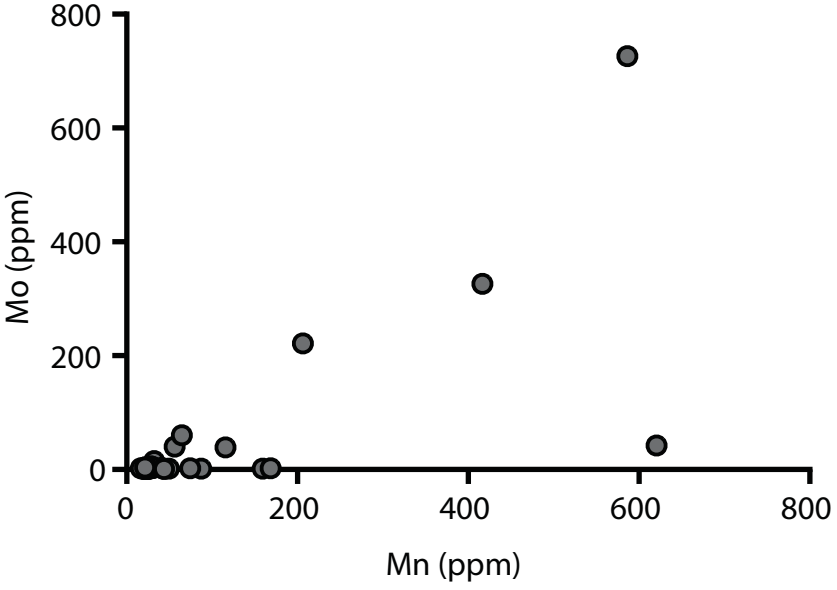

Figure 7: Cross-plot of Mo and Mn concentrations (both ppm).

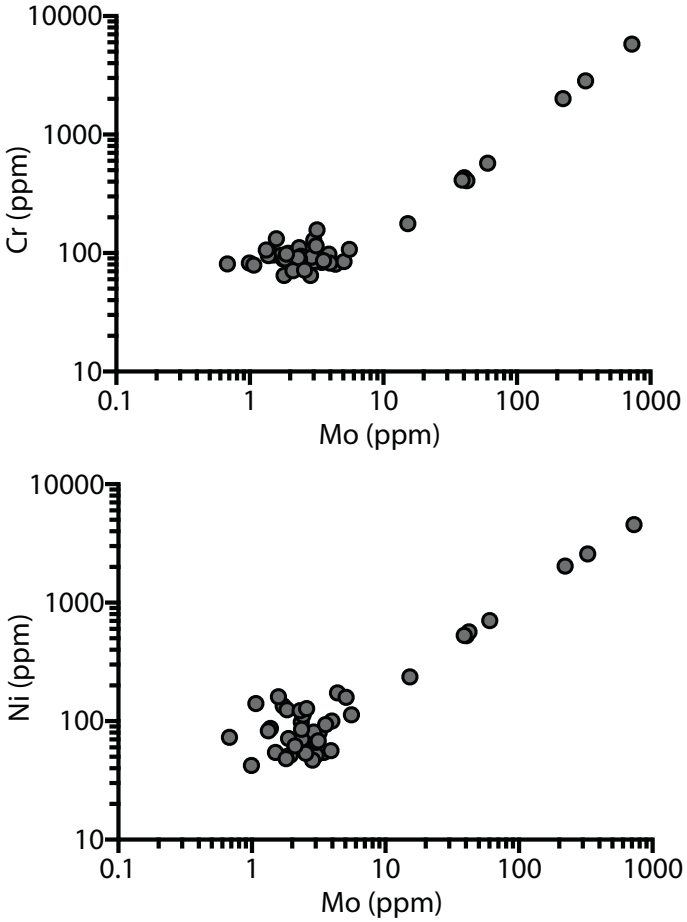

Figure 8: Cross-plots of Mo and Cr (top; ppm) and Mo and Ni (bottom; ppm). All Note log scale on all axes.

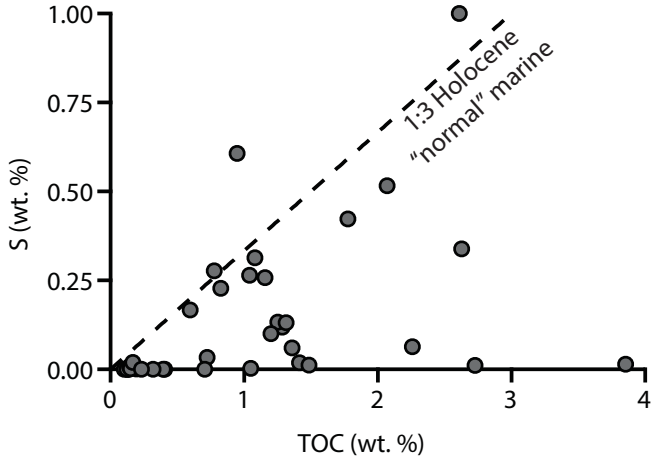

Figure 9: Cross-plot of TOC and S (both weight %). Dashed line represents the Holocene "normal" marine S/TOC ratios (1:3) from Raiswell et al. (1986).

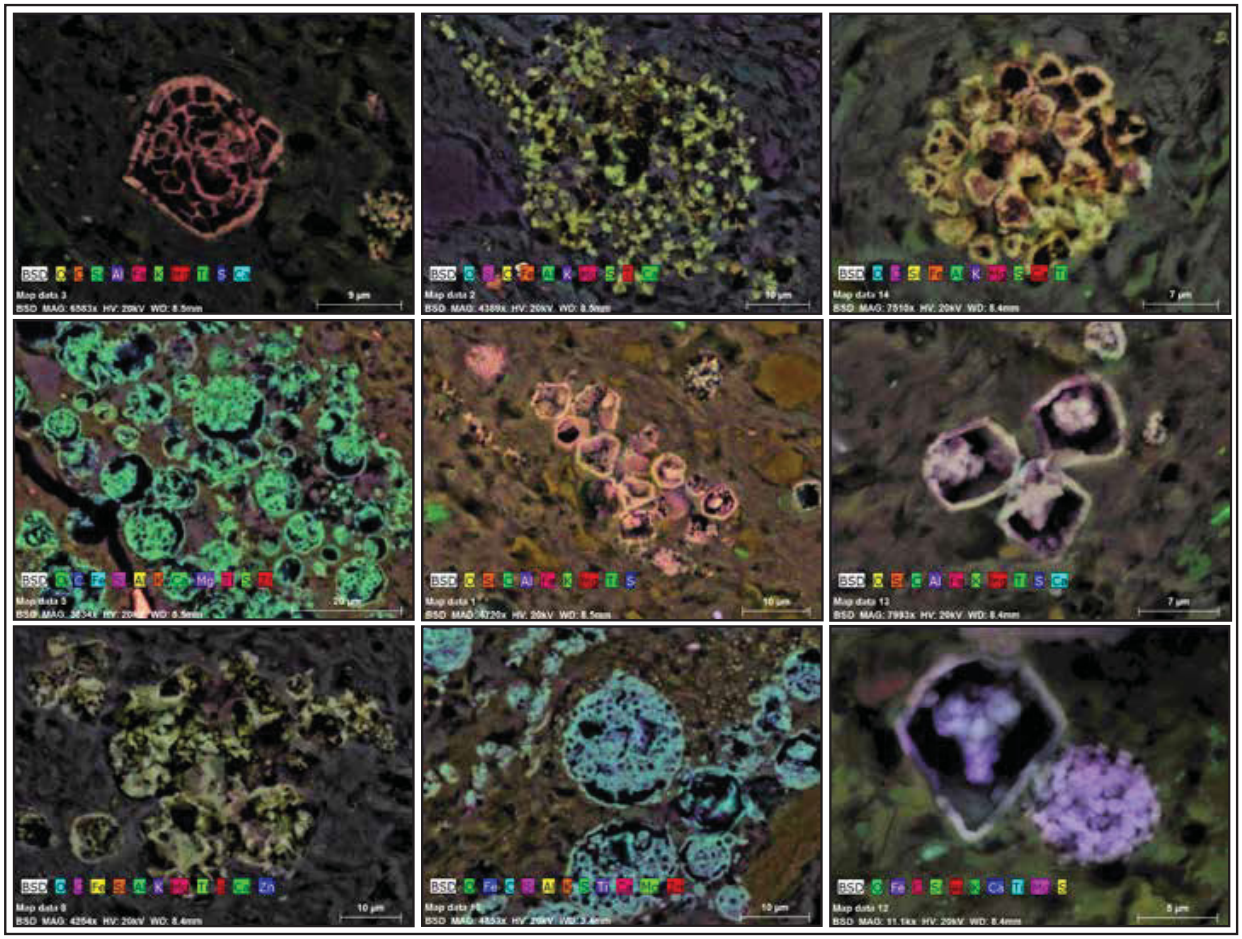

Figure 10: SEM images of the backscattered-electron signal overlain by false color elemental maps showing pyrite "ghost" crystals altered to iron oxy(hydr)oxide from sample M103-458.3 at 362 m stratigraphic height. See appendix for EDS results.

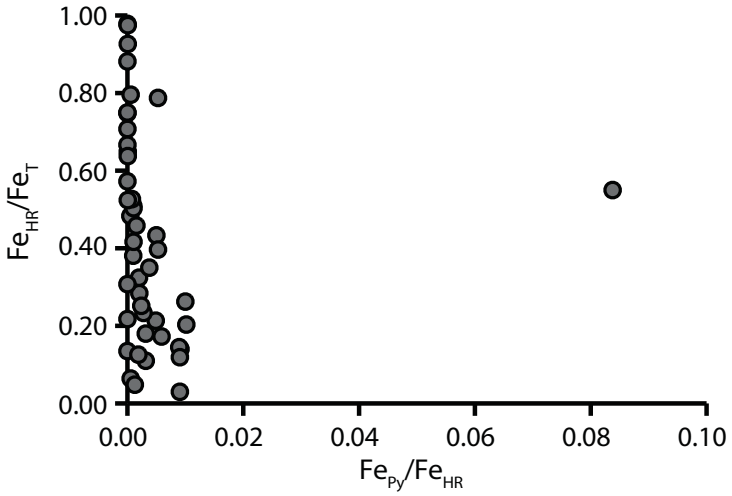

Figure 11: Cross-plot of the ratios of pyrite iron to highly reactive iron (Fe_{Py}/Fe_{HR}) versus highly reactive iron to total iron (Fe_{HR}/Fe_T).

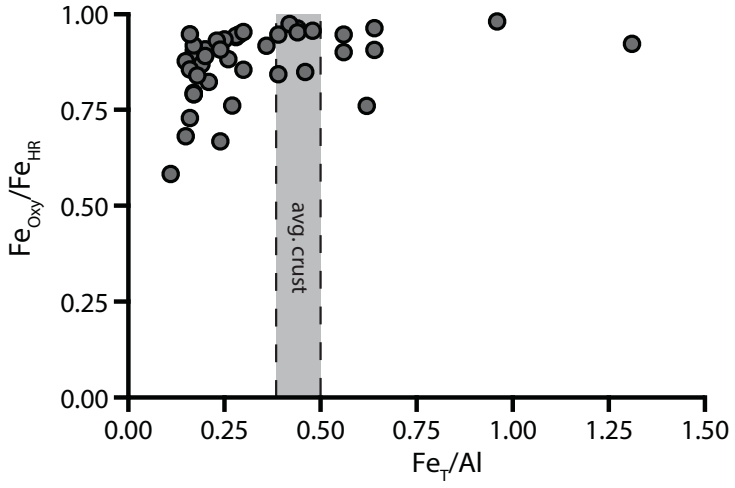

Figure 12: Cross-plot of the ratios of total iron to aluminum (Fe_T/Al) versus iron oxy(hydr)oxide to highly reactive iron (Fe_{Oxy}/Fe_{HR}).

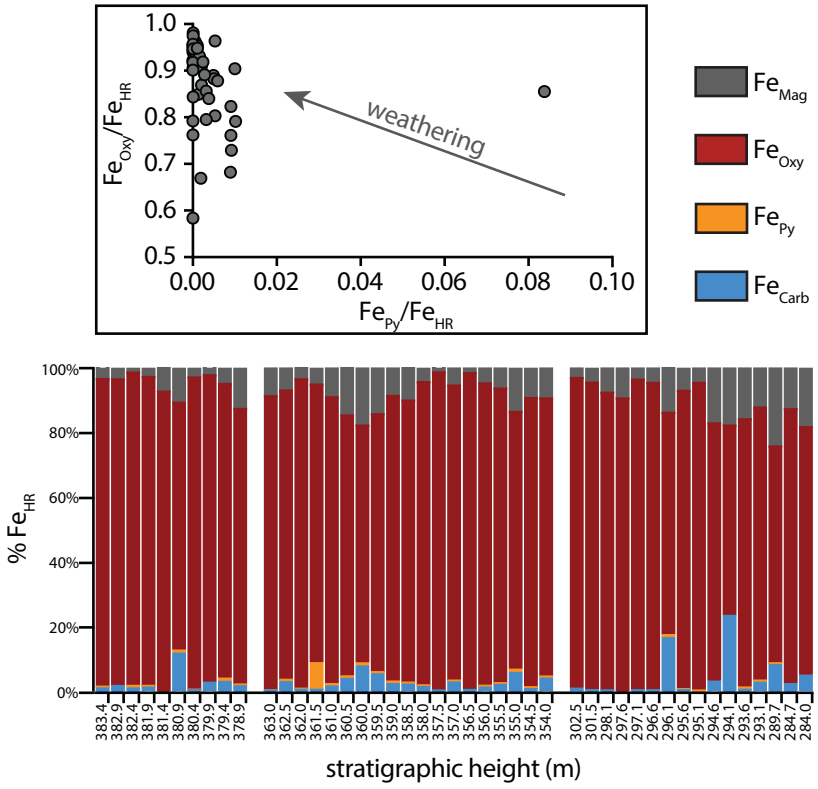

Figure 13: Overview of iron speciation results. Cross-plot of the ratios of pyrite iron to highly reactive iron (Fe_{Py}/Fe_{HR}) versus iron oxy(hydr)oxide to highly reactive iron (Fe_{Oxy}/Fe_{HR}). The arrow shows the trend from oxidative weathering of pyrite (Ahm et al., 2017). Proportion of highly reactive iron (% Fe_{HR}) from carbonate (Fe_{Carb}), pyrite (Fe_{Py}), oxy(hydr)oxide (Fe_{Oxide}); and magnetite (Fe_{Mag}).

References

Adelson, J. M., Helz, G. R., and Miller, C. V., 2001, Reconstructing the rise of recent coastal anoxia; molybdenum in Chesapeake Bay sediments: Geochimica et Cosmochimica Acta, v. 65, p. 237-252.

Ader, M., Sansjofre, P., Halverson, G. P., Busigny, V., Trindade, R. I. F., Kunzmann, M., and Nogueira, A. C. R., 2014, Ocean redox structure across the Late Neoproterozoic Oxygenation Event: A nitrogen isotope perspective: Earth and Planetary Science Letters, v. 396, p. 1-13.

Ahm, A. S. C., Bjerrum, C. J., and Hammarlund, E. U., 2017, Disentangling the record of diagenesis, local redox conditions, and global seawater chemistry during the latest Ordovician glaciation: Earth and Planetary Science Letters, v. 459, p. 145-156.

Algeo, T. J., 2004, Can marine anoxic events draw down the trace element inventory of seawater?: Geology, v. 32, p. 1057-1054.

Algeo, T. J., and Lyons, T. W., 2006, Mo-total organic carbon covariation in modern anoxic marine environments: Implications for analysis of paleoredox and paleohydrographic conditions: Paleoceanography, v. 21, p. 23.

Algeo, T. J., Lyons, T. W., Blakey, R. C., and Over, D. J., 2007, Hydrographic conditions of the Devono-Carboniferous North American Seaway inferred from sedimentary Mo-TOC relationships: Palaeogeography Palaeoclimatology Palaeoecology, v. 256, p. 204-230.

Algeo, T. J., and Tribovillard, N., 2009, Environmental analysis of paleoceanographic systems based on molybdenum-uranium covariation: Chemical Geology, v. 268, p. 211-225.

Anbar, A. D., Jarzecki, A. A., and Spiro, T. G., 2005, Theoretical investigation of iron isotope fractionation between Fe(H2O)63+ and Fe(H2O)62+: Implications for iron stable isotope geochemistry: Geochimica et Cosmochimica Acta, v. 69, p. 825-837.

Anbar, A. D., and Rouxel, O., 2007, Metal stable isotopes in paleoceanography: Annual Review of Earth and Planetary Sciences, v. 35, p. 717-746.

Andersen, T., and Raiswell, R., 2004, Sources and mechanisms for the enrichment of highly reactive iron in euxinic Black Sea sediments: American Journal of Science, v. 304, p. 203-233.

Anderson, T. M., Neiwert, W. A., Kirk, M. L., Piccoli, P. M., Schultz, A. J., Koetzle, T. F., Musaev, D. G., Morokuma, K., Cao, R., and Hill, C. L., 2004, A late-transition metal oxo complex: K7Na9[O=PtIV(H2O)L2], L = [PW9O34]9: Science, v. 306, p. 2074-2077.

Asael, D., Tissot, F. L. H., Reinhard, C. T., Rouxel, O., Dauphas, N., Lyons, T. W., Ponzevera, E., Liorzou, C., and Cheron, S., 2013, Coupled molybdenum, iron and uranium stable isotopes as oceanic paleoredox proxies during the Paleoproterozoic Shunga Event: Chemical Geology, v. 362, p. 193-210.

Balci, N., Bullen, T. D., Witte-Lien, K., Shanks, W. C., Motelica, M., and Mandernack, K. W., 2006, Iron isotope fractionation during microbially stimulated Fe(II) oxidation and Fe(III) precipitation: Geochimica et Cosmochimica Acta, v. 70, p. 622-639.

Bau, M., Hohndorf, A., Dulski, P., and Beukes, N. J., 1997, Sources of rare-earth elements and iron in paleoproterozoic iron-formations from the Transvaal Supergroup, South Africa: Evidence from neodymium isotopes: Journal of Geology, v. 105, p. 121-129.

Beard, B. L., Handler, R. M., Scherer, M. M., Wu, L. L., Czaja, A. D., Heimann, A., and Johnson, C. M., 2010, Iron isotope fractionation between aqueous ferrous iron and goethite: Earth and Planetary Science Letters, v. 295, p. 241-250.

Beard, B. L., and Johnson, C. M., 2004, Fe isotope variations in the modern and ancient earth and other planetary bodies: Geochemistry of Non-Traditional Stable Isotopes, v. 55, p. 319-357.

Beard, B. L., Johnson, C. M., Cox, L., Sun, H., Nealson, K. H., and Aguilar, C., 1999, Iron isotope biosignatures: Science, v. 285, p. 1889-1892.

Beard, B. L., Johnson, C. M., Skulan, J. L., Nealson, K. H., Cox, L., and Sun, H., 2003a, Application of Fe isotopes to tracing the geochemical and biological cycling of Fe: Chemical Geology, v. 195, p. 87-117.

Beard, B. L., Johnson, C. M., Von Damm, K. L., and Poulson, R. L., 2003b, Iron isotope constraints on Fe cycling and mass balance in oxygenated Earth oceans: Geology, v. 31, p. 629-632.

Bekker, A., and Holland, H. D., 2012, Oxygen overshoot and recovery during the early Paleoproterozoic: Earth and Planetary Science Letters, v. 317, p. 295-304.

Bekker, A., Holland, H. D., Wang, P. L., Rumble, D., 3rd, Stein, H. J., Hannah, J. L., Coetzee, L. L., and Beukes, N. J., 2004, Dating the rise of atmospheric oxygen: Nature, v. 427, p. 117-120.

Bekker, A., Slack, J. F., Planavsky, N., Krapez, B., Hofmann, A., Konhauser, K. O., and Rouxel, O. J., 2010, Iron Formation: The Sedimentary Product of a Complex Interplay among Mantle, Tectonic, Oceanic, and Biospheric Processes: Economic Geology, v. 105, p. 467-508.

Bennett, S. A., Rouxel, O., Schmidt, K., Garbe-Schonberg, D., Statham, P. J., and German, C. R., 2009, Iron isotope fractionation in a buoyant hydrothermal plume, 5 degrees S Mid-Atlantic Ridge: Geochimica et Cosmochimica Acta, v. 73, p. 5619-5634.

Bergquist, B. A., and Boyle, E. A., 2006, Iron isotopes in the Amazon River system: Weathering and transport signatures: Earth and Planetary Science Letters, v. 248, p. 54-68.

Berner, R. A., and Raiswell, R., 1983, Burial of Organic-Carbon and Pyrite Sulfur in Sediments over Phanerozoic Time - a New Theory: Geochimica et Cosmochimica Acta, v. 47, p. 855-862.

Berner, R. A., and Raiswell, R., 1984, C/S method for distinguishing freshwater from marine sedimentary rocks: Geology, v. 12, p. 365-368.

Berney, C., and Pawlowski, J., 2006, A molecular time-scale for eukaryote evolution recalibrated with the continuous microfossil record: Proc Biol Sci, v. 273, p. 1867-1872.

Blamey, N. J. F., Brand, U., Parnell, J., Spear, N., Lecuyer, C., Benison, K., Meng, F. W., and Ni, P., 2016, Paradigm shift in determining Neoproterozoic atmospheric oxygen: Geology, v. 44, p. 651-654.

Brumsack, H. J., 2006, The trace metal content of recent organic carbon-rich sediments: Implications for Cretaceous black shale formation: Palaeogeography Palaeoclimatology Palaeoecology, v. 232, p. 344-361.

Bullen, T. D., White, A. F., Childs, C. W., Vivit, D. V., and Schulz, M. S., 2001, Demonstration of significant abiotic iron isotope fractionation in nature: Geology, v. 29, p. 699-702.

Bura-Nakić, E., Andersen, M. B., Archer, C., Souza, G. F. d., Margus, M., and Vance, D., 2018, Coupled Mo-U abundances and isotopes in a small marine euxinic basin: Constraints on processes in euxinic basins: Geochimica et Cosmochimica Acta, v. 222, p. 212-229.

Calvert, S. E., and Pedersen, T. F., 1993, Geochemistry of Recent Oxic and Anoxic Marine-Sediments - Implications for the Geological Record: Marine Geology, v. 113, p. 67-88.

Canfield, D. E., 2005, The early history of atmospheric oxygen: homage to Robert M. Garrels: Annual Review of Earth and Planetary Sciences, v. 33, p. 1-36.

Canfield, D. E., Poulton, S. W., Knoll, A. H., Narbonne, G. M., Ross, G., Goldberg, T., and Strauss, H., 2008, Ferruginous conditions dominated later neoproterozoic deep-water chemistry: Science, v. 321, p. 949-952.

Canfield, D. E., Poulton, S. W., and Narbonne, G. M., 2007, Late-Neoproterozoic deep-ocean oxygenation and the rise of animal life: Science, v. 315, p. 92-95.

Chever, F., Rouxel, O. J., Croot, P. L., Ponzevera, E., Wuttig, K., and Auro, M., 2015, Total dissolvable and dissolved iron isotopes in the water column of the Peru upwelling regime: Geochimica et Cosmochimica Acta, v. 162, p. 66-82.

Cohen, P. A., and Macdonald, F. A., 2015, The Proterozoic Record of Eukaryotes: Paleobiology, v. 41, p. 610-632.

Cole, D. B., Reinhard, C. T., Wang, X. L., Gueguen, B., Halverson, G. P., Gibson, T., Hodgskiss, M. S. W., McKenzie, N. R., Lyons, T. W., and Planavsky, N. J., 2016, A shale-hosted Cr isotope record of low atmospheric oxygen during the Proterozoic: Geology, v. 44, p. 555-558.

Cole, D. B., Zhang, S., and Planavsky, N. J., 2017, A new estimate of detrital redox-sensitive metal concentrations and variability in fluxes to marine sediments: Geochimica et Cosmochimica Acta, v. 215, p. 337-353.

Conway, T. M., and John, S. G., 2014, Quantification of dissolved iron sources to the North Atlantic Ocean: Nature, v. 511, p. 212-215.

Cox, G. M., Jarrett, A., Edwards, D., Crockford, P. W., Halverson, G. P., Collins, A. S., Poirier, A., and Li, Z. X., 2016, Basin redox and primary productivity within the Mesoproterozoic Roper Seaway: Chemical Geology, v. 440, p. 101-114.

Craig, H., 1957, Isotopic standards for carbon and oxygen and correction factors for mass-spectrometric analysis of carbon dioxide: Geochimica et cosmochimica acta, v. 12 , p. 133-149.

Croal, L. R., Johnson, C. M., Beard, B. L., and Newman, D. K., 2004, Iron isotope fractionation by Fe(II)-oxidizing photoautotrophic bacteria: Geochimica et Cosmochimica Acta, v. 68, p. 1227-1242.

Crosby, H. A., Johnson, C. M., Roden, E. E., and Beard, B. L., 2005, Coupled Fe(II)-Fe(III) electron and atom exchange as a mechanism for Fe isotope fractionation during dissimilatory iron oxide reduction: Environmental Science & Technology, v. 39, p. 6698-6704.

Crosby, H. A., Roden, E. E., Johnson, C. M., and Beard, B. L., 2007, The mechanisms of iron isotope fractionation produced during dissimilatory Fe(III) reduction by Shewanella putrefaciens and Geobacter sulfurreducens: Geobiology, v. 5, p. 169-189.

Crowe, S. A., Jones, C., Katsev, S., Magen, C., O'Neill, A. H., Sturm, A., Canfield, D. E., Haffner, G. D., Mucci, A., Sundby, B., and Fowle, D. A., 2008, Photoferrotrophs thrive in an Archean Ocean analogue: Proc Natl Acad Sci U S A, v. 105, p. 15938-15943.

Crusius, J., Calvert, S., Pedersen, T., and Sage, D., 1996, Rhenium and molybdenum enrichments in sediments as indicators of oxic, suboxic and sulfidic conditions of deposition: Earth and Planetary Science Letters, v. 145, p. 65-78.

Cullen, J. T., Chong, M., and Ianson, D., 2009, British Columbian continental shelf as a source of dissolved iron to the subarctic northeast Pacific Ocean: Global Biogeochemical Cycles, v. 23.

Dahl, T. W., Chappaz, A., Hoek, J., McKenzie, C. J., Svane, S., and Canfield, D. E., 2017, Evidence of molybdenum association with particulate organic matter under sulfidic conditions: Geobiology, v. 15, p. 311-323.

Dahl, T. W., Hammarlund, E. U., Anbar, A. D., Bond, D. P., Gill, B. C., Gordon, G. W., Knoll, A. H., Nielsen, A. T., Schovsbo, N. H., and Canfield, D. E., 2010, Devonian rise in atmospheric oxygen correlated to the radiations of terrestrial plants and large predatory fish: Procedings of the National Academy of Science, U.S.A, v. 107, p. 17911-17915.

Dale, A. W., Nickelsen, L., Scholz, F., Hensen, C., Oschlies, A., and Wallmann, K., 2015, A revised global estimate of dissolved iron fluxes from marine sediments: Global Biogeochemical Cycles, v. 29, p. 691-707.

Dauphas, N., John, S. G., and Rouxel, O., 2017, Iron Isotope Systematics: Non-Traditional Stable Isotopes, v. 82, p. 415-510.

Dauphas, N., and Rouxel, O., 2006, Mass spectrometry and natural variations of iron isotopes: Mass Spectrom Rev, v. 25, p. 515-550.

Dellwig, O., Leipe, T., Marz, C., Glockzin, M., Pollehne, F., Schnetger, B., Yakushev, E. V., Bottcher, M. E., and Brumsack, H. J., 2010, A new particulate Mn-Fe-P-shuttle at the redox boundary of anoxic basins: Geochimica et Cosmochimica Acta, v. 74, p. 7100-7115.

Derry, L. A., and Jacobsen, S. B., 1990, The Chemical Evolution of Precambrian Seawater - Evidence from Rees in Banded Iron Formations: Geochimica et Cosmochimica Acta, v. 54, p. 2965-2977.

Diamond, C., Planavsky, N., Wang, C., and Lyons, T., 2018, What the~ 1.4 Ga Xiamaling Formation can and cannot tell us about the mid-Proterozoic ocean: Geobiology, v. 16, p. 219-236.

Dohrmann, M., and Worheide, G., 2017, Dating early animal evolution using phylogenomic data: Sci Rep, v. 7, p. 3599.

Duce, R. A., and Tindale, N. W., 1991, Atmospheric Transport of Iron and Its Deposition in the Ocean: Limnology and Oceanography, v. 36, p. 1715-1726.

Elrod, V. A., Johnson, K. S., Fitzwater, S. E., and Plant, J. N., 2008, A long-term, high-resolution record of surface water iron concentrations in the upwelling-driven central California region: Journal of Geophysical Research-Oceans, v. 113, p. 1-13.

Emerson, S. R., and Huested, S. S., 1991, Ocean Anoxia and the Concentrations of Molybdenum and Vanadium in Seawater: Marine Chemistry, v. 34, p. 177-196.

Erickson, B. E., and Helz, G. R., 2000, Molybdenum(VI) speciation in sulfidic waters: Stability and lability of thiomolybdates: Geochimica et Cosmochimica Acta, v. 64, p. 1149-1158.

Erwin, D. H., Laflamme, M., Tweedt, S. M., Sperling, E. A., Pisani, D., and Peterson, K. J., 2011, The Cambrian conundrum: early divergence and later ecological success in the early history of animals: Science, v. 334, p. 1091-1097.

Fan, H. F., Zhu, X. K., Wen, H. J., Yan, B., Li, J., and Feng, L. J., 2014, Oxygenation of Ediacaran Ocean recorded by iron isotopes: Geochimica et Cosmochimica Acta, v. 140, p. 80-94.

Fantle, M. S., and DePaolo, D. J., 2004, Iron isotopic fractionation during continental weathering: Earth and Planetary Science Letters, v. 228, p. 547-562.

Farquhar, J., Bao, H., and Thiemens, M., 2000, Atmospheric influence of Earth's earliest sulfur cycle: Science, v. 289, p. 756-759.

Fike, D. A., Grotzinger, J. P., Pratt, L. M., and Summons, R. E., 2006, Oxidation of the Ediacaran ocean: Nature, v. 444, p. 744-747.

Fischer, W. W., and Knoll, A. H., 2009, An iron shuttle for deepwater silica in Late Archean and early Paleoproterozoic iron formation: Geological Society of America Bulletin, v. 121, p. 222-235.

Force, E. R., and Cannon, W. F., 1988, Depositional Model for Shallow-Marine Manganese Deposits around Black Shale Basins: Economic Geology, v. 83, p. 93-117.

Frei, R., Gaucher, C., Poulton, S. W., and Canfield, D. E., 2009, Fluctuations in Precambrian atmospheric oxygenation recorded by chromium isotopes: Nature, v. 461, p. 250-253.

Frierdich, A. J., Beard, B. L., Reddy, T. R., Scherer, M. M., and Johnson, C. M., 2014a, Iron isotope fractionation between aqueous Fe(II) and goethite revisited: New insights based on a multi-direction approach to equilibrium and isotopic exchange rate modification: Geochimica et Cosmochimica Acta, v. 139, p. 383-398.

Frierdich, A. J., Beard, B. L., Scherer, M. M., and Johnson, C. M., 2014b, Determination of the Fe(II)(aq)-magnetite equilibrium iron isotope fractionation factor using the three-isotope method and a multi-direction approach to equilibrium: Earth and Planetary Science Letters, v. 391, p. 77-86.

Fung, I. Y., Meyn, S. K., Tegen, I., Doney, S. C., John, J. G., and Bishop, J. K. B., 2000, Iron supply and demand in the upper ocean: Global Biogeochemical Cycles, v. 14, p. 281-295.

Gilleaudeau, G. J., Frei, R., Kaufman, A. J., Kah, L. C., Azmy, K., Bartley, J. K., Chernyavskiy, P., and Knoll, A. H., 2016, Oxygenation of the mid-Proterozoic atmosphere: clues from chromium isotopes in carbonates: Geochemical Perspectives Letters, v. 2, p. 178-186.

Gilleaudeau, G. J., and Kah, L. C., 2015, Heterogeneous redox conditions and a shallow chemocline in the Mesoproterozoic ocean: Evidence from carbon-sulfur-iron relationships: Precambrian Research, v. 257, p. 94-108.

Guilbaud, R., Butler, I. B., Ellam, R. M., and Rickard, D., 2010, Fe isotope exchange between Fe(II)(aq) and nanoparticulate mackinawite (FeSm) during nanoparticle growth: Earth and Planetary Science Letters, v. 300, p. 174-183.

Guilbaud, R., Poulton, S. W., Butterfield, N. J., Zhu, M. Y., and Shields-Zhou, G. A., 2015, A global transition to ferruginous conditions in the early Neoproterozoic oceans: Nature Geoscience, v. 8, p. 466-468.

Gumsley, A. P., Chamberlain, K. R., Bleeker, W., Soderlund, U., de Kock, M. O., Larsson, E. R., and Bekker, A., 2017, Timing and tempo of the Great Oxidation Event: Proc Natl Acad Sci U S A, v. 114, p. 1811-1816.

Halverson, G. P., Hoffman, P. F., Schrag, D. P., Maloof, A. C., and Rice, A. H. N., 2005, Toward a Neoproterozoic composite carbon-isotope record: Geological Society of America Bulletin, v. 117, p. 1181-1207.

Halverson, G. P., Macdonald, F. A., Strauss, J. V., Cox, G. M., and Hubert-Theou, L., 2012, Updated definition and correlation of the lower Fifteenmile Group in the central and eastern Ogilvie Mountains: Yukon Exploration and Geology 2011 p. 75-90.

Halverson, G. P., Maloof, A. C., Schrag, D. P., Dudas, F. O., and Hurtgen, M., 2007, Stratigraphy and geochemistry of a ca 800 Ma negative carbon isotope interval in northeastern Svalbard: Chemical Geology, v. 237, p. 5-27.

Hardisty, D. S., Lu, Z. L., Planavsky, N. J., Bekker, A., Philippot, P., Zhou, X. L., and Lyons, T. W., 2014, An iodine record of Paleoproterozoic surface ocean oxygenation: Geology, v. 42, p. 619-622.

Helz, G. R., Miller, C. V., Charnock, J. M., Mosselmans, J. F. W., Pattrick, R. A. D., Garner, C. D., and Vaughan, D. J., 1996, Mechanism of molybdenum removal from the sea and its concentration in black shales: EXAFS evidence: Geochimica et Cosmochimica Acta, v. 60, p. 3631-3642.

Holland, H. D., 2006, The oxygenation of the atmosphere and oceans: Philos Trans R Soc Lond B Biol Sci, v. 361, p. 903-915.

Homoky, W. B., John, S. G., Conway, T. M., and Mills, R. A., 2013, Distinct iron isotopic signatures and supply from marine sediment dissolution: Nature Commununications, v. 4, p. 2143.

Homoky, W. B., Severmann, S., Mills, R. A., Statham, P. J., and Fones, G. R., 2009, Pore-fluid Fe isotopes reflect the extent of benthic Fe redox recycling: Evidence from continental shelf and deep-sea sediments: Geology, v. 37, p. 751-754.

Icopini, G. A., Anbar, A. D., Ruebush, S. S., Tien, M., and Brantley, S. L., 2004, Iron isotope fractionation during microbial reduction of iron: The importance of adsorption: Geology, v. 32, p. 205-208.

Ingri, J., Malinovsky, D., Rodushkin, I., Baxter, D. C., Widerlund, A., Andersson, P., Gustafsson, O., Forsling, W., and Ohlander, B., 2006, Iron isotope fractionation in river colloidal matter: Earth and Planetary Science Letters, v. 245, p. 792-798.

Isley, A. E., 1995, Hydrothermal Plumes and the Delivery of Iron to Banded Iron-Formation: Journal of Geology, v. 103, p. 169-185.

John, S. G., Mendez, J., Moffett, J., and Adkins, J., 2012, The flux of iron and iron isotopes from San Pedro Basin sediments: Geochimica et Cosmochimica Acta, v. 93, p. 14-29.

Johnson, C. M., and Beard, B. L., 2005, Geochemistry. Biogeochemical cycling of iron isotopes: Science, v. 309, p. 1025-1027.

Johnson, C. M., Beard, B. L., Beukes, N. J., Klein, C., and O'Leary, J. M., 2003, Ancient geochemical cycling in the Earth as inferred from Fe isotope studies of banded iron formations from the Transvaal Craton: Contributions to Mineralogy and Petrology, v. 144, p. 523-547.

Johnson, C. M., Beard, B. L., Klein, C., Beukes, N. J., and Roden, E. E., 2008a, Iron isotopes constrain biologic and abiologic processes in banded iron formation genesis: Geochimica et Cosmochimica Acta, v. 72, p. 151-169.

Johnson, C. M., Beard, B. L., and Roden, E. E., 2008b, The iron isotope fingerprints of redox and biogeochemical cycling in the modern and ancient Earth: Annual Review of Earth and Planetary Sciences, v. 36, p. 457-493.

Johnson, C. M., Beard, B. L., Roden, E. E., Newman, D. K., and Nealson, K. H., 2004, Isotopic constraints on biogeochemical cycling of Fe: Geochemistry of Non-Traditional Stable Isotopes, v. 55, p. 359-408.

Johnson, C. M., Roden, E. E., Welch, S. A., and Beard, B. L., 2005, Experimental constraints on Fe isotope fractionation during magnetite and Fe carbonate formation coupled to dissimilatory hydrous ferric oxide reduction: Geochimica et Cosmochimica Acta, v. 69, p. 963-993.

Johnson, C. M., Skulan, J. L., Beard, B. L., Sun, H., Nealson, K. H., and Braterman, P. S., 2002, Isotopic fractionation between Fe(III) and Fe(II) in aqueous solutions: Earth and Planetary Science Letters, v. 195, p. 141-153.

Johnston, D. T., Poulton, S. W., Dehler, C., Porter, S., Husson, J., Canfield, D. E., and Knoll, A. H., 2010, An emerging picture of Neoproterozoic ocean chemistry: Insights from the Chuar Group, Grand Canyon, USA: Earth and Planetary Science Letters, v. 290, p. 64-73.

Kappler, A., Pasquero, C., Konhauser, K. O., and Newman, D. K., 2005, Deposition of banded iron formations by anoxygenic phototrophic Fe(II)-oxidizing bacteria: Geology, v. 33, p. 865-868.

Klar, J. K., James, R. H., Gibbs, D., Lough, A., Parkinson, I., Milton, J. A., Hawkes, J. A., and Connelly, D. P., 2017, Isotopic signature of dissolved iron delivered to the Southern Ocean from hydrothermal vents in the East Scotia Sea: Geology, v. 45, p. 351-354.

Knoll, A. H., 2014, Paleobiological perspectives on early eukaryotic evolution: Cold Spring Harb Perspect Biol, v. 6, p. a016121-a016121.

Konhauser, K. O., Hamade, T., Raiswell, R., Morris, R. C., Grant Ferris, F., Southam, G., and Canfield, D. E., 2002, Could bacteria have formed the Precambrian banded iron formations?: Geology, v. 30, p. 1079-1082.

Konhauser, K. O., Newman, D. K., and Kappler, A., 2005, The potential significance of microbial Fe(III) reduction during deposition of Precambrian banded iron formations: Geobiology, v. 3, p. 167-177.

Krapez, B., Barley, M. E., and Pickard, A. L., 2003, Hydrothermal and resedimented origins of the precursor sediments to banded iron formation: sedimentological evidence from the Early Palaeoproterozoic Brockman Supersequence of Western Australia: Sedimentology, v. 50, p. 979-1011.

Kunzmann, M., Bui, T. H., Crockford, P. W., Halverson, G. P., Scott, C., Lyons, T. W., and Wing, B. A., 2017a, Bacterial sulfur disproportionation constrains timing of Neoproterozoic oxygenation: Geology, v. 45, p. 207-210.

Kunzmann, M., Gibson, T. M., Halverson, G. P., Hodgskiss, M. S. W., Bui, T. H., Carozza, D. A., Sperling, E. A., Poirier, A., Cox, G. M., and Wing, B. A., 2017b, Iron isotope biogeochemistry of Neoproterozoic marine shales: Geochimica et Cosmochimica Acta, v. 209, p. 85-105.

Kunzmann, M., Halverson, G. P., Hodgskiss, M. S. W., Sansjofre, P., and Schumann, D., 2014, The early Neoproterozoic Chandindu Formation of the Fifteenmile Group in the ogilvie Mountains: Yukon Explorationand Geology, p. 93-107.

Kunzmann, M., Halverson, G. P., Scott, C., Minarik, W. G., and Wing, B. A., 2015, Geochemistry of Neoproterozoic black shales from Svalbard: Implications for oceanic redox conditions spanning Cryogenian glaciations: Chemical Geology, v. 417, p. 383-393.

Lau, K. V., Macdonald, F. A., Maher, K., and Payne, J. L., 2017, Uranium isotope evidence for temporary ocean oxygenation in the aftermath of the Sturtian Snowball Earth: Earth and Planetary Science Letters, v. 458, p. 282-292.

Liu, X. M., Kah, L. C., Knoll, A. H., Cui, H., Kaufman, A. J., Shahar, A., and Hazen, R. M., 2016, Tracing Earth's O2 evolution using Zn/Fe ratios in marine carbonates: Geochemical Perspectives Letters, v. 2, p. 24-34.

Lohan, M. C., and Bruland, K. W., 2008, Elevated Fe(II) and dissolved Fe in hypoxic shelf waters off Oregon and Washington: an enhanced source of iron to coastal upwelling regimes: Environmental Science and Technology, v. 42, p. 6462-6468.

Lyons, T. W., Anbar, A. D., Severmann, S., Scott, C., and Gill, B. C., 2009, Tracking Euxinia in the Ancient Ocean: A Multiproxy Perspective and Proterozoic Case Study: Annual Review of Earth and Planetary Sciences, v. 37, p. 507-534.

Lyons, T. W., and Severmann, S., 2006, A critical look at iron paleoredox proxies: New insights from modern euxinic marine basins: Geochimica et Cosmochimica Acta, v. 70, p. 5698-5722.

Macdonald, F. A., Halverson, G. P., Strauss, J. V., Smith, E. F., Cox, G., Sperling, E. A., and Roots, C. F., 2012, Early Neoproterozoic Basin Formation in Yukon, Canada: Implications for the make-up and break-up of Rodinia: Geoscience Canada, v. 39, p. 77-99.

Macdonald, F. A., and Roots, C. F., 2010, Upper Fifteenmile Group in the ogilvie Mountains and correlations of early neoproterozoic strata in the northern Cordillera: Yukon Exploration and Geology 2009, p. 237-252.

Macdonald, F. A., Schmitz, M. D., Crowley, J. L., Roots, C. F., Jones, D. S., Maloof, A. C., Strauss, J. V., Cohen, P. A., Johnston, D. T., and Schrag, D. P., 2010, Calibrating the Cryogenian: Science, v. 327, p. 1241-1243.

Macdonald, F. A., Smith, E. F., Strauss, J. V., Cox, G. M., Halverson, G. P., and Roots, C. F., 2011, Neoproterozoic and early paleozoic correlations in the western ogilvie Mountains, Yukon: Yukon Exploration and Geology 2009, p. 161-182.

Magyar, B., Moor, H. C., and Sigg, L., 1993, Vertical-Distribution and Transport of Molybdenum in a Lake with a Seasonally Anoxic Hypolimnion: Limnology and Oceanography, v. 38, p. 521-531.

Matthews, A., Morgans-Bell, H. S., Emmanuel, S., Jenkyns, H. C., Erel, Y., and Halicz, L., 2004, Controls on iron-isotope fractionation in organic-rich sediments (Kimmeridge Clay, Upper Jurassic, southern England): Geochimica et Cosmochimica Acta, v. 68, p. 3107-3123.

McLennan, S. M., 2001, Relationships between the trace element composition of sedimentary rocks and upper continental crust: Geochemistry Geophysics Geosystems, v. 2, p. 1-24.

Medig, K. P. R., Thorkelson, D. J., Davis, W. J., Gibson, H. D., Rainbird, R. H., and Marshall, D. D., 2012, The Proterozoic Pinguicula Group, Wernecke Mountains, Yukon: A siliciclastic and carbonate slope to basin succession with local and exotic sediment provenance: Yukon Exploration and Geology 2011, p. 129-149.

Murray, J. W., 1975, The interaction of metal ions at the manganese dioxide-solution interface: Geochimica et Cosmochimica Acta, v. 39, p. 505-519.

Noffke, A., Hensen, C., Sommer, S., Scholz, F., Bohlen, L., Mosch, T., Graco, M., and Wallmann, K., 2012, Benthic iron and phosphorus fluxes across the Peruvian oxygen minimum zone: Limnology and Oceanography, v. 57, p. 851-867.

Obrien, G. W., Milnes, A. R., Veeh, H. H., Heggie, D. T., Riggs, S. R., Cullen, D. J., Marshall, J. F., and Cook, P. J., 1990, Sedimentation Dynamics and Redox Iron-Cycling - Controlling Factors for the Apatite-Glauconite Association on the East Australian Continental-Margin: Phosphorite Research and Development, v. 52, p. 61-86.

Parfrey, L. W., Lahr, D. J., Knoll, A. H., and Katz, L. A., 2011, Estimating the timing of early eukaryotic diversification with multigene molecular clocks: Proceedings of the National Academy of Science U.S.A., v. 108, p. 13624-13629.

Partin, C. A., Bekker, A., Planavsky, N. J., Scott, C. T., Gill, B. C., Li, C., Podkovyrov, V., Maslov, A., Konhauser, K. O., Lalonde, S. V., Love, G. D., Poulton, S. W., and Lyons, T. W., 2013a, Large-scale fluctuations in Precambrian atmospheric and oceanic oxygen levels from the record of U in shales: Earth and Planetary Science Letters, v. 369, p. 284-293.

Partin, C. A., Lalonde, S. V., Planavsky, N. J., Bekker, A., Rouxel, O. J., Lyons, T. W., and Konhauser, K. O., 2013b, Uranium in iron formations and the rise of atmospheric oxygen: Chemical Geology, v. 362, p. 82-90.

Pavlov, A. A., and Kasting, J. F., 2004, Mass-Independent Fractionation of Sulfur Isotopes in Archean Sediments: Strong Evidence for an Anoxic Archean Atmosphere: Astrobiology, v. 2, p. 27-41.

Planavsky, N., Rouxel, O. J., Bekker, A., Hofmann, A., Little, C. T. S., and Lyons, T. W., 2012a, Iron isotope composition of some Archean and Proterozoic iron formations: Geochimica et Cosmochimica Acta, v. 80, p. 158-169.

Planavsky, N. J., Bekker, A., Hofmann, A., Owens, J. D., and Lyons, T. W., 2012b, Sulfur record of rising and falling marine oxygen and sulfate levels during the Lomagundi event: Proc Natl Acad Sci U S A, v. 109, p. 18300-18305.

Planavsky, N. J., Cole, D. B., Reinhard, C. T., Diamond, C., Love, G. D., Luo, G., Zhang, S., Konhauser, K. O., and Lyons, T. W., 2016, No evidence for high atmospheric oxygen levels 1,400 million years ago: Proceedings of the National Academy of Science US.A., v. 113, p. E2550-2551.

Planavsky, N. J., McGoldrick, P., Scott, C. T., Li, C., Reinhard, C. T., Kelly, A. E., Chu, X., Bekker, A., Love, G. D., and Lyons, T. W., 2011, Widespread iron-rich conditions in the mid-Proterozoic ocean: Nature, v. 477, p. 448-451.

Planavsky, N. J., Reinhard, C. T., Wang, X., Thomson, D., McGoldrick, P., Rainbird, R. H., Johnson, T., Fischer, W. W., and Lyons, T. W., 2014, Earth history. Low mid-Proterozoic atmospheric oxygen levels and the delayed rise of animals: Science, v. 346, p. 635-638.

Poulton, S. W., and Canfield, D. E., 2005, Development of a sequential extraction procedure for iron: implications for iron partitioning in continentally derived particulates: Chemical Geology, v. 214, p. 209-221.

Poulton, S. W., and Canfield, D. E., 2011, Ferruginous Conditions: A Dominant Feature of the Ocean through Earth's History: Elements, v. 7, p. 107-112.

Poulton, S. W., Fralick, P. W., and Canfield, D. E., 2010, Spatial variability in oceanic redox structure 1.8 billion years ago: Nature Geoscience, v. 3, p. 486-490.

Poulton, S. W., and Raiswell, R., 2002, The low-temperature geochemical cycle of iron: From continental fluxes to marine sediment deposition: American Journal of Science, v. 302, p. 774-805.

Rainbird, R. H., McNicoll, V. J., Thériault, R. J., Heaman, L. M., Abbott, J. G., Long, D. G. F., and Thorkelson, D. J., 1997, Pan-continental River System Draining Grenville Orogen

Recorded by U-Pb and Sm-Nd Geochronology of Neoproterozoic Quartzarenitesand Mudrocks, Northwestern Canada: Journal of Geology, v. 105, p. 1-17.

Raiswell, R., 2011a, Iceberg-hosted nanoparticulate Fe in the Southern Ocean: Mineralogy, origin, dissolution kinetics and source of bioavailable Fe: Deep-Sea Research Part Ii-Topical Studies in Oceanography, v. 58, p. 1364-1375.

Raiswell, R., 2011b, Iron Transport from the Continents to the Open Ocean: The Aging-Rejuvenation Cycle: Elements, v. 7, p. 101-106.

Raiswell, R., and Berner, R. A., 1985, Pyrite Formation in Euxinic and Semi-Euxinic Sediments: American Journal of Science, v. 285, p. 710-724.

Raiswell, R., 1986, Pyrite and Organic-Matter in Phanerozoic Normal Marine Shales: Geochimica et Cosmochimica Acta, v. 50, p. 1967-1976.

Raiswell, R., and Canfield, D. E., 1998, Sources of iron for pyrite formation in marine sediments: American Journal of Science, v. 298, p. 219-245.

Raiswell, R., Hardisty, D., Lyons, T., Canfield, D., Owens, J., Planavsky, N., Poulton, S., and Reinhard, C., 2018, The iron paleoredox proxies: A guide to the pitfalls, problems and proper practice: American Journal of Science.

Reinhard, C. T., Planavsky, N. J., Robbins, L. J., Partin, C. A., Gill, B. C., Lalonde, S. V., Bekker, A., Konhauser, K. O., and Lyons, T. W., 2013, Proterozoic ocean redox and biogeochemical stasis: Proceedings of the National Academy of Sciences U.S.A., v. 110, p. 5357-5362.

Rooney, A. D., Strauss, J. V., Brandon, A. D., and Macdonald, F. A., 2015, A Cryogenian chronology: Two long-lasting synchronous Neoproterozoic glaciations: Geology, v. 43, p. 459-462.

Rouxel, O., Shanks, W. C., Bach, W., and Edwards, K. J., 2008, Integrated Fe- and S-isotope study of seafloor hydrothermal vents at East Pacific rise 9-10 degrees N: Chemical Geology, v. 252, p. 214-227.

Rouxel, O. J., and Auro, M., 2010, Iron Isotope Variations in Coastal Seawater Determined by Multicollector ICP-MS: Geostandards and Geoanalytical Research, v. 34, p. 135-144.

Rouxel, O. J., Bekker, A., and Edwards, K. J., 2005, Iron isotope constraints on the Archean and Paleoproterozoic ocean redox state: Science, v. 307, p. 1088-1091.

Rowe, H. D., Loucks, R. G., Ruppel, S. C., and Rimmer, S. M., 2008, Mississippian Barnett Formation, Fort Worth Basin, Texas: Bulk geochemical inferences and Mo-TOC constraints on the severity of hydrographic restriction: Chemical Geology, v. 257, , p. 16-25.

Sahoo, S. K., Planavsky, N. J., Jiang, G., Kendall, B., Owens, J. D., Wang, X., Shi, X., Anbar, A. D., and Lyons, T. W., 2016, Oceanic oxygenation events in the anoxic Ediacaran ocean: Geobiology, v. 14, p. 457-468.

Sahoo, S. K., Planavsky, N. J., Kendall, B., Wang, X., Shi, X., Scott, C., Anbar, A. D., Lyons, T. W., and Jiang, G., 2012, Ocean oxygenation in the wake of the Marinoan glaciation: Nature, v. 489, p. 546-549.

Saito, M. A., Noble, A.E., Tagliabue, A. , Goepfert, T.J., Lamborg, C.H., Jenkins, W.J. , 2013, Slow-spreading submarine ridges in the South Atlantic as a significant oceanic iron source: Nature Geoscience, v. 6, p. 5.

Scholz, F., Severmann, S., McManus, J., and Hensen, C., 2014, Beyond the Black Sea paradigm: The sedimentary fingerprint of an open-marine iron shuttle: Geochimica et Cosmochimica Acta, v. 127, p. 368-380.

Scott, C., and Lyons, T. W., 2012, Contrasting molybdenum cycling and isotopic properties in euxinic versus non-euxinic sediments and sedimentary rocks: Refining the paleoproxies: Chemical Geology, v. 324, p. 19-27.

Scott, C., Lyons, T. W., Bekker, A., Shen, Y., Poulton, S. W., Chu, X., and Anbar, A. D., 2008, Tracing the stepwise oxygenation of the Proterozoic ocean: Nature, v. 452, p. 456-459.

Scott, C., Wing, B. A., Bekker, A., Planavsky, N. J., Medvedev, P., Bates, S. M., Yun, M., and Lyons, T. W., 2014, Pyrite multiple-sulfur isotope evidence for rapid expansion and contraction of the early Paleoproterozoic seawater sulfate reservoir: Earth and Planetary Science Letters, v. 389, p. 95-104.

Scott, C. T., Slack, J. F., and Kelley, K. D., 2017, The hyper-enrichment of V and Zn in black shales of the Late Devonian-Early Mississippian Bakken Formation (USA): Chemical Geology, v. 452, p. 24-33.

Severmann, S., Johnson, C. M., Beard, B. L., German, C. R., Edmonds, H. N., Chiba, H., and Green, D. R. H., 2004, The effect of plume processes on the Fe isotope composition of

hydrothermally derived Fe in the deep ocean as inferred from the Rainbow vent site, Mid-Atlantic Ridge, 36 degrees 14' N: Earth and Planetary Science Letters, v. 225, p. 63-76.

Severmann, S., Johnson, C. M., Beard, B. L., and McManus, J., 2006, The effect of early diagenesis on the Fe isotope compositions of porewaters and authigenic minerals in continental margin sediments: Geochimica et Cosmochimica Acta, v. 70, p. 2006-2022.

Severmann, S., Lyons, T. W., Anbar, A., McManus, J., and Gordon, G., 2008, Modern iron isotope perspective on the benthic iron shuttle and the redox evolution of ancient oceans: Geology, v. 36, p. 487-490.

Severmann, S., McManus, J., Berelson, W. M., and Hammond, D. E., 2010, The continental shelf benthic iron flux and its isotope composition: Geochimica et Cosmochimica Acta, v. 74, p. 3984-4004.

Schaffer, G., 1986, Phosphate pumps and shuttles in the Black Sea: Nature, v. 321, p. 515-517.

Skulan, J. L., Beard, B. L., and Johnson, C. M., 2002, Kinetic and equilibrium Fe isotope fractionation between aqueous Fe(III) and hematite: Geochimica et Cosmochimica Acta, v. 66, p. 2995-3015.

Slotznick, S. P., Eiler, J. M., and Fischer, W. W., 2017, The Effects of Metamorphism on Iron Mineralogy and the Iron Speciation Redox Proxy: Geochimica et Cosmochimica Acta, v. 224, p. 96-115.

Slotznick, S. P., Winston, D., Webb, S. M., Kirschvink, J. L., and Fischer, W. W., 2016, Iron mineralogy and redox conditions during deposition of the mid-Proterozoic Appekunny Formation, Belt Supergroup, Glacier National Park, Belt Basin: Window to Mesoproterozoic Earth, Volume 522, Geological Society of America, p. 221-242.

Slotznick, S. P., Zieg, J., Webb, S. M., Kirschvink, J. L., and Fischer, W. W., 2015, Iron mineralogy and redox chemistry of the Mesoproterozoic Newland Formation in the Helena Embayment, Belt Supergroup, Montana: Journal of the Tobacco Root Geological Society, p. 1-18.

Snyder, R., and Bish, D. L., 1989, Quantitative analysis: Reviews in Mineralogy and Geochemistry, v. 20, p. 101-144.

Sossi, P. A., Halverson, G. P., Nebel, O., and Eggins, S. M., 2015, Combined separation of Cu, Fe and Zn from rock matrices and improved analytical protocols for stable isotope determination: Geostandards and Geoanalytical Research, v. 39, p. 129-149.

Sperling, E. A., Halverson, G. P., Knoll, A. H., Macdonald, F. A., and Johnston, D. T., 2013, A basin redox transect at the dawn of animal life: Earth and Planetary Science Letters, v. 371-372, p. 143-155.

Sperling, E. A., Rooney, A. D., Hays, L., Sergeev, V. N., Vorob'eva, N. G., Sergeeva, N. D., Selby, D., Johnston, D. T., and Knoll, A. H., 2014, Redox heterogeneity of subsurface waters in the Mesoproterozoic ocean: Geobiology, v. 12, p. 373-386.

Sperling, E. A., Wolock, C. J., Morgan, A. S., Gill, B. C., Kunzmann, M., Halverson, G. P., Macdonald, F. A., Knoll, A. H., and Johnston, D. T., 2015, Statistical analysis of iron geochemical data suggests limited late Proterozoic oxygenation: Nature, v. 523, , p. 451-454.

Srodon, J., Drits, V. A., McCarty, D. K., Hsieh, J. C., and Eberl, D. D., 2001, Quantitative X-ray diffraction analysis of clay-bearing rocks from random preparations: Clays and Clay Minerals, v. 49, p. 514-528.

Staubwasser, M., von Blanckenburg, F., and Schoenberg, R., 2006, Iron isotopes in the early marine diagenetic iron cycle: Geology, v. 34, p. 629-632.

Strauss, J. V., Macdonald, F. A., Halverson, G. P., Tosca, N. J., Schrag, D. P., and Knoll, A. H., 2015, Stratigraphic Evolution of the Neoproterozoic Callison Lake Formation: Linking the Break-up of Rodinia to the Islay Carbon Isotope Excursion: American Journal of Science, v. 315, p. 881-944.

Strauss, J. V., Roots, C. F., Macdonald, F. A., Halverson, G. P., Eyster, A., and Colpron, M., 2014, Geological map of the Coal Creek inlier, Ogilvie Mountains (NTS 116B/10-15 and 116C/9,16): 1:100,000 scale.

Sundby, B., 2006, Transient state diagenesis in continental margin mud: Marine chemistry, v. 102, p. 2-12.

Sundby, B., Martinez, P., and Gobeil, C., 2004, Comparative geochemistry of cadmium, rhenium, uranium, and molybdenum in continental margin sediments: Geochimica et Cosmochimica Acta, v. 68, p. 2485-2493.

Swanner, E. D., Wu, W. F., Schoenberg, R., Byrne, J., Michel, F. M., Pan, Y. X., and Kappler, A., 2015, Fractionation of Fe isotopes during Fe(II) oxidation by a marine photoferrotroph is controlled by the formation of organic Fe-complexes and colloidal Fe fractions: Geochimica et Cosmochimica Acta, v. 165, p. 44-61.

Swanson-Hysell, N. L., Maloof, A. C., Condon, D. J., Jenkin, G. R. T., Alene, M., Tremblay, M. M., Tesema, T., Rooney, A. D., and Haileab, B., 2015, Stratigraphy and geochronology of the Tambien Group, Ethiopia: Evidence for globally synchronous carbon isotope change in the Neoproterozoic: Geology, v. 43, p. 323-326.

Tangalos, G. E., Beard, B. L., Johnson, C. M., Alpers, C. N., Shelobolina, E. S., Xu, H., Konishi, H., and Roden, E. E., 2010, Microbial production of isotopically light iron(II) in a modern chemically precipitated sediment and implications for isotopic variations in ancient rocks: Geobiology, v. 8, p. 197-208.

Thomson, D., Rainbird, R. H., Planavsky, N., Lyons, T. W., and Bekker, A., 2015, Chemostratigraphy of the Shaler Supergroup, Victoria Island, NW Canada: A record of ocean composition prior to the Cryogenian glaciations: Precambrian Research, v. 263, p. 232-245.

Toner, B. M., Fakra, S.C., Manganini, S.J., Santelli, C.M., Marcus, M.A., Moffett, J.W., Rouxel, O.J., German, C.R., Edwards, k.J., 2009, Preservation of iron (II) by carbon-rich matrices in a hydrothermal plume: Nature Geoscience, v. 2, p. 5.

Tribovillard, N., Algeo, T. J., Baudin, F., and Riboulleau, A., 2012, Analysis of marine environmental conditions based on molybdenum-uranium covariation-Applications to Mesozoic paleoceanography: Chemical Geology, v. 324, p. 46-58.

Tribovillard, N., Algeo, T. J., Lyons, T., and Riboulleau, A., 2006, Trace metals as paleoredox and paleoproductivity proxies: An update: Chemical Geology, v. 232, p. 12-32.

van Cappellen, P., Viollier, E., Roychoudhury, A., Clark, L., Ingall, E., Lowe, K., and Dichristina, T., 1998, Biogeochemical cycles of manganese and iron at the oxic - anoxic transition of a stratified marine basin (Orca Basin, Gulf of Mexico) Environmental Science and Technology, p. 1-9.

Van der Weijden, C. H., 2002, Pitfalls of normalization of marine geochemical data using a common divisor: Marine Geology, v. 184, p. 167-187.

Vorlicek, T. P., and Helz, G. R., 2002, Catalysis by mineral surfaces: Implications for Mo geochemistry in anoxic environments: Geochimica et Cosmochimica Acta, v. 66, p. 3679-3692.

Vorlicek, T. P., Kahn, M. D., Kasuya, Y., and Helz, G. R., 2004, Capture of molybdenum in pyrite-forming sediments: Role of ligand-induced reduction by polysulfides: Geochimica et Cosmochimica Acta, v. 68, p. 547-556.

Wagner, M., Chappaz, A., and Lyons, T. W., 2017, Molybdenum speciation and burial pathway in weakly sulfidic environments: Insights from XAFS: Geochimica et Cosmochimica Acta, v. 206, p. 18-29.

Wallace, M. W., Hood, A. V. S., Shuster, A., Greig, A., Planavsky, N. J., and Reed, C. P., 2017, Oxygenation history of the Neoproterozoic to early Phanerozoic and the rise of land plants: Earth and Planetary Science Letters, v. 466, p. 12-19.

Welch, S. A., Beard, B. L., Johnson, C. M., and Braterman, P. S., 2003, Kinetic and equilibrium Fe isotope fractionation between aqueous Fe(II) and Fe(III): Geochimica et Cosmochimica Acta, v. 67, p. 4231-4250.

Widdel, F., Schnell, S., Heising, S., Ehrenreich, A., Assmus, B., and Schink, B., 1993, Ferrous Iron Oxidation by Anoxygenic Phototrophic Bacteria: Nature, v. 362, p. 834-836.

Wiesli, R., Beard, B., and Johnson, C., 2004, Experimental determination of Fe isotope fractionation between aqueous Fe(II), siderite and "green rust" in abiotic systems: Chemical Geology, v. 211, p. 343-362.

Wijsman, J. W. M., Middelburg, J. J., and Heip, C. H. R., 2001, Reactive iron in Black Sea Sediments: implications for iron cycling: Marine Geology, v. 172, p. 167-180.

Wilkin, R. T., and Barnes, H. L., 1997, Formation processes of framboidal pyrite: Geochimica et Cosmochimica Acta, v. 61, p. 323-339.

Wilkin, R. T., Barnes, H. L., and Brantley, S. L., 1996, The size distribution of framboidal pyrite in modern sediments: An indicator of redox conditions: Geochimica et Cosmochimica Acta, v. 60, p. 3897-3912.

Wu, L. L., Druschel, G., Findlay, A., Beard, B. L., and Johnson, C. M., 2012, Experimental determination of iron isotope fractionations among Fe-aq(2+)-FeSaq-Mackinawite at low temperatures: Implications for the rock record: Geochimica et Cosmochimica Acta, v. 89, p. 46-61.

Yamaguchi, K. E., Johnson, C. M., Beard, B. L., and Ohmoto, H., 2005, Biogeochemical cycling of iron in the Archean-Paleoproterozoic Earth: Constraints from iron isotope variations in

sedimentary rocks from the Kaapvaal and Pilbara Cratons: Chemical Geology, v. 218, p. 135-169.

Yeung, L. Y., 2017, Low oxygen and argon in the Neoproterozoic atmosphere at 815 Ma: Earth and Planetary Science Letters, v. 480, p. 66-74.

Zhang, F. F., Zhu, X. K., Yan, B., Kendall, B., Peng, X., Li, J., Algeo, T. J., and Romaniello, S., 2015, Oxygenation of a Cryogenian ocean (Nanhua Basin, South China) revealed by pyrite Fe isotope compositions: Earth and Planetary Science Letters, v. 429, p. 11-19.

Zhang, S., Wang, X., Wang, H., Bjerrum, C. J., Hammarlund, E. U., Costa, M. M., Connelly, J. N., Zhang, B., Su, J., and Canfield, D. E., 2016a, Sufficient oxygen for animal respiration 1,400 million years ago: Proceedings of the National Academy of Sciences, v. 113, p. 1731-1736.

Zhang, S., Wang, X., Wang, H., Bjerrum, C. J., Hammarlund, E. U., Dahl, T. W., and Canfield, D. E., 2016b, Reply to Planavsky et al.: Strong evidence for high atmospheric oxygen levels 1,400 million years ago: Proceedings of the National Academy of Sciences, v. 113, p. E2552-2553.

Zheng, Y., Anderson, R. F., van Geen, A., and Kuwabara, J., 2000, Authigenic molybdenum formation in marine sediments: A link to pore water sulfide in the Santa Barbara Basin: Geochimica et Cosmochimica Acta, v. 64, p. 4165-4178.

Zhu, X. K., O'Nions, R. K., Guo, Y., and Reynolds, B. C., 2000, Secular variation of iron isotopes in north atlantic deep water: Science, v. 287, p. 2000-2002.

8. Appendix

8.1. Atlas 5 Image Mosaics

The light microscopy mosaic of sample M103-475.2 and a cell phone overview picture for sample M103-458.3 were imported into the Atlas 5 projects. The entire polished surfaces of sample M103-475.2 was imaged with an accelerating voltage of 15 kV using the backscattered electron (BSE) detector, a working distance of 11 mm, a 120 μm aperture, a 3 μs dwell time, and a resolution of 50 nm/pixel. The resulting large-area mosaic comprises 841 images, with each image tile consisting of 8192 x 8192 pixels (410.3 x 410.3 μm), and a total pixel count of 56.4 gigapixels

(Fig 1A) The large area image mosaic of sample M103-458.3 was also acquired with the BSE detector under the following imaging conditions: accelerating voltage 14kV, working distance 8 mm, 120 µm aperture, 1.6 µs dwell time, 50 nm/pixel, 6000 x 6000 pixels per image (300.1 x 300.1 µm), 671 image tiles, and total pixel count of 24.2 gigapixels. Once the large-area image mosaics were acquired, stitched, and image correction performed, the entire Atlas 5 data sets were exported to an autonomous series of files called the Browser-Based Viewer, which allows anyone on a PC with a web browser to look at the complete data set at full resolution in a similar manner to that known from the application Google Earth™. The computer mouse is used for zooming in and out as well as for navigating through the large area image mosaic. SEM Point analyses can be viewed from the Browser-Based Viewer by clicking with the mouse in the green rectangular regions that mark the locations in which the analyses were performed. After clicking, a new browser window will open and the PDF or the JPG file can be viewed and/or downloaded.

Full Browser-Based Viewer datasets of the shale samples (including SEM data for M103-475.2) can be viewed by following the links:

Sample M103-458.3:
http://www.petapixelproject.com/mosaics/Tim-Gibson/M103_458_3-BBV/M103_458_3-BBV-BSD/index.html

Sample M103-475.2:
http://www.petapixelproject.com/mosaics/Tim-Gibson/M103-475_2-BBV/M103-475_2-BBV-BSD-LM-EDS/M103-475_2-BBV-BSD-LM/index.html

Supplemental Figures

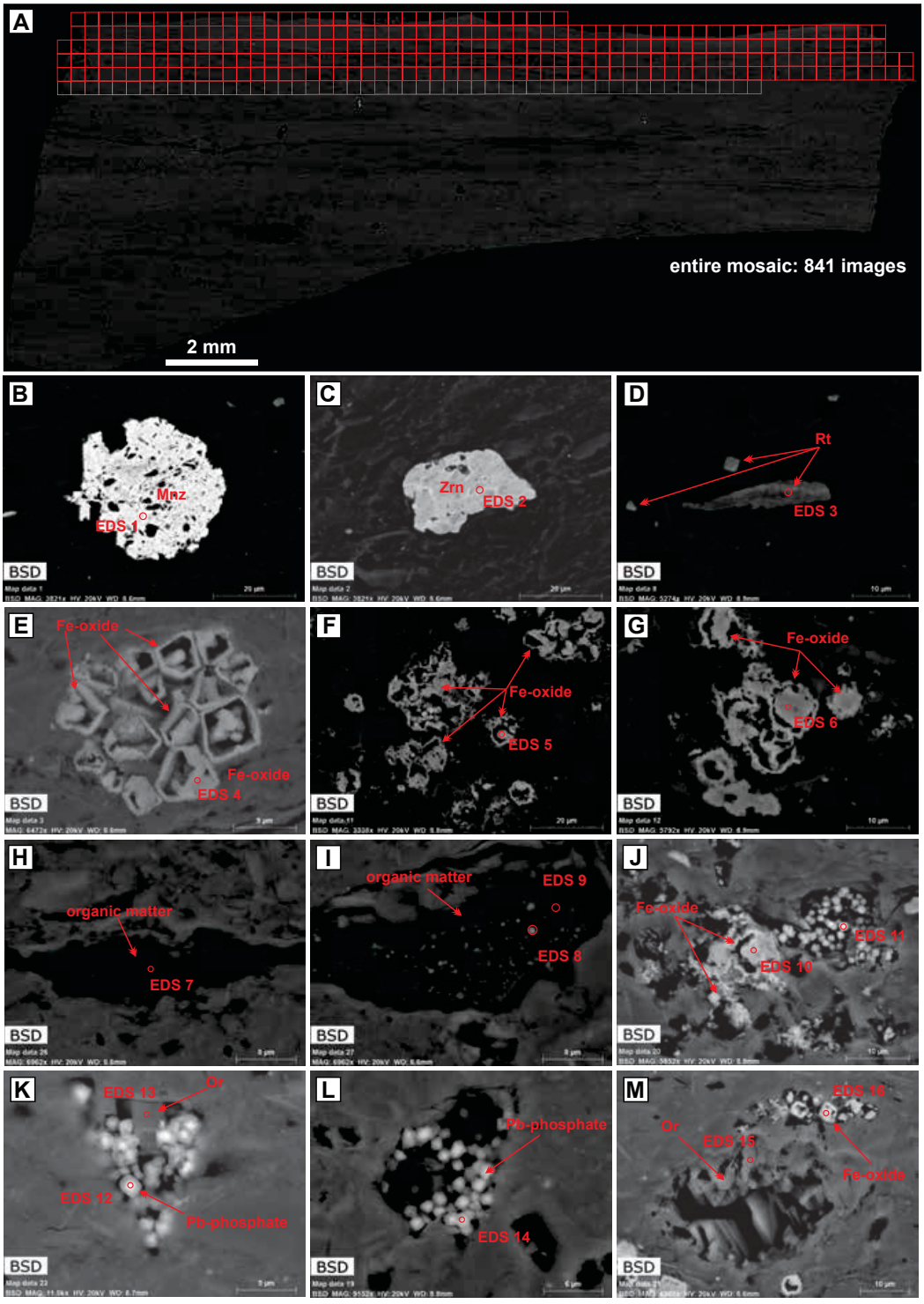

Figure A1: Scanning electron microscope (SEM) images of sample M103-475.2 showing EDS point analyses for spectra shown in Figure A1. (A) Atlas 5 large-area image mosaic of the entire sample, (B) diagenetic monazite, (C) zircon, (D) rutile. (E–G) iron oxide after pyrite, (H–I) organic matter, (J–L) secondary lead-phosphate minerals in pore spaces, (M) altered potassium feldspar.

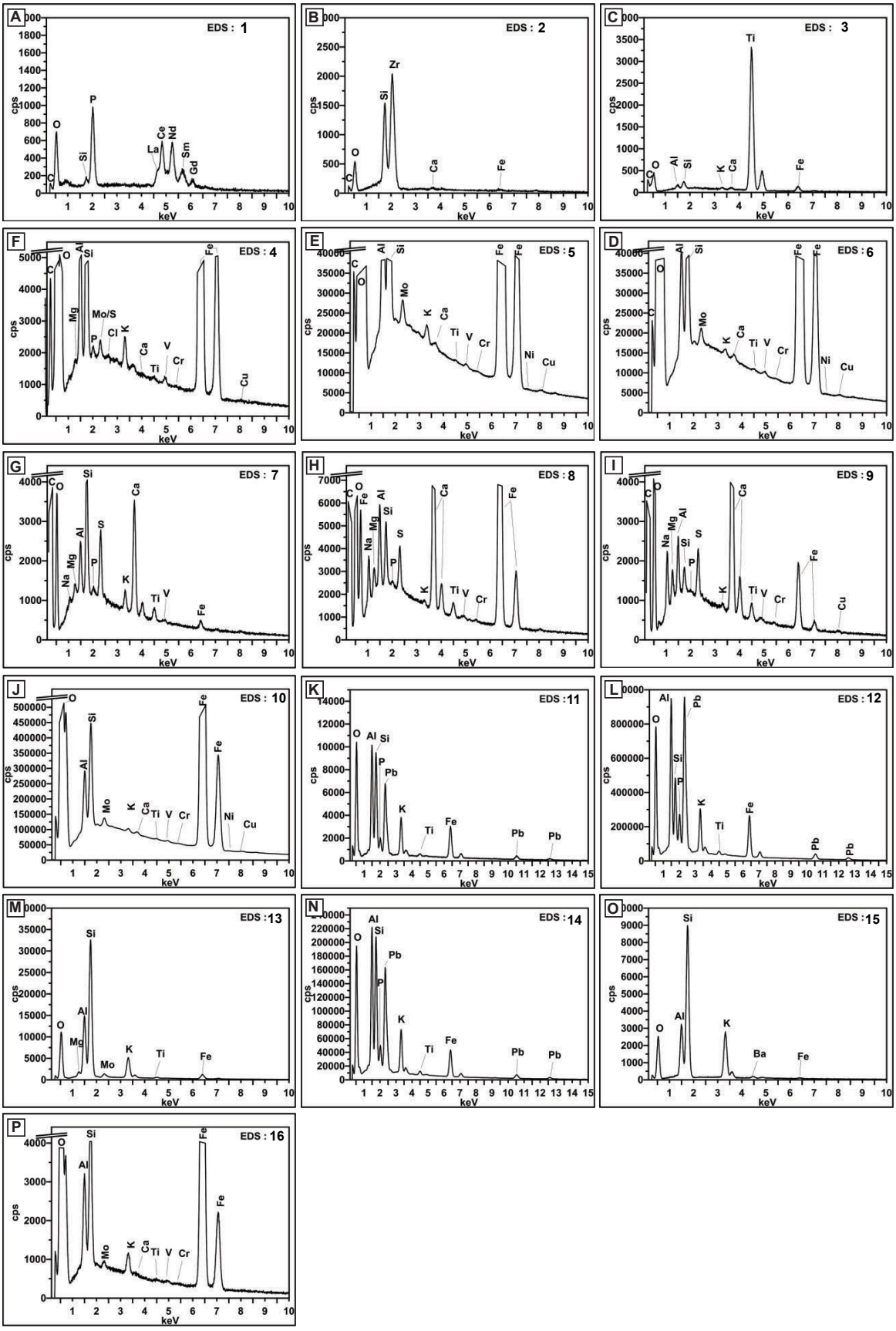
A
EDS : 1
O
Si
P
La
Ce
Nd
Sm
Gd
B
EDS : 2
O
Si
Zr
Ca
Fe
C
EDS : 3
Ti
O
Al
Si
K
Ca
Fe
F
EDS : 4
C
O
Al
Si
Mg
Mo/S
P
Cl
K
Ca
Ti
V
Cr
Fe
Cu
E
EDS : 5
C
O
Al
Si
Mo
K
Ca
Ti
V
Cr
Fe
Ni
Cu
D
EDS : 6
O
Al
Si
Mo
K
Ca
Ti
V
Cr
Fe
Ni
Cu
G
EDS : 7
C
O
Na
Mg
Al
Si
P
S
K
Ca
Ti
V
Fe
H
EDS : 8
C
O
Fe
Na
Mg
Al
Si
P
S
K
Ca
Ti
V
Cr
Fe
I
EDS : 9
C
O
Na
Mg
Al
Si
P
S
K
Ca
Ti
V
Cr
Fe
Cu
J
EDS : 10
O
Al
Si
Mo
K
Ca
Ti
V
Cr
Fe
Ni
Cu
K
EDS : 11
O
Al
Si
P
Pb
K
Ti
Fe
Pb
Pb
L
EDS : 12
O
Al
Si
P
Pb
K
Ti
Fe
Pb
Pb
M
EDS : 13
O
Mg
Al
Si
Mo
K
Ti
Fe
N
EDS : 14
O
Al
Si
P
Pb
K
Ti
Fe
Pb
Pb
O
EDS : 15
O
Al
Si
K
Ba
Fe
P
EDS : 16
O
Al
Si
Mo
K
Ca
Ti
V
Cr
Fe
cps
keV

Figure A2: Energy-dispersive spectroscopy (EDS) point analyses of the mineral phases shown in Figure A1. (A) EDS 1—monazite, (B) EDS 2—zircon, (C) EDS 3—rutile, (D-F) EDS 4, 5, 6—iron oxide phase (ghost pyrite), (G) EDS 7—maceral with nano-scale mineral phases, (H) EDS 8—iron oxide phase growing in the maceral, (I) EDS 9—maceral, (J) EDS 10—iron oxide phase (ghost pyrite), (K-L) EDS 11, 12—lead phosphate phase, (M) EDS 13—orthoclase, (N) EDS 14—lead phosphate phase, (O) EDS 15—orthoclase, (P) EDS 16—iron oxide phase (ghost pyrite).

Conclusions and Future Directions

This thesis implements diverse techniques to characterize the depositional history, age, geobiology, and biogeochemistry of evolutionarily important late Mesoproterozoic to early Neoproterozoic sedimentary environments. This work highlights dynamic interactions between Earth systems during an interval that is commonly cited as the dullest of our planet's history. While there is no evidence for major climate catastrophes between 1200 and 800 Ma, it is becoming increasingly clear that the building blocks for late Proterozoic global change (e.g., eukaryotic radiation, enhanced chemical weathering, oxygenation of the atmosphere and oceans, etc.) emerged earlier than previously appreciated. Results from this thesis offer substantial improvements to the age and stratigraphic architecture of the Bylot Supergroup and tectonic evolution of the Borden Basin. These results also provide a revised timeline in which to investigate when photosynthetic eukaryotes began fueling the global biosphere.

Although photosynthetic eukaryotes evolved ca. 1250 Ma and algae emerged by ca. 1050 Ma (Butterfield et al., 2000; Gibson et al., 2017), diverse eukaryotic fossil assemblages and crown group taxa are relatively uncommon until the middle Tonian Period, after ca. 800 Ma (Cohen and Macdonald, 2015; Riedman and Sadler, 2017). Furthermore, recent biomarker compilations indicate that algae did not dominate global ecosystems until the terminal Cryogenian Period (ca. 645 Ma; Brocks et al., 2017; Hoshino et al., 2017). Together, these data suggest a significant lag between early photosynthetic eukaryotes and their proliferation in global oceans; however, considering (1) the propensity for ancient biological records to suffer from preservational and sampling biases, and (2) the limited biomarker data available using rigorous protocols (i.e., French et al., 2015), these interpretations regarding the cadence of eukaryotic evolution are nascent at best.

Therefore, I plan to interrogate sedimentary records spanning 1050 to 645 Ma to calibrate our current understanding of the nature and pace of photosynthetic eukaryotic evolution and the rise of algae to ecological dominance. Specifically, I will study thermally immature organic-rich strata to assess their hydrocarbon biomarkers. Identifying diagnostic steranes (C_{29}>C_{27}) and sterane/hopane ratios characteristic of algal primary productivity from this interval will fundamentally alter current perspectives for when algae began controlling global biogeochemical cycles (Kodner et al., 2008). I will also obtain Re-Os and U-Pb radiometric dates from theses strata

to constrain the age of these and other paleontological data acquired by collaborators. These data will allow me to test the hypotheses that eukaryotes underwent a "diversification event" ca. 800 Ma and that the algae remained ecological insignificant until the Cryogenian Period, at least 400 million years after their emergence.

References

Brocks, J. J., Love, G. D., Summons, R. E., Knoll, A. H., Logan, G. A., and Bowden, S. A., 2005, Biomarker evidence for green and purple sulphur bacteria in a stratified Palaeoproterozoic sea: Nature, v. 437, p. 866-870.

Butterfield, N. J., 2000, Bangiomorpha pubescens n. Gen., n. sp.: Implications for the evolution of sex, multicellularity, and the Mesoproterozoic/ Neoproterozoic Radiation of Eukaryotes: Paleobiology, p. 386-404.

Cohen, P. A., and Macdonald, F. A., 2015, The Proterozoic Record of Eukaryotes: Paleobiology, v. 41, p. 610-632.

French, K., Hallmann, C., Hope, J. M., Schoon, P. L., Zumberge, J. A., Hoshino, Y., Peters, C. A., George, S. C., Love, G. D., Brocks, J. J., Buick, R., and Summons, R. E., 2015, Reappraisal of hydrocarbon biomarkers in Archean rocks: Proceedings of the National Academy of Sciences, v. 112, p. 5915-5920.

Gibson, T. M., Shih, P. M., Cumming, V. M., Fischer, W. W., Crockford, P. W., Hodgskiss, M. S. W., Wörndle, S., Creaser, R. A., Rainbird, R. H., Skulski, T. H., and Halverson, G. P., 2017, Precise age of *Bangiomorpha pubescens* dates the origin of eukaryotic photosynthesis: Geology, v. 46, p. 135-138.

Hoshino, Y., Poshibaeva, A., Meredith, W., Snape, C., Poshibaev, V., Versteegh, G. J. M., Kuznetsov, N., Leider, A., van Maldegem, L., Neumann, M., Naeher, S., Moczydlowska, M., Brocks, J. J., Jarrett, A. J. M., Tang, Q., Xiao, S., McKirdy, D., Das, S. K., Alvaro, J. J., Sansjofre, P., and Hallmann, C., 2017, Cryogenian evolution of stigmasteroid biosynthesis: Science Advances, v. 3.

Knoll, A. H., and Nowak, M. A., 2017, The timetable of evolution: Science advances, v. 3, p. e1603076.

Kodner, R. B., Pearson, A., Summons, R. E., and Knoll, A. H., 2008, Sterols in red and green algae: quantification, phylogeny, and relevance for the interpretation of geologic steranes: Geobiology, v. 6, p. 411-420.

Riedman, L. A., and Sadler, P. M., 2017, Global species richness record and biostratigraphic potential of early to middle Neoproterozoic eukaryote fossils: Precambrian Research, *in press*.